

Thermal Control of High-Powered Desktop and Laptop Microprocessors Using Two-Phase and Single-Phase Loop Cooling Systems

A thesis submitted in fulfilment of the requirements for
the degree of Doctor of Philosophy

Randeep Singh

B.Tech.

School of Aerospace, Mechanical and Manufacturing Engineering,
RMIT University,

March 2006

*Dedicated to my parents, Mamma and Papa,
For their guidance, inspiration, encouragement and love throughout my life*

Declaration

I, Randeep Singh, hereby submit the thesis titled “*Thermal Control of High-Powered Desktop and Laptop Microprocessors Using Two-Phase and Single-Phase Loop Cooling Systems*” for the degree of Doctor of Philosophy and certify that except where due acknowledgement has been made; the work is that of the candidate alone; the work has not been submitted previously, in whole or in part, for any other academic award and that the content of the thesis is the result of work which has been carried out since the official commencement of the approved research program.

Randeep Singh

March 2006

Acknowledgements

Throughout my research program, I have gained valuable experience and advice from many people and at this point I really feel obliged to thank them all for being so helpful to me. First and foremost, I would like to express my sincere gratitude to my supervisor, Prof. Aliakbar Akbarzadeh from RMIT University for his continuous support, valuable guidance and fruitful discussions in every aspect of my research work. I would also like to thank my co-supervisor Mr. Chris Dixon from RMIT University for providing me with practical knowledge in heat transfer systems and for this help in preparing the drafts of this thesis.

I am indebted to Dr. Mochizuki from Fujikura Ltd. Japan, for his guidance and support during my research work in Japan. The work was a great learning experience and contributed immensely to building up my industrial and research skills. I am pleased to acknowledge generous assistance from various personnel working in the Thermal Technology Division of Fujikura throughout my research experience. Dr. Yuji Saito, Dr. Thang Nguyen and Mr. Vijit Wuttijumnong provided valuable suggestions relating to my research project. Mr. Eiji Takenaka and Mr. Tetsu Sadahiro provided continuous help with my experiments in the thermal laboratory. Mr. Tien Nguyen provided assistance and support in the 3D modelling. A special thanks are due to Ms. Suzuko Iwata for her kind nature and support in a place distant away from my home.

I would like to express sincere thanks to my research consultant Dr. Roger R Riehl for sharing with me his expertise knowledge of two phase cooling technology.

Most importantly, I must thank my family back in India for their care and encouragement throughout my student years: my mother Harbhajan for her concern and love, father Joginder for his constant motivation and inspiration, sister Karamjit for her guidance and advice, brother Jatinder for taking care of all my responsibilities at home while I was overseas and grandfather Pritam for his love towards me.

Thanks to Ashwani for being a true friend, Babneet for his motivation and best wishes, and Gagan and Aman for their special consideration towards me. I would also like to acknowledge RMIT Energy CARE group and my colleagues in the research office who have always provided assistance where necessary.

Table of Contents

	<i>Page</i>
Declaration	iii
Acknowledgments	iv
Table of Contents	v
List of Figure Captions	xi
List of Table Captions	xxiii
Nomenclature	xxiv
Abstract	xxx
 Chapters	
1. Introduction	1
1.1 Background	1
1.2 Thermal Control of Computer Microprocessors	2
1.2.1 Laptop Thermal Control	2
1.2.1.1 Hybrid System	3
1.2.1.2 Remote Heat Exchanger	4
1.2.1.3 Vapour Chambers	5
1.2.2 Desktop Thermal Control	6
1.2 Thesis Outline	10
1.3 List of Publications	12
2. Introduction and Literature review	14
2.1 Two Phase Cooling System Using Loop Heat Pipes: Introduction	15
2.2 Background	15
2.3 Two-Phase Loops	17
2.3.1 Differences in LHP and CPL Technology	18
2.4 Loop Heat Pipe: Physical Concept	19
2.5 Problem Description	22
2.6 Research Scope	22
2.7 Research Objectives	23
2.8 Literature Review on Loop Heat Pipes	24
2.8.1 LHP Background	24

2.8.2	LHP Evaporator	25
2.8.2.1	Vapour Removal Channel	25
2.8.2.2	Capillary Structure	25
2.8.3	Compensation Chamber	27
2.8.4	Condenser	28
2.8.5	Working Fluid	30
2.8.6	Material Compatibility Study	31
2.8.7	Development of miniature Loop Heat Pipes (mLHPs)	32
2.8.7.1	mLHPs with Cylindrical Evaporators	34
2.8.7.2	mLHPs with Flat Evaporators	35
2.9	Conclusions from the Current Body of Knowledge	38
2.10	Single Phase Liquid Cooling System: Introduction	39
2.11	Problem Description	40
2.12	Scope of the Research Work	41
2.13	Objectives of the Research Work	41
2.14	Literature Review of Single Phase Liquid Cooling Systems	42
2.14.1	Single Phase Liquid Cooling using a Microchannel Heat Sink (MHS)	42
2.14.2	Conclusions from the Current Body of Knowledge	45
2.14.3	Single Phase Liquid Cooling using a Sintered Porous Heat Sink (SPHS)	46
2.14.4	Conclusions from the Current Body of Knowledge	47
3.	Theoretical Modelling of Loop Heat Pipe	50
3.1	Principle and Operation	50
3.2	Conditions of LHP Serviceability	52
3.2.1	Maximum Capillary Pressure Limit	52
3.2.2	Wick limitation	53
3.2.3	Liquid Line Boiling Limit	54
3.3	LHP Mathematical Model	54
3.3.1	Fluid Properties	55
3.3.2	Energy Balance	56
3.3.3	Heat Leakage across the Wick	60
3.3.4	Pressure Analysis	61
3.3.4.1	Vapour Pressure Drop	62
3.3.4.2	Liquid Pressure Drop	63
3.3.4.3	Hydrostatic Losses	64
3.3.5	Effective Thermal Conductivity of Wetted Wick	64
3.3.6	Return Liquid Subcooling	65
3.3.7	Fin-and-Tube Condenser Analysis	66
3.3.7.1	Heat Transfer Rate per Unit Length of the Condenser	67
3.3.7.2	Mass Flow Rate of Fan Air	68
3.3.7.3	Heat Transfer Coefficient of Air	68
3.3.7.4	Overall Surface Efficiency of the Condenser	68

	3.3.7.5 Log Mean Temperature Difference (LMTD)	69
	3.3.7.6 Two Phase Length (Active Portion) of the Condenser	69
	3.3.7.7 Liquid Temperature at the Condenser Outlet	70
	3.3.7.8 mLHP Operating Temperature	70
3.4	mLHP Maximum Heat Transfer Capacity	71
3.5	Thermal Resistance	72
3.6	Summary	74
<hr/>		
4.	mLHP with Disk Shaped Evaporator: Experimental Apparatus and Method	75
<hr/>		
4.1	mLHP Prototype Description	75
4.1.1	Evaporator Structure	76
4.1.1.1	Evaporator Bottom Portion	78
4.1.1.2	Evaporator Heat Acquisition Region	79
4.1.1.3	Wick Structure	80
4.1.1.4	Compensation Chamber (Evaporator Top Portion)	81
4.1.1.5	Fin and Tube Condenser	82
4.2	Cleaning Procedure	83
4.3	Charging Procedure	83
4.4	Testing Method	85
4.5	Summary	87
<hr/>		
5.	mLHP with Disk Shaped Evaporator: Results and Discussion	89
<hr/>		
5.1	Thermal Characteristics of the mLHP	90
5.1.1	Start-Up Phenomena	90
5.1.2	Steady State Operation	92
5.2	mLHP Failure Mode Analysis	97
5.2.1	Start-Up Failure due to Leakage	97
5.2.2	Start-up Failure due to Insufficient Fluid Inventory	99
5.3	Start-up Trends of the mLHP	101
5.4	Comparison of Theoretical and Experimental Models	104
5.5	Effect of the Fluid Inventory on mLHP Thermal Performance	107
5.6	Effect of Tilt on the mLHP Thermal Performance	109
5.7	Thermal Performance of the mLHP under Different Heating Modes	112
5.8	Thermal Performance of the mLHP with Different Wick Configurations	117
5.8.1	Effect of the Wick Material	117
5.8.2	Effect of the Physical Properties	120
5.8.3	Effect of the Wick Structure	123

5.9	Effect of Non Condensable Gases (NCGs) on the mLHP Thermal Performance	125
5.9.1	NCG Detection	127
5.9.2	Effect of the NCG on the Steady State Performance of a mLHP	127
5.9.3	Effect of the NCG on the Start-up Process	131
5.9.4	Purging of NCG from a mLHP	132
5.9.5	Methods to Decrease NCG Generation inside a mLHP	135
5.10	Summary	136
<hr/>		
6.	mLHP with Flat Rectangular Evaporator	138
6.1	Introduction	138
6.2	Description of the mLHP Prototype	139
6.3	Experimental Apparatus and Testing Method	145
6.4	Results and Discussion	146
6.4.1	Thermal Characteristics of the Flat Rectangular Evaporator mLHP	146
6.5	Comparison of the Thermal Performance of the Disk Shaped and Rectangular Shaped Evaporators	149
6.6	Summary	153
<hr/>		
7.	Liquid Cooling using a Microchannel Heat Sink (MHS)	155
7.1	Introduction	155
7.2	Description of Microchannel Heat Sink Prototype	156
7.3	Experimental Setup and Test Procedure	158
7.4	Heat Transfer Analysis	163
7.4.1	Heat Transfer Correlations	165
7.5	Result and Discussion	168
7.5.1	Thermal Characteristics of MHS using 11x13 mm ² Heat Source	168
7.5.2	Thermal Performance of MHS with Different Heater Sizes	170
7.5.3	Thermal Performance of MHS with Different Flow Rates	172
7.6	Comparison of Experimental and Predicted Results	175
7.7	Summary	177
<hr/>		
8.	Liquid Cooling using a Sintered Porous Heat Sink	179
8.1	Introduction	179
8.2	Description of the Sintered Porous Heat Sink Prototype	180
8.3	Experimental Setup and Test Procedure	184
8.4	Data Reduction	186

8.5	Results and Discussion	188
	8.5.1 Pressure Drop	188
	8.5.2 Heat Transfer	188
8.6	Comparison of Thermal Performance of Microchannel and Sintered Porous Heat Sinks	191
8.7	Summary	195
<hr/>		
9.	Comparative Study: Two-Phase Vs Liquid Cooling	196
9.1	Introduction	196
9.2	Experimental Setup and Test Procedure	197
	9.2.1 Heat Pipe Cooling Unit (Two-Phase Heat Transfer System)	197
	9.2.2 Liquid Cooling Unit (Single Phase Heat Transfer System)	201
9.3	Results and Discussion	205
	9.3.1 Single Heat Source Cooling	205
	9.3.2 Multiple Heat Source Cooling	207
9.4	Summary	210
<hr/>		
10.	Conclusions and Recommendations	211
10.1	Concluding Remarks	211
10.2	Conclusions from Study on Two-Phase Cooling Systems	212
	10.2.1 Miniature Loop Heat Pipe with a Flat Disk Shaped Evaporator	212
	10.2.2 Miniature Loop Heat Pipe with a Flat Rectangular Shaped Evaporator	215
	10.2.3 Capillary Pumped Loop with a Cylindrical Evaporator	216
10.3	Conclusions from Study on Single Phase Cooling Systems	216
	10.3.1 Liquid Cooling using a Microchannel Heat Sink	217
	10.3.2 Liquid Cooling using a Sintered Porous Heat Sink	217
10.4	Conclusions on Measurement of Properties of Porous Structures	218
10.5	Recommendations for Future Work	218
<hr/>		
	References	220
<hr/>		
	Appendix A: mLHP Modelling Data	228
<hr/>		
	Appendix B: Case Study: Capillary Pumped Loop (CPL) with Cylindrical Evaporator	230
<hr/>		
B.1	Introduction	230
B.2	Objective of Study	232
B.3	Description of Capillary Pumped Loop (CPL) Prototype	233

B.3.1	Evaporator Structure	234
B.3.2	Condenser	236
B.3.3	Liquid and Vapour Transport Lines	236
B.3.4	Reservoir	237
B.4	Loop Pressure Analysis	237
B.5	Experimental Setup	238
B.6	Experimental Procedure	240
B.7	Results and Discussion	241
B.8	Summary	246
<hr/> Appendix C: Experimental Determination of Properties of a Porous Structure		248
C.1	Introduction	248
C.2	Description of Experimental Samples	250
C.3	Experimental Scope	251
C.4	Objectives of the Study	251
C.5	Physical Properties	251
C.5.1	Permeability	252
	C.5.1.1 Concept	252
	C.5.1.2 Measurement	252
C.5.2	Pore Radius	255
	C.5.2.1 Concept	255
	C.5.2.2 Measurement	256
	C.5.2.2.1 Measurement of Largest Pore Radius	256
	C.5.2.2.2 Measurement of Effective Pore Radius	260
C.5.3	Porosity	262
	C.5.3.1 Concept	262
	C.5.3.2 Measurement	262
C.5.4	Effective Thermal Conductivity	264
	C.5.4.1 Concept	264
	C.5.4.2 Measurement	265
C.6	Summary	267

List of Figure Captions

	<i>Page</i>
Figure 1.1 Trends in Thermal Solutions for Laptop PCs	3
Figure 1.2 Hybrid thermal control system for laptop microprocessors.	4
Figure 1.3 Remote Heat Exchanger for cooling laptop microprocessors.	5
Figure 1.4 Different designs of vapour chamber used for laptop cooling	5
Figure 1.5 Thermal control system with vapour chamber for laptop cooling	6
Figure 1.6 Different Types of Thermal Solution for Desktop Computer Cooling	7
Figure 1.7 Thermal Solution Trends	9
Figure 2.1 Conventional Capillary Driven Heat Pipe	15
(a) Bottom Heat Mode Operation (Evaporator-Below-Condenser)	
(b) Top Heat Mode Operation (Evaporator-Above-Condenser)	
Figure 2.2 Arterial Heat Pipes	16
Figure 2.3 Separated lines heat pipe	16
Figure 2.4 Loop Scheme	17
Figure 2.5 Loop Heat Pipe (LHP)	18
Figure 2.6 Capillary Pumped Loop (CPL)	18
Figure 2.7 Schematic of Loop Heat Pipe	20
Figure 2.8 Scheme of organisation of evaporation zone by the principle of an inverted meniscus	20
Figure 2.9 Available cooling space inside the laptop computer	22
(a) Top View	
(b) Side View	
Figure 2.10 Different variants of LHP condenser	29
(a) Fin-and-Tube Type Condenser	
(b) Concentric Tube Type Condenser	

	(c) Collector Type Condenser	
	(d) Coil and Plate Type Condenser	
Figure 2.11	Schematic of a Microchannel Heat Sink	43
	(a) Top View	
	(b) Sectional View (A-A)	
	(c) Side View	
Figure 2.12	Schematic of a Sintered Porous Heat Sink	46
	(a) Top View	
	(b) Sectional View (A-A)	
	(c) Side View	
Figure 3.1	LHP schematic (<i>Ref: Maydanik & Fershtater, 1997</i>)	51
Figure 3.2	P-T diagram of the LHP working cycle	51
Figure 3.3	Schematic of the miniature LHP showing various control volumes for the energy balance	56
Figure 3.4	Energy Balance inside Control Volume 1	56
Figure 3.5	Energy Balance inside Control Volume 2	57
Figure 3.6	Energy Balance inside Control Volume 3	58
Figure 3.7	Schematics of the LHP condenser	66
	(a) Top View	
	(b) Side View	
Figure 3.8	Thermal circuit diagram for the mLHP showing thermal resistances of different components	72
Figure 4.1	Prototype of Miniature Loop Heat Pipe (mLHP) showing the different components	76
Figure 4.2	Exploded view of the capillary evaporator showing the different parts	77
Figure 4.3	mLHP Evaporator	78
	(a) External view	
	(b) Internal View (Section A-A)	

Figure 4.4	Details of Vapour removal channels	79
(a)	Top view	
(b)	Sectional Detail (B-B)	
(c)	Side view	
Figure 4.5	Details of Fin-and-Tube Condenser	82
(a)	Side view	
(b)	Sectional View (D-D)	
(c)	Sectional View (C-C)	
(d)	Top view	
Figure 4.6	Charging procedure for mLHP	84
Figure 4.7	Schematic of the experimental prototype and test layout for the mLHP	86
(a)	Sectional view of the heater face	
(b)	Cross sectional view of the heater block	
(c)	Bottom view	
(d)	Top view	
(e)	Side view	
Figure 5.1	Start-up of the mLHP at 15W input power	91
Figure 5.2	Heat load dependence of the evaporator surface temperature	93
Figure 5.3	Heat transfer coefficient versus applied heat load	94
Figure 5.4	Heat pipe thermal resistance versus applied heat load	95
Figure 5.5	Total thermal resistance versus applied heat load	96
Figure 5.6	Evaporator thermal resistance versus applied heat load	96
Figure 5.7	Start-up failure due to leakage in external sealing	98
Figure 5.8	Start-up failure due to internal leakage	98
Figure 5.9	Start-up failure of the mLHP under 30% fluid charge	100
Figure 5.10	Start-up failure of the mLHP under 40% fluid charge	100
Figure 5.11	Start-up trend shown by the mLHP when the liquid-vapour interface is already present in the evaporator before heat load is applied	101

Figure 5.12	Start-up trend shown by the mLHP when in the pre start state the vapour removal channels are completely flooded with liquid	102
Figure 5.13	Start-up trend shown by the mLHP when in the pre start state insufficient fluid inventory is present in the compensation chamber	103
Figure 5.14	Comparison of theoretically predicted and experimentally determined results for the mLHP design with sintered nickel capillary structure	104
Figure 5.15	Comparison of predicted and experimental results for the mLHP design with sintered copper capillary structure	105
Figure 5.16	Effect of the fluid charge on the evaporator wall temperature for the given range of applied heat loads	108
Figure 5.17	Test setup to measure the thermal performance of the mLHP at different tilt angles	109
Figure 5.18	Effect of the tilt angle on the thermal performance of the mLHP	110
Figure 5.19	Change in the fluid distribution inside the compensation chamber with the increase in the tilt angle	111
Figure 5.20	Start-up of the mLHP with uniform heating of the evaporator active face at input power of 20 W	113
Figure 5.21	Start-up of the mLHP with non-uniformly heating of the evaporator active face at input power of 20 W	113
Figure 5.22	Thermal performance (evaporator wall temperature versus applied heat load) of mLHP for uniform as well as non uniform heating modes	114
Figure 5.23	Evaporator thermal resistance versus applied heat load for uniform and non uniform heating modes	115
Figure 5.24	Heat pipe thermal resistance versus applied heat load for uniform and non-uniform heating modes	116
Figure 5.25	Total thermal resistance versus applied heat load for uniform and non uniform heating modes	116
Figure 5.26	Heat load dependence of the evaporator wall temperature with nickel and copper wicks	118

Figure 5.27	Heat load dependence of the evaporator wall temperature for mLHP with nickel and copper wicks	119
Figure 5.28	Evaporator thermal resistance versus applied heat load for mLHP with nickel and copper wicks	120
Figure 5.29	Heat load dependence of the evaporator wall temperature for monoporous copper wicks with different physical properties	122
Figure 5.30	Structure of biporous wick	123
Figure 5.31	Combined Copper wick showing monoporous and biporous layers	124
(a)	Side View of the combined copper wicks	
(b)	Monoporous layer as an absorbing face of the combined wick	
(c)	Biporous layer as an evaporating face of the combined wick	
Figure 5.32	Heat load dependence of the evaporator wall temperature for mLHP with monoporous and combined wick	124
Figure 5.33	Evaporator temperature trend with respect to the applied heat load for the number of trial runs made on the mLHP over a period of time	128
Figure 5.34	Change in the absolute pressure inside the loop due to the generation of NCG over a period of time.	128
Figure 5.35	Oxidation of the container and wick material due to the reaction and absorption of the NCG gas accumulated inside the compensation chamber	130
Figure 5.36	Temperature profile on the surface of the compensation chamber taken with the help of five K-Type thermocouples	131
Figure 5.37	Start-up trend shown by the mLHP with and without NCG	132
Figure 5.38	Design arrangement for purging the NCG from the mLHP system	133
Figure 5.39	Experimental Set-up for purging the NCG from the mLHP	134
Figure 5.40	Operational Characteristics of the mLHP before and after purging procedure	134

Figure 5.41	Operational Characteristics of the mLHP before and after degassing procedure	135
Figure 6.1	Schematic of Flat Rectangular Evaporator mLHP showing the components	140
Figure 6.2	Exploded view of the capillary evaporator showing the parts	141
Figure 6.3	mLHP Evaporator	142
(a)	External view	
(b)	Sectional View (A-A)	
Figure 6.4	Plan view of the evaporator body	142
Figure 6.5	Details of vapour removal channels	143
(a)	Top view	
(b)	Side view	
(c)	Sectional View (B-B)	
Figure 6.6	Details of Fin-and-Tube Condenser	144
(a)	Side view	
(b)	Sectional View (D-D) showing Fin Geometry	
(c)	Sectional View (C-C) showing Condenser Details	
Figure 6.7	Experimental set up for testing the flat rectangular evaporator mLHP	145
(a)	Bottom View	
(b)	Top View	
Figure 6.8	Start-up of rectangular evaporator mLHP at 20 W input power	146
Figure 6.9	Heat load dependence of the rectangular evaporator mLHP evaporator temperature	147
Figure 6.10	Evaporator thermal resistance versus applied heat load for the rectangular evaporator mLHP	148
Figure 6.11	Total thermal resistance versus applied heat load for the rectangular evaporator mLHP	148
Figure 6.12	Comparison of the heater interface temperature for the disk shaped evaporator mLHP and rectangular evaporator mLHP at the same range of input heat loads.	149

Figure 6.13	Comparison of the evaporator temperature for the disk shaped evaporator mLHP and rectangular evaporator mLHP at the same range of input heat loads.	149
Figure 6.14	Cross section of the disk shaped evaporator showing internal structures and directions of the liquid and heat flows relative to each other	150
Figure 6.15	Cross section of the rectangular shaped evaporator showing internal structures and directions of the liquid and heat flows relative to each other	150
Figure 6.16	Evaporator thermal resistance for the disk shaped evaporator mLHP and rectangular evaporator mLHP at the same range of input heat loads.	152
Figure 6.17	Total thermal resistance for the disk shaped evaporator mLHP and rectangular evaporator mLHP at the same range of input heat loads.	153
Figure 7.1	Layout of the Microchannel heat sink assembly	156
(a)	Exploded View showing the Details of the Top Portion	
(b)	Exploded View showing the Details of the Bottom Portion	
Figure 7.2	Schematic of the Microchannels	157
(a)	Side View	
(b)	Top View	
(c)	Enlarged View of the Fin-Channel Section (B-B)	
(d)	Sectional View of Microchannel Heat Sink (A-A)	
Figure 7.3	Internal details and liquid flow path inside the microchannel heat sink	158
(a)	Side View	
(b)	Isometric Cross Sectional View	
Figure 7.4	Experimental Setup to test microchannel heat sink	159
Figure 7.5	Cross sectional view of the microchannel heat sink and distributed finned heat exchanger showing the fluid flow pattern inside the cooling unit.	160
Figure 7.6	Test bed for the Microchannel heat sink	160
Figure 7.7	Experimental setup for open loop system	161
Figure 7.8	Experimental setup for closed loop system	161

Figure 7.9	Test facility for the heat sink showing the location of the thermocouples on the microchannel heat sink	162
Figure 7.10	Test facility for the heat sink showing the location of the thermocouples on the Finned Heat Exchanger	163
Figure 7.11	Heat load dependence of the Interface temperature of the microchannel heat sink with the 11mm x 13mm heat source	169
Figure 7.12	Cold plate thermal resistance and total thermal resistance of the microchannel heat sink with respect to the applied heat load using 11mmx13mm heat source	169
Figure 7.13	Heat load dependence of the Interface temperature of the microchannel heat sink with different heater sizes (7 x7 mm ² , 11 x13 mm ²)	170
Figure 7.14	Variation of the cold plate thermal resistance of the microchannel heat sink with the applied heat load with different heater sizes (7 x7 mm ² , 11 x13 mm ²)	171
Figure 7.15	Variation of the total thermal resistance of the microchannel heat sink with the applied heat load for different heater sizes (7 x7 mm ² , 11 x13 mm ²)	172
Figure 7.16	Heat load dependence of the interface temperature for the microchannel heat sink for different flow rates	173
Figure 7.17	Cold plate thermal resistance of the microchannel heat sink with respect to the applied heat load for different flow rates	173
Figure 7.18	Heat transfer coefficient of the microchannel heat sink with respect to the applied heat load for different flow rates	174
Figure 7.19	Variation of the heat transfer coefficient with applied heat load: Comparison of the experimental and the predicted results by using different entry length conditions and flow regimes	175
Figure 7.20	Variation of the Nusselt number with Reynolds number: Comparison of the experimental and the predicted results by using different entry length conditions and flow regimes	176
Figure 8.1	Layout of Sintered Porous Heat Sink	180

Figure 8.2	Internal structure of the Sintered Porous Heat Sink	181
Figure 8.3	Picture of the cooling section showing the Porous Insert inside the machined rectangular channel	181
Figure 8.4	Exploded View of the Sintered Porous Heat Sink	182
Figure 8.5	Sample of the sintered porous material at different magnifications showing rounded irregular copper granular particles fused together as the result of the sintering process	183
Figure 8.6	Cross Sectional view of the sintered porous heat sink showing the liquid flow pattern inside the cooling section	184
Figure 8.7	Experimental Setup of the Sintered Porous Heat Sink	185
Figure 8.8	Test Facility for the Sintered Porous Heat Sink showing the location of the thermocouple points	186
Figure 8.9	Pressure drop versus flow rate for the Sintered Porous Heat Sink	188
Figure 8.10	Interface temperature versus flow rate for applied heat load of 100 W	189
Figure 8.11	Relationship between the interface temperature and the applied heat load for different flow rates	189
Figure 8.12	Heat transfer coefficient versus applied heat load for different flow rates	190
Figure 8.13	Cold plate thermal resistance versus applied heat load for different flow rates	190
Figure 8.14	Cold plate thermal resistance versus flow rate for applied heat load of 100 W	191
Figure 8.15	Comparison of the cold plate thermal resistance for Microchannel and Sintered Porous Heat Sinks	192
Figure 8.16	Comparison of the overall heat transfer coefficient (based on the heater active face area) for Microchannel and Sintered Porous Heat Sink	193
Figure 8.17	Comparison of the pressure drop across the heat sink versus flow rate for Microchannel and Sintered Porous Heat Sink	194

Figure 9.1	Heat Pipe Cooling Unit	198
Figure 9.2	Heat Pipe Module	198
Figure 9.3	Cross Section of the Heat Pipe showing internal configuration	198
Figure 9.4	Bottom perspective view of the Heat Pipe cooling unit showing the evaporator sections and related components.	200
Figure 9.5	Side View of the Heat Pipe Cooling Unit showing the heater locations	200
Figure 9.6	Liquid Cooling Unit	201
Figure 9.7	Microchannel for CPU size heater	202
Figure 9.8	Microchannel for MPU/GPU size heater	202
Figure 9.9	Bottom perspective view of the liquid cooling unit showing the evaporator sections and related components.	203
Figure 9.10	Side View of the liquid cooling unit showing the heater locations	203
Figure 9.11	Perspective view of the liquid cooling unit showing the fluid flow pattern inside the loop and location of each microchannel section.	204
Figure 9.12	Heat load dependence of the interface temperature for the heat pipe and liquid cooling unit	206
Figure 9.13	Total thermal resistance versus applied heat load for the heat pipe and liquid cooling unit	207
Figure 9.14	CPU Interface temperature versus CPU applied heat load for different power inputs to the GPU and MPU units (Heat pipe cooling unit)	208
Figure 9.15	CPU Interface temperature versus CPU applied heat load for different power inputs to the GPU and MPU units (Liquid cooling unit)	209

Figure 9.16	CPU Interface temperature versus CPU applied heat load for different power inputs to the GPU and MPU units : Comparison between heat pipe cooling unit and liquid cooling unit	209
Figure B.1	Schematic of CPL	231
Figure B.2	Layout of the Capillary Pumped Loop Experimental Model	233
Figure B.3	Design and detail of the axially grooved evaporator tube	234
(a)	Cross Section	
(b)	Axially Grooved Evaporator Tube	
(c)	Groove Specification	
Figure B.4	Exploded view of the Capillary Evaporator	235
Figure B.5	Schematic of CPL Evaporator	235
Figure B.6	Heat and Fluid flow inside the capillary evaporator	236
Figure B.7	CPL Experimental Setup	238
Figure B.8	CPL Test Bed	239
Figure B.9	Start up of CPL at 50 W heat load	241
Figure B.10	Start-up of CPL at 100 W heat load	242
Figure B.11	Evaporator temperature versus applied heat load for low heat inputs	243
Figure B.12	Evaporator temperature versus applied heat load for high heat inputs	244
Figure B.13	Variation of the evaporator thermal resistance with the applied heat load	245
Figure B.14	Variation of the total thermal resistance with the applied heat load	246
Figure C.1	Apparatus to measure permeability using a constant pressure reservoir	253
Figure C.2	Apparatus to measure permeability using pressure tuning arrangement	254

Figure C.3	Variation of specific permeability and mass flow rate with applied pressure across the porous structure	254
Figure C.4	U-Tube bubble point testing system	256
Figure C.5	Mechanism of bubble formation	257
Figure C.6	Modified form of bubble point testing system to measure the largest pore size in the fine pored wicks	259
Figure C.7	Method to determine mean pore size of the wick sample	261
Figure C.8	Comparison of porosity of the UHMW Polyethylene wick as determine by different methods	263
Figure C.9	Test sample showing the location of the heater and the finned heat exchanger	265
Figure C.10	Experimental setup for measuring the effective thermal conductivity of the copper wick saturated with water	266
Figure C.11	Effective thermal conductivity versus applied heat load for the copper wick saturated with water	266

List of Table Captions

	<i>Page</i>
Table 5.1	Maximum heat transfer capacity of the mLHP calculated on the basis of theoretical and experimental approaches. 106
Table 5.2	Physical properties of the monoporous copper wick 121
Table 8.1	Physical properties of copper wick (# 100-200 mesh size) 183
Table 9.1	Geometrical dimensions of the Heat Pipe Prototype 199
Table 9.2	Specifications of the Microchannels 202
Table A.1	Coefficients for fifth order polynomials for different thermodynamic properties with respect to saturation temperature, for water as working fluid 228
Table A.2	Nusselt numbers and friction factors for fully developed laminar flow in tubes of different cross section. (<i>Ref: Incropera and DeWitt, Page-496, Table 8.1</i>) 229
Table B.1	Major pressure drops in CPL 238
Table C.1	Permeability measurement for different types of copper wick 255
Table C.2	Largest Pore radius for UHMW Polyethylene wicks measured with U-tube bubble point testing system. 258
Table C.3	Largest pore radius measurement for different grades of copper wick measured with U-tube bubble point testing system. 260
Table C.4	Porosity measurement for different grades of copper wick 264

Nomenclature

Symbols		<i>Units</i>
A	Area of cross section	m^2
A_{ac}	Active heat transfer area of the condenser	m^2
A_{ae}	Active heat transfer area of the evaporator	m^2
A_{ft}	Total surface area of the fins in the entire fin stack	m^2
A_t	Total surface area of fins including the unfinned surface	m^2
A_w	Liquid absorption area of the wick	m^2
c_p	Specific heat	$J/Kg.K$
d	Depth	m
D	Internal diameter of the line	m
D_h	Hydraulic diameter	m
f	Darcy frictional factor	<i>dimensionless</i>
f_1, f_2	Functional relations	
g	Free fall acceleration	m/s^2
h	Heat transfer coefficient	$W/m^2.K$
h_l	Enthalpy of saturated liquid	J/Kg
h_{lv}	Latent heat of vaporization	J/Kg
h_v	Enthalpy of saturated vapour	J/Kg
H	Height	m
ΔH	Height difference	m
H_{evap}^{\bullet}	Enthalpy gain during the evaporation process,	W
H_{sc}^{\bullet}	Enthalpy gain by liquid due to change in temperature from saturation to subcooled state	W
I	Input current	A
k	Thermal conductivity	$W/m.K$
k_e	Effective thermal conductivity of the wetted wick structure	$W/m.K$
k_{ws}	Specific permeability of the wick structure	m^2

K	Darcy's permeability	$N.s$
l	Effective length of the device	m
L	Length of the channel or line	m
$L^{1\phi}$	Length of the single phase portion of the condenser	m
$L^{2\phi}$	Length of the two phase portion (active portion) of the condenser	m
m^\bullet	Mass flow rate	Kg/s
$m_a^{\bullet 1\phi}$	Mass flow of air through the single phase portion of the condenser	Kg/s
M	Merit number of heat transfer working fluid.	
N	Number of microchannels	
p	Perimeter	m
P	Pressure	Pa
ΔP	Pressure difference, pressure loss	Pa
$\Delta P_{l,ll}$	Liquid pressure drop due to the liquid flow in the liquid line	Pa
$\Delta P_{l,w}$	Liquid pressure drop due to the liquid filtration in the wick structure	Pa
$\Delta P_{v,c}$	Vapour pressure drop due to the vapour flow in the condenser	Pa
$\Delta P_{v,e}$	Vapour pressure drop due to vapour flow in the evaporator grooves	Pa
$\Delta P_{v,vl}$	Vapour pressure drop due to vapour flow in the vapour line	Pa
$(\Delta P_{cap})_{max}$	Maximum capillary pressure generated by the wick on liquid	Pa
q	Heat flux,	W/m^2
q_s''	Surface Heat flux	W/m^2
Q^\bullet	Heat flow	W
Q_a^\bullet	Applied heat load	W
$Q_c^{\bullet 2\phi}$	Heat rejected in the two phase portion of condenser	W
$Q_c^{\bullet 1\phi}$	Heat rejected in the liquid portion of condenser	W

$Q_{c/l}^{\bullet}$	Heat transfer rate per unit length of the condenser	W
Q_{cc-a}^{\bullet}	Heat exchange between the compensation chamber and surroundings	W
Q_{e-cc}^{\bullet}	Heat flow (or heat leaks) from the evaporator to the compensation chamber	W
Q_{ll-a}^{\bullet}	Heat exchange between the liquid line and surroundings	W
Q_{vl-a}^{\bullet}	Heat exchange between the vapour line and surroundings	W
r	Pore radius	m
r_{me}	Mean effective pore radius of porous structure	m
R	Thermal resistance	$^{\circ}C/W, K/W$
$R_{c,a}$	Thermal resistance from condenser to surroundings	$^{\circ}C/W, K/W$
t	Thickness	m
T	Temperature	$^{\circ}C, K$
$T_{a,i}$	Temperature of the air at the inlet of the fin channels of the condenser	$^{\circ}C, K$
$T_{a,o}$	Temperature of the air at the outlet of the fin channels of the condenser	$^{\circ}C, K$
$T_{c,i}$	Temperature of the vapour at the condenser inlet	$^{\circ}C, K$
$T_{c,o}$	Temperature of the liquid at the condenser outlet	$^{\circ}C, K$
$T_{e,o}$	Temperature of the vapour at the evaporator outlet	$^{\circ}C, K$
$T_{l,o}$	Liquid outlet temperature	$^{\circ}C, K$
$T_{l,i}$	Liquid inlet temperature	$^{\circ}C, K$
T_{mc}	Mean temperature of the condenser surface	$^{\circ}C, K$
T_{me}	Mean temperature of the evaporator surface	$^{\circ}C, K$
T_{mf}	Mean of the fluid inlet and outlet temperatures	$^{\circ}C, K$
ΔT	Temperature difference	$^{\circ}C, K$
ΔT_w	Temperature difference across the wick	$^{\circ}C, K$
$T_{lm,f-a}$	Log mean temperature difference between fin surface and ambient air	$^{\circ}C, K$

u	Velocity	m/s
V	Volume	m^3
$V \bullet$	Volume flow rate	m^3/s
V_e	Input voltage,	V
W	Width	m
x	Vapour quality / dryness fraction	$\%$
Y	Fluid Property	
$\left. \frac{dP}{dT} \right _{T_s}$	Slope of the saturation curve at a saturation temperature, T_s on the P-T diagram	$Pa/K, Pa/^{\circ}C$

Dimensionless numbers

Pr	Prandtl number	<i>dimensionless</i>
Re	Reynolds number	<i>dimensionless</i>
Nu	Nusselt number	<i>dimensionless</i>

Greek symbols

σ	Surface tension	N/m
μ	Viscosity	$Pa.s, N.s/m^2$
ρ	Density	Kg/m^3
v	Specific volume	m^3/Kg
η	Efficiency	$\%$
ϕ	Slope of the device referred to the horizontal plane	$^{\circ}$
ε	Porosity	$\%$
α	Aspect ratio	

Subscripts

a	Air, ambient
b	Fin base
c	Condenser

<i>ch</i>	Channel
<i>cl</i>	Condenser line
<i>cp</i>	Cold plate
<i>Cu</i>	Copper
<i>e</i>	Evaporator
<i>ec</i>	Ethanol column
<i>eg</i>	Evaporator groove
<i>et</i>	Ethanol
<i>f</i>	Fin
<i>fc</i>	Fin channel
<i>fd</i>	Fan duct
<i>fg</i>	Fin gap
<i>gr</i>	Gravitational field or gravity
<i>h</i>	Heater
<i>hp</i>	Heat pipe
<i>hsb</i>	Heat sink base
<i>hx</i>	Heat exchanger
<i>j</i>	Junction
<i>l</i>	Liquid
<i>ll</i>	Liquid line
<i>m</i>	Mean
<i>max</i>	Maximum
<i>o</i>	Overall
<i>p</i>	Pool
<i>pb</i>	Porous block
<i>ps</i>	Porous space
<i>s</i>	Saturation condition
<i>sc</i>	Subcooled liquid
<i>sp</i>	Specimen
<i>t</i>	Total
<i>ts</i>	Transportation section

v	Vapour
vl	Vapour line
w	Wick
wc	Water column
wl	Wall
wf	Working fluid
wm	Wick material

Constants

a...f	Coefficients (as in Table A1)
α	0.59 (as in Equation 3.45 and 12.10)
π	3.14

Abstract

The development of high-end and compact computers has resulted in a considerable rise in the power dissipation requirements of their microprocessors. At present, the waste heat release by the Central Processing Unit (CPU) of a desktop and server computer is 80 to 130 W and a notebook computer is 25 to 50 W. New systems have already been built with thermal outputs as high as 200 W for desktops and around 70 W for laptops. At the same time, the heating areas of the chipsets have become as small as 1 to 4 cm². This problem is further complicated by both the limited available space and the restriction to maintain the chip surface temperature below 100 °C. It is expected that conventional two phase technologies like heat pipes and vapour chambers as well as current designs of single phase cooling systems will not be able to meet these future thermal needs of computer systems. With the intention of finding a solution to this problem, different thermal designs based on both two-phase and single-phase heat transfer were developed and characterized for the thermal control of high density microprocessors. In the domain of two phase technology, two investigative prototypes of capillary driven passively operating loop heat pipes with characteristic thickness as small as 5 or 10 mm and capable of dissipating heat fluxes as high as 70 W/cm² were designed and tested. These devices responded very well to the thermal needs of laptop microprocessors. The thermal characteristics of single phase cooling systems were enhanced with the purpose of handling concentrated heat fluxes as high as 400 W/cm². This was made possible by developing heat sinks with innovative microstructures that include microchannels or sintered microporous media. As an outcome of the present research work, it is concluded that two phase cooling units provide a highly reliable thermal solution for the cooling of laptop microprocessors with high heat fluxes and limited available space for accommodating thermal devices. However the thermal performance of the passive devices is limited at very high magnitudes of heat flux. Therefore cooling technology needs to be further explored for the effective management of future high powered electronic systems. Liquid cooling systems can handle extremely high heat fluxes very effectively but they are structurally complex and unreliable due to the requirement for an active component (like a pump) in the system that also requires power for its operation.

Chapter 1

Introduction

1.1 Background

Thermal control is a generic need of electronic equipment. In general, heat is rejected by every electrical system due to the excitation of electrons, when current flows. If the quantity of waste heat given out by the system is small and the area for heat rejection is large enough, direct natural convection is sufficient to dissipate all of the generated heat to the surroundings without need for any other cooling system. For example, some electronic devices that we use in our daily life including digital players, televisions, camcorders, mobile phones and other handheld devices do not require any forced cooling for their thermal management. For other electronic devices like computers that consist of microprocessors with a large number of integrated circuits in small spaces, heat dissipation by natural convection is far from sufficient. For such devices, depending on the extent of the output waste heat and the active heat dissipation area, an appropriate thermal control device is needed.

The main function of the cooling unit is to transfer heat from the source to the surroundings. Two important components of some heat transfer devices can be a heat spreading block and a heat rejection block (Sauciuc et al, 2005). In the heat spreading block, the heat from the miniature footprint of the heat source is spread to a larger area from where it can be dissipated to the surroundings with the help of the heat rejection block. Depending upon the processor heat load, different options for a heat spreader range from a simple metal heat sink to a complicated two phase vapour chamber. Heat transfer in two phase systems is accomplished on the basis of an evaporation-condensation cycle that is maintained at the expense of capillary pumping of the liquid from the sink to the hot source. It should be noted that in the cooling of microprocessors inside compact electronic devices like laptops, the waste heat has to be rejected at a location remote from where it is produced. This is necessary to prevent heating of the enclosed electronics around the microprocessor. For this purpose, the thermal device has to perform an additional function

of transferring heat from the source to a remotely located heat sink. In this situation, reliable two-phase heat transfer devices like heat pipes that can transport heat from the chipset to the distantly located heat sink with minimal temperature difference (Faghri, 1995) are used. The heat rejection block of the thermal control device involves heat removal by forced convection of ambient air using a fan.

1.2 Thermal Control of Computer Microprocessors

Heat pipes and vapor chambers have emerged as the most appropriate technology and cost effective thermal solution due to their excellent heat transfer capabilities, high efficiency and structural simplicity. Basically, the heat pipe and vapor chamber are two-phase heat transfer devices. They involve an evacuated and sealed container with a small quantity of working fluid. One end of the container is provided with waste heat from the chipset, causing the contained liquid to vaporize. The vapor flows to the cold end of the container where it condenses. Since the latent heat of evaporation is much larger than the sensible heat capacity of a fluid considerable quantities of heat can be transported using these devices with a very small end to end temperature difference. A heat pipe behaves as a device of very high thermal conductance with the equivalent thermal conductivity of several hundred times than that of a solid copper device of the same outer dimensions.

Different types of thermal solution that are being currently used for the cooling of the laptop and desktop computer microprocessors are discussed in the next section. It should be noted that the literature on thermal control systems for computers represents the thermal products of Fujikura Ltd. Japan and has been taken from publications (Mochizuki et al, 2005) made by the company.

1.2.1 Laptop Thermal Control

Depending on the internal configuration, available space, number and power dissipation capacity of the microprocessor chipsets inside the laptop, thermal designs (Mochizuki et al, 2005) as shown in Figure 1.1 are commonly used. It is evident that to maximize the performance and push air cooling to the limit, the design needs multiple heat pipes or a vapor chamber with high density finning and multiple fans.

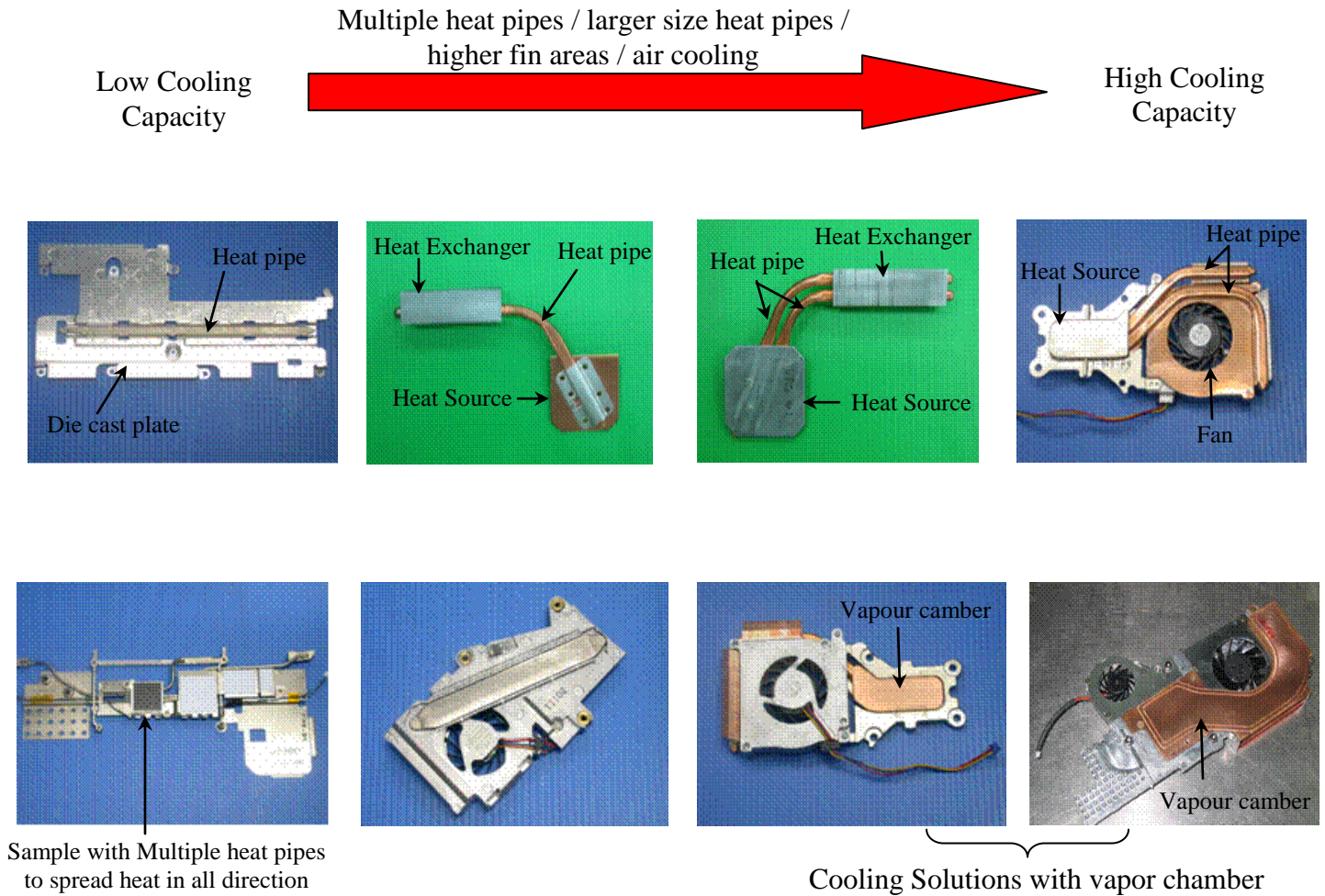


Figure 1.1 Trends in Thermal Solutions for Laptop PCs

Some of the above thermal control systems are discussed below with the help of examples (Mochizuki et al, 2005):

1.2.1.1 Hybrid System

The hybrid system consisted of heat pipes, diecast plate, fins and fans as shown in Figure 1.2. In this case, heat pipes were used to spread heat on the aluminum die cast plate. Aluminum fins were attached to the ends of the heat pipes by a soldering process. In order to dissipate heat from the fins, two radial fans were used to blow air directly through fins. In the example shown in Figure 1.2, three heat pipes were used for heat spreading purposes. The total thermal

resistance from the CPU case surface to the surroundings (commonly denoted by R_{ca}) for this system was about $1.8\text{ }^{\circ}\text{C}/\text{W}$. The hybrid system was capable of dissipating heat load of up to 26W while maintaining the CPU surface temperature below $100\text{ }^{\circ}\text{C}$.

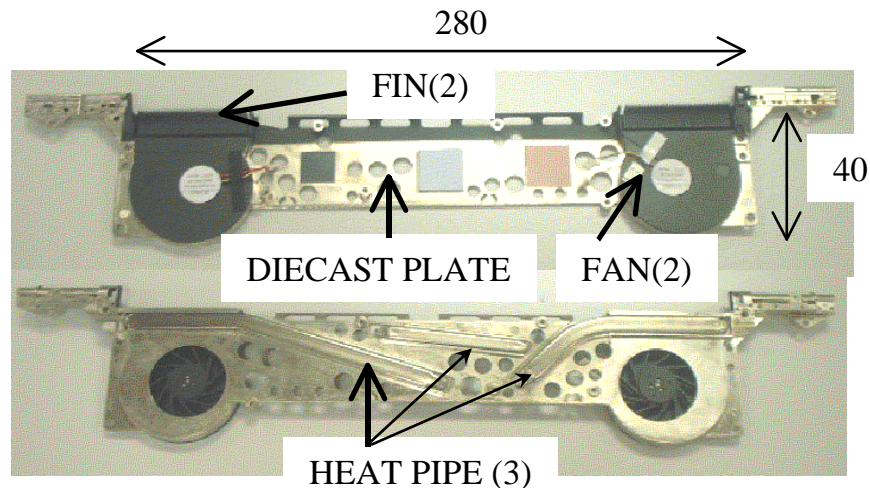


Figure 1.2 Hybrid thermal control system for laptop microprocessors.

1.2.1.2 Remote Heat Exchanger

Basically, the remote heat exchanger consisted of heat pipe, fin and fan as shown in Figure 1.3. Here, the heat was removed from the CPU and transferred to the remote location by using heat pipes. In the example given in Figure 1.3, the fan size was approximately $45\text{mm} \times 45\text{mm}$ and 10mm thick with an estimated air flow rate of $0.15\text{ m}^3/\text{min}$. The R_{ca} for this design was approximately $1.1\text{ }^{\circ}\text{C}/\text{W}$ with a cooling capacity of approximately 40W .

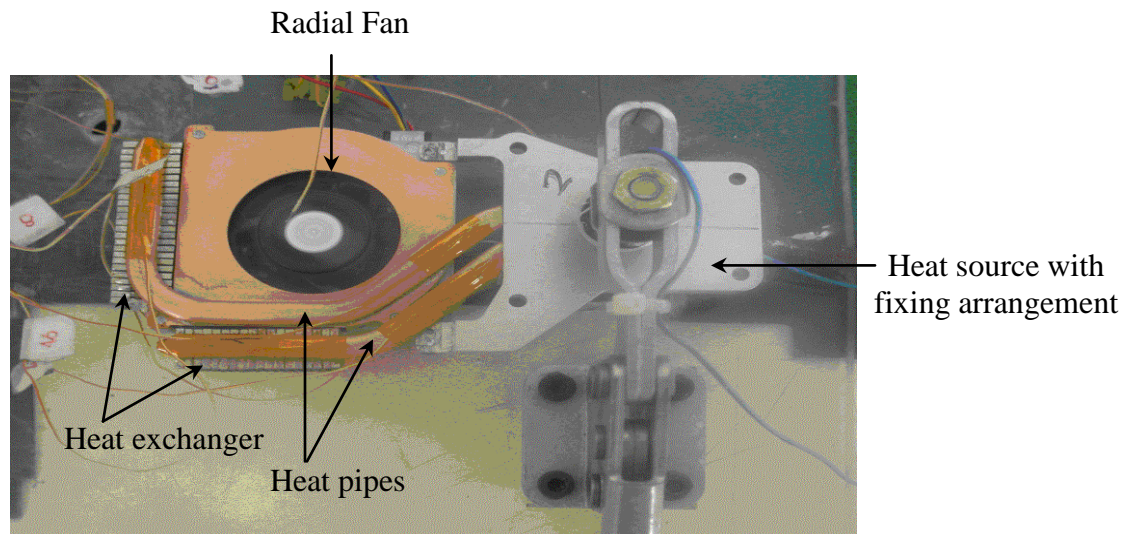


Figure 1.3 Remote Heat Exchanger for cooling laptop microprocessors.

1.2.1.3 Vapour Chambers

The principle of operation of a vapor chamber is similar to a heat pipe which is a two-phase heat transfer device. A heat pipe is made from round pipe and after sealing the ends can be bent and flattened to the required shape. The vapor chamber container can be made by stamping, cold forging, or machining processes so that the shape is fixed and it can not be bent or flattened. Figure 1.4 shows photos of various vapor chamber shapes and sizes.

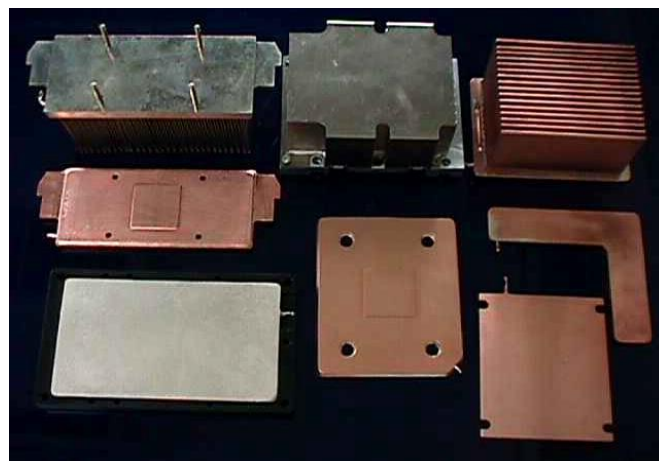


Figure 1.4 Different designs of vapour chamber used for laptop cooling

An example of a vapor chamber solution is shown in Figure 1.5. The Rca of this system is approximately $0.6\text{ }^{\circ}\text{C}/\text{W}$. It has been mentioned in the reference (Mochizuki et al, 2005) that the cooling solution with vapour chamber can dissipate approximately 60W.

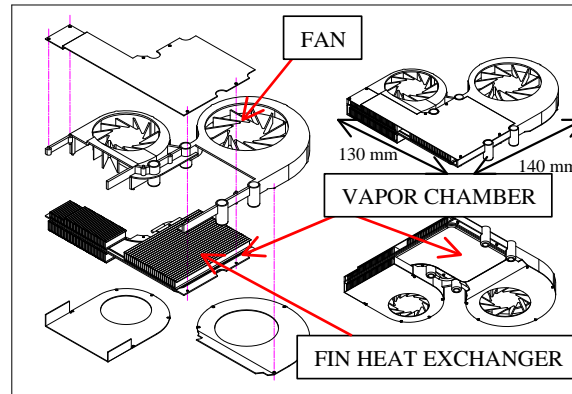


Figure 1.5 Thermal control system with vapour chamber for laptop cooling

1.2.2 Desktop Thermal Control

Depending on the power dissipating potential of the microprocessor, different thermal solutions have also been developed for desktop computers. Figure 1.6 shows the types of the thermal solution that are currently used in desktop PCs. The desktop thermal designs are broadly categorized into five different types in order of the increasing air cooling potential. For the designs depicted in Figure 1.6, the dimensions of the cooling module are approximately 90 mm x 90 mm x 65 mm height. The acoustic level at the maximum specification in general is 45 dB at 1m from the source. Below is a description of the designs.

Type 1: Normal extrusion heat sink with fin count of approximately 7 fins per inch, 1.2 mm fin thickness, pitch 3.5 mm and 30 mm fin height. The Rca range for these heat sinks is $0.4\text{-}0.5\text{ }^{\circ}\text{C}/\text{W}$.

Type 2: High aspect extrusion heat sink. In this design extrusion had been pushed to the limiting capability. Fin count approximately 10 fins per inch, 1 mm fin thickness, pitch 2.3 mm and 30 mm fin height. The aluminum base had a copper block soldered onto it in order to minimize the heat spreading resistance. The Rca range for high aspect extrusion heat sinks is $0.3\text{-}0.4\text{ }^{\circ}\text{C}/\text{W}$.

Type 3: In this type, the design changes from parallel fin extrusion to radial type extrusion. The heat sink core has an integrated copper core to improve heat conduction from base to fins. In general radial fins capture the air from the fan better than parallel plate fins, thus providing higher fin-air heat transfer coefficient and more efficient cooling. The Rca is approximately $0.3 - 0.35 \text{ }^\circ\text{C/W}$.

Type 4: In this type, high density stack fins are soldered to a metal base. The fin thickness can be as low as 0.2 mm, and the fin gap less than 1mm. The Rca is approximately $0.25 - 0.3 \text{ }^\circ\text{C/W}$.

Type 5: In order to further reduce Rca (less than $0.25 \text{ }^\circ\text{C/W}$) for the same specification constraints, a heat sink base made from heat pipes or a vapor chamber have been considered to maximize the heat transfer from source to fins and thus to maximise cooling efficiency.

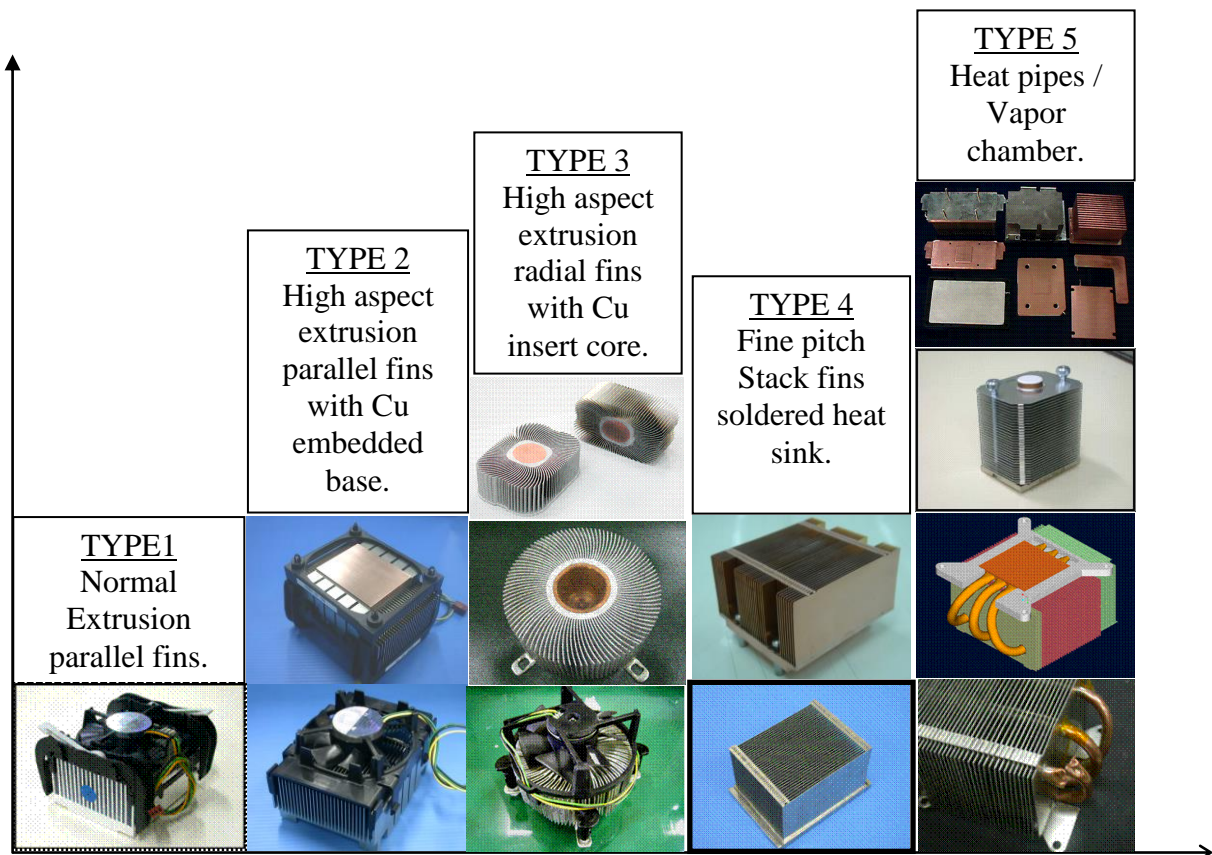


Figure 1.6 Different Types of Thermal Solution for Desktop Computer Cooling

With the development of silicon technology, the number of circuits on microprocessors multiplies every year. This has resulted in very large scale integrated (VLSI) circuits with high heat flux capabilities. To cope with these increased heat fluxes, a parallel development must follow in the design of the thermal control devices. To this effect, liquid cooling based single phase heat transfer systems have been introduced to cool microprocessors with highly concentrated heat fluxes. Nonetheless, looking at the current power dissipating trends of microprocessors, it is anticipated that the current state of technology in two phase as well as single phase systems will not be able to meet the thermal needs of future electronic systems. In order to develop reliable thermal solutions for new generation computers, innovative designs of heat pipes with spatial separation of the liquid-vapour phases and localization of the wick structure, as discussed in the following chapter, have been developed. Also, an enhanced form of liquid cooling system with microstructural heat sink made from microchannels or sintered porous structures is being investigated worldwide by different researchers for thermal management of high order fluxes.

Figure 1.7 presents the current and future expectation of thermal solutions for laptop and desktop PCs units on the basis of the required thermal resistance or thermal performance, R_{ca} (case temperature of CPU to ambient air temperature) against the cost of the solution. For the laptop PC, the current thermal solution of a heat pipe remote heat exchanger is able to deliver R_{ca} performance of approximately $1.5\text{ }^{\circ}\text{C}/\text{W}$. Further performance improvement is possible with the help of the vapor chamber solution. For the next generation high powered laptops, a loop heat pipe solution must be considered. The estimated cost for a laptop PC solution including fan is in the range of 5-15 \$US depending on the performance requirement. For the desktop PC, the majority still use traditional solutions such as high aspect aluminum extrusion parallel or radial fin heat sinks, with aluminum or copper plate fins soldered to aluminum or copper metal bases. However, as the performance requirement tightens, the trend is towards using heat pipes and vapor chambers to maximize the performance and to extend the air cooling capability to the limit. For a very high powered desktop microprocessor, a liquid cooling solution using microchannel/porous structure, thermoelectric coolers and vapour compression refrigeration must be considered.

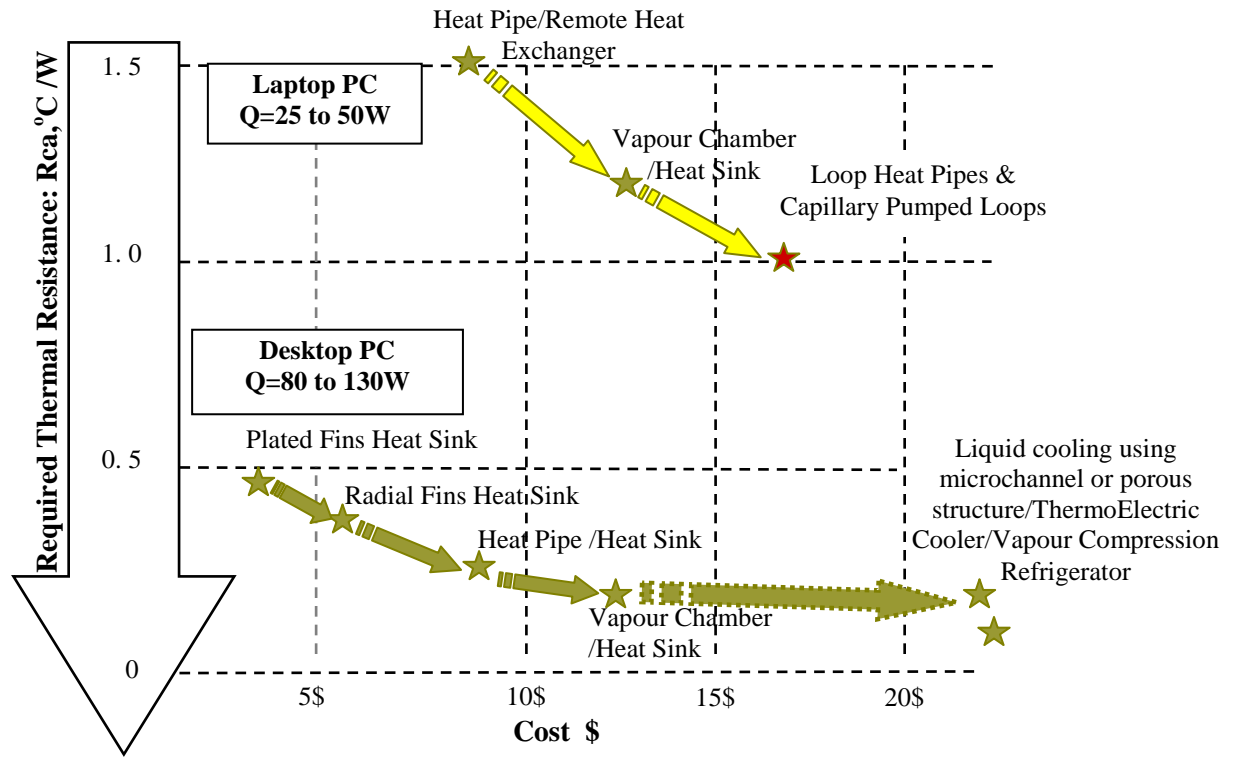


Figure 1.7 Thermal Solution Trends

The main objective of this research work is to investigate and develop different thermal designs, based on two-phase and single phase cooling that can be used in the thermal control of microprocessors for laptops and desktop computers. Detailed objectives and concept introduction have been given in the respective sections. The technologies used and the methodologies developed in this research work are the original work of the author and the research supervisors. The two phase thermal designs using miniature loop heat pipes are developed from fundamental knowledge of heat pipes and thermodynamics principles and represents original contributions of the author to thermal science. For the single-phase thermal designs, some experience and existing knowledge developed and used by Fujikura Ltd. Japan was deployed. It should be noted that the research technology developed in this project did not use any product that was developed from the public domain. The research project was financially as well as technically supported by the Thermal Technology Division of Fujikura Ltd. Japan.

1.3 Thesis Outline

Chapter 1: Introduction - This chapter gives a brief introduction to the thermal needs of electronic devices, particularly computers. Detailed description of the thermal control technologies for the laptop and desktop computers has been provided. Also, an outline of the thesis is given here.

Chapter: 2 Introduction and Literature Review – This chapter is divided into two sections. In the first section, a critical review of two-phase cooling using loop heat pipes is presented. The section discusses briefly the background and physical concepts of loop heat pipes and the objectives of the present research work on loop heat pipes for laptop cooling. The differences between the two types of loop system: Capillary Pumped Loop (CPL) and Loop Heat Pipe (LHP) are brought forward. A detailed survey is provided of the available literature on loop heat pipes, in particular the miniature Loop Heat Pipe (mLHP) which is the main focus of the current research. Based on the literature survey, in this research program two prototypes of miniature loop heat pipes were developed for the thermal control of laptop microprocessors. In the second section, single phase liquid cooling using microchannel and microporous heat sink are discussed. The section gives the scope and objectives of the research work on single phase liquid cooling for thermal control of desktop computers. A detailed literature survey has been done on the cooling capabilities of microchannel heat sinks and sintered porous heat sinks. Different designs of these heat sinks which have been developed and tested by researchers worldwide are briefly summarised. Based on the present literature survey, the potential of liquid cooling systems with a microchannel heat sink or a sintered porous heat sink for the thermal control of the desktop microprocessors with very high heat dissipation tendency was explored.

Chapter 3: Theoretical Modelling of a Loop Heat Pipe – This chapter discusses the theory of LHPs and a mathematical model is proposed for prediction of the loop operating temperature from a given set of input parameters. The main operating characteristics that are used to determine the loop thermal performance are also defined.

Chapter 4: mLHP with a Disk Shaped Evaporator: Experimental Apparatus and Method – The chapter presents the constructional details and procedure for testing the mLHP with a flat disk shaped evaporator of 30 mm diameter and 10 mm thickness. As two phase

systems are very vulnerable to Non Condensable Gas (NCG) formation, cleaning and charging procedures are specifically explained in this chapter.

Chapter 5: mLHP with a Disk Shaped Evaporator: Results and Discussion - Thermal characteristics of a mLHP with regard to the startup behaviour and steady state operation of the loop system are explained. In addition to this, the effect of the fluid inventory, positive inclination (evaporator above condenser), heating mode (uniform heating, non-uniform heating), wick characteristics and non condensable gases on the thermal performance of the loop have been studied. Different approaches to detection and flushing of NCG from the mLHP have been proposed and successfully tested.

Chapter 6: mLHP with a Rectangular Evaporator – In this chapter, the design and results of testing on a mLHP with a flat rectangular evaporator of only 5 mm thickness are explained. Thermal performance of the mLHP was studied with respect to the start up process and steady state operation. In the final section, comparison of the rectangular evaporator mLHP is made to the previously discussed disk shaped evaporator mLHP.

Chapter 7: Liquid Cooling using a Microchannel Heat Sink – The chapter discusses the single phase liquid cooled microchannel heat sink for cooling microprocessors with extremely high heat fluxes. Complete description of the prototype and experimental setup is given. Different correlations based on various entry length conditions are discussed for the predictions of heat transfer inside the microchannels. Finally, results of the experiments are discussed and comparison is made with predictions made on the basis of the heat transfer correlations.

Chapter 8: Liquid Cooling using a Sintered Porous Heat Sink – In this chapter, experimental investigation is described of a liquid cooled sintered porous heat sink for handling heat fluxes given out by high powered desktop microprocessors. A description of the prototype, experimental setup and testing method is given. The thermal performance of the sintered porous heat sink was assessed at different water flow rates and thermal load inputs. Finally, comparison is made between the microchannel heat sink and the sintered porous heat sink.

Chapter 9: Comparative Study: Two-Phase Vs Liquid Cooling – In this chapter, a comparative study has been carried out for two-phase and single phase cooling systems. Two prototypes; one with a heat pipe module and the second with microchannel based liquid

cooling were developed to carry out the investigation. Detailed description of both cooling units is provided. The thermal performance of each cooling unit was assessed and compared on the basis of a single heat source as well as multiple heat sources.

Chapter 10: Conclusions – Conclusions drawn from the complete research work are presented in this chapter.

1.4 List of Publications

The outcomes of the research work have been presented internationally in the form of the following publications:

- Singh, R, Akbarzadeh, A, Dixon, C, Mochizuki, M, ‘Novel Design of a Miniature Loop Heat Pipe Evaporator for Electronic Cooling’, *ASME Journal of Heat Transfer* (Under Review)
- Singh, R, Akbarzadeh, A, Dixon, C, Mochizuki, M, Riehl, RR, ‘Miniature Loop Heat Pipe with Flat Evaporator for Cooling Computer CPUs’, *IEEE Transactions on Components and Packaging Technologies* (Accepted for Publication).
- Singh, R, Akbarzadeh, A, Dixon, C, Mochizuki, M, ‘Thermal Characteristics of the Miniature Loop Heat Pipe with Water as the Working Fluid’, *Proceedings of 8th International Heat Pipe Symposium, September 24-27, 2006, Kumamoto, Japan.*
- Singh, R, Akbarzadeh, A, Mochizuki, M, Nguyen, T, Kiyooka, F, Wuttijumnong, V, ‘Thermal Performance of Miniature LHP Operating Under Different Heating Modes’, *ASME, Proceedings of ITherm2006, May 30 – June 2, San Diego, California, USA.*
- Singh, R, Akbarzadeh, A, Mochizuki, M, Nguyen, T, Wuttijumnong, V, ‘Experimental Investigation of the Miniature Loop Heat Pipe with Flat Evaporator’, *Proceedings of IPACK 2005, July 17-22, San Francisco, California, USA.*
- Singh, R, Akbarzadeh, A, Mochizuki, M, Nguyen, T, Wuttijumnong, V, Kao, B, Takaneka, E, Saito, Y, Sataphan, T, ‘Flat Miniature Heat Pipe with Composite Wick Structure For Cooling Mobile Handheld Devices’, *Proceedings of IPACK 2005, July 17-22, San Francisco, California, USA.*
- Singh, R, Akbarzadeh, A, Mochizuki, M, ‘Capillary Pumped Loops: An Overview’, *Proceedings of the 1st International. Seminar on Heat Pipes and Heat Recovery Systems, December 8-9, 2004, Kuala Lumpur, Malaysia.*

-
- Singh, R, Akbarzadeh, A, Mochizuki, M, ‘Effective Thermal Management using Capillary Pumped Loop (CPL)’, *Proceedings of 1st International Forum on Heat Transfer, November 24-26, 2004, Kyoto, Japan.*
 - Singh, R, Akbarzadeh, A, Dixon, C, Mochizuki, M, ‘Experimental Determination of the Physical Properties of a Porous Plastic Wick Useful for Capillary Pumped Loop Applications’, *Proceedings of the 13th International Heat Pipe Conference, 21-25 September, 2004, Shanghai, China.*
 - Singh, R, Akbarzadeh, A, Dixon, C, Riehl, RR, Mochizuki, M, ‘Design, Analysis and Investigation of a Medium Scale Capillary Pumped Loop’, *Proceedings of the 13th International. Heat Pipe Conference, September 21-25, 2004, Shanghai China.*

Chapter 2

Introduction and Literature Review

The chapter has been divided into two sections: two phase cooling systems using loop heat pipes that were developed for laptop cooling applications and single phase cooling systems using liquid cooling that were developed for desktop cooling applications. In the first section, a detailed literature survey on Loop Heat Pipes (LHPs) is presented. A brief history and the physical concept of the loop scheme are explained. Different architectures based on the loop principle namely Capillary Pumped Loops (CPLs) and Loop heat Pipes (LHPs) are compared. In the main body of the section, the development of the loop heat pipe and different design embodiments are discussed in detail. Thorough investigation of the definition, design and development of miniature loop heat pipes has been done which is the main focus of the current research. In conclusion, the scope and objectives of this research work on two phase systems are summarized.

In the second section, a detailed literature review is presented on single phase liquid cooling systems using microchannel and microporous structures. With increase in processing speed and miniaturisation of electronic packages, the need for reliable thermal design for cooling high-end electronic equipment like desktops and servers is increasing. Performance of liquid cooling systems can be readily enhanced using different forms of microstructures like microchannels and sintered microporous media. Initially, the need for the present research work is discussed. After this, the scope and objectives of this work on single phase liquid cooling are presented. In the main body of the section, a detailed literature survey has been carried out for the cooling capabilities of microchannel heat sinks and sintered porous heat sinks. Different designs of these heat sinks, which have been developed and tested by researchers worldwide, are also briefly summarised.

2.1 Two phase cooling systems using Loop Heat Pipes: Introduction

Loop Heat Pipes (LHPs) are two-phase heat transfer devices that depend on the capillary forces developed in a fine pore wick to circulate the working fluid in the closed loop. LHPs possess all the advantages of conventional heat pipes and additionally, provide reliable operation over long distance at any orientation in the gravity field. These devices can be considered as one of the most promising thermal control technologies for ground based, as well as space, applications. Different designs of LHPs ranging from powerful large size LHPs to miniature LHPs have been developed and successfully employed in a wide range of applications.

2.2 Background

Heat pipes are excellent heat transfer devices but their applications are mainly confined to transferring relatively small heat loads over relatively short distances with the evaporator and condenser at similar horizontal levels. These limitations on the part of the heat pipe are mainly related to the major pressure losses associated with liquid flow through the porous wick structure, present along the entire length of the heat pipe, and viscous interaction between the vapour and liquid phases, also called entrainment losses (Faghri, 1995).

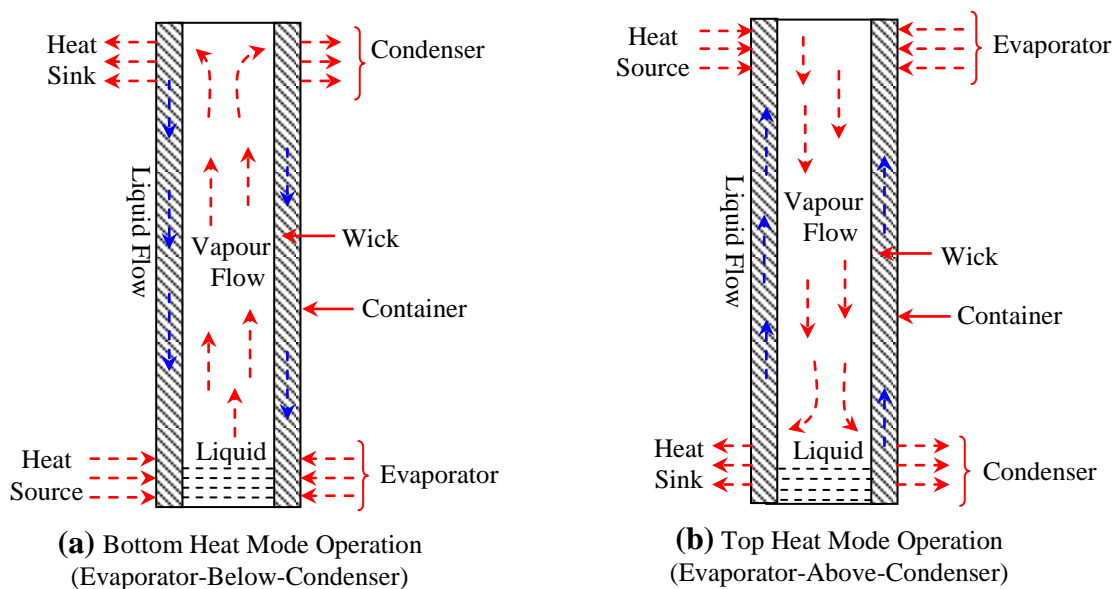


Figure 2.1 Conventional Capillary Driven Heat Pipe

For applications involving transfer of large heat loads over long distances, the thermal performance of heat pipes is badly affected by increase in these losses. For the same reason conventional heat pipes are very sensitive to the change in orientation in gravitational field. For the unfavourable slopes in evaporator-above-condenser configurations, the gravitational pressure losses add to the total pressure losses and further affect the efficiency of the heat transfer process. Figure 2.1 shows the schematics and different mode of operation of the conventional capillary driven heat pipe.

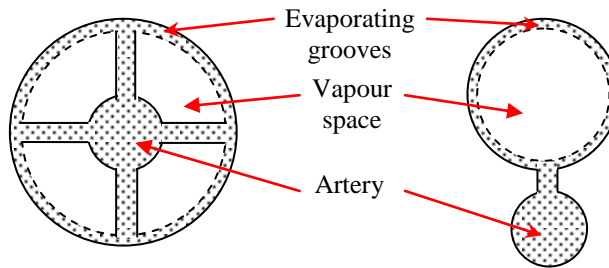


Figure 2.2 Arterial Heat Pipes

As a result of these limitations, different solutions involving structural modification of the conventional heat pipe have been proposed. Some of these modified versions of heat pipes incorporated an arterial tube with very low hydraulic resistance to the return of the liquid to the heat supply zone e.g. arterial heat pipes (Roukis et al, 1975) (Figure 2.2) while others provided spatial separation of the vapour and liquid phases of a working fluid at the transportation section e.g. separated lines heat pipes (Shlosinger, 1970) (Figure 2.3).

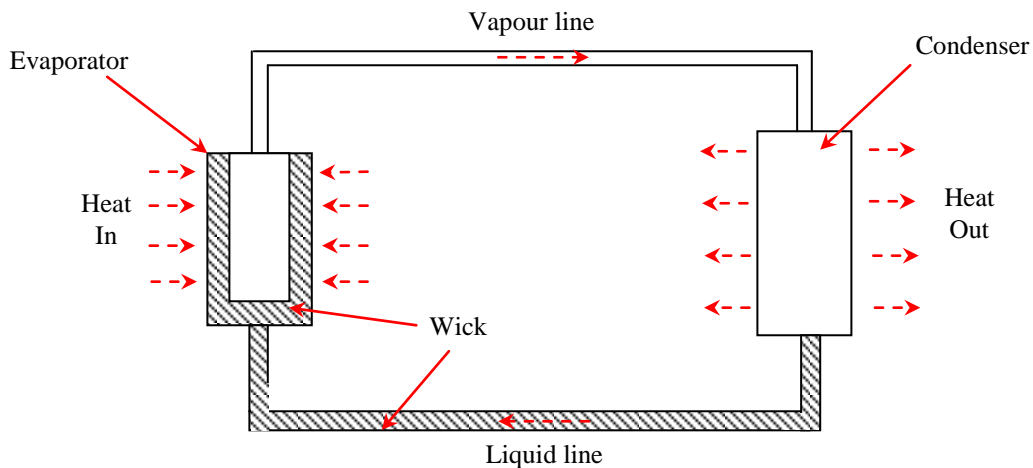


Figure 2.3 Separated lines heat pipe

Although these heat pipes were able to increase heat transport length and transferred significant heat flows they remained very sensitive to orientation in the gravity field. To extend functional possibilities of two-phase systems for applications involving otherwise inoperable slopes in the gravity field, the advantages provided by the spatial separation of the transportation line and usage of a non-capillary artery were combined in the loop scheme (Maydanik & Fershtater, 1997) as shown in Figure 2.4. As a result, the loop scheme makes it possible to develop heat pipes with higher heat transfer characteristics while maintaining normal operation at any orientation in the mass force field. The loop principle forms the basis of the physical concept of the Two-Phase Loops (TPLs).

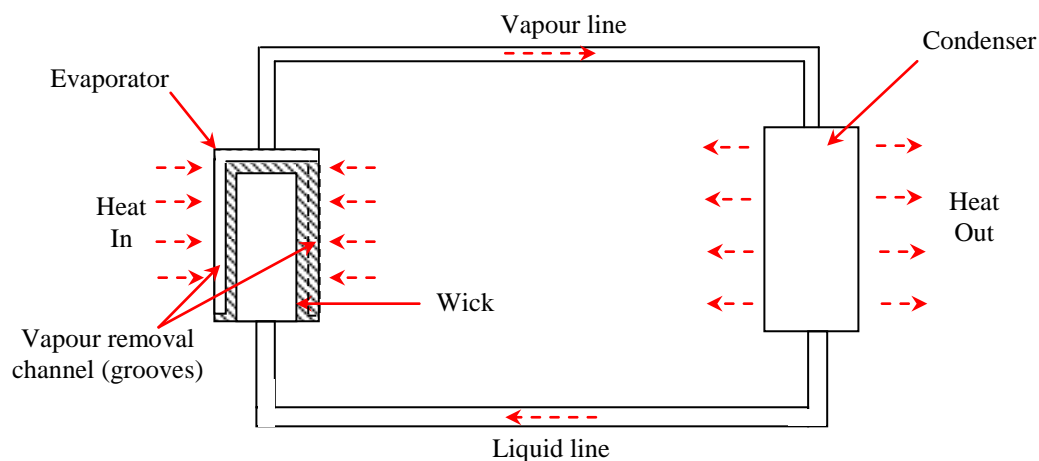


Figure 2.4 Loop Scheme

2.3 Two-Phase Loops

Two-phase loops such as Loop Heat Pipes (LHPs) and Capillary Pumped Loops (CPLs) are highly efficient heat transfer devices developed on the basis of a capillary driven loop scheme. LHPs and CPLs utilize capillary pressure developed by the fine pore wick to circulate the working fluid, and latent heat of vaporization and condensation of the working fluid to acquire and transport heat loads. Historically, LHPs and CPLs were developed independently of each other for different spheres of application. CPLs were created in the USA by Stenger (1966) in the late sixties for application in space technology, mainly as a complex and powerful thermal control system (TCS). Independent of this, LHPs appeared in the early seventies in the USSR as an attempt to create a heat pipe capable of operating at any orientation in the gravity field.

2.3.1 Differences in LHP and CPL Technology

Baseline schematics of a LHP and a CPL are provided in Figures 2.5 and 2.6. A typical loop system consists of a capillary evaporator or (heat acquisition section), condenser (heat dissipation section), liquid and vapour lines (heat transportation section), and a two-phase reservoir (fluid accumulator).

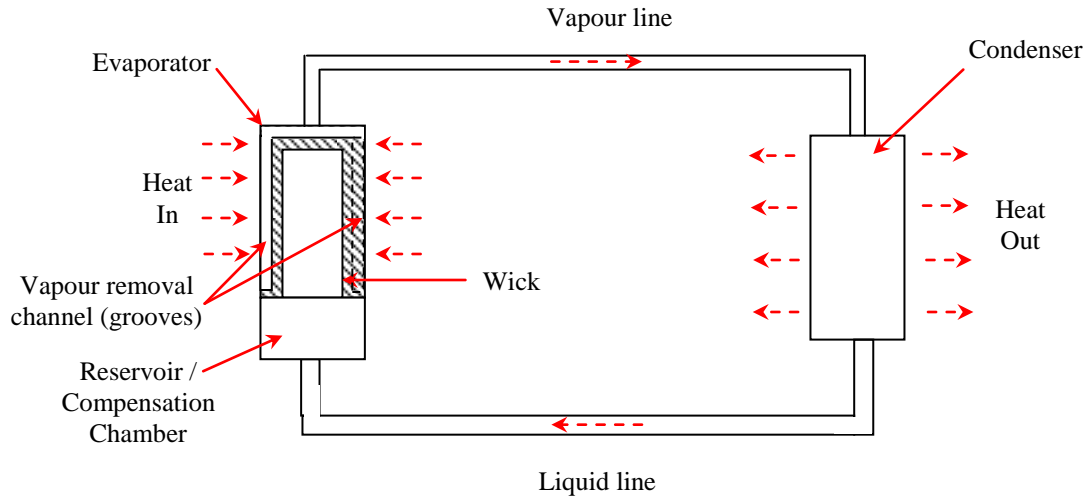


Figure 2.5 Loop Heat Pipe (LHP)

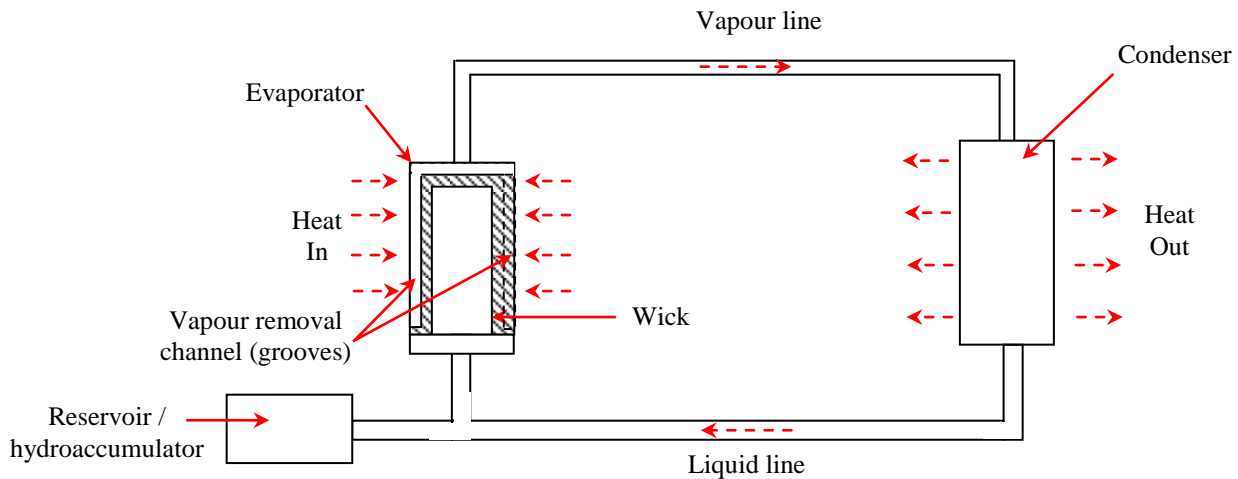


Figure 2.6 Capillary Pumped Loop (CPL)

The primary difference between a LHP and a CPL is the different location of the reservoir, and this provides them with their unique operating characteristics. CPLs are provided with a remotely located reservoir connected to the liquid line whilst a LHP reservoir, also called a

compensation chamber, is thermally and hydraulically combined with the evaporator in one body. The co-location of the reservoir with the evaporator provides the LHP with additional functional features over a CPL including robust startup of the device without need of active control such as a starter pump or a pre-heater on the reservoir. The LHP also has low sensitivity of the device to non-condensable gases (NCGs). Another important difference between the LHP and CPL is that the LHP is more reliable and hence a preferable system for space as well as ground based application when a single evaporator and single condenser are required (Maydanik, 1999). The CPL, on the other hand, is more reliable in a microgravity condition when a complex system with multiple evaporators/condensers, also called a ramified system, is required. However investigations towards the development of ramified LHPs have been made and great advances on this technology have been achieved, resulting in a promising option for future applications (Ku and Birur, 2001) where the CPL is more indicated.

The CPL is structurally more complex than the LHP but via active temperature control of the reservoir can provides an effective control over the whole system operating temperature even with changing input heat to the evaporator. However, the issues relating to startup in CPLs are still a concern and an important consideration during their operation.

2.4 Loop Heat Pipe: Physical Concept

A basic LHP schematic is shown in Figure 2.7. The typical LHP consist of a capillary evaporator, vapour line, condenser, liquid line and compensation chamber (fluid reservoir). Generally, the evaporator consists of a metallic cylindrical tube with vapour removal grooves on the internal surface of the tube and a force fitted capillary structure. In principle, the capillary structure of a LHP is localized in the heat supply zone. Here, the capillary wick is provided over the evaporator active zone. On one hand, this approach helps to minimize the length of the liquid flow path through the porous structure while on the other hand, it enables the use of fine pore wicks with high capillary pressure to enable the operation of the device at adverse tilt angles. The internal surface of the capillary wick is the absorbing one while the external surface serves as the evaporating surface. The evaporation zone is formed by the distributed system of vapour removal channels at the wick-wall interface.

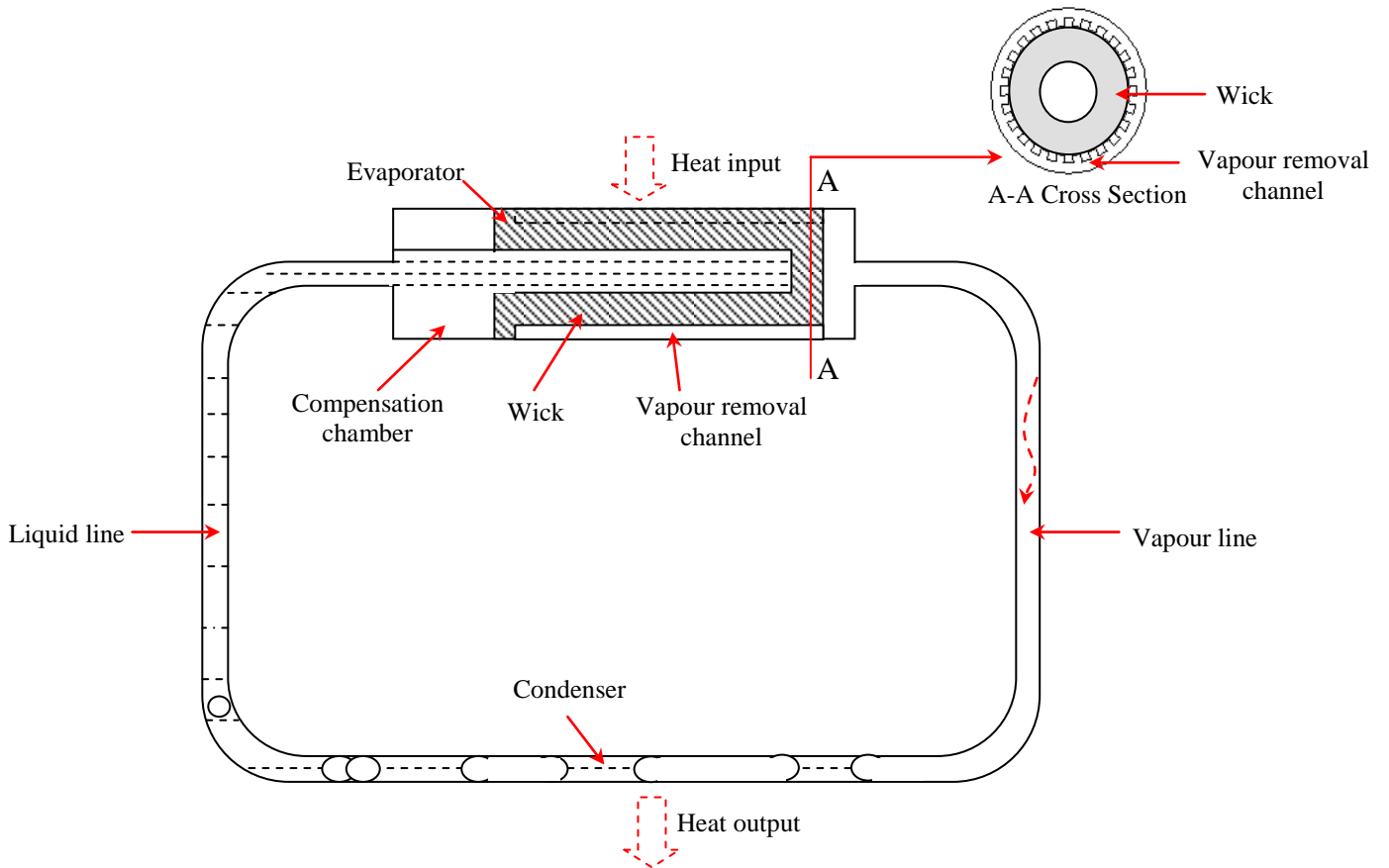


Figure 2.7 Schematic of Loop Heat Pipe

Contrary to conventional heat pipes in which heat is acquired through the liquid layer, effective heat exchange is organized in the evaporator of a loop heat pipe by the principle of an inverted meniscus (Chernysheva et al, 1999) and segmented wick contact with the wall as shown in Figure 2.8. In this case, the evaporating surfaces of menisci are close to the heated wall via the contact between the wick and wall therefore a low value of thermal resistance is achievable in the evaporation zone.

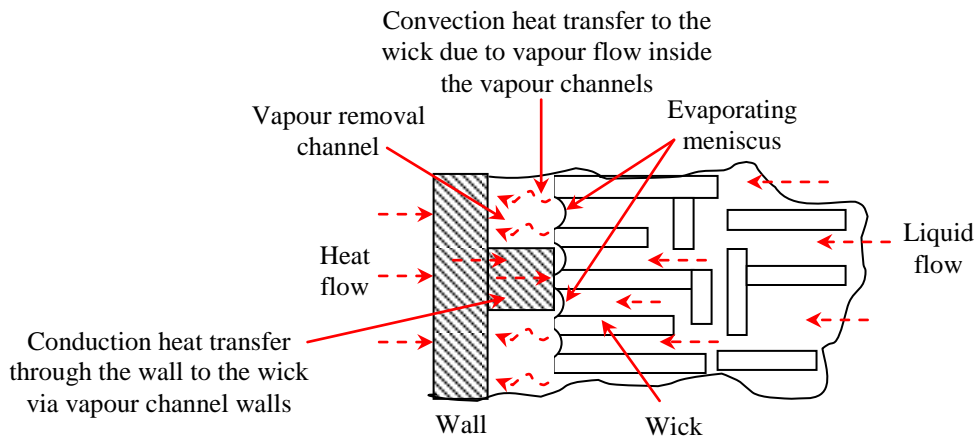


Figure 2.8 Scheme of organisation of evaporation zone by the principle of an inverted meniscus

In LHPs, separated liquid-vapour lines made from wickless smooth tubes are used for the transportation section thereby eliminating the thermal and viscous interaction between the counter flow of liquid and vapour. The absence of wicks inside the transport lines make them easy to bend and thus provide mechanical flexibility and adaptability to the system. A special requirement for realization of the LHP concept is provision for reliable liquid supply to the wick structure before startup as well as during normal working. The reason is that liquid return to the evaporator must occur along a non-capillary liquid line. In case of any boiling in the liquid line the capillary action will be locked which in turn may ultimately result in evaporator deprime or increase in the operating temperature. This can be avoided by taking special measures to subcool the liquid in the condenser before feeding it to the evaporator. To achieve this, the LHP condenser is designed in such a way that part of it serves to condense vapour (active condenser) while the rest provides subcooling to the condensate (inactive condenser).

Another important outcome of the loop principle is the inclusion of the hydroaccumulator (fluid reservoir) with the evaporator. Unlike heat pipes, where liquid is mostly bound inside the wick structure, in LHPs a considerable amount of liquid inside the loop is in an unbound state. This liquid is used to fill the condenser, liquid line and wick core. As the heat load or heat sink conditions change, the liquid vapour meniscus inside the active condenser zone moves. The LHP hydroaccumulator is co-located with the evaporator as an integral part of it and accepts extra liquid pushed out from the condenser and serves as a liquid source for the condenser when the latter needs to decrease the condensation surface. In the same way during startup, the hydroaccumulator plays an important role and compensates for extra liquid released from the evaporator grooves, vapour line and part of the condenser surface. The hydroaccumulator also guarantees wetted capillary structure at all the times. When the LHP operates at its maximum designed heat load, the hydroaccumulator should be able to hold the displaced liquid from the evaporator vapour grooves, vapour line and condenser. Therefore, this is one of the most important design parameters for LHPs (Ku, 1999)

It should be noted that satisfaction of the physical concept requirements is the necessary condition to provide normal operation of a LHP.

2.5 Problem Description

A solution was needed for the thermal control of laptop microprocessors with heat dissipating capacities of up to 70 W and heat transport distances (i.e. distance between the heat source and heat sink) of up to 150 mm (Figure 2.9a). The maximum dimensions of the heat dissipation device (or condenser) and heat acquisition device (or evaporator) were fixed by the available cooling space and design constraints.

The basis for condenser cooling was forced convection using a centrifugal fan with specific flow characteristics. Due to the compactness of portable computers, the thickness of the cooling device is the critical dimension and should not exceed 10 mm (Figure 2.9b).

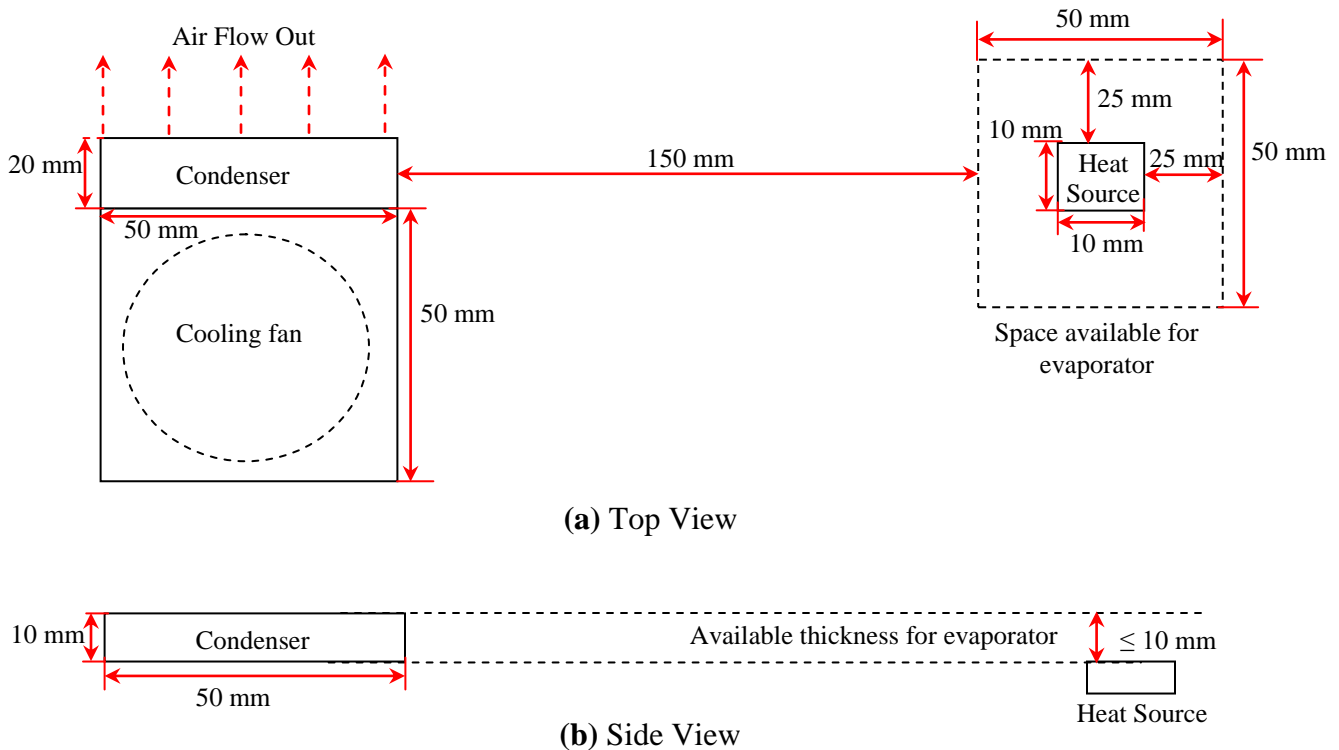


Figure 2.9 Available cooling space inside the laptop computer

2.6 Research Scope

Cooling systems for electronic and computer equipment require compact and efficient heat transfer devices. The scope of the present research work is to investigate a miniature loop heat pipe with a flat disk shaped evaporator for the thermal management of the high heat flux

chipsets in portable and personal computers. Miniature loop heat pipes with flat evaporators can be made very compact and thin and can easily be integrated into the electronic equipment to be cooled. Until now, most mLHP prototypes have been focused on the thermal control of space related equipment with power saturated chipsets. Under such circumstances, low temperature working fluids like ammonia and durable materials like stainless steel for the loop container are the best options. For terrestrial applications such as computer equipment, certain safety measures must be observed that restrict the use of high pressure, toxic or inflammable working fluids like ammonia, acetone or different grades of alcohol. Water can be considered as one of the preferred choice for such applications. Copper and water are compatible and affordable and are also widely used in conventional heat pipes. Copper-water mLHPs can serve as potential replacements for conventional heat pipes with least alteration to the manufacturing materials.

The main advantages of the mLHPs that have attracted their interest for computer cooling can be listed as follow:

- ❑ A mLHP has very reliable temperature control for a range of heat loads. This capability is determined by the size of the compensation chamber, evaporator structure and container material.
- ❑ These devices are able to maintain good performance at high heat fluxes and with long distance heat transfer because of separate and smooth walled liquid and vapour lines and therefore having low pressure losses.
- ❑ As the wick structure is present only in the evaporator, the vapour and liquid lines can be bent to fit the mLHP architecture into the available space.
- ❑ mLHPs have the ability to collect and dissipate heat from multiple heat sources to multiple heat sinks.

These advantages can support the proposition that LHPs can replace the current state of technology of conventional heat pipes in electronics cooling.

2.7 Research Objectives

The main objectives of the research work are as follow:

- To design & develop a mLHP prototype with a flat shaped evaporator of thickness in the range of 5 to 10 mm.

- To improve understanding of the physical concepts and operating principle of the loop scheme.
- To determine the thermal performance of the mLHP:
 - Using a wick structure made of copper and nickel with different physical properties (pore size, porosity and permeability)
 - Using heating areas of different sizes such as 10 x10 mm², 25 x 25 mm²
- To study the start up phenomena and steady state operation in detail
- To study the effect of change in working fluid inventory, elevation/tilt etc on the overall performance of the mLHP.
- To conduct detailed study and devise methods to detect Non Condensable Gases (NCG) in the mLHP system, methods to purge NCG from the loop and means to avoid the production of NCG in the proposed systems.

2.8 Literature Review on Loop Heat Pipes (LHPs)

2.8.1 LHP Background

Originally known as Antigravitational Heat Pipe (AGHP), the Loop Heat Pipe (LHP) is a versatile and robust heat transfer device that has considerably extended the functional possibilities and sphere of application of two-phase systems based on the capillary pumping mechanism. The first LHP was created and tested by the Russian Scientists Gerasimov and Maydanik from the Ural Polytechnical Institute in 1972 (Maydanik, 2005). It was able to transfer a 1 kW heat load over a distance of 1.2 m, using water as the working fluid and successfully established the viability of the loop principle. The prime objective in developing this model was to design a passive operating anti-gravitational heat transfer system for aerospace applications. Later in 1986, the Institute of Thermal Physics (ITP) in Russia initiated further development of LHPs for space applications. These devices got international attention when they were demonstrated at the 8th International Heat Pipe Conference (IHPC) in Minsk, Russia in 1990. At present, LHPs with different architectures and performance capabilities are widely used in space applications. Various aspects of the loop heat pipe have been studied and investigated by organizations and researchers worldwide. Research has been done widely to further expand the application regime of the LHPs by proposing new designs and enhancing the thermal performance of the LHP components.

2.8.2 LHP Evaporator

The evaporator is the most critical and main structural element of the loop heat pipe. Within the framework of the evaporator, there is considerable scope to increase the limiting density of heat load and to intensify the heat exchange process. This can be achieved by optimizing the structure topology and geometric parameters of vapour escape channels as well as the structural and thermal characteristics of the wick. Here, the main aim is to reduce the thermal resistance of the heat exchange process in the evaporation zone.

2.8.2.1 Vapour Removal Channel

It is important to have a system of vapour removal channels that will provide a stable, well-developed evaporation surface in the vicinity of the heating wall. In a typical design of a LHP evaporator, the vapour removal channels are present either on the internal wall of the evaporator metallic case or on the external surface of the capillary structure. This approach helps in very efficient removal of the vapour from the evaporation zone. Another approach is the two step system (North et al, 1997) of vapour removal with azimuthal grooves (in the form of fine spiral thread) made on the wall of the evaporator body (first step) and longitudinal channels situated on the external surface of the wick (second step). This system has been developed to enhance the vapour removal process in order to handle very high heat fluxes.

2.8.2.2 Capillary Structure

Further enhancement of the capillary evaporator can be made by optimizing the wick characteristics. The main function of the capillary structure is to pump the working fluid around the loop. The LHP concept with its short liquid path through the wick enables the use of capillary structure with very fine pore size that provide high capillary pressure, a considerable part of which can be used to promote operation against gravity. Apart from the capillary pump, the wick structure acts as a thermal as well as a hydraulic block between the evaporator and compensation chamber. Vapour block is provided by the presence of the liquid in the fine pores of the capillary structure. Unlike in conventional heat pipes, the wick structure used in the LHP should not have excessive thermal conductivity to avoid back conduction to the liquid present in the evaporator core and compensation chamber. It should

be noted that there is a need for compromise here between this problem and the desire for good wick conductivity at the evaporating zone. Also, the wick material should be wettable by the working fluid and cheap to fabricate.

The capillary structure can be made from plastic or metal. Plastic wicks are generally made from polyethylene, polypropylene or Teflon material. These plastic wicks, made from thermoplastic polymeric powder by a sintering process, present very low thermal conductivity and can be customized to obtain pore size and porosity over a wide range. Boo & Chung (2004) demonstrated successful operation of an LHP with a polypropylene wick of 0.5 μm to 25 μm average pore size. Kobayashi et al. (2003) fabricated and tested a LHP using R134a as working fluid and Teflon as a wick material that transported 135 W in a horizontal orientation. In their study of a loop heat pipe, Riehl & Dutra (2005) made use of a polyethylene wick with average pore size of 7 μm and acetone as working fluid.

Plastic wicks provide very low thermal conductivity that is essential for the desirable operation of a LHP but there exists a limit on the maximum value of the porosity of these wicks. In most cases, the porosity (which is defined as the ratio of the porous volume to the total volume of the wick structure) of these wicks is generally less than 50% which imposes a limit on the maximum heat transfer capacity of the LHPs. A comprehensive study done by the author (Singh, 2004) on the determination of the physical properties of polyethylene wicks shows that such wicks generally exhibit porosity value of less than 38% for a pore size in the range 8 μm – 20 μm . Also, the permeability (which is defined as the flow rate of the fluid through the wick of known dimensions under a given constant pressure head) of plastic wicks is quite low, of the order 10^{-14} m^2 . Plastic wicks are also limited by the maximum allowed operation temperature. For example, a maximum permissible temperature for polyethylene is 120 °C and for Teflon is 250 °C.

Compared with the abovementioned wick structures, sintered metal wicks can be easily obtained with an effective pore radius as small as 2 μm and a porosity of 55 – 75 %. Nickel can be considered to be one of the most acceptable wick materials for loop heat pipes. Reimbrecht et al (1999) in their work on sintered nickel wicks presented the procedure for the

production and characterization of the wick. In order to characterize porous wicks, they studied the influence of sintering time, temperature and powder size on the porosity, mechanical strength and roundness of the wick. As part of their work, pore sizes in the range of 2 to 24 μm and porosity up to 50% were investigated. Li and Xuan (2003) conducted a similar study and developed a slip casting technique and hydrogen deoxidized sintering method to prepare nickel wicks for loop heat transfer systems. Following the developed procedure, it was possible to obtain sintered wicks with porosity greater than 68%, mean pore size about 4 μm and permeability in the range of 10^{-12} to 10^{-13} m^2 . The samples also showed high mechanical strength and low distortion.

Nickel wicks are invariably used in most LHPs (Maydanik, 2004) due to their low thermal conductivity and ability to be formed in fine pore sizes with high porosity as discussed above. Titanium is another frequently used wick material with desirable properties as a capillary structure. Stainless steel, due to its low thermal conductivity and good chemical compatibility with working fluids like ammonia and acetone, is also used as a wick material. Copper wicks have also been used successfully as capillary pumps in LHPs. However at high heat fluxes the high conductivity of copper can cause back conduction problems in transmitting heat through the wick to the liquid in the compensation chamber. The wick structures as discussed above show quite efficient performance and are mostly used as monoporous wicks i.e. their pore size distribution is similar to the Poisson distribution and characterized by average pore size. To improve the performance of the evaporator at very high heat flux, a porous medium with two characteristic capillary pore radii known as biporous capillary structure has been proposed (Wang & Catton 2004). Maydanik et al (1997) utilized the concept of bidisperse wicks and organized an efficient three step vapour removal channel system.

2.8.3 Compensation Chamber

As discussed previously, the compensation chamber is very important structural element of the LHP which is linked to the evaporator and helps to compensate for the change in the liquid charge during start-up and for varying heat loads. The generic location of the compensation chamber provides LHPs with their robust start up behavior and temperature control capability (so called auto regulation or self regulation) under fluctuating power input.

As the compensation chamber is connected to the capillary evaporator, special consideration should be given to its design to promote desirable device operation. Different variants of typical arrangement of the compensation chamber as an integral part of the evaporator have been designed and tested. These include prototypes with the compensation chamber detached from the capillary evaporator body (Mulholland et al, 1999) and dual compensation chambers on either side of the capillary evaporator with their diameters greater than or equal to that of the evaporator (Gerhart & Gluck, 1999). As a result of comparison between the configuration with the compensation chamber being an integral part and that detached from the capillary evaporator, it has been shown that compensation chamber geometry can affect the LHP thermal performance and operating temperature (Riehl, 2004). The geometry of the compensation chamber is decided by number of factors that include available space, permissible evaporator temperature, available heat fluxes and internal volume of the LHP.

LHPs can self-regulate the operating temperature of the evaporator within certain regimes without use of any active control device. The range of heat loads in which this property of LHPs manifests itself depends upon the dimensions of the compensation chamber and condenser, and on the intensity of cooling of the latter. Larger condensers have a wider range of self-control. However, this self-regulation range is largely limited by the LHP operating temperature and condenser temperature. LHPs also allow active control of the evaporator temperature with the help of the controllable thermal action of the compensation chamber. Such a thermal action may be positive (heating) or negative (cooling), and its value does not usually exceed 5-10% of the heat load transferred by the LHP.

2.8.4 Condenser

Condensation in a loop heat pipe takes place on the smooth internal surface and is of film character. Depending upon the heat removal conditions, condensers of different design and shape can be incorporated in LHPs. Figure 2.10 shows the main types of condenser used currently for LHPs. The condenser with external fins as shown in Figure 2.10a is the simplest design and may be used for LHPs with low heat capacities. This type of condenser is best suited for compact electronics and is generally used with forced convection. Figure 2.10b shows another variant of condenser based on a concentric tube type of heat exchanger which

uses forced convection of a liquid or gas flowing through the annular space to effect heat transfer.

The collector type condenser as in Figure 2.10c consists of well developed internal as well as external surfaces and is commonly used for powerful LHPs with high heat capacities. It is best suited for the mode of cooling using forced convection. A coil on plate type condenser (Figure 2.10d) is best suited for applications where large surface area is available for heat rejection or the primary mode of heat exchange is radiation, for example in space cooling applications. It consists of tubular coil that is soldered or fastened to a flat plate of relatively large size with or without fins. This is the most versatile version of the LHP condenser where cooling can be done in number of ways including natural and/or forced convection and with radiation heat exchange or heat rejection to a thermal mass or cold plate.

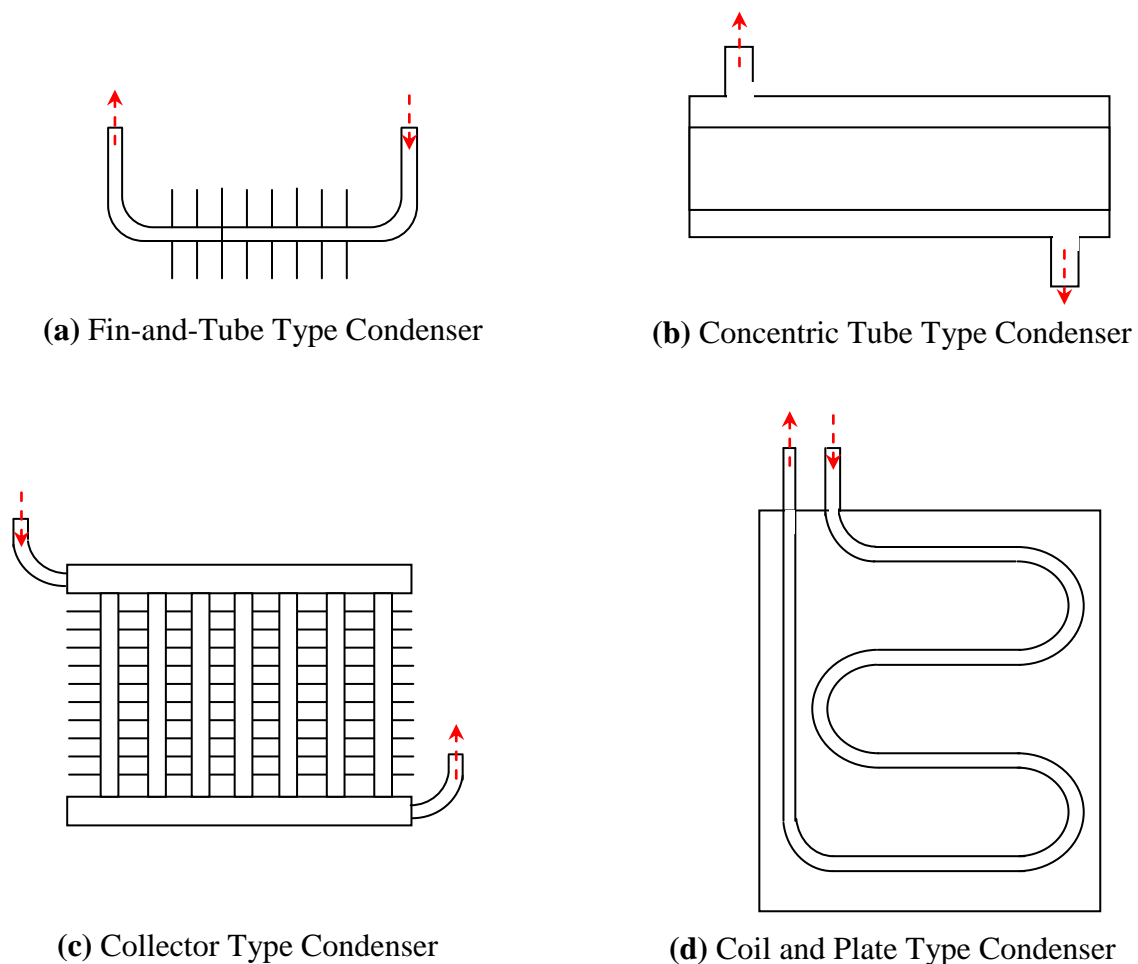


Figure 2.10 Different variants of LHP condenser

The LHP principle makes it possible to create heat transfer devices with different numbers of evaporators and condensers (Ku and Birur, 2001) (so called ramified system) situated in different ways with respect to each other. These ramified LHPs can be considered for thermal management of large contact surfaces, scattered heat sources or in cases where there are several heat sinks removed from one another. Also, in contrast to the traditional structure of a LHP that acts as a thermal diode and allows only for heat flow in the direction from evaporator to condenser, there is possibility of developing special reversible loop heat pipes (Sudakov et al, 2002) that can allow heat flow in either direction.

LHPs have also been investigated at a miniature scale as a potential substitute for less efficient conventional heat pipes in cooling power saturated electronic equipment. Research and development of miniature LHPs have been discussed in detail later in this chapter keeping in view the present research which is mainly focused on exploring the potential of miniature loop heat pipes for electronic cooling.

2.8.5 Working Fluid

The first consideration in the selection of the working fluid is the operating vapour temperature range. Water is mostly used for high temperature application unlike ammonia and acetone, which are favorable for low temperature applications. Ammonia (Maydanik & Pastukhov, 1999, Dickey & Peterson, 1994) and Acetone (Bazzo & Riehl, 2003) have been investigated by a number of researchers and meet most of the heat transport requirements. They are desirable fluids in the temperature range of 270-350 K. Ammonia is very costly to obtain in a highly pure state and requires careful handling to retain high purity. Also, due to its toxic nature and high pressure it is not the most indicated working fluid in terrestrial applications, instead it is extensively used in space applications. Acetone, although inferior in performance to ammonia, is also a preferred working fluid in LHPs and can be obtained in high-grade assay at relatively low cost. Also, acetone can operate in the same temperature range as ammonia, with a great advantage related to its freezing temperature, which is $-93.15\text{ }^{\circ}\text{C}$ while ammonia freezes at $-78\text{ }^{\circ}\text{C}$ (Dunn and Reay, 1994). This is an important parameter to be considered because in space applications, the LHP must be designed to provide reliable start-up at frozen states.

Water is superior for operation (Dunn and Reay, 1994) in the temperature range of 350-500 K where the alternative organic fluids tend to have low merit numbers. Merit number M is a means of ranking heat pipe working fluid. Fluids with higher merit number are more desirable. The Merit Number is defined as the ratio of the product of liquid density ρ_l , liquid surface tension σ_l , and latent heat h_{lv} to the liquid viscosity μ_l .

$$\text{i.e. } M = \frac{\rho_l \sigma_l L}{\mu_l} \quad (2.1)$$

High surface tension, high latent heat and availability in abundance are some of the incentives for using water. But due to low vapour density and low vapour pressure of water at typical operating temperatures, high vapour velocities are encountered which tend to increase the vapour pressure losses in the vapour line and evaporator grooves.

Other heat transfer fluid like toluene (Baumann & Rawal, 2001), Ethanol, Methanol (Boo & Chung, 2004), Propylene (Gherlone, 1995), Nitrogen (Baumann et al, 1998) are also acceptable working fluids for loop heat pipes depending on the application, temperature, heat flux and heat transport distance involved during operation.

2.8.6 Material Compatibility

The wick and container material used in the loop system should be compatible with the working fluid at low as well as high temperatures. Copper is compatible with most of the working fluids except ammonia. Due to its high thermal conductivity, copper can only be used as wick material in LHP if subcooling of the working fluid is provided to counteract the effect of back conduction. Water shows excellent results with copper but presents compatibility issues with most of the other container and wick materials commonly used in capillary pumped loops (CPL) and loop heat pipes (LHP). Nickel (Riehl and Dutra, 2005), Titanium (Pastukhov et al, 1999) and stainless steel (Khrustalev and Semenov, 2003) are widely used as wick materials with ammonia and acetone. Stainless steel produces Non Condensable Gases (NCG) with water at elevated temperatures. Titanium has also been successfully used as a wick material with water (Baumann and Rawal, 2001). Aluminum, due to its low mass and good thermal conductivity, is used as the containment material with

ammonia and acetone for various aerospace applications. A new class of plastic wick structures made from Ultra High Molecular Weight (UHMW) polyethylene (Chen and Lin, 2001) and Polypropylene (Boo and Chung, 2004) have also been tested and used successfully in LHP/CPL with different working fluids.

In summary, for LHPs with water as the working fluid, copper is invariably used as containment and wick material. For low temperature working fluids like ammonia and acetone, generally stainless steel and/or aluminum are used as containment materials with nickel, titanium, stainless steel or combinations of these as wick material. Plastic wicks have been used with most of these working fluids without any compatibility issues.

2.8.7 Development of miniature Loop Heat Pipes (mLHPs)

For a particular application, the design of a LHP is dictated by a variety of factors including total thermal load, heat transfer distance, operating temperature, orientation in the local gravity field, space available for the cooling system, heat sink conditions etc. As discussed previously, different configurations of LHP have been designed and tested for thermal management of various ground based and space applications. Most of the configurations described have focused on thermal management of aerospace applications. In order to use loop heat pipes for cooling compact electronic and computer equipment including portable computers, their feasibility in the direction of miniaturization must be evaluated. This is discussed later, and most of the examples of mLHP prototypes being investigated use ammonia as working fluid and stainless steel, nickel or titanium as wick. To promote the application of these devices for the computer cooling, use must be made of safer working fluids like water and high thermal conductive materials like copper, which are fully compatible and easily machinable for mass production.

LHPs may be regarded as miniature (Maydanik, 2004) if the outer diameter of the cylindrical evaporator does not exceed 8 mm and the internal diameter of the vapour and the liquid lines is below 3 mm. In this case the length of the evaporator active zone to which a heat load may be applied is usually in the range from 10-50 mm, and the total length of the heat transportation zone is normally no more than 500 mm. In the case of flat evaporators, the

geometric equivalent of the diameter is the thickness. As a rule, the overall thickness of the flat evaporator also includes the compensation chamber. Therefore the only criterion used here for characterizing a LHP as miniature is the diameters of the vapour and the liquid lines, as the thickness of the evaporator may vary over a wide range.

When developing miniature loop heat pipes (mLHPs) two main problems arise. The first is connected with the reduction of the evaporator diameter. There is necessarily a corresponding reduction of the thickness of the wick separating the absorbing and evaporating surfaces. This reduction results in increase in parasitic heat flow from the evaporator heat zone to the compensation chamber via the wick structure. To initiate startup and thereby the fluid circulation process in the LHP, certain temperature and pressure drops must be created across the wick which may be very difficult to create in the case of a thin wick. As a result, increase in back conduction causes increase of the operating temperature and increase in the minimum value of the start-up heat load. The use of a wick with low thermal conductivity does not fully solve the problem, as the flows over the evaporator body may increase because of reduction of the efficiency of the heat exchange process in the evaporation zone. Heat flows from the evaporator active surface to the wick via the vapour channel walls and further spreads along the evaporating surface of the wick by conduction through the wick skeleton. A wick structure with low thermal conductivity will reduce the percentage of the applied heat being utilized in the evaporation zone for the vaporization of the fluid. This will increase heat flows from the active zone to the compensation chamber along the evaporator wall. As a result of these heat flows to the compensation chamber an overall rise in the evaporator surface temperatures will occur. This aggravates the problem of decreasing the thermal resistance of the miniature LHP. The active zone area of the miniature evaporator corresponds to that of the heat load source and therefore is quite limited. The active surface of the condenser which corresponds to the conditions of the heat removal may be much larger. Therefore one of the means of decreasing the thermal resistance is at the expense of intensification of the heat exchange process in the evaporation zone by using a sufficiently heat conducting capillary structure like copper (Maydanik, 2004).

2.8.7.1 mLHPs with Cylindrical Evaporators

Investigative prototypes of mLHPs with 6-8 mm diameter evaporators have been developed and tested by number of researchers and organizations around the world. Most often the working fluid used in them has been ammonia. Wicks were made of sintered metal powders, and the bodies of stainless steel and aluminum. The first such mLHP, with an effective length of approximately 570 mm and equipped with a cylindrical evaporator 6 mm in diameter with lines for vapour and liquid 1.6 mm in diameter, was developed at the Institute of Thermophysics (ITP) in Russia (Pastukhov et al, 1999). The device was tested at three different orientations in 1 g conditions with slope of -90° , 0° and $+90^\circ$ and showed a maximum capacity of 22, 17 and 13 W respectively. In the vertical orientation, the minimum value of evaporator thermal resistance of 0.25°C/W was achieved at a heat load of 8.5 W. Ammonia mLHPs with an effective length of about 300 mm developed at Swales Aerospace (Garzon et al, 2002) demonstrated, in a horizontal orientation, effective operation in the heat range from 5 to 20 W. The minimum evaporator thermal resistance was 0.13°C/W .

Pastukhov et al (2003) developed different prototypes of miniature loop heat pipes with a nominal capacity of 25-30 W and a heat transfer distance up to 250 mm intended for cooling electronic components and CPUs of mobile PCs. These prototypes had stainless steel evaporators of 5 and 6 mm diameter were equipped with titanium or stainless steel wicks and the working fluids used were ammonia or acetone. The cylindrical evaporator was equipped with an aluminum saddle that helped thermal connection to the heat source. The liquid and vapour lines were made from stainless steel tubing of 1.3 mm inner diameter. For cooling purposes, a condenser with external fins or a plate type arrangement was used. The condenser was cooled by using force convection driven by a centrifugal fan. Under air cooling the total thermal resistance (interface to ambient) of such a system lay in the range of $1.7 - 4.0^\circ\text{C/W}$ with the thermal resistance of the mLHP in the range of 0.3 to 1.2°C/W .

In their work on mLHPs, Maydanik et al (2005) developed and tested different prototypes of mLHP with cylindrical evaporators 5 and 6 mm in diameter and capable of transferring heat loads of 100-200 W for distances up to 300 mm. These mLHPs evaporators were equipped with flat copper surfaces of 20x20 mm for mounting a heat load simulator. Ammonia (with a

stainless steel evaporator) and water (with a copper evaporator) were used as the working fluids to illustrate the performance of these devices. The condensers had fins measuring 15 x 25 mm with thicknesses varying from 0.3 to 0.4 mm. Cooling was provided by air flow with a temperature of 22 ± 2 °C circulated by a fan. These devices were able to operate in the temperature range of 50-100 °C at any orientation in 1-g conditions. Tests showed a nominal heat load (i.e. heat load at which evaporator achieved a surface temperature of 80 ± 5 °C) of 70 W for an ammonia mLHP and a larger value of 130 W for a water mLHP. The corresponding minimum values of internal thermal resistance of the devices were 0.12 °C/W and 0.10 °C/W, and the total thermal resistance “evaporator-air” were respectively 0.68 °C/W and 0.58 °C/W. The work clearly illustrates the potential of the copper-water mLHP for electronic cooling applications. It was also shown that with more intensive cooling of the condenser using water, the maximum capacity of the devices can be further increased.

An ammonia charged mini-LHP was designed, built and tested at Dynatherm Corporation Inc. (DCI) (Bienert et al, 1999) for low power management and temperature control for electronic components especially for spacecraft applications. It was constructed primarily of aluminum and weighed less than 160 grams. The cylindrical evaporator of the mLHP was designed to manage heat loads in the range 5 to 10 W. To maintain the temperature within a narrow range, active thermal control that consumed 1.5 to 3.5 W of power was fitted on the compensation chamber with the feedback thermal sensor installed on the liquid line at the compensation chamber inlet. The mini LHP was able to maintain a constant evaporator temperature of 42 °C with an accuracy of ± 0.25 °C for variation in the condenser cooling temperature from 35 °C to -40 °C and drop in evaporator power from 10 to 5 W.

2.8.7.2 mLHPs with Flat Evaporators

In most cases, cylindrical evaporators need to have a special thermal interface (saddle) which is a cylinder-plane reducer located at the surface of the evaporator active zone and provides a thermal contact with the heat load source. Despite the fact that such saddles are usually made of heat conducting materials such as copper or aluminum, they create an additional thermal resistance and increase the LHP total mass. To overcome such drawbacks, a flat evaporator can be considered as the preferred design. The critical design parameters of flat evaporators

are the thickness and the diameter of a disk or length and width of a rectangular shaped body. The possibilities for reducing the body thickness here are quite limited. This is because the evaporator is combined in one body with the compensation chamber, whose volume must correspond to the dimensions of the vapour line and the condenser. Beside this, the wick structure in a flat evaporator cannot be made very thin because of problems associated with back conduction to the compensation chamber. Various prototypes of mLHP with flat evaporators with ammonia-stainless steel configuration have been developed for space as well as ground based applications.

The first mLHP with a flat disk shaped evaporator 30 mm in diameter with a rectangular flange forming a thermocontact surface 30x30 mm was developed in Matra Marconi Space (Dunbar et al, 1997). The device was made of stainless steel and porous polytetrafluoroethylene (PTFE) was used as wick. Here also, ammonia was used as the working fluid due to its compatibility with stainless steel and permissibility in space applications. Although, the device showed high thermal resistance and moderate capacity, it demonstrated the possibility of creating mLHPs with flat evaporators.

Boo & Chung (2005) demonstrated the successful operation of a mLHP with a flat evaporator, 40mm x50 mm area and 30 mm thickness, using various polypropylene wicks with different pore sizes in the range 0.5 μm to 25 μm . The active heating zone was 35 x35 mm and there were nine axial grooves provided for vapour removal from the evaporation zone. The inner diameters of liquid and vapour transport lines were 2.0 mm and 4.0 mm respectively and the lengths of the two lines were each 0.5 m. The container and tubing of the system were made of stainless steel and several working fluids including methanol, ethanol, acetone and ammonia were used to test the thermal performance of the device. The mLHP with ammonia exhibited the lowest thermal resistance of 0.65 $^{\circ}\text{C}/\text{W}$ while ethanol mLHP showed the lowest heat load capability as compared with acetone and methanol. The thermal resistances of the acetone and methanol mLHPs were comparable to that of the ammonia mLHP for heat loads above 50 W. For the mLHP using ammonia, the maximum heat load of 87 W was achieved with the condenser temperature of 0 $^{\circ}\text{C}$ at a horizontal position.

A prototype of an ammonia mLHP was developed with a flat rectangular evaporator (Pastukhov et al, 2003) 5.5 mm in thickness and with a heat transfer length of 75 mm. The body and wick were made of stainless steel and the internal diameters of the liquid and vapour lines were 1.2 mm. The radiator (12 mm x 50 mm x 20 mm) was made in the form of corrugated copper foil 0.3 mm thick with a gap of 0.5 mm between fins. Maximum heat load with air blowing was 30 W with the total thermal resistance “evaporator-air” of 2 °C/W. With water cooling, the thermal resistance was approximately equal to 1 °C/W up to a heat load of 40 W.

Delil et al (2002) report the development of a mini LHP having a flat disk shaped evaporator 44 mm diameter and 22 mm thickness. Different types of wick structure including metal felt, nickel and titanium wicks were tested inside the flat evaporator with ethanol as the working fluid. It was concluded that increasing anti-gravity height results in an increase of the temperature drop between evaporator and condenser and thus thermal resistance increases. The device was able to transfer a maximum thermal load 120 W with thermal resistance in the range of 0.62 – 1.32 °C/W at different orientations in a gravity field.

Different variants of mLHPs with flat evaporators of stainless steel from 500 to 1000 mm in length were developed and tested at the Institute of Thermal Physics (ITP) in Russia (Chernysheva et al, 2002). All the devices used ammonia as the working fluid and had disk-shaped evaporators with an active zone diameter of 30 mm and thickness in the range from 10 to 13 mm. One of the mLHP, with a flat evaporator 13 mm thick which made use of a monoporous nickel wick with pore radius 1.2 µm, had a capacity of 120-160 W depending on the orientation. A minimum value of the thermal resistance of the evaporators of 0.25 °C/W was achieved with this device. Another mLHP with an evaporator 10 mm thick demonstrated maximum capacity of 140 W. The evaporator thermal resistance in this device was reduced to 0.14 - 0.15 °C/W at the expense of a decrease in the wall thickness and the use of a stratified nickel-titanium wick with a biporous layer.

It is clear from the above review that ammonia has been mostly used as the working fluid in the current LHPs prototypes due to its good figure of merit, its feasibility in the low

temperatures of space application where water would freeze and compatible containment/wick material can be readily obtained. In order to exploit the potential of mLHPs for ground based electronic cooling including personal and mobile computers, working fluids like water that can operate at close to atmospheric pressure and temperature, and do not show any toxic or flammable properties must be evaluated. The flat evaporator geometry has more potential to reduce the evaporator thermal resistance, and enhance heat exchange in the evaporator zone compared with a cylindrical evaporator. In addition, flat evaporators can be easily integrated into the compact space inside the object to be cooled.

2.9 Conclusions from the Current Body of Knowledge

Loop Heat Pipes (LHPs) are very reliable and versatile two phase heat transfer devices that are based on the capillary driven loop principle. LHPs possess all the main advantages of conventional heat pipes and are additionally capable of transferring large heat loads for distances up to several meters in any orientation in the gravity field. In contrast to the capillary pumped loops (CPLs), LHPs are more robust and do not require any active thermal control to initiate startup.

Significant progress has been made in the development of capillary evaporators with wicks of fine pore size and high porosity that provide strong capillary action to bring the liquid up to the evaporation zone by utilizing the principle of an inverted meniscus. Different variants of the compensation chamber and condenser have also been employed depending on the intended application and design restrictions. Nickel and titanium are mostly used as the capillary structure inside the evaporator. The container and transportation lines are generally made from stainless steel and aluminum. By far and until now, ammonia is the most widely used working fluid in loop heat pipes due to its excellent heat transfer characteristics and permissibility for low temperature range (30-80 °C). LHPs have been widely accepted and implemented as thermoregulation devices in spacecraft and satellites. Different variants of the LHP from large and powerful LHPs to miniature LHPs have been designed and tested.

With the growing interest in LHPs in electronic cooling, performance evaluation of these devices at the miniature scale is needed. LHPs for cooling Notebook PCs need to be

extremely compact and easy to integrate in the objects to be cooled. Miniature LHPs with cylindrical evaporators 6-8 mm in diameter and flat evaporators from 5.4 to 15 mm in thickness have been developed and successfully tested. The diameters of the vapour and liquid line lie below 3 mm and their effective length lies in range of 50-1000 mm. mLHP devices designed with the above combinations are capable of transferring maximum heat flows of 50-200 W at any orientation in 1-g conditions and possess evaporator thermal resistance in the range 0.14-0.25 °C/W with the total thermal resistance in the range 1-4 °C/W. Combinations like copper and water are best suited for ground based electronic cooling. Although this combination is not yet fully exploited in mLHPs, some of the investigative prototypes have shown their superior performance and heat transfer potential.

2.10 Single phase liquid cooling systems: Introduction

With the rapid evolution of new generation computers having more extensive capabilities and compact size, major design challenges in the thermal control of their microprocessors have been raised. At present, the waste heat released by the laptop CPUs is 25 to 50 W (Mochizuki et al, 2005). Different thermal designs are available that can dissipate heat loads up to 50 W given out by laptop chipset while coping with the space constraint. For still higher heat loads up to 70 W, as discussed in the previous section, two-phase passively operating loop heat pipes are able to manage the waste heat given out by laptop microprocessors quite efficiently. Different variants of the miniature loop heat pipe (mLHP) with flat evaporators of very small thickness were designed that were capable of adapting to the available space inside a portable PC. The designed mLHPs were able to transfer a maximum heat load of 70 W up to a distance of 150 mm from the heat source with an active thermal footprint of 1 cm² (10x10 mm²) and proved to provide efficient thermal control strategies for high performance and compact heat sources. For desktop and server computers the quantity of the waste heat given by the CPU microprocessor is 80 to 130 W (Mochizuki et al, 2005). Various technologies ranging from simple air cooling to two phase passive cooling have been proposed and effectively employed for the thermal control of desktop CPUs (Sauciuc et al, 2005) with such thermal requirements. Heat pipes and vapour chambers have emerged as the most appropriate technology and cost effective thermal solution due to their excellent heat transfer capabilities, high efficiency and structural simplicity. However with further increase in the processing

speed of the computer CPU and decrease in its heat dissipation area there is a corresponding upswing in its heat flux and surface power density. In the near future, it is expected that the heat dissipation requirement of the desktop/server chips will go much higher than its present value due to the added processing and graphic capabilities of workstations. Nonetheless the cooling potential of the current thermal control devices has already reached a critical limit and does not enable the heat load management of such high-end power equipments. This has instigated the need to focus on research and development of efficient thermal designs for cooling high powered computer microprocessors.

Two phase passive cooling systems including heat pipes and vapour chambers are certainly the most reliable and efficient cooling solution for future electronics. However the technology is not mature enough to cope with the drastic rise in the power dissipation trends of computer processors. In addition, the potential two phase systems like loop heat pipes and capillary pumped loops that are optimum for the thermal cooling of future electronic systems are not very cost effective and require complicated manufacturing techniques to fabricate them. Although research work has already been initiated for the development of loop systems with low cost fabrication practices (Huang, 2004) and high performance operation for commercial applications, the technology development will require time before the device is successfully implement inside high-end computers. Single phase liquid cooling can provide an approach for removing heat fluxes well beyond the current air cooling limits, usually in the order of hundreds of W/cm^2 . With liquid cooling, high heat sink performance can be achieved by making heat sinks with innovative microstructures such as microchannels /microfins and even porous structures. The later sections review the literature on single phase liquid cooling using innovative microstructures.

2.11 Problem Description

During the course of the ongoing research work on cooling of electronic equipment, one challenge of cooling a computer microprocessor with heat dissipation capacity of as high as 200 W from a thermal footprint area as small as 0.49 cm^2 was brought forward by the chip developer. For that reason the present research is focused on the development of a thermal design for cooling a microprocessor with extremely high heat flux, of the order of $408 \text{ W}/\text{cm}^2$.

In this case, the microprocessor is part of, and intended to handle the data processing needs of, the desktop computer and servers with dedicated cabinets. Therefore close restrictions on the maximum thickness of the cold plate (cooling section or active zone) and the condenser, as observed in the cooling of the laptop computers, were not encountered here. In other words, enough space was available to accommodate the overall thermal design. For the thermal control of heat fluxes of such a high magnitude, liquid cooling can be considered as the viable option. On this basis, the current research work aims at exploring the potential of liquid cooling systems with microstructural heat sinks for cooling the extreme high heat fluxes given out by desktop microprocessors.

2.12 Scope of the Research Work

Single phase liquid cooling is providing new and efficient design architectures for cooling high-end electronic devices. The scope of the present work is to investigate single phase forced convection liquid cooling using microchannels and sintered porous structure for the thermal management of high heat flux chipsets in electronic equipment. With the proposed micro structural design, liquid cooling will be able to cope up with the ever increasing thermal fluxes of the integrated packages that have resulted from increase in the number of circuits and miniaturization of the chipsets. Microchannel heat sinks are widely regarded as being among the most effective heat removal techniques for space-constrained electronic devices. The current work also examines the potential of the microchannel heat sink for thermal control of multiple heat sources by forced convection liquid cooling. In conclusion, this research work will lay further pathways to development of the thermal technology for future chipsets with extremely high heat loads.

2.13 Objectives of the Research Work

The main objectives of the research work are as follow:

- To design and develop a microchannel heat sink (MHS) for cooling a concentrated heat source in a desktop computer using forced convection single phase liquid cooling.
- To study the operational principles and thermodynamics of microchannel heat sinks.
- To test the thermal performance of the designed heat sink:
 - Using heating areas of different sizes (e.g. $7 \times 7 \text{ mm}^2$, $11 \times 13 \text{ mm}^2$)

- Using different heat loads
- Using different liquid flow rates
- To design and develop a sintered porous heat sink (MHS) for cooling a concentrated heat source in a desktop computer using forced convection single phase liquid cooling.
- To study the operational principles and thermodynamics of sintered porous heat sinks.
- To determine the thermal performance of the designed system:
 - Using different heat loads
 - Using different liquid flow rates
- To compare the thermal efficiency of the microchannel heat sink with that of the sintered porous heat sink working on the basis of forced convection of liquid (single phase).
- To design and develop a microchannel heat sink as a single phase heat transfer system and a heat pipe cooling unit as a two-phase heat transfer system for the thermal control of multiple heat sources (MHS), for applications in portable computers with limited space
- To determine the thermal performance of the designed systems under different heat loads
- To compare the thermal efficiency of the single phase liquid cooling system using a microchannel (as mention above) to that of a two phase cooling system using heat pipes, for the thermal control of multiple heat sources in laptops.

2.14 Literature Survey on single phase liquid cooling systems

2.14.1 Single Phase Liquid Cooling using a Microchannel Heat Sink (MHS)

As an appropriate classification all devices with characteristic dimensions between 1 μm and 1 mm are classified as micro-devices. In the past, many researchers have devoted efforts to the development of liquid cooled heat sinks containing microchannels with hydraulic diameters less than 1 mm. Microchannel heat sinks have emerged as one of the effective cooling techniques for high heat flux removal in electronic devices. Figure 8.1 shows a schematic of a microchannel heat sink used for electronic cooling applications.

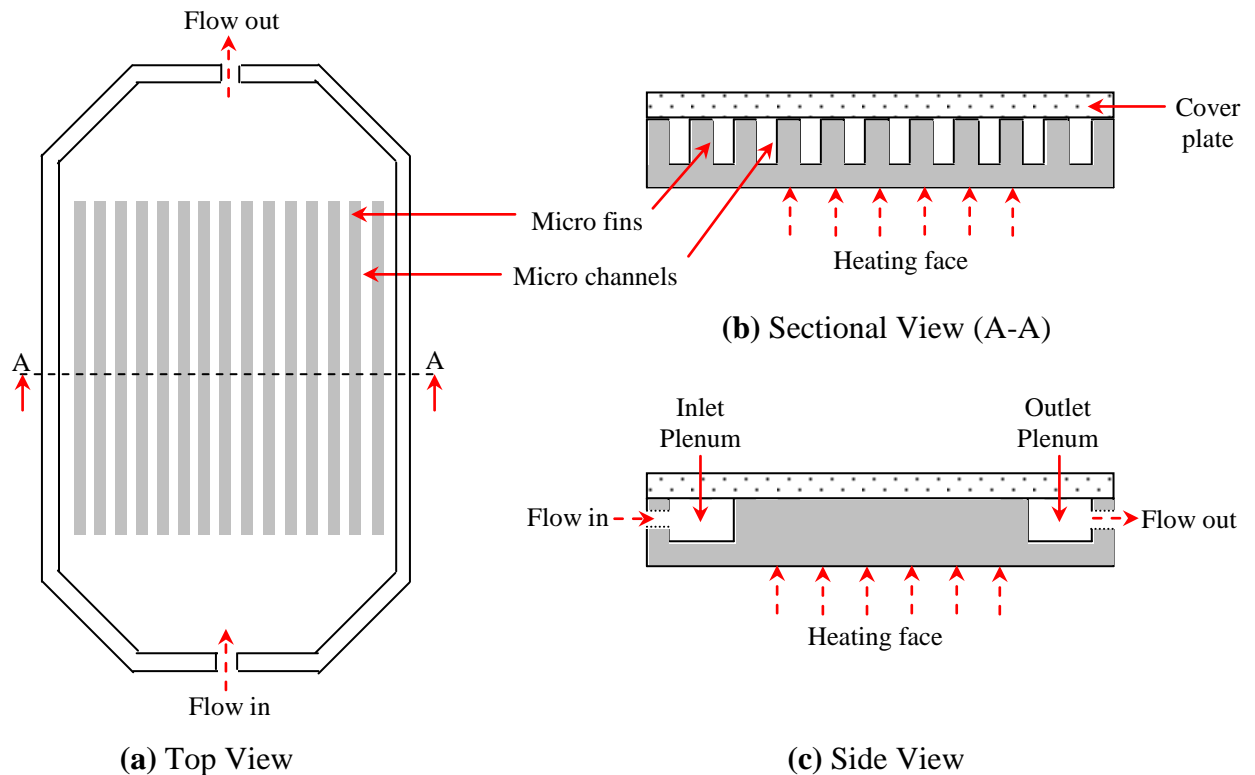


Figure 2.11 Schematic of a Microchannel Heat Sink

The cold plate design includes numerous micro channels and fins arranged in parallel on a metallic substrate with a cover plate for flow management. These microchannels provide extended surface area for heat transfer to the coolant. Due to the extremely small hydrodynamic diameter and high surface area to volume ratio of the microchannels the cooling performance is very good. The coolant enters from the inlet plenum and flows through the micro channels to carry away the heat produced by the electronic components. After absorbing the heat, the hot fluid exits the heat sink through the outlet plenum. Tuckerman and Pease (1981) first introduced the concept of microchannels and built a water cooled integral heat sink with microscopic flow channels machined on a silicon wafer. The designed MHS was able to dissipate heat flux as high as 790 W/cm^2 with the chip temperature maintained below $110 \text{ }^\circ\text{C}$ and successfully demonstrated that extremely high power chips can be effectively cooled using microchannel heat transfer. Their results also indicated that the heat transfer coefficient of laminar flow through microchannels might be higher than that of turbulent flow through normally sized channels. Following the work of Tuckerman and Pease,

numerous studies (Morini, 2004) have been performed in the area of microchannels for heat transfer applications.

Peng et al (1994) experimentally investigated the flow and heat transfer characteristics of water flowing through rectangular stainless steel microchannels with hydraulic diameters of 133 – 367 μm at channel aspect ratios of 0.33 – 1. In the study the onset of transition was observed to occur at Reynolds numbers from 200 to 700. Experiments were conducted by Wang and Peng (1994) to study the single phase forced convection of water and methanol flowing through rectangular microchannels machined on a stainless steel plate. Six kinds of microchannel structures with different widths between 0.2 to 0.8 mm and identical heights of 0.7 mm were utilized in the investigation. It was observed that a fully developed heat transfer regime is initiated at approximately $\text{Re} = 1000 - 1500$ and the transition to turbulent mode is influenced by liquid temperature, velocity and microchannel size. Transition and laminar heat transfer in microchannels prove to be very complicated when compared to the conventionally sized situation.

Zhang et al (2005) reported study of a single phase liquid cooled microchannel heat sink for cooling high heat flux electronic packages. The microchannel heat sink was made of aluminium with each channel 0.21 mm wide and 2 mm high, and deionised water was used as the coolant. Two chip array packages with different chip footprints, 12 mm x 12 mm and 10 mm x 10 mm, were used for high heat flux characterizations. The measured junction to inlet fluid thermal resistances ranged from 0.44 to 0.32 C/W for the 12 mm chip under the test flow rate range while for the 10 mm chip higher thermal resistance ranging from 0.59 to 0.44 C/W was obtained due to higher heat spreading resistance. .

Qu et al (2000) investigated the heat transfer characteristics of water flowing through trapezoidal silicon microchannels with a hydraulic diameters ranging from 62 to 169 μm . On comparing the experimental results with the numerical predictions they found that the measured Nusselt numbers were lower than the predicted values. They concluded that the lower Nusselt numbers can be due to the effect of surface roughness of the microchannel walls. Rahman (2000) conducted experimental measurements for pressure drop and convective heat transfer in a microchannel heat sink with water as coolant. Fabrication of the

devices was carried out using standard silicon-100 wafers with channel width of 1 mm and the spacing between the channels was 2 mm. The results showed that the measured values of the average Nusselt number were usually larger than those predicted by the conventional correlations. In order to explain the larger values of the Nusselt numbers the author highlighted the influence of the surface roughness on the velocity boundary layer.

Wu and Cheng (2003) investigated experimentally 13 different trapezoidal silicon microchannels ($D_h = 25.1 - 29.1 \mu\text{m}$). They found that the laminar Nusselt number and apparent friction coefficient increased with increase of surface roughness and surface hydrophilic property. The Nusselt number increased almost linearly with the Reynolds number. Kandlikar et al (2001) found that the relative roughness affected the Nusselt number such that heat transfer increased with higher relative roughness. Lee et al (2005) conducted a systemic investigation of single phase heat transfer in rectangular microchannels with hydraulic diameters ranging from of 318 to 903 μm at flow Reynolds number of 300 – 3500. The heat sink was machined on a copper substrate and deionized water was used as the working fluid. In the study, numerical predictions were obtained based on a classical, continuum approach and were found to be in close agreement with the experimental data.

2.14.2 Conclusions from the Current Body of Knowledge

From the experimental data quoted in the open literature on convective flow through microchannels it is evident that extensive design and thermal characteristics study of microchannel heat sinks has been done to effectively handle extremely high heat fluxes from electronic chips. However in accordance with published studies on microchannel heat sinks, it is evident that experimental results do not consistently agree with the conventional theory for microchannels (Morini, 2004). Some authors found that predictions from conventional theory agreed with experimental results, whereas other authors, for the relevant range of hydraulic diameters, found the opposite result. Various reasons have been proposed to explain these differences by invoking rarefaction, compressibility, viscous dissipation effects, surface conditions (roughness), property variation with temperature, electro-osmotic effects (electric double layer) etc. Some authors proposed new correlations in order to predict the friction factor and Nusselt number for microchannels. The new correlations are in general based on

few experimental points and no theoretical analysis. For these reasons, the reliability of the correlations proposed for microchannels is uncertain.

2.14.3 Single Phase Liquid Cooling using a Sintered Porous Heat Sink (SPHS)

Porous media have been extensively utilized in various heat transfer applications including electronic cooling, thermal energy absorption, geothermal systems and many others. Porous structures can be considered as an effective heat transfer augmentation technique that help to intensify fluid flow mixing and increase the surface area in contact with the coolant from which to dissipate heat. The porous structures can be made in the form of non sintered packed powder beds, sintered powder structure or foams. For the purpose of electronics cooling, convective heat transfer in porous media has been widely investigated both experimentally and theoretically by researchers worldwide. Figure 8.2 shows a schematic of a typical sintered porous heat sink used for electronic cooling applications.

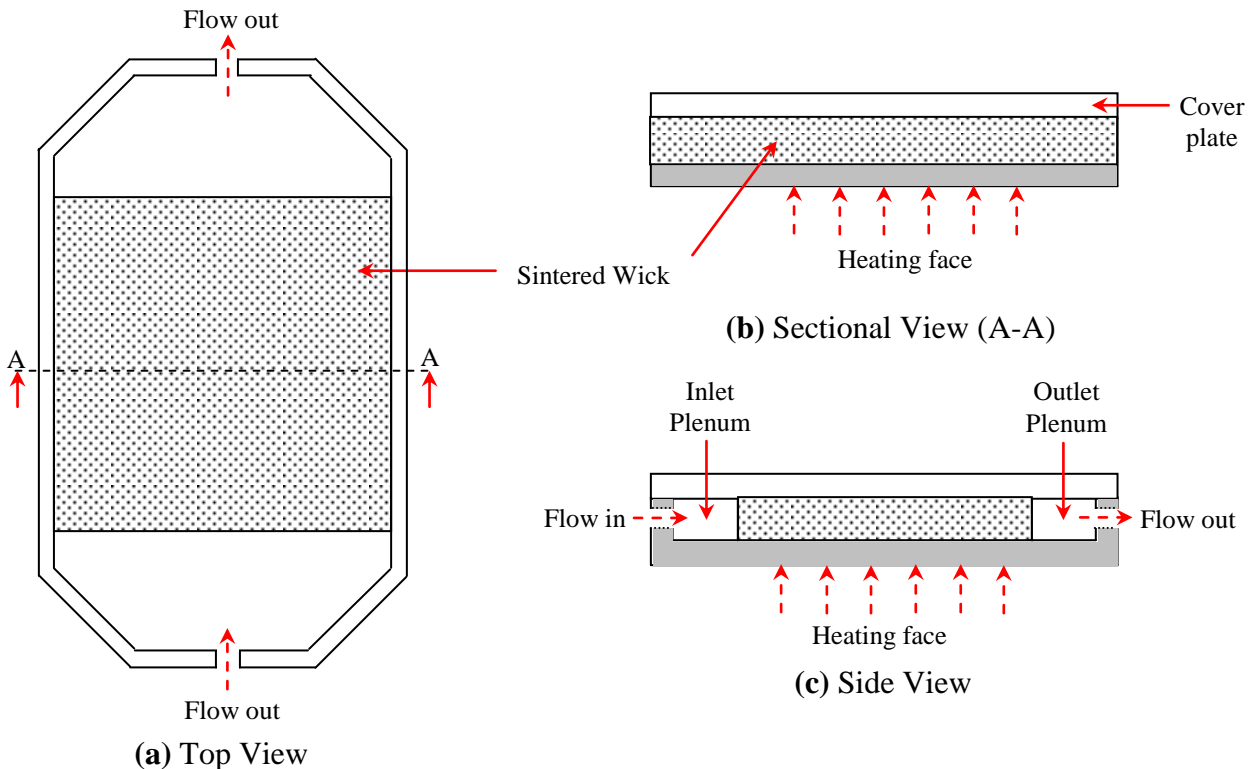


Figure 2.12 Schematic of a Sintered Porous Heat Sink

The cold plate design includes a porous sintered medium fixed between a metallic substrate and a cover plate for flow management. These sintered porous structures provide very high contact surface area to volume ratio and networks of microchannels which provides an efficient way of managing very high heat fluxes. The coolant enters from the inlet plenum manifold and flows through the porous structure to carry away the heat produced by the electronic components. After absorbing the heat, the hot fluid exits the heat sink through the outlet plenum.

Jiang et al (2004) experimentally investigated forced convection heat transfer in water and air in sintered porous plate channels made of bronze particles sintered to a thin copper plate which was placed in the stainless steel channel. Heat load as high as 0.9 MW/m^2 was transferred at a pressure drop of 1.29 MPa/m with single phase water flow. The effects of fluid velocity, particle diameter of bronze material ($d = 0.6, 1.2$ and 1.7 mm), type of porous medium (sintered or non-sintered) and type of fluid (air or water) on the heat enhancement were examined. The results showed that convective heat transfer in the sintered porous plate channel was more intense than in the non-sintered porous plate channel, due to the reduced thermal contact resistance and the reduced porosity at the wall in the sintered channels. For the conditions in the study, the sintered porous medium enhanced the local heat transfer coefficient 15 times for water and up to 30 times for air compared to the empty channel design. They also reported that the effective thermal conductivity of the sintered channels was much higher than that of the non sintered media due to the improved thermal contact from the sintering process.

In his study on a porous channel with sintered copper beads, Tzeng et al (2005) conducted experiments to study the effect of the bead particle size on the efficiency of heat exchange between the fluid and the solid phases for the heat sink. Three different test sections of sintered porous medium were made using copper beads of $0.71, 0.84$ and 1.15 mm particle size respectively and high pressure air was used as the cooling medium. It was reported that in the case of a smaller particle size, the overall wall temperature distribution is lower than with the bigger particles for the same input heat flux due to the larger contact area involved with the smaller particle beads.

In their study of metal foam heat sinks, Hsieh et al (2004) performed an experimental investigation of the effects of porosity, pore density and air velocity on the heat transfer characteristics of aluminum foam heat sink under forced convective cooling conditions using air as the coolant. Results showed that the Nusselt number increased with increase in the pore density and porosity of the aluminum foam, due to the fact that the heat transfer area of the foam increases as pore density and porosity increase. It was also noted that the temperature difference between the solid and the gas phases decreased with the increase of the Reynolds number of the air flow and increase in the porosity and pore density of the aluminum foam.

Heat transfer and pressure drop in a rectangular channel with sintered porous stainless steel inserts of different porosity were investigated experimentally by Hetsroni et al (2005) for the purpose of cooling mini-devices. Heat flux up to 6 MW/m^2 was removed by using a porous sample with 32% porosity and $20 \mu\text{m}$ average pore size. Under the experimental conditions, the difference between the wall and the inlet water temperatures did not exceed 55 K and the pressure drop was 4.5 bar. The authors also compared the efficiency of a sintered porous heat sink to an aluminum compressed foam heat sink and showed that the former provided very high heat transfer performance however it was accomplished by a drastic increase in pumping power.

Jeigarnik et al (1991) examined convective heat transfer in water on flat plates and in channels filled with porous materials such as sintered spherical particles, nets, porous metal and felts. They found that the porous media increased the heat transfer coefficient 5-10 times although the hydraulic resistance increased even more. Lage et al (1996) numerically studied a low permeability microporous heat sink for cooling phased-array radar systems. Their results suggested that an increased overall heat transfer coefficient could be obtained using such a heat sink which would reduce the operational temperature of the electronics for the same waste heat generation rate.

Tzeng et al (2006) measured local and average heat transfer characteristics of asymmetrically heated sintered porous channels with metallic baffles. The fluid medium was air. Solid baffles were inserted periodically into the sintered metallic material in four modes – without baffles,

with periodic baffles on the top portion, with periodic baffles on the bottom portion and with staggered periodic baffles on both sides. As an outcome of this study it was concluded that copper baffles helped to enhance the thermal conductivity through the solid matrix and promoted the heat transfer coefficient between the fluid and solid media. However, baffles also have some adverse effects that include reduction in the volume of the porous media (i.e. reducing the effective dissipation area) and preventing proper coolant flow into the regions around the neighboring baffles. In the study, the effect of bead diameter was also studied and it was seen that the heat transfer by forced convection in all modes increased as the bead diameter decreased.

2.14.4 Conclusions from the Current Body of Knowledge

From the above discussion, it is concluded that extremely high heat fluxes can be efficiently transferred by using porous metal heat sinks. Of the available forms of porous media, the sintered porous type is the most efficient. For sintered metallic porous media, the porosity at the wall and the thermal contact resistance are less than with non-sintered porous media, therefore the heat transport from the wall to the interior of the porous medium is more intense for sintered metallic porous media which enhances the overall heat transfer coefficient at the wall. Even compared to highly porous foam with large contact area, the sintered porous metallic medium is more effective, because of the high overall thermal conductivity. Regarding the coolant, as pointed out by the Jiang et al (2004) and Hsieh et al (2004), the heat transfer capabilities of water are superior to those of air for the removal of high and concentrated heat fluxes. However, the flow mechanism of the water through the porous medium involves high hydraulic losses that require high pressure pumps with drastic increase in the pumping power. Therefore sintered porous heat sinks are considered effective for cooling electronic devices with very high heat release in order to rationalize the pumping power and the overall cost of the cooling system.

The next chapter discusses in detail the theory and modelling of loop heat pipes.

Chapter 3

Theoretical Modelling of Loop Heat Pipe

This chapter discusses the theory of loop heat pipes (LHPs) in detail. The basic operating principle of the LHP is explained with the help of a pressure-temperature diagram. For the LHP there are some conditions that must be fulfilled for the proper serviceability of the device, these necessary conditions have been elaborated. In order to validate the proposed design of a miniature LHP, a mathematical model to predict the operating temperature of the loop has been proposed. Beside this, the main operating characteristics that are helpful in determining the loop efficiency and thus understanding the thermodynamics of the LHP are formulated.

3.1 Principle and Operation

The basic principle of operation of loop heat pipes is similar to that of conventional heat pipes i.e. a closed evaporation-condensation cycle maintained with the help of capillary pumping of the working fluid. However, due to the unique design features of the LHP these physical processes are organised in quite a different way. Unlike in conventional heat pipes, the wick structure in a LHP performs a variety of functions. To determine these functions and explain the working of the LHP, the schematic presented in Figure 3.1 can be used.

In the absence of any heat load, the free surface of the working fluid is at a certain level A-A located in the liquid line and the evaporator. In this case the wick is saturated with liquid, and the vapour line and the condenser completely filled. Heat applied to the evaporator results in liquid evaporation from the wick both in the evaporation zone and in the compensation chamber. Since the wick possess a definite thermal resistance, the temperature and pressure of the vapour in the evaporation zone become higher than in the compensation chamber. In this case, the wick performs a function of a thermal lock by resisting heat flow to the compensation chamber. At the same time the vapour cannot penetrate through to compensation chamber through the saturated wick owing to the capillary force generated by the liquid present inside it. Here, the function of the wick as a hydraulic lock manifests itself.

The arising saturation pressure difference across the cooler absorbing and warmer evaporating faces of the wick causes displacement of the working fluid from the vapour line and condenser and filling of the compensation chamber. The resulting fluid displacement causes three interfaces to form in the LHP simultaneously: in the evaporation zone, in the condenser and in the compensation chamber. Depending on the applied heat load, the vapour-liquid interface in the condenser and compensation chamber may move. In most cases, liquid-vapour may be already present inside the compensation chamber prior to the start-up process.

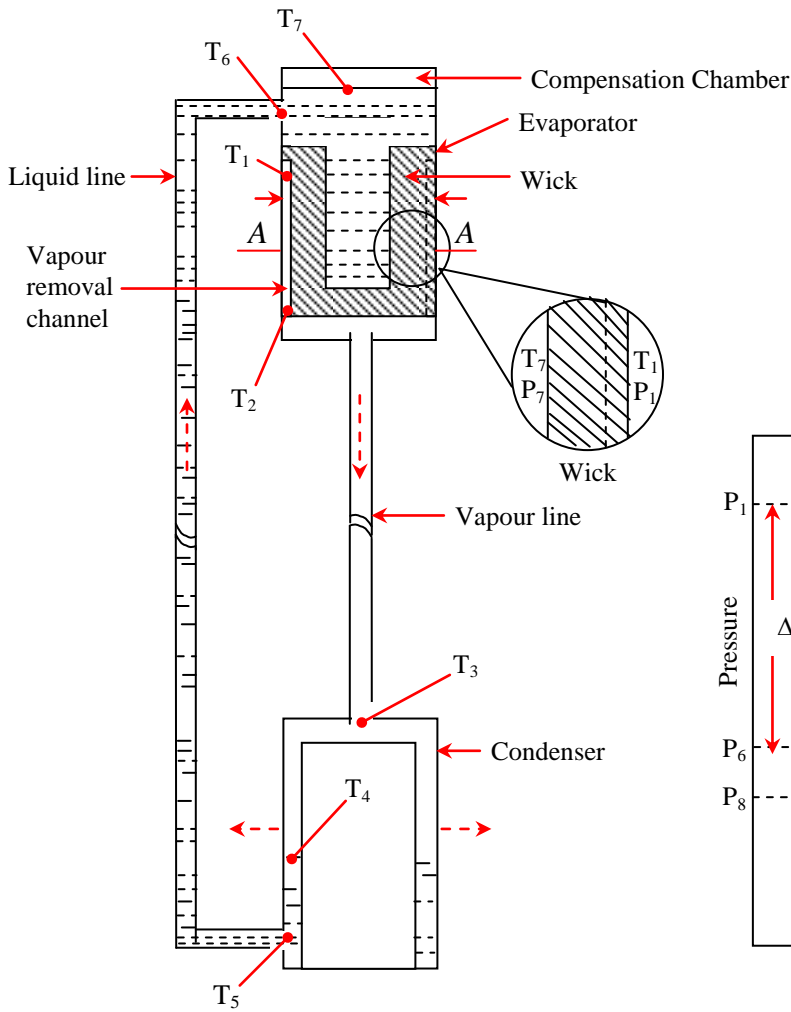


Figure 3.1 LHP schematic
(Ref: Maydanik & Fershtater, 1997)

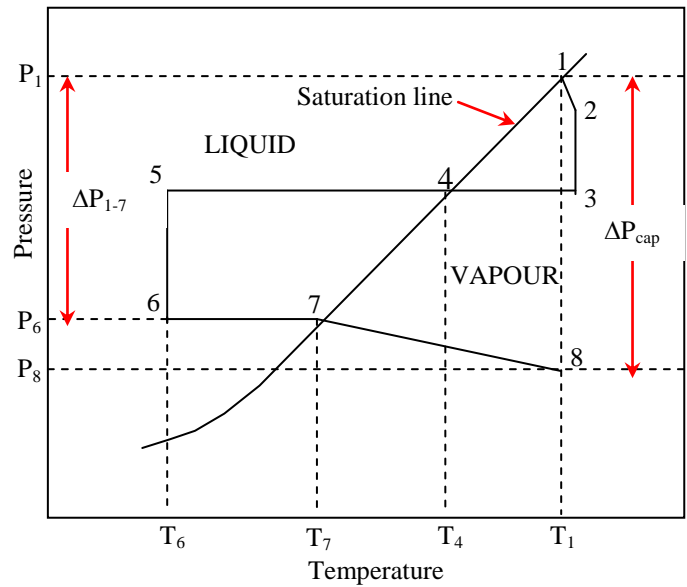


Figure 3.2 P-T diagram of the LHP working cycle

For analyzing LHP operation it is convenient to use the P-T diagram of the working cycle with respect to the saturation line of the working fluid, as shown in Figure 3.2 in idealized form. The point 1 on the saturation line identifies the vapour state with parameters P_1 , T_1

above the evaporating menisci in the wick and the section 1-2 corresponds to the vapour motion in the vapour removal channel into the vapour line. Since the vapour motion here proceeds along the hot wall of the evaporator, a decrease in its pressure is accompanied by a slight superheat. The vapour motion in the vapour line presented along section 2-3 can be ideally considered as close to isothermal. The vapour is condensed along section 3-4 followed by subcooling of the liquid condensate in the latter part of the condenser from 4-5. Pressure losses in the LHP condenser are usually negligible. Further the motion of the working fluid in the liquid line along section 5-6 is accompanied by pressure losses mainly due to the hydrostatic resistance of the liquid column while the LHP is operating at adverse tilts. Here, the process is shown as ideally isothermal, though in many cases there may be considerable heating or cooling owing to heat exchange with the surrounding medium. Liquid with parameters P_6 , T_6 enters the compensation chamber and is heated to temperature T_7 due to heat flowing back from the evaporator to the compensation chamber (i.e. back conduction of heat through the wick). The section 7-8 corresponds to liquid filtration through the wick into the evaporation zone. As the liquid proceeds through the wick, the pressure loss due to flow resistance takes place. This causes a drop in the pressure inside the wick. Since the local pressure is lower than the corresponding saturation pressure for the local temperature, the liquid presents a condition of superheating. It should be noted that the liquid may prove to be superheated inside the wick but boiling does not take place due to the short residence time in such a state. In other words, the liquid is in a metastable condition and the simple perturbation of reaching the boundary (meniscus) is enough to evaporate the substance which changes instantly into the state of superheated vapour. The point 8 determines the state of the working fluid in the vicinity of the evaporating menisci and the pressure drop ΔP_{1-8} corresponds to the value of the total pressure losses in all sections of the working fluid circulation (Maydanik, 2005).

3.2 Conditions of LHP Serviceability

3.2.1 Maximum Capillary Pressure Limit

The main condition that needs to be satisfied for the proper operation of the LHP is the same as for any other heat pipe and relates to the balance of the capillary pressure generated by the

porous structure on the working fluid and the total pressure drop in the loop. This can be stated mathematically as follows:

$$(\Delta P_{cap})_{\max} \geq \Delta P_v + \Delta P_l + \Delta P_{gr} = \Delta P_t \quad (3.1)$$

where, $(\Delta P_{cap})_{\max}$ is the maximum capillary pressure, ΔP_t is the total pressure drop in the loop which includes: ΔP_v - pressure loss due to vapour flow, ΔP_l - pressure loss incurred due to the liquid flow and ΔP_{gr} - hydrostatic pressure loss due to the unfavorable slopes of the device in the gravity field.

The maximum capillary pressure, which depends upon the surface tension coefficient (σ_l) of the liquid working fluid and mean effective pore radius (r_{me}) of the porous structure, is given by the Young-Laplace equation as:

$$(\Delta P_{cap})_{\max} = \frac{2\sigma_l}{r_{me}} \quad (3.2)$$

3.2.2 Wick Limitation

The second condition of serviceability, characteristic only of LHPs, is related to the minimum pressure drop requirement between the evaporating and absorbing surfaces of the wick. This pressure drop is to be equal to ΔP_{1-7} (Figure 3.2), which is the sum of pressure losses in all the sections of circulation of the working fluid except the wick. This criterion for a minimum pressure drop, which may be regarded as a thermodynamic one, is required for displacing the liquid from the vapour line and evaporator grooves, and filling the liquid line and compensation chamber. The condition can be stated with reference to Figure 3.2 as follow:

$$\left. \frac{dP}{dT} \right|_{T_s} \Delta T_{1-7} = \Delta P_{1-7} \quad (3.3)$$

where, ΔT_{1-7} and ΔP_{1-7} are the temperature and pressure differences of saturated vapour above the liquid-vapour interface between the evaporation zone and compensation chamber respectively.

$\frac{dP}{dT}$ is the derivative determined by the slope of the saturation line at the point with temperature T_s (vapour saturation temperature). The slope of the saturation pressure-

temperature line at a given temperature, T_s can be calculated by the well known Clausius-Clapeyron equation as follow:

$$\left. \frac{dP}{dT} \right|_{T_s} = \frac{h_{lv}}{T_s(v_v - v_l)} \quad (3.4)$$

where, h_{lv} is the latent heat of evaporation and v_v and, v_l are the specific volumes of vapour and liquid at temperature, T_s .

This second condition of serviceability means that to ensure proper working of the LHP, a difference of vapour temperatures and pressures between the liquid-vapour interfaces in the evaporation zone and compensation chamber must be created to initiate start-up and maintain steady state operation of the LHP.

3.2.3 Liquid Line Boiling Limit

The working fluid should be sufficiently subcooled in the condenser after condensation in order to avoid boiling in the liquid line as a result of pressure losses and heating from external heat inflows and from heat conducted from the evaporator to the liquid line. The amount of required subcooling, ΔT_{4-6} is related to the liquid pressure drop, ΔP_{5-6} inside the liquid line due to frictional pressure loss, $\Delta P_{l,ll}$ and gravitational resistance, ΔP_{gr} and is determined by the following inequality.

$$\left. \frac{dP}{dT} \right|_{T_s} \Delta T_{4-6} \geq \Delta P_{5-6} = \Delta P_{l,ll} + \Delta P_{gr} \quad (3.5)$$

This condition may be regarded as the third condition of LHP serviceability.

3.3 LHP Mathematical Model

A mathematical model of a LHP was developed, on the basis of the conservation laws of mass and energy in order to predict the steady state behaviour at given set of operating conditions. Using the model the steady state evaporator temperature, which is the main operating parameter of the loop heat pipe, is calculated as a function of the input power at the given conditions. The specified loop conditions include the sink/ambient temperature and the associated mode of cooling at the condenser. The proposed model was simplified by making the following assumptions:

1. The LHP achieves a steady state for a given loop condition.
2. Single phase flow correlations are used to calculate the pressure drop in the condenser
3. Heat exchange due to natural convection between the vapour line, liquid line and compensation chamber with the surroundings is assumed to be negligibly small.
4. For a given heat load, the surface temperature of the condenser is considered to be constant and equal to the loop saturation temperature.
5. Heat exchange between the wick wall and the liquid flowing through it is neglected. However, there is allowance for heat going from absorbing face of the wick into the liquid passing through the compensation chamber.
6. Saturated liquid enters the wick absorbing face and saturated vapour leaves the evaporation zone.

For a given heat load and sink temperature, the loop saturation temperature can be calculated from energy balances for each LHP component. To solve the resulting equations, fluid properties, system pressure drop, mass flow rate, heat transfer coefficients etc are required as functions of saturation temperature which are determined as follows.

3.3.1 Fluid Properties

The relevant fluid properties of the working fluid are functions of the loop operating temperature. In order to denote the dependence of the fluid properties on the temperature, each of these properties is curve fitted into a fifth order polynomial with respect to loop saturation temperature in the range of 0 to 125 °C. At a particular temperature, T , each fluid property, Y , is calculated as follow:

$$Y = a + bT + cT^2 + dT^3 + eT^4 + fT^5 \quad (3.6)$$

The coefficients ($a...f$) of the polynomials for water as the working fluid are given in Table A1 in the Appendix A. For each curve fitting, the error of the predictions from these coefficients compared to the values from the steam tables was not more than 5 %.

3.3.2 Energy Balance

The schematic of the proposed miniature LHP model shown in Figure 3.3 depicts the constructional details of the device. The design of the miniature LHP consists of a flat disk shaped evaporator and fin-and-tube condenser connected by separate vapour and liquid transport lines. The thickness of the flat evaporator is determined by the vapour removal passage, wick structure and the compensation chamber. For steady state at given loop conditions, the energy balance is carried out for the loop by dividing it into three control volume as shown in Figure 3.3.

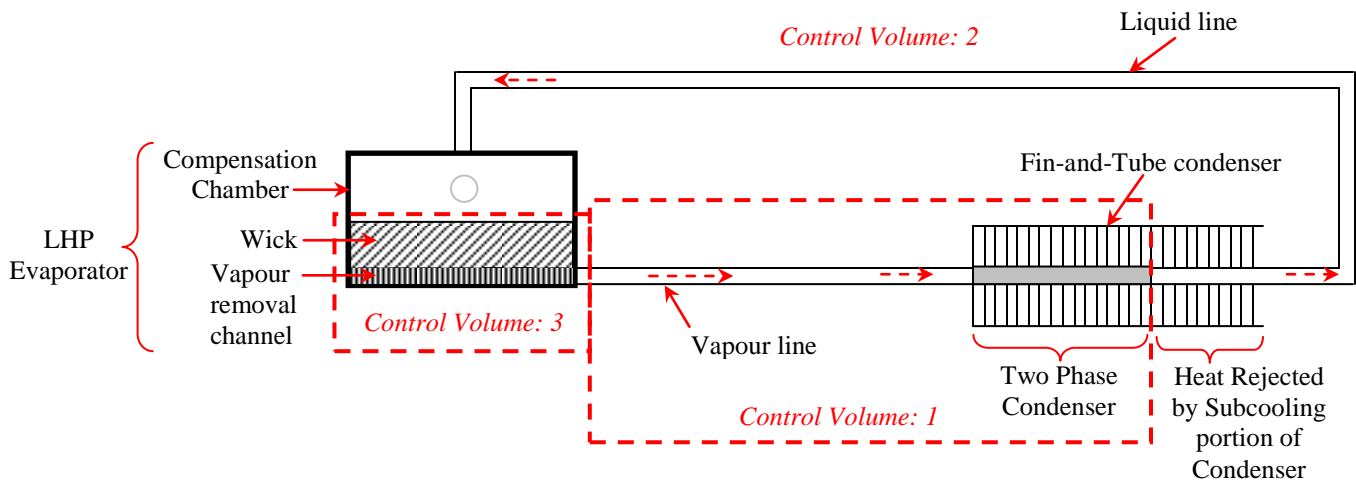


Figure 3.3 Schematic of the miniature LHP showing various control volumes for the energy balance

The energy balance is performed on each of the control volumes as follow:

Control Volume 1

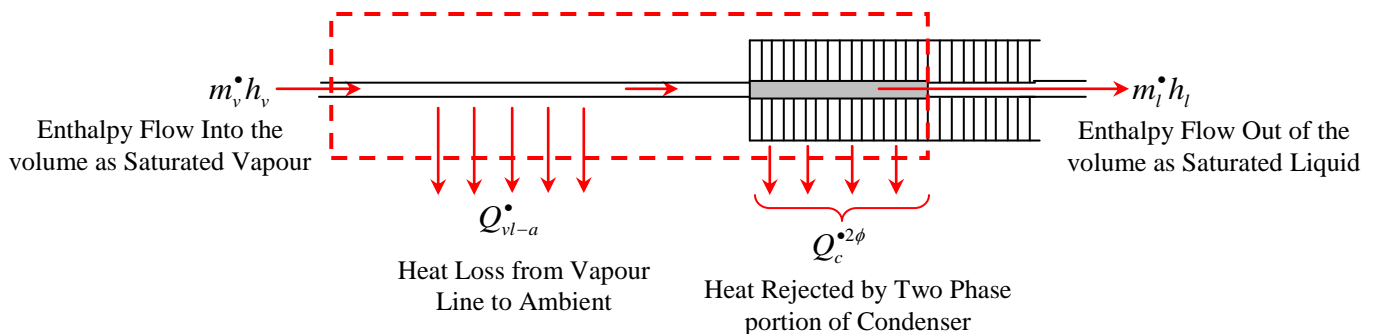


Figure 3.4 Energy Balance inside Control Volume 1

From Figure 3.4 equating net energy input to net energy output

$$m_v \dot{h}_v = Q_{vl-a} + Q_c^{*2\phi} + m_l \dot{h}_l \quad (3.7)$$

rearranging gives:

$$m_v \dot{h}_v - m_l \dot{h}_l = Q_{vl-a} + Q_c^{*2\phi} \quad (3.8)$$

The mass flow rate of vapour, $m_v \dot{h}_v$ is equal to the mass flow rate of the liquid, $m_l \dot{h}_l$ which can be written as mass flow rate of the working fluid, $m_{wf} \dot{h}_l$ i.e.

$$m_v \dot{h}_v = m_l \dot{h}_l = m_{wf} \dot{h}_l \quad (3.9)$$

therefore,

$$m_{wf} \dot{h}_l (h_v - h_l) = Q_{vl-a} + Q_c^{*2\phi} \quad (3.10)$$

Control Volume 2

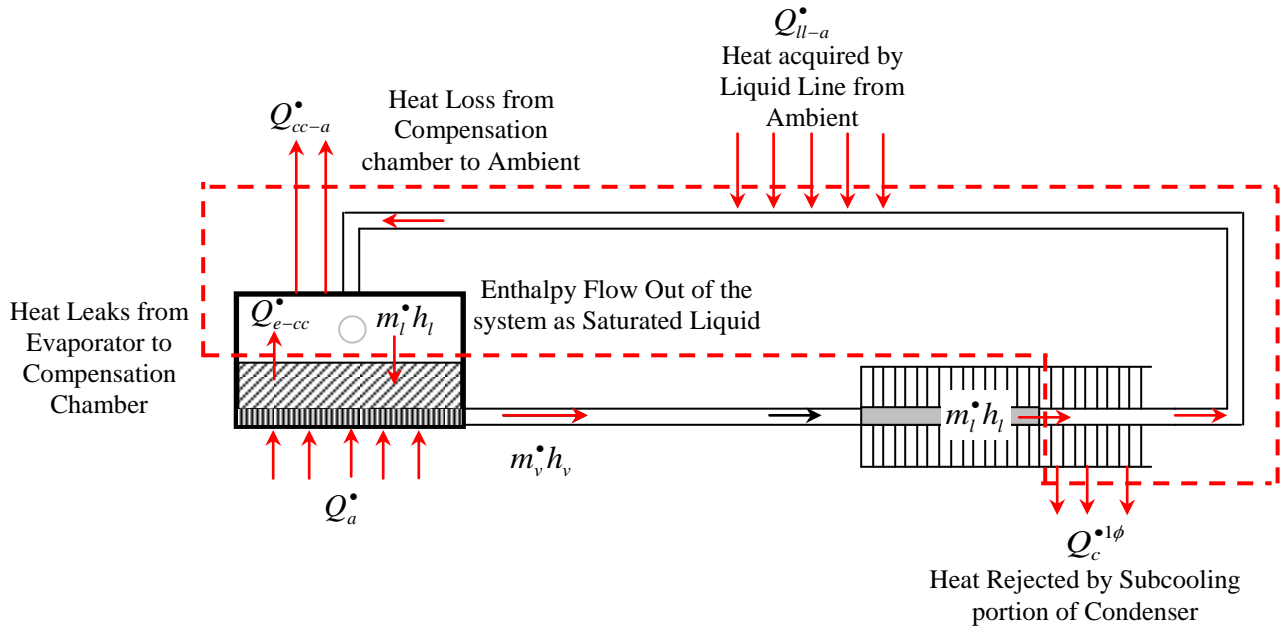


Figure 3.5 Energy Balance inside Control Volume 2

From Figure 3.5 equating net energy input to net energy output

$$m_l \dot{h}_l + Q_{cc-a} + Q_c^{*1\phi} = m_l \dot{h}_l + Q_{e-cc} + Q_{ll-a} \quad (3.11)$$

solving Equation (3.11)

$$Q_{cc-a} + Q_c^{*1\phi} = Q_{e-cc} + Q_{ll-a} \quad (3.12)$$

Control Volume 3

In a LHP, the compensation chamber dictates the saturation temperature of the loop. The compensation chamber temperature is affected by three heat transfer paths. These paths include heat exchange between the evaporator and the compensation chamber, Q_{e-cc}^{\bullet} , known as heat leak or back conduction, heat exchange between the compensation chamber and the returning subcooled liquid from the condenser (with enthalpy gain H_{sc}^{\bullet}), and heat exchange between the compensation chamber and the surroundings, Q_{cc-a}^{\bullet} . Under steady state conditions, the compensation chamber temperature and consequently the loop operating temperature results from these processes.

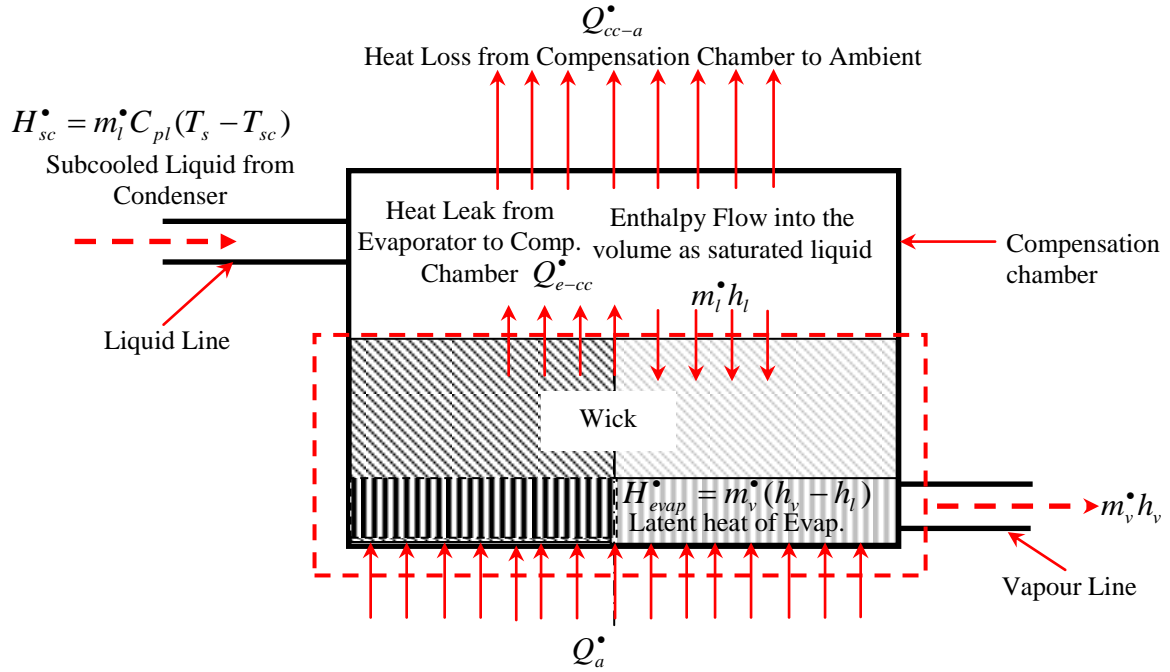


Figure 3.6 Energy Balance inside Control Volume 3

From Figure 3.6 equating net energy input to net energy output

$$m_v^{\bullet} h_v + Q_{e-cc}^{\bullet} = m_l^{\bullet} h_l + Q_a^{\bullet} \quad (3.13)$$

rearranging Equation (13)

$$m_v^{\bullet} h_v - m_l^{\bullet} h_l = Q_a^{\bullet} - Q_{e-cc}^{\bullet} \quad (3.14)$$

using, $m_v^{\bullet} = m_l^{\bullet} = m_{wf}^{\bullet}$

$$m_{wf}^{\bullet} (h_v - h_l) = Q_a^{\bullet} - Q_{e-cc}^{\bullet} \quad (3.15)$$

Now, $m_{w,f}^{\bullet}(h_v - h_l)$ is the enthalpy gain by the fluid during the phase change process from liquid to vapour which can be denoted as H_{evap}^{\bullet}

$$\text{So, that } H_{evap}^{\bullet} = m_{w,f}^{\bullet}(h_v - h_l) \quad (3.16)$$

It should be noted that due to the small size of the LHP, the heat exchange due to natural convection between the vapour line, liquid line and compensation chamber is small enough to be neglected without admitting any considerable error (assumption 2). In light of the above statement and using equation (3.16), the energy Equations (3.10), (3.12) & (3.15) can be written in the modified form as follow:

$$H_{evap}^{\bullet} = Q_c^{\bullet 2\phi} \quad (3.17)$$

$$Q_c^{\bullet 1\phi} = Q_{e-cc}^{\bullet} \quad (3.18)$$

$$H_{evap}^{\bullet} = Q_a^{\bullet} - Q_{e-cc}^{\bullet} \quad (3.19)$$

Equation (3.17) states that the latent heat of evaporation utilized during the evaporation process, H_{evap}^{\bullet} is equal to the heat removal by the condensation process in the two phase portion of the condenser, $Q_c^{\bullet 2\phi}$. Equation (3.18) states that heat rejected in the single phase (i.e. subcooling) portion of the condenser is just enough to compensate for the heat conducted to the compensation chamber as a result of conduction through the saturated metal wick.

Heat rejected in the single phase portion of the condenser can be given as:

$$Q_c^{\bullet 1\phi} = m_l^{\bullet} c_{pl}(T_s - T_{sc}) \quad (3.20)$$

where, T_{sc} is the temperature of the subcooled liquid at the outlet of the condenser and T_s is the saturation temperature of the liquid inside the condenser,

In the light of Equation (3.18) it can be inferred that the enthalpy gain of the subcooled liquid, H_{sc}^{\bullet} with reference to the saturation state leaving the condenser and entering the compensation chamber is the same as the heat rejected by the single phase portion of the condenser, $Q_c^{\bullet 1\phi}$.

$$\text{i.e. } H_{sc}^{\bullet} = Q_c^{\bullet 1\phi} \quad (3.21)$$

This implies that back conduction from the evaporation zone to the compensation chamber via

the wick is counteracted by subcooling of the liquid achieved in the single phase portion of the condenser provided that the heat rejected by the compensation chamber to the surroundings and the heat gained by the liquid line from the surroundings are negligible.

Equation (3.19) states that heat utilized in the evaporation zone for evaporation purposes, H_{evap}^{\bullet} is the difference between the heat applied at the evaporator, Q_a^{\bullet} , and the heat exchange from the evaporation zone to the compensation chamber, Q_{e-cc}^{\bullet} .

The mathematical model is based on equation (3.18) in which each term is substituted in terms of loop saturation temperature - T_s , as discussed in the subsequent sections. The resulting equation is then iteratively solved for T_s .

3.3.3 Heat leakage across the wick, Q_{e-cc}^{\bullet}

Part of the heat applied to the evaporator flows to the compensation chamber by conduction through the wetted wick structure and is given by:

$$Q_{e-cc} = \frac{k_e A_w}{t_w} \Delta T_w \quad (3.22)$$

where, k_e is the effective thermal conductivity of the wetted wick, A_w and t_w are the absorbing surface area and thickness respectively of the disk shaped wick structure and ΔT_w is the temperature difference across the wick.

It should be noted in accordance with the assumption 5 that heat transfer from the wick into the liquid passing through it is neglected.

The temperature difference, ΔT_w , is between the liquid-vapour interfaces in the evaporator and compensation chamber and is caused by the pressure difference across the wick structure. In order to calculate, ΔT_w , the serviceability condition 2, related to minimum pressure drop as discussed in the previous section, can be employed. This condition can be stated as:

$$\left. \frac{dP}{dT} \right|_{T_s} \Delta T_w = \Delta P_t - \Delta P_{l,w} \quad (3.23)$$

rearranging the equation

$$\Delta T_w = \frac{\Delta P_t - \Delta P_{l,w}}{\left. \frac{dP}{dT} \right|_{T_s}} \quad (3.24)$$

$$\text{or, } \Delta T_w = \left(\left. \frac{dT}{dP} \right|_{T_s} \right) (\Delta P_t - \Delta P_{l,w}) \quad (3.25)$$

The slope of the liquid-vapour saturation line at the saturation temperature T_s ,

$\left. \frac{dP}{dT} \right|_{T_s}$ can be calculated by using the Clausius-Clapeyron relation as in Equation (3.4):

$$\left. \frac{dP}{dT} \right|_{T_s} = \frac{h_{lv}}{T_s (v_v - v_l)}, \text{ where } h_{lv} \text{ is the latent heat of evaporation and } v_v \text{ and } v_l \text{ are the specific}$$

volumes of vapour and liquid at temperature, T_s .

The slope $\left. \frac{dP}{dT} \right|_{T_s}$ can also be accurately predicted by differentiating the fifth order polynomial

relationship between saturation pressure, P_s and saturation temperature, T_s as given by Equation (6) and shown below:

$$P_s = a + bT_s + cT_s^2 + dT_s^3 + eT_s^4 + fT_s^5$$

differentiating P_s w.r.t. T_s

$$\frac{dP_s}{dT_s} = b + cT_s + dT_s^2 + eT_s^3 + fT_s^4 \quad (3.26)$$

the values of the constants ($b...f$) are given in the Table A1 in the Appendices.

The second term on the right side of the Equation (3.25) ($\Delta P_t - \Delta P_{l,w}$) is calculated as discussed in the section below:

3.3.4 Pressure Analysis

The total pressure drop in the loop, ΔP_t , is the sum of the pressure losses due to vapour flow, ΔP_v , liquid flow ΔP_l , and hydrostatic pressure loss due to the tilt of the device in the gravitational field, ΔP_{gr} .

$$\Delta P_t = \Delta P_v + \Delta P_l + \Delta P_{gr} \quad (3.27)$$

The pressure drop due to friction losses in liquid and vapour flow through the loop (for laminar or turbulent flows, circular or non-circular pipes, smooth or rough surfaces) is given by Darcy-Weisbach equation as:

$$\Delta P = f \frac{L}{D} \frac{\rho}{2} u^2 \quad (3.28)$$

Where, f , a dimensionless quantity and function of Reynolds number, is the Darcy friction factor. For perfectly smooth pipes/channels, the friction factor, f is given by:

$$f = \frac{64}{\text{Re}}, \text{ Re} < 2300 \text{ (laminar flow)} \quad (3.29)$$

$$f = \frac{0.316}{\text{Re}^{0.25}}, \text{ Re} > 2300 \text{ (Turbulent flow)} \quad (3.30)$$

Reynolds number is given by,

$$\text{Re} = \frac{\rho u D_h}{\mu} \quad (3.31)$$

Where, velocity of flow, u is calculated from continuity equation,

$$u = \frac{\dot{m}}{\rho A} \quad (3.32)$$

and mass flow rate is given by $\dot{m} = \frac{Q_a}{h_{lv}}$ (3.33)

It should be noted that calculation of the mass flow rate, \dot{m} of the working fluid from the applied heat load Q_a provides a conservative approach in the determination of the total pressure loss inside the loop. Even for the adverse back conduction of the applied heat load to the compensation chamber (i.e. for cases of Q_{e-cc} to be 10 to 50% of the Q_a), the above approach introduces an error of not more than 4%, in the prediction of the loop saturation temperature, T_s .

3.3.4.1 Vapour pressure drop, ΔP_v

Vapour pressure drop includes flow resistance due to vapour flow in the vapour transport line $\Delta P_{v,vl}$, the evaporator grooves $\Delta P_{v,e}$ and the condenser line, $\Delta P_{v,c}$. By using the similar approach to that in section 3.3.4 the following correlation is obtained for laminar flow in the vapour line:

$$\Delta P_{v,vl} = \left(\frac{32}{\pi} \right) \left(\frac{L_{vl}}{D_{vl}^4} \right) \left(\frac{\mu_v}{\rho_v h_{lv}} \right) Q_a \quad (3.34)$$

The vapour pressure loss in the vapour line is the major resistance that the fluid must overcome in order to circulate continuously under the capillary head.

In order to calculate the pressure drop ($\Delta P_{v,e}$) due to vapour flow through the grooves of the evaporator, the Reynolds number for flow is based on the hydraulic diameter defined as:

$$(D_h)_{eg} = \frac{4A_{eg}}{p_{eg}}, \quad (3.35)$$

where A_{eg} is the cross sectional area of the groove/channel and p_{eg} is its wetted perimeter.

Therefore, for laminar flow in the vapour removal channels, the vapour frictional pressure loss can be obtained as follow:

$$\Delta P_{v,e} = 32 \left(\frac{L_{eg}}{(D_h)_{eg}^2 A_{eg}} \right) \left(\frac{\mu_v}{\rho_v h_{lv}} \right) Q_a \quad (3.36)$$

For the condenser line

$$\Delta P_{v,c} = \left(\frac{32}{\pi} \right) \left(\frac{L_{cl}}{D_{cl}^4} \right) \left(\frac{\mu_v}{\rho_v h_{lv}} \right) Q_a \quad (3.37)$$

It should be noted that pressure loss in the condenser line is calculated by assuming vapour flow inside the condenser.

3.3.4.2 Liquid Pressure Drop, ΔP_l

Pressure drop due to laminar flow of liquid in the liquid transport line, $\Delta P_{l,ll}$ can be calculated using the following relations:

For the liquid transport line

$$\Delta P_{l,ll} = \left(\frac{32}{\pi} \right) \left(\frac{L_{ll}}{D_{ll}^4} \right) \left(\frac{\mu_l}{\rho_l h_{lv}} \right) Q_a \quad (3.38)$$

Note that the liquid pressure drop inside the evaporator core and the compensation chamber is small and can be neglected.

The pressure drop due to liquid flow through the wick thickness, $\Delta P_{l,w}$ can be determined by Darcy's law of fluid flow through porous media which denotes the influence of applied pressure on the flow rate of fluid for the given physical properties of the porous structure. This is given by (Faghri, 1995) as:

$$\Delta P_{l,w} = \left(\frac{t_w}{A_w} \right) \left(\frac{\mu_l}{\rho_l h_{lv}} \right) \left(\frac{1}{k_{ws}} \right) Q_a \quad (3.39)$$

where, k_{ws} is the permeability of the evaporator wick and describes its ability to transport liquid under an applied pressure gradient. As evident from Equation (3.39) pressure losses are magnified for smaller values of permeability.

3.3.4.3 Hydrostatic losses, ΔP_g

The hydrostatic losses, for cases where liquid is pumped uphill, are determined as:

$$\Delta P_{gr} = (\rho_l - \rho_v) g l \sin \varphi \quad (3.40)$$

as $\rho_l \gg \rho_v$

$$\Delta P_{gr} = \rho_l g l \sin \varphi \quad (3.41)$$

where, ρ_l and ρ_v are the liquid and vapour densities respectively, g is gravitational acceleration, l is the effective length of the device and φ is the slope from the horizontal plane.

In the horizontal configuration, $\varphi = 0$ and therefore the hydrostatic resistance is non existent.

The total pressure loss can therefore be calculated by substituting values from equations (3.34), (3.36), (3.37), (3.38), (3.39) and (3.41) into the equation below:

$$\Delta P_t = \Delta P_{v,vl} + \Delta P_{v,e} + \Delta P_{l,ll} + \Delta P_{v,c} + \Delta P_{l,w} + \Delta P_{gr} \quad (3.42)$$

3.3.5 Effective Thermal Conductivity of Wetted Wick, k_e

The effective thermal conductivity of the wick is a very important parameter to be considered during the selection of the wick material and design of the capillary evaporator. It is a useful parameter to correctly calculate the wick thickness which is the most critical factor relating to evaporator design. There are different correlations that can be used to calculate the effective thermal conductivity of the wick.

Dunn and Reay (1995) proposed the following correlation to calculate the effective thermal conductivity, k_e of the isotropic wick structure.

$$k_e = k_w \left(\frac{2 + (k_l / k_w) - 2\varepsilon[1 - (k_l / k_w)]}{2 + (k_l / k_w) + \varepsilon[1 - (k_l / k_w)]} \right) \quad (3.43)$$

where, ε is the porosity of the wick and k_w and k_l are the thermal conductivities of the wick material and the working fluid respectively.

Effective thermal conductivity of the wick can also be obtained by volume averaging the thermal conductivities of the wick material and the working fluid as follows:

$$k_e = k_w(1 - \varepsilon) + \varepsilon k_l \quad (3.44)$$

Alexander (1972) gives a relationship for calculating the effective conductivity of the homogeneous wick structure as:

$$k_e = k_l \left(\frac{k_l}{k_w} \right)^{-(1-\varepsilon)\alpha} \quad (3.45)$$

where, α is a constant equal to 0.59.

3.3.6 Return Liquid Subcooling, H_{sc}^*

The amount of the subcooling required for the liquid returning from the condenser depends upon the quantity of heat leakage from the evaporator to the compensation chamber. In order to avoid boiling in the non capillary liquid line, which can lock the capillary action and decrease the supply of liquid to the evaporator, the condenser in the LHP is arranged in such a way that part of the condenser serves to condense vapour while the reminder works as a liquid subcooler. In most cases, the maximum heat capacity of the LHP is limited by the condition of cooling and size of the condenser which in turn are set by the available space and design constraints.

Proper analysis of the condenser includes calculation of the two phase length of the condenser i.e. active length of the condenser and extent of subcooling achieved in the single phase length of the condenser and the temperature at the outlet of the condenser.

3.3.7 Fin-and-Tube Condenser Analysis

The schematic of the fin-and-tube condenser (also called a compact heat exchanger) in Figure 3.7, is used as the basis for the thermal analysis of the heat exchanger. The mode of condenser cooling is forced convection using a centrifugal fan.

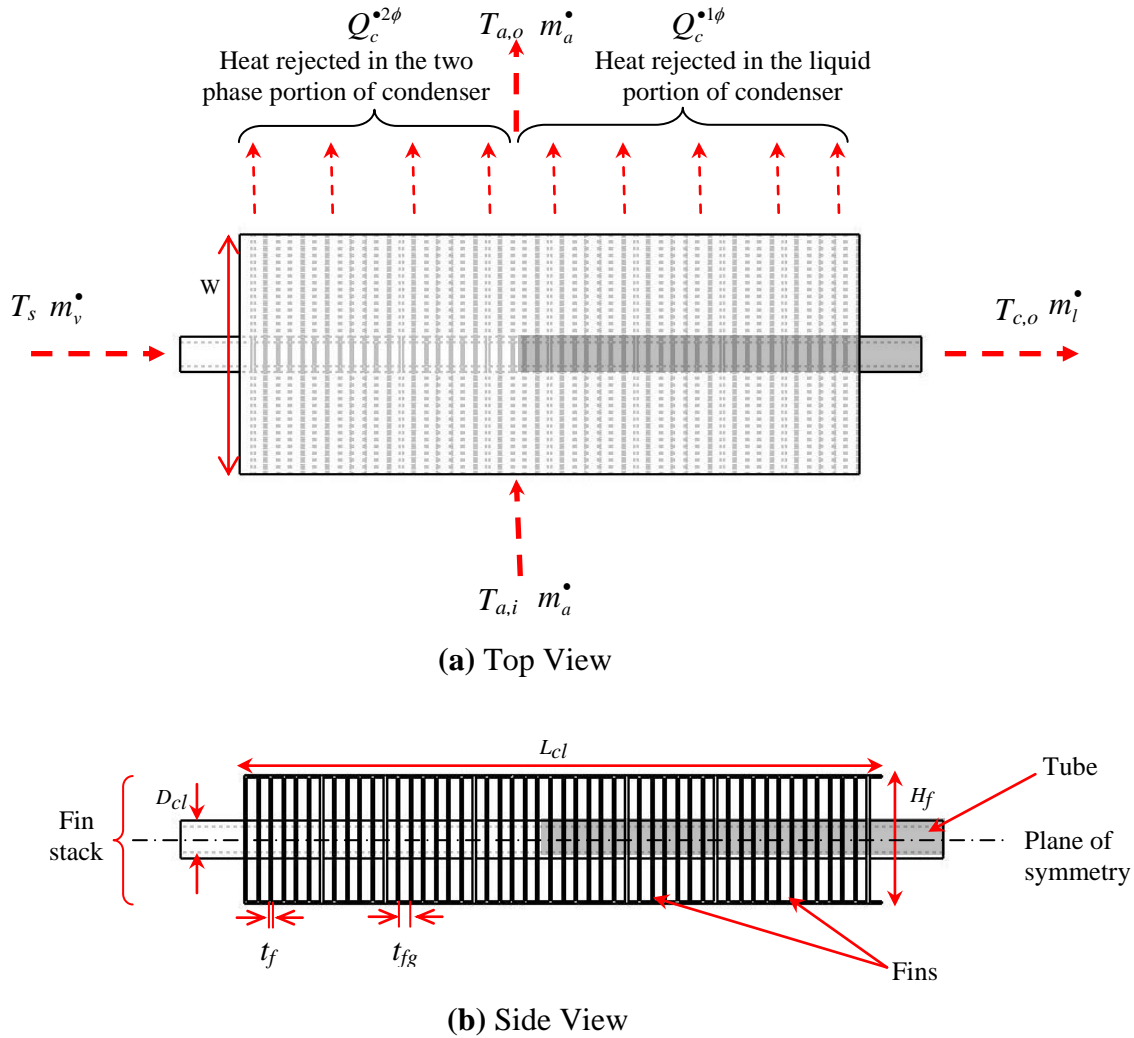


Figure 3.7 Schematics of the LHP condenser

From the energy balance, the heat rejected in the two phase region of the condenser, $Q_c^{2\phi}$ from Equations (17) and (19) is given as:

$$Q_c^{2\phi} = Q_a^* - Q_{e-cc}^* \tag{3.46}$$

In order to calculate the heat transfer rate of the condenser per unit length, the air flow through the rectangular fin array is considered. It is assumed that flow through the fin stack is fully developed and that the surface temperature of the base and the fins on the condenser is uniform. The latter assumption is correct within an accuracy of $\pm 5\%$ as verified by the experimental results. Thermocouples installed on the condenser surface displayed the surface temperature within $\pm 5\%$ of each other and justified this assumption.

3.3.7.1 Heat Transfer Rate per Unit Length of the Condenser, $Q_{c/l}^{\bullet}$

In order to determine the heat transfer capacity of the entire fin stack, as shown in Figure 3.7b, the following approach is used:

Total heat transfer rate per unit length of the entire fin stack (i.e condenser), $Q_{c/l}^{\bullet}$ is calculated as:

$$Q_{c/l}^{\bullet} = \frac{h_a A_t \eta_o T_{lm,f-a}}{L_{cl}} \quad (3.47)$$

where,

h_a is the heat transfer coefficient of air

A_t is the total surface area of the fins including the unfinned surface or flow area of the entire stack.

$T_{lm,f-a}$ is the log mean temperature difference between the fin surface and ambient air

η_o is the overall surface efficiency or temperature effectiveness of the surface of the fins

L_{cl} is the total finned length of the condenser

$Q_{c/l}^{\bullet}$ can also be expressed as:

$$Q_{c/l}^{\bullet} = \frac{m_a^{\bullet} c_{pa} (T_{a,o} - T_{a,i})}{L_{cl}} \quad (3.48)$$

where,

m_a^{\bullet} is the total mass flow rate of the air

c_{pa} is the specific heat of air

$T_{a,i}$ is the inlet temperature of the air to the condenser

$T_{a,o}$ is the outlet temperature of the air from the condenser

Each term in Equations (3.47) and (3.48) is calculated as discussed in the following sections:

3.3.7.2 Mass Flow Rate of Fan Air, m_a^*

$$m_a^* = V_a^* \rho_a \quad (3.49)$$

where the volume flow rate of fan air is:

$$V_a^* = u_a A_{fd} \quad (3.50)$$

3.3.7.3 Heat Transfer Coefficient of Air, h_a

To evaluate the flow regime, Reynolds number for the flow can be calculated as:

$$Re_D = \frac{\rho_a u_a (D_h)_{fc}}{\mu_a} \quad (3.51)$$

where, $(D_h)_{fc} = \frac{4A_{fc}}{p_{fc}}$ and is the hydraulic diameter of the channels between the fins.

For fully developed laminar flow and given Aspect Ratio ($\alpha = \frac{W_f}{H_f} = \frac{b}{a}$) of the fins, the

Nusselt number, Nu_D can be seen from Table A.2 in Appendices.

$$Nu_D = \frac{h_a D_h}{k_a} \quad (3.52)$$

rearranging for h_a ,

$$h_a = \frac{Nu_D k_a}{D_h} \quad (3.53)$$

3.3.7.4 Overall Surface Efficiency of the Condenser, η_o

The overall surface efficiency of the heat exchanger can be determined by the following equation:

$$\eta_o = 1 - \frac{A_{ft}}{A_t} (1 - \eta_f) \quad (3.54)$$

where,

A_{ft} is the total surface area of the fins in the entire fin stack.

The fin efficiency, η_f is calculated by using the following equation:

$$\eta_f = \frac{\tanh m \frac{H_f}{2}}{m \frac{H_f}{2}} \quad (3.55)$$

$$\text{where, } m = \sqrt{\frac{h_a P_c}{k_a A_c}} \quad (3.56)$$

3.3.7.5 Log Mean Temperature Difference (LMTD), $T_{lm,f-a}$

LMTD from the fin surface to the ambient air is given by the following formula:

$$T_{lm,f-a} = \frac{(T_s - T_{a,o}) - (T_s - T_{a,i})}{\ln \left[\frac{(T_s - T_{a,o})}{(T_s - T_{a,i})} \right]} \quad (3.57)$$

Here, the temperature of the fin, T_f is assumed to be equal to the temperature of the fin base - T_b which is assumed to be equal to the saturation temperature of the fluid passing through the condenser - T_s so that:

$$T_f = T_b = T_s \quad (3.58)$$

In this analysis, it is worth noting that the only thermal resistance regarded as significant in the condenser is that due to the convective heat transfer between the fins and the air.

In Equation (3.57) for $T_{lm,f-a}$, the outlet temperature of the hot air, $T_{a,o}$ from the condenser can be determined as below:

$$T_{a,o} = T_s - (T_s - T_{a,i}) \exp \left(\frac{h_a A_f \eta_o}{c_{pa} \dot{m}_a} \right) \quad (3.59)$$

3.3.7.6 Two Phase Length (Active Portion) of the Condenser, $L^{2\phi}$

Based on the preceding discussion, the length of the condenser in which actual condensation of the vapour takes place can be calculated as:

$$L^{2\phi} = Q_c \cdot 2\phi \int_{x_{in}}^{x_{out}} \frac{dx}{Q_{c/l}} \quad (3.60)$$

If the result of the integration of Equation 3.60 with respect to the quality from $x_{in} = 1$ to $x_{out} = 0$ is less than the total length of the condenser, then the liquid-vapour interface is situated inside the condenser. In the case, where the active length comes out to be more than the condenser length then the liquid-vapour interface lies in the liquid line in which case vapour will flow to the compensation chamber imposing limitation on the maximum heat transfer rate of the mLHP. At this condition, the condenser will operate in a so-called fully-opened condition. In practise, this condition is usually avoided as the condenser is designed to operate at the maximum heat load applied to the capillary evaporator.

3.3.7.7 Liquid Temperature at the Condenser Outlet, T_{sc}

Since the two phase length of the condenser is known, it is possible to calculate the liquid temperature at the condenser exit by using the energy balance equation in the liquid portion of the condenser i.e.

$$\frac{Q_c^{2\phi}}{h_{fg}} c_{pl} (T_s - T_{c,o}) = m_a^{1\phi} c_{pa} (T_{a,o} - T_{a,i}) \quad (3.61)$$

where, $m_a^{1\phi}$ is the mass flow of the air through the subcooling portion (i.e. liquid phase) of condenser and is given by:

$$m_a^{1\phi} = \frac{m_a^* L^{1\phi}}{L_c} \quad (3.62)$$

$L^{1\phi}$ is the subcooling length of the condenser.

Since the heat loss from the liquid line is neglected, the amount of liquid subcooling required for the returning liquid is determined in terms of T_s by putting values of c_{pl} , m_l^* and $T_{c,o}$ as calculated from Equation (3.6), (3.33) and (3.61) in the equation below:

$$H_{sc}^* = Q_c^{1\phi} = m_l^* c_{pl} (T_s - T_{c,o}) \quad (3.63)$$

3.3.7.8 mLHP Operating Temperature, T_s

Rewriting equation (18) to calculate T_s

$$Q_{e-cc}^* - H_{sc}^* = 0 \quad (3.64)$$

Substituting Equations (3.22) and (3.63) into Equation (3.64) gives an equation of the form:

$$f_1(T_s, T_a, Q_a^*) - f_2(T_s, T_a, Q_a^*) = 0 \quad (3.65)$$

where, f_1 and f_2 are known functions. For the given T_a and Q_a , the mLHP operating/saturation temperature T_s can be determined by solving equation (3.65) iteratively for T_s using Microsoft Excel software.

The criterion for convergence is set as follow:

$$f_1(T_s, T_a, Q_a) - f_2(T_s, T_a, Q_a) < 10^{-3} \quad (3.66)$$

3.4 mLHP Maximum Heat Transfer Capacity

The maximum capacity of a mLHP is limited by three main conditions that include

1. The maximum permissible operating temperature of the source,
2. Mode of cooling of the condenser (or maximum heat dissipation capacity of the condenser)
3. Capillary limit of the wick structure.

In the case of electronics cooling, the upper value of the operating temperature of the cooling device (in this case a mLHP) is generally less than or equal to $100\text{ }^\circ\text{C}$. Based on the mathematical model discussed above, for a given constant value of ambient temperature T_a , the operating temperature T_s is iteratively solved for the given input value of applied heat load, Q_a^* . For $T_s \leq 100\text{ }^\circ\text{C}$, the maximum value of the Q_a^* i.e. Q_{\max}^* can be obtained as limited by condition (1). Similarly, the value of the heat load at which the location of the liquid vapour interface is situated at the exit of the condenser gives the maximum value of the heat load according to condition (2).

The first condition of serviceability can be used to calculate the maximum value of heat load, Q_{\max}^* as limited by condition (3). The condition can be mathematically stated by rewriting Equation (1) as follow:

$$(\Delta P_{cap})_{\max} \geq \Delta P_t \quad (3.67)$$

Substituting for ΔP_t from Equation (42):

$$(\Delta P_{cap})_{\max} \geq \Delta P_t = \Delta P_{v,vl} + \Delta P_{v,e} + \Delta P_{l,ll} + \Delta P_{v,c} + \Delta P_{l,w} + \Delta P_{gr} \quad (3.68)$$

$$\Rightarrow (\Delta P_{cap})_{\max} \geq \Delta P_{v,vl} + \Delta P_{v,e} + \Delta P_{l,ll} + \Delta P_{v,c} + \Delta P_{l,w} + \Delta P_{gr} \quad (3.69)$$

By substituting from equations (3.2), (3.34), (3.36) to (3.39) and (3.41) in Equation (3.69) gives the following relationship:

$$\begin{aligned} \frac{2\sigma_l}{r_{me}} \geq & \left(\frac{32}{\pi} \right) \left(\frac{L_{vl}}{D_{vl}^4} \right) \left(\frac{\mu_v}{\rho_v h_{lv}} \right) Q_a^\bullet + 32 \left(\frac{L_{eg}}{(D_h)_{eg}^2 A_{eg}} \right) \left(\frac{\mu_v}{\rho_v h_{lv}} \right) Q_a^\bullet + \left(\frac{32}{\pi} \right) \left(\frac{L_{ll}}{D_{ll}^4} \right) \left(\frac{\mu_l}{\rho_l h_{lv}} \right) Q_a^\bullet + \\ & \left(\frac{32}{\pi} \right) \left(\frac{L_{cl}}{D_{cl}^4} \right) \left(\frac{\mu_v}{\rho_v h_{lv}} \right) Q_a^\bullet + \left(\frac{t_w}{A_w} \right) \left(\frac{\mu_l}{\rho_l h_{lv}} \right) \left(\frac{1}{k_{ws}} \right) Q_a^\bullet + \rho_l g l \sin \varphi \end{aligned} \quad (3.70)$$

In the Equation 3.70, values for the geometrical parameters of each component of the mLHP and the relevant fluid properties at the given saturation temperature T_s , are input to obtain the maximum value of $Q_a^\bullet = Q_{\max}^\bullet$ as limited by condition (3). It should be mentioned here that for a mLHP in most cases the value of Q_{\max}^\bullet is limited by conditions (1) and (2) rather than by condition (3) which is always very high due to the use of fine pore wicks in mLHP evaporators.

3.5 Thermal resistance, R

Apart from the evaporator operating temperature and maximum heat capacity, the efficiency of the mLHP is measured on the basis of the thermal resistance- R . Figure 3.8 shows the thermal circuit diagram for the mLHP showing the whole sequence of resistances from heat source to heat sink.

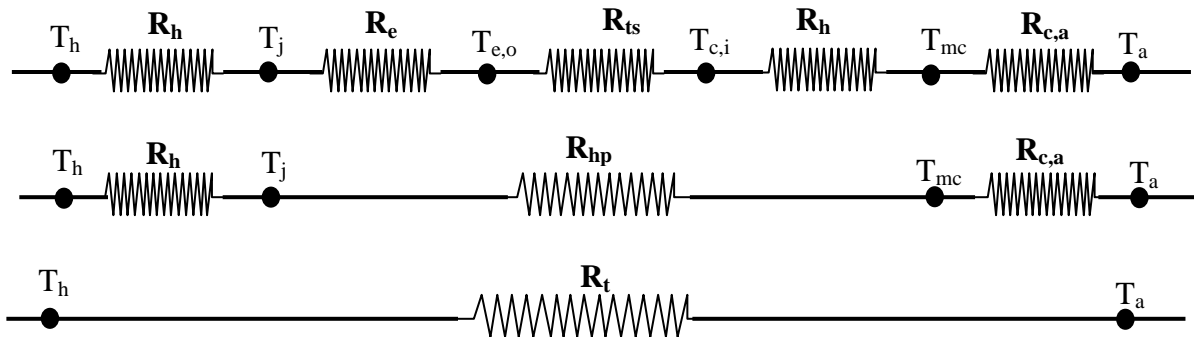


Figure 3.8 Thermal circuit diagram for the mLHP showing thermal resistances of different components

The main components of the total thermal resistance, R_t which are classified on the basis of temperature measurements at the characteristic points are the evaporator thermal resistance - R_e and mLHP/heat pipe thermal resistance (i.e. thermal resistance between evaporator surface to condenser surface) R_{hp} . The following equations (3.71 – 3.73) are used to calculate these thermal resistances.

Evaporator thermal resistance

$$R_e = \left(\frac{T_j - T_{e,o}}{\dot{Q}_a} \right) \quad (3.71)$$

Heat Pipe thermal resistance

$$R_{hp} = \left(\frac{T_j - T_{mc}}{\dot{Q}_a} \right) \quad (3.72)$$

Total thermal resistance

$$R_t = \frac{(T_j - T_a)}{\dot{Q}_a} \quad (3.73)$$

In the above equations, T_j is the temperature at the junction of the heater and the evaporator active surface. This temperature dictates the maximum permissible temperature of the source and should be generally below 100 °C.

R_{hp} , as in the case of conventional heat pipes, can also be determined on the basis of the following equation:

$$R_{hp} = \frac{1}{h_e A_{ae}} + \frac{1}{h_c A_{ac}} \quad (3.74)$$

Calculation for the heat transfer coefficient in the evaporator and condenser can be made by using the given relations:

$$h_e = \frac{\dot{Q}_a}{A_{ae} (T_{me} - T_{e,o})} \quad (3.75)$$

$$h_c = \frac{\dot{Q}_a}{A_{ac} (T_{e,o} - T_{mc})} \quad (3.76)$$

It should be noted that the saturation temperature of the loop, T_s is assumed to be equal to the temperature of the fluid at the evaporator outlet $T_{e,o}$ in carrying out the above calculations.

Thermal resistance for the heater-evaporator junction, R_j , the transportation section, R_{ts} , the heat exchanger, R_{hx} and condenser to ambient, $R_{c,a}$ can also be calculated on similar lines, with the help of Figure 3.8, in order to assess the performance of each component and improve the overall efficiency of the heat transfer process.

This section concludes the current chapter on the theory of loop heat pipes. The mathematical model described in this chapter can be used to validate the design of the mLHP and verify whether the proposed design is consistent with the maximum heat load capacity required for the intended application with the given working fluid. Performance indices like thermal resistance, operating temperature and heat transfer coefficient can be used to evaluate the efficiency of the proposed mLHP at the given loop conditions. In addition to this, the model can assist in understanding and refining the outcomes of the experimental studies.

3.6 Summary

In this chapter, a thermal analytical model of loop heat pipes is discussed. For the proper operation of a LHP, three main conditions of serviceability that includes maximum capillary pressure limit, wick limitation and liquid line boiling limit must be obeyed. A mathematical model based on energy balances inside the loop system is derived for the prediction of the mLHP steady state operating temperature. The predictions made by the theoretical model can be used in the refinement of the experimental studies. For the measurement of the thermal performance of a mLHP, thermal resistance between different loop components, loop steady state operating temperature and evaporator heat transfer coefficient were used.

The following chapter explains the experimental apparatus and testing procedure used for the thermal testing of a miniature LHP with a flat disk shaped evaporator.

Chapter 4

mLHP with Disk Shaped Evaporator: Experimental Apparatus and Method

The construction details of the miniature loop heat pipe are described in this section. As two phase heat transfer devices are very sensitive to any kind of impurity present inside the system, the cleaning and charging procedures are specifically explained. In the final part, the method used for testing the mLHP is stated. It should be noted that before the actual designing of the miniature mLHP was undertaken, a medium scale capillary pumped loop (CPL) prototype (Appendix B) was built and tested as a case study to gain experience on the design and integration of the system components and to better comprehend the working of two phase loop systems. In addition to this, the medium scale CPL was made to study the unique characteristics of the capillary pumped loop system.

4.1 mLHP Prototype Description

A miniature LHP (mLHP) with a flat disk shaped evaporator was designed to transfer 70 W of heat load over distances of up to 150 mm at a specified mode of condenser cooling. The prototype of the mLHP is shown in Figure 4.1 and consists of a flat evaporator and a fin-and-tube condenser which are connected by separate vapour and liquid lines. The main challenge here was to design the evaporator with limited thickness (≤ 10 mm) while preserving the functionalities of the wick and thermal performance of the two phase heat transfer process. The mLHP body and the transport lines were made of copper.

The design of the mLHP was performed on the basis of a pressure analysis in order to obey the first condition of serviceability. According to this condition, for a LHP with the given cooling capacity of the condenser and operating at the maximum heat load, the sum of the pressure losses in each loop component should be less than the maximum capillary pressure generated by the wick structure. Apart from this condition, other factors that are critical from the point of a design of mLHP are the condenser capability, maximum

heat load, available cooling space, heat transfer fluid used inside the loop and wick characteristics. The design and dimensions of the mLHP were decided to some extent by the available space inside the laptop enclosure as explained in the section 2.5 of the problem description. Some aspects of the mLHP design were also inspired from the work by Maydanik (2005). Each component of the mLHP is explained in detail in the following sections.

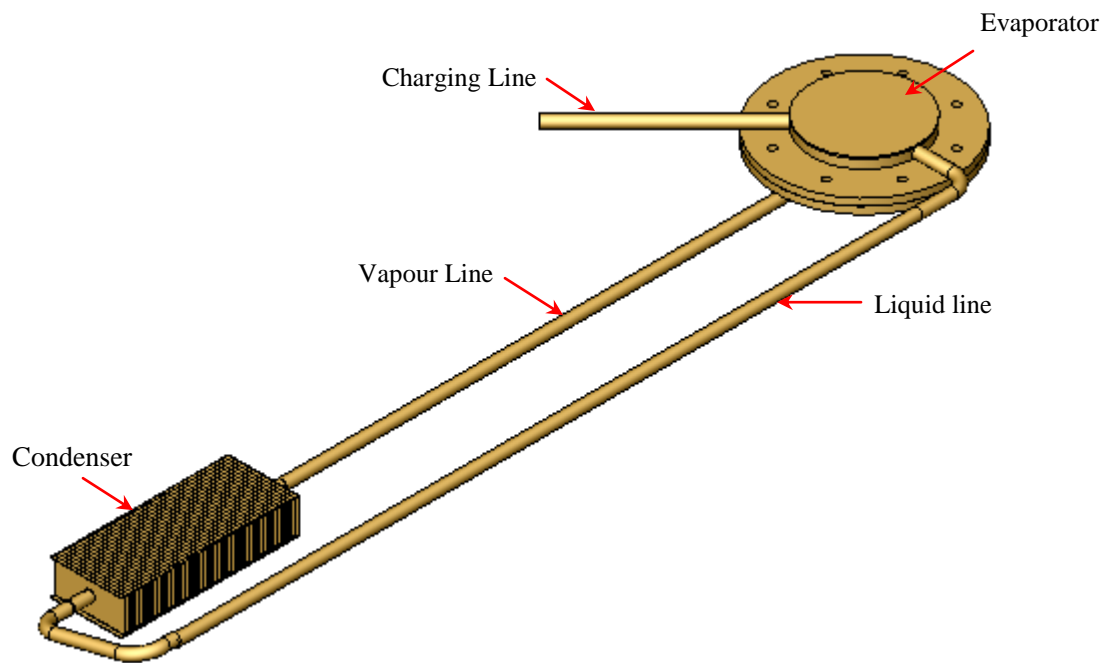


Figure 4.1 Prototype of Miniature Loop Heat Pipe (mLHP) showing the different components

4.1.1 Evaporator Structure

In the case of the evaporator, the maximum thickness and diameter of disk were fixed by the available space. The thickness of the mLHP evaporator consisted of the system of vapour removal channels and wick structure that formed the evaporator bottom portion and compensation chamber that formed the evaporator top portion. The internal details of the evaporator particularly the vapour flow channels were decided on the basis of the pressure loss analysis in the loop. This structural arrangement of the evaporator can be well understood from the exploded view of the capillary evaporator shown in Figure 4.2.

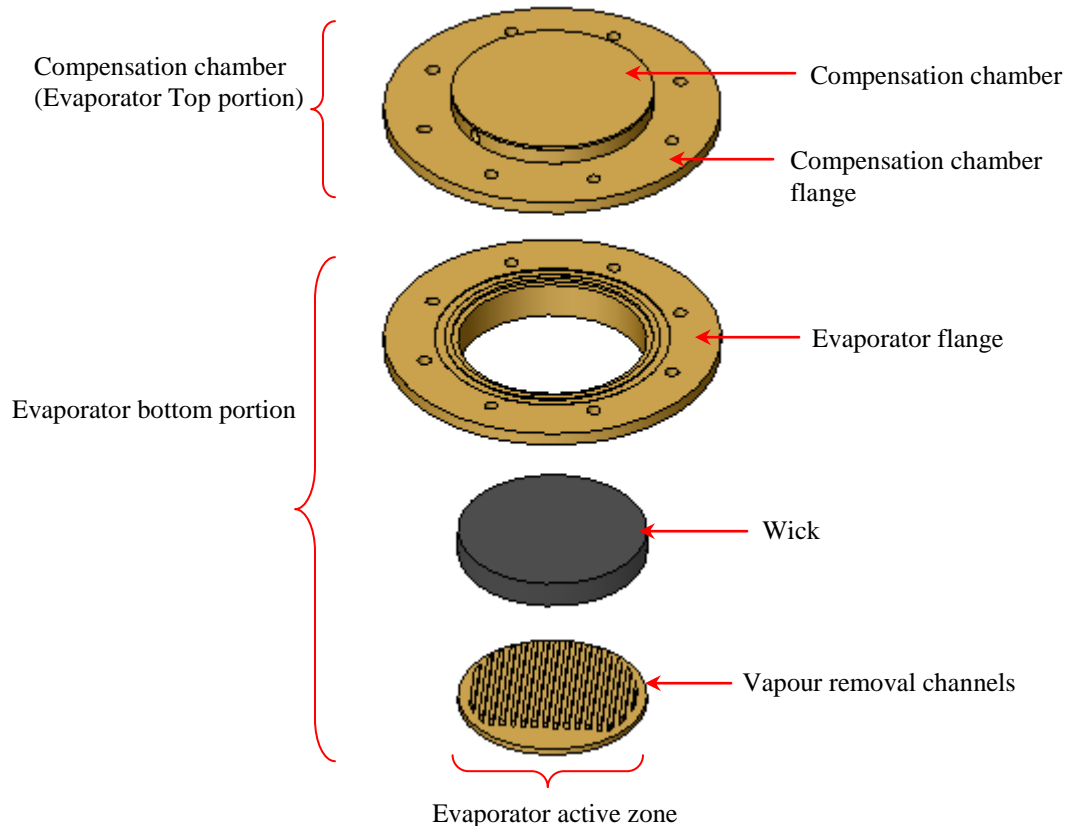


Figure 4.2 Exploded view of the capillary evaporator showing the different parts

The evaporator structure interacts with the rest of the loop via the vapour line, 150 mm in length and 2 mm internal diameter (ID), which was connected to the bottom half of the evaporator and inline with the vapour removal passages, and the liquid line, 290 mm length and 2 mm ID, attached to the compensation chamber (or evaporator top portion) (Figure 4.3). The lengths of the liquid/vapour lines denote the nominal heat transport distance of the loop with the given configuration and operating under maximum heat load.

Charging and evacuation of the mLHP was made possible by the charging line, 100 mm length and 2 mm ID, linked to the compensation chamber.

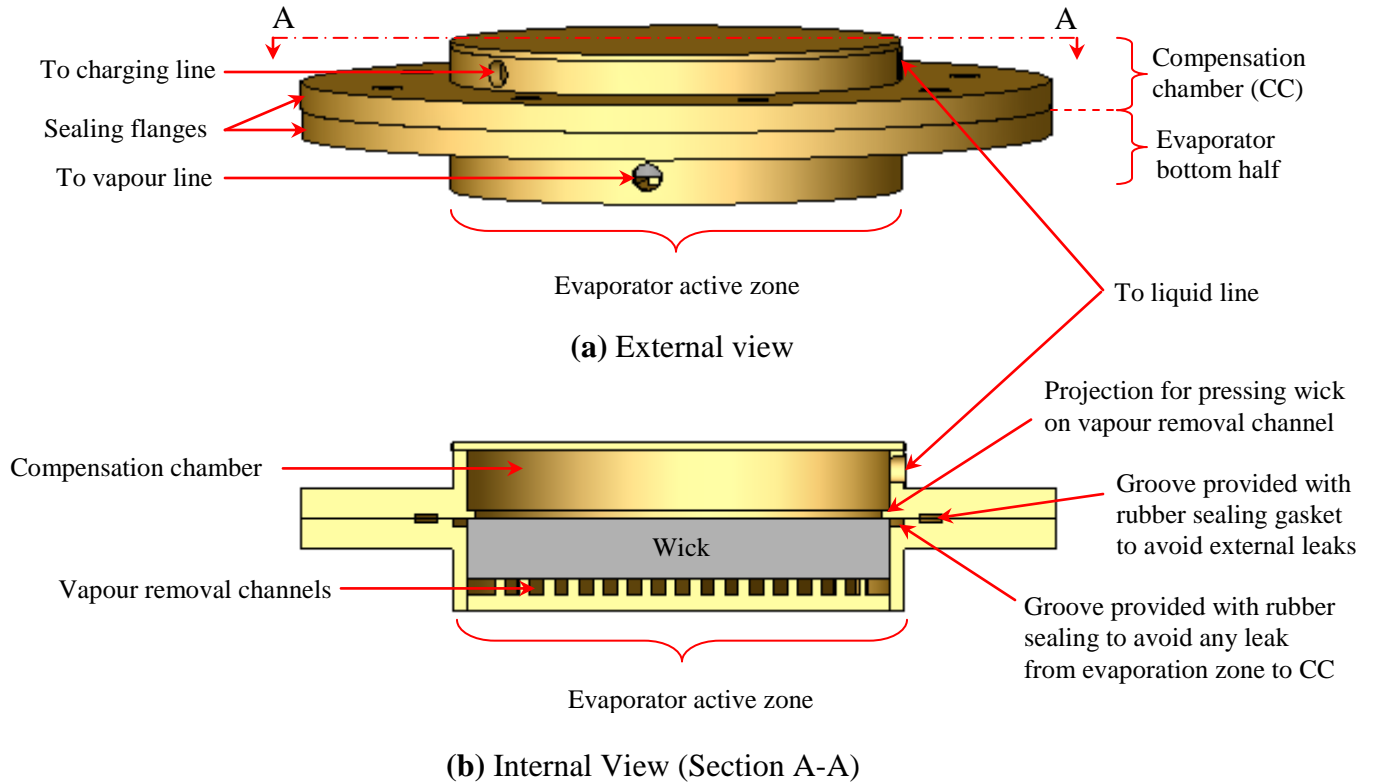


Figure 4.3 mLHP Evaporator

An Ethylene Propylene Diene Monomer (EPDM) gasket was used between the flanges (Figure 4.3b) for making the system leak proof. To avoid any internal leaks between the evaporation zone and the compensation chamber, a small groove was machined on the inside of the flange on the evaporator bottom portion and was packed with the EPDM ring. A small projection was also made on the inside of the evaporator top half in order to apply pressure on the wick structure and keep it against the micro channel for better thermal contact. To ensure proper thermal contact between the wick and the channel fins, the mating surfaces should be perfectly flat. Surface contact tests were conducted to align the surfaces for proper contact. These tests used a thin strip of transparent material that changed colour under pressure on the contact area.

4.1.1.1 Evaporator Bottom Portion

The bottom Portion of the flat evaporator behaves as a heat acquisition system and consists of the evaporator active zone, vapour removal channels and wick structure. The heat load that

provides the necessary motivation force to cause the capillary circulation of the working fluid is applied at the bottom part of the evaporator.

4.1.1.2 Evaporator Heat Acquisition Region

The evaporator heat acquisition region comprises the active zone and the vapour removal channels. The evaporator active zone is the region in which the heat load is actually applied to the evaporator. In this case, the active zone is flat in shape with a characteristic diameter of 30 mm. The flat diametric face of the evaporator provides direct contact with the heat source without the need of any interface saddle material that is required in the case of cylindrical evaporators. On the inside face of the active heating surface, an efficient system of vapour removal channels is formed by machining 15 micro grooves with rectangular cross-section of 1 mm depth and 0.9 mm width (Figure 4.4).

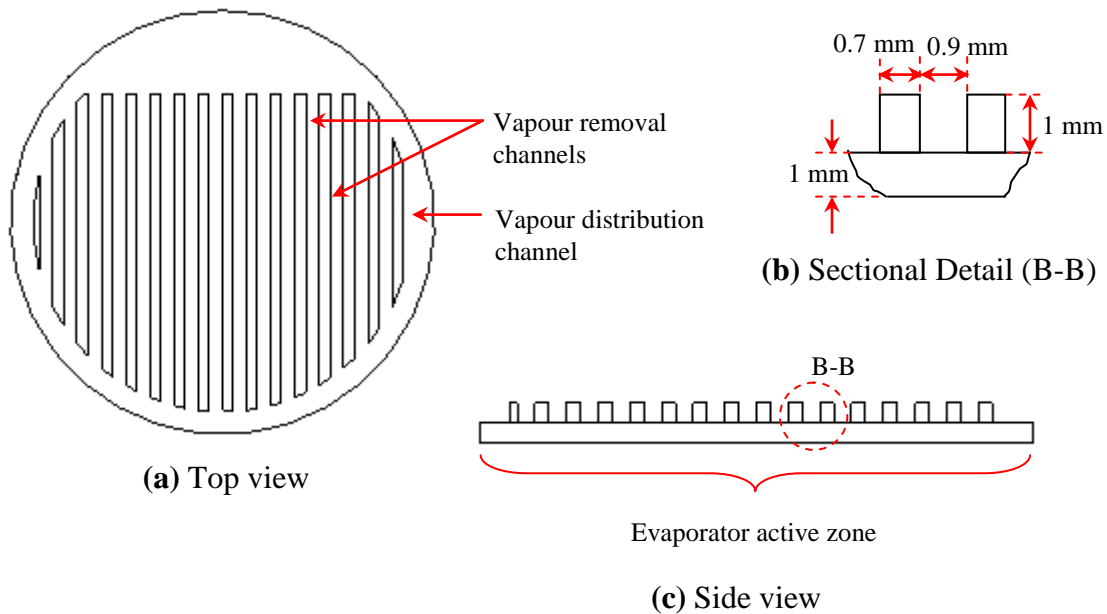


Figure 4.4 Details of Vapour removal channels

In the design of the vapour channels it should be noted that the distance travelled by the vapour along the heated evaporator wall should be kept to a minimum and dead ends should not be present to avoid unnecessary accumulation of vapour in the channels. These design imperfections can result in an increase of the degree of superheating of vapour and eventually in increase of the evaporator wall temperature. In the light of the above discussion, a system

of parallel channels with their ends connected to a common vapour distribution passage as shown in Figure 4.4 serves as an optimum design for the current design of mLHP. The evaporation zone is formed at the wick-wall interface made by the ramified system of vapour removal passages. The system of fins and channels formed by vapour removal passages performs three main functions: firstly, they provide a path for the conductive heat transfer from the evaporator active zone to the wick and thus help to perform evaporation from the liquid-vapour interface present inside the wick micro pores. Secondly, they help to achieve very high values of convective heat transfer coefficient inside the evaporation zone. Thirdly, they help in the collection and removal of vapour from the evaporation zone to the vapour line.

4.1.1.3 Wick Structure

Due to the miniature size of the LHP the pressure losses associated with flow resistance are relatively high. For that reason, it is imperative to use a wick structure with fine pore size that can provide sufficient capillary pressure to keep the working fluid in continuous circulation during loop operation. Apart from providing capillary pumping, the wick structure also functions as a hydraulic and thermal lock to inhibit reverse heat flow and prevent any reverse vapour flow from the evaporation zone to the compensation chamber. The vapour lock is provided by the presence of the liquid in the fine pores of the capillary structure while the thermal lock is provided by the thermal resistance of the wetted capillary structure. In the design of miniature LHPs, the thickness of the whole evaporator can be decreased but this is at the expense of the wick thickness. The main obstacle in this case is the so called parasitic heat flows (i.e. back heat flow) from the evaporation zone to the compensation chamber. These heat flows to the compensation chamber (CC) can give rise to high temperatures at the evaporator due to the heating of the incoming liquid in the compensation chamber. To overcome these limitations wick structures made from low thermal conductivity material like nickel have been used. Here again, a wick with low thermal conductivity while solving the problem of back heat flow introduces the problem of reduced heat transfer in the desired evaporation zone. In this case, the heat flows over the evaporator body may increase owing to a decrease in the efficiency of heat exchange process in the evaporation zone. Hence for effective heat transfer in the evaporation zone, it can be concluded that wicks with high thermal conductivity material like copper are advantageous. Clearly this is a situation of

compromise between back conduction through the wick and effective heat transfer in the evaporation zone. Within the framework of the proposed design, different grades of sintered nickel and sintered copper wicks with a thickness of 3 mm were used to test the thermal performance of the mLHP under different heat loads. It should be noted that within the abovementioned constraints, the wick thickness was decided on the basis of the maximum permissible thickness of the evaporator and the thickness of the vapour removal channel, compensation chamber and evaporator wall. Ethylene-Propylene Diene Monomer (EPDM) packing was used around the wick sides to prevent any internal leaks of vapour from the evaporation zone to the compensation chamber/reservoir and to minimize heat conduction from the evaporator side walls to the wick structure.

4.1.1.4 Compensation Chamber (Evaporator Top Portion)

The thickness of the whole evaporator structure also incorporates the compensation chamber which is thermally and hydraulically connected to the evaporation zone through the wick structure. The compensation chamber forms the evaporator top portion. The function of the compensation chamber is to accommodate the excess liquid inventory displaced from the evaporator grooves, vapour line and condenser during start-up and to provide the wick structure with direct access to the liquid. Apart from this, the compensation chamber helps in the auto regulation of the LHP temperature for the range of heat loads which depends on the dimensions of the compensation chamber and condenser, and on the cooling capacity of the latter. The inherent location of the reservoir in the LHP (in contrast to CPL) is responsible for the reliable startup and robust behaviour of LHPs. In the design of the compensation chamber, the total volume of the loop and the extent of auto regulation behaviour desired from the given loop configuration is taken into account. An optimum volume for the compensation chamber should be equal to the entire volume of the evaporator grooves, vapour line and condenser, when the LHP is operating at its maximum heat load. Excess liquid is beneficial for the LHP operation but can result in a pressure surge or temperature oscillations. In the present case, the volume of the compensation chamber was made equal to the total volume of the loop such that it is able to accommodate most of the displaced fluid inventory and should be at least 50% full of liquid working fluid in the cold state i.e. the state when the loop is not operating or before start-up.

4.1.1.5 Fin and Tube Condenser

A fin-and-tube condenser was used to reject the latent heat of condensation of vapour to the surroundings (i.e. the heat sink). Part of the condenser helps to condense the vapour while the rest provides subcooling which is necessary to avoid boiling of the liquid in the liquid line or compensation chamber.

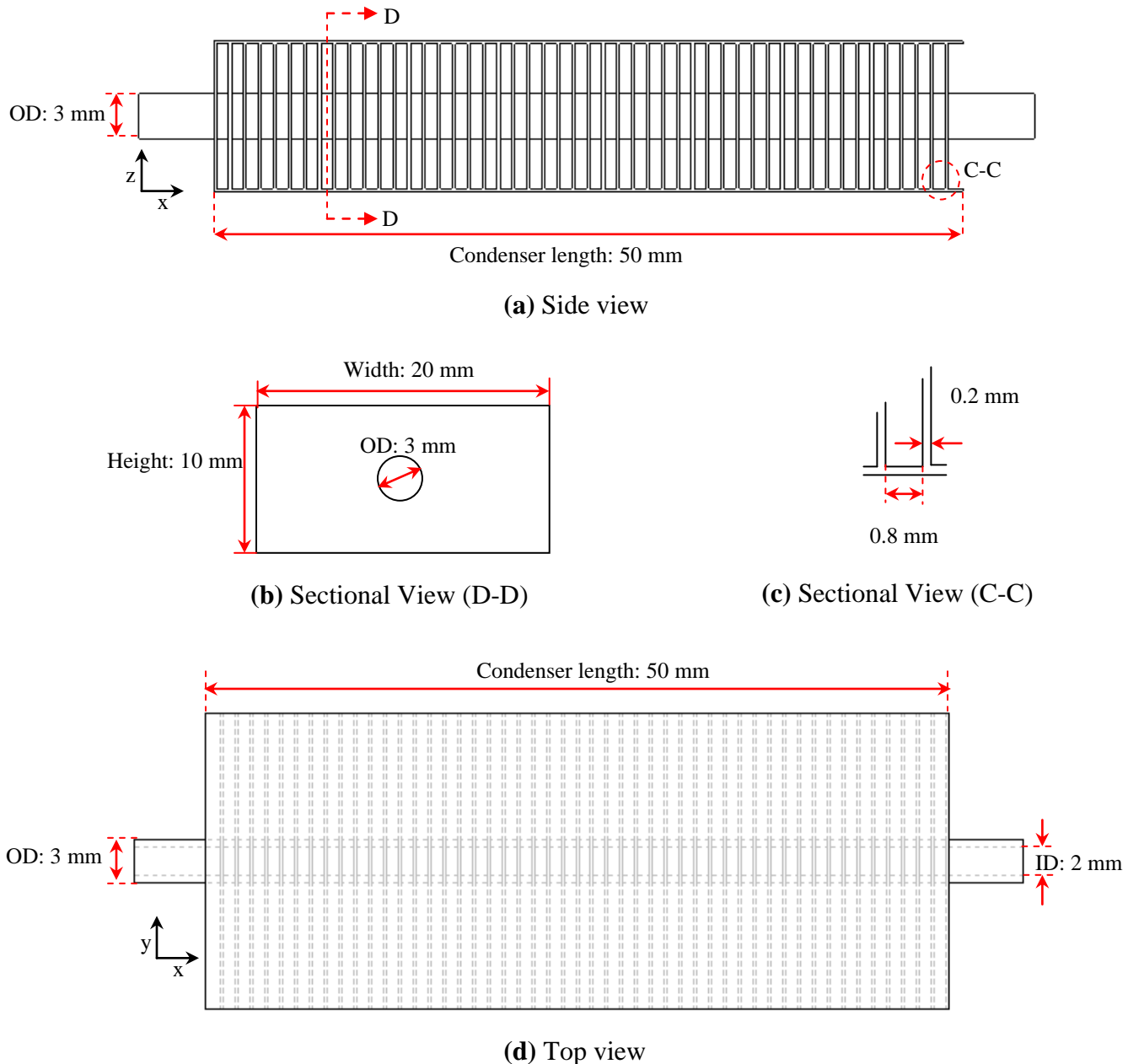


Figure 4.5 Details of Fin-and-Tube Condenser

The condenser length of 50 mm and height of 10 mm was limited by the dimensions of the fan duct and maximum available thickness in the Z-direction. The condenser of the mLHP

was provided with external fins (Figure 4.5) measuring 20x10 mm with a thickness of 0.2 mm. Copper fins were joined to the copper line (ID: 2mm, OD: 3 mm) using thermally conductive epoxy resin. It should be noted that for the condenser, the standard design of fin-and-tube type heat exchanger used in laptop computers was used.

4.2 Cleaning Procedure

Proper care was given to the cleaning of the mLHP before it was charged with the working fluid. The following cleaning method was used in the listed sequence:

- Heating in a furnace at a temperature of around 150 °C for 30 minutes to remove any organic as well as inorganic impurities from the process of manufacturing
- Cleaning using Acetic Acid / Vinegar (CH_3COOH)
- Washing / Rinsing using boiling water followed by cleaning using compressed air (this process was repeated 3-4 time to remove any residual cleaning agent)
- Each hardware component (nut/bolt/gasket) was cleaned by using boiling water
- The wick structure was re-sintered if it showed poor wetting with the working fluid or provided any evidence of contamination based on visual inspection

4.3 Charging Procedure

The charging line was connected to a three way valve as shown in Figure 4.6. This was used to connect the mLHP to the vacuum pump (via port A and C) or the charging station (via port A and B) for the evacuation or charging of the mLHP respectively. Water was used as working fluid. In order to avoid any Non Condensable Gas (NCG) formation inside the mLHP, the water should be deionised, distilled and degassed before it is charged into the mLHP. The charging station was provided with a graduated cylinder filled with the appropriate quantity of liquid water. Charging of the mLHP was done by using liquid water under vacuum condition. This is because liquids under pressure always contain some percentage of dissolved gases. In addition to this, the water was cooled to near freezing point before charging to avoid any vapour bubble formation due to vacuum conditions inside the evaporator wick and compensation chamber. Vapour bubbles inside the compensation chamber can result in local dry spots on the absorbing surface of the wick which can increase the evaporator surface temperature during operation.

The charging procedure was as follow:

- Initially, all valves and ports are closed
- Next, valves X and Y are closed, port A is connected to port C and the vacuum pump is operated to evacuate air from the system. After the required vacuum is achieved, ports A and C are disconnected and the system is kept under vacuum of around 0.001 mm of Hg for 24 hours to check for any leaks that might degrade its performance.
- If the system passes the vacuum test, then charging is done otherwise in case of evidence of any leak, the leak points are identified using a leak detection test and repaired.
- Degassing of the pure water is done by connecting the charging cylinder to the vacuum pump. For this, valve X and Y are opened and the vacuum pump is operated until no air bubbles are seen coming out of the liquid. Ports A, B and C are still in a closed state.
- For charging, firstly valve Y is opened and then port A is connected to port B to charge the mLHP with the calculated volume of the liquid inventory
- After charging, valve Y is closed and ports A, B and C are disconnected from each other.

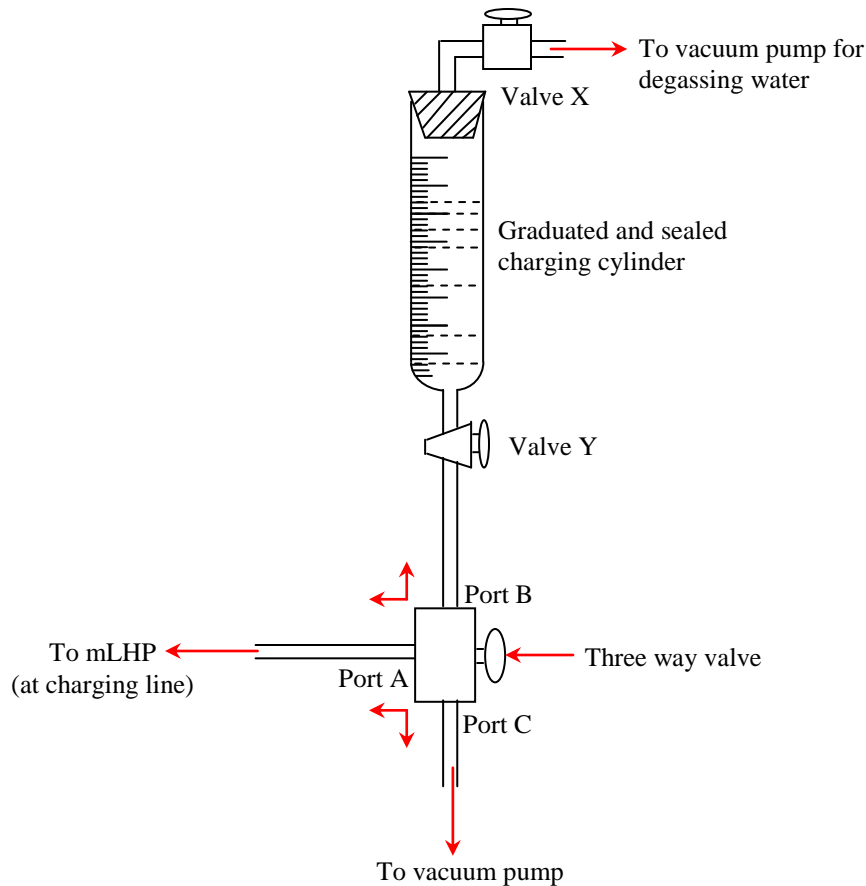


Figure 4.6 Charging procedure for mLHP

The liquid quantity charged into the mLHP is decided on the basis of the compensation chamber volume, porous volume of the wick and volume of the liquid line. The loop was charged with 70 to 80% of its internal volume with water as the working fluid. Also, tests were conducted with different volumes of water charge to study the effect of liquid inventory on the heat transfer capability of the device.

4.4 Testing Method

The thermal characteristics of the designed miniature LHP were studied by using a heater of 3.75 cm^2 ($25 \times 15 \text{ mm}^2$) area. The heat load simulator (Figure 4.7b) was in the form of a copper block with two embedded cylindrical cartridge heaters. The heater block was attached symmetrically to the center of the circular heat absorbing face. Thermal performance of the mLHP was studied and compared under uniform heating mode and non uniform heating mode of the evaporator using heaters of 6.25 cm^2 and 1 cm^2 respectively. Tests were also conducted using capillary structures of different material namely nickel and copper sintered wicks. Thermal characteristics of the mLHP with regard to start up behaviour and steady state operation were studied over the range of applied power. Optimum working fluid charge for reliable startup of the mLHP was determined experimentally. Also the effect on the thermal performance of the mLHP with change in orientation was explored. Tests were carried out to determine the effect of non-condensable gases (NCG) on the efficiency of the mLHP. Methods to detect NCG inside the loop system and possible remedies to avoid NCG formation in the two phase systems were developed. Condenser cooling was accomplished by forced convection provided by an air cooling fan using ambient air with a temperature of $24 \pm 2^\circ\text{C}$. The maximum flow rate of the fan was $0.1 \text{ m}^3/\text{s}$ using a 5 V, 0.1 A power supply. A digital wattmeter with precision of $\pm 0.1 \text{ W}$ was used to measure and control the input heat load to the heat simulator. The power input to the heat simulator was increased in steps of 5 W during the test. The temperature was measured at different points on the mLHP using Twelve T-Type thermocouples with maximum error of $\pm 0.5^\circ\text{C}$. Figure 4.7 (a, c & d) shows the experimental set up for testing the mLHP along with the location of the thermocouples. Data from these thermocouples was acquired every 10 s by a Keyence data acquisition system.

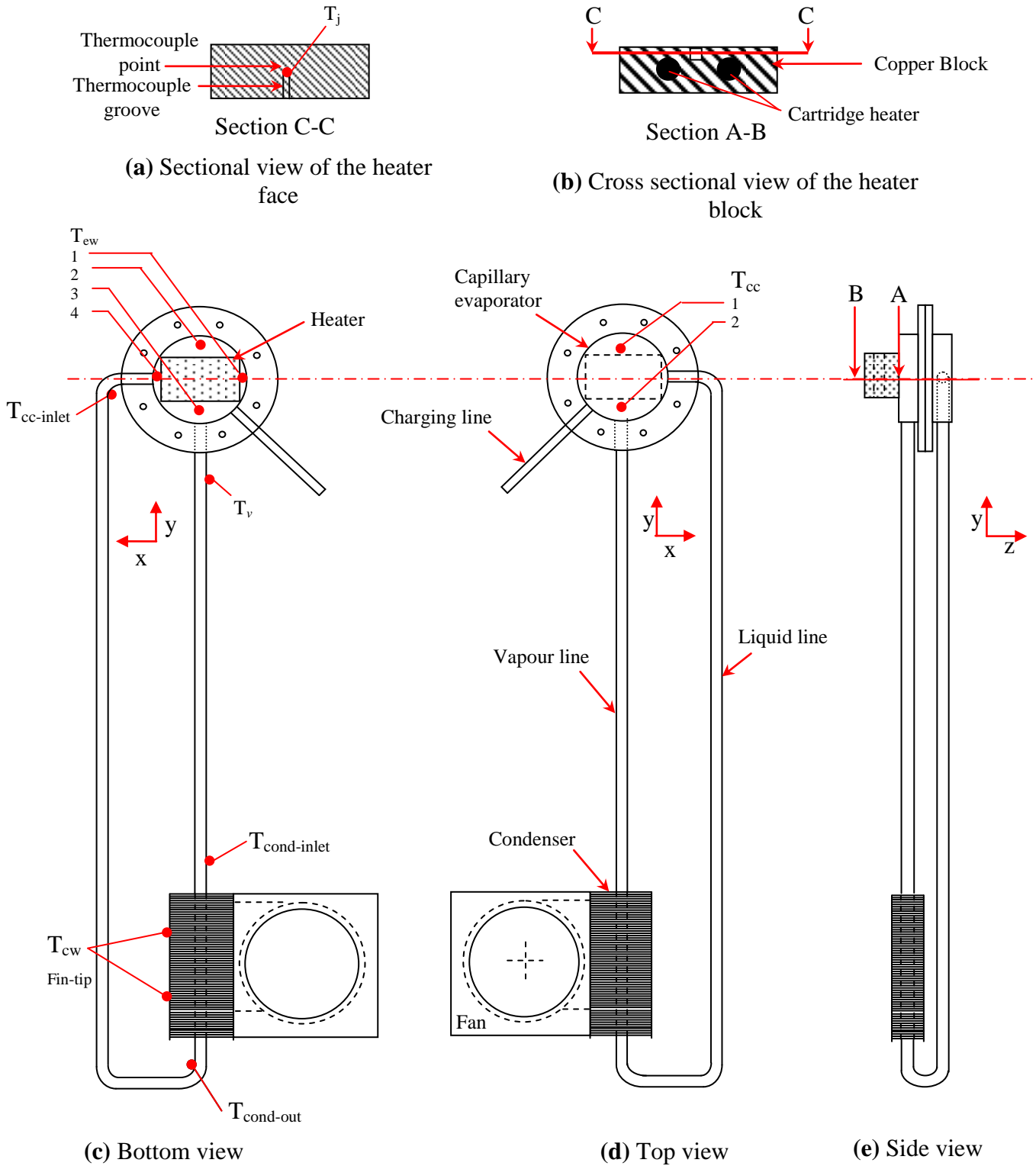


Figure 4.7 Schematic of the experimental prototype and test layout for the mLHP

The thermal performance of the mLHP was characterised on the basis of the evaporator temperature, maximum heat capacity, evaporator thermal resistance, mLHP/heat pipe thermal resistance and total thermal resistance of the device. In the determination of heat transfer coefficient – h , (from temperatures and heat load measurements) uncertainty was estimated to be $\pm 15\%$. It should be noted that for thermal resistance – R , the error of estimation will be larger at low heat loads due to the high value of fluid and wall temperature differences. Therefore, the uncertainty analysis of the resistance was carried out at the low heat loads used in the experiment and uncertainty lies within $\pm 8\%$. For measuring the temperature at the junction of the mLHP evaporator and the heat load simulator, a special groove (Figure 4.7a) was made at the center of the heating face of the simulator block in which the thermocouple point was fixed using thermal epoxy resin. While the mLHP evaporator active face is attached to the thermal footprint of the heater, it is important for the thermocouple T_j to have contact with the evaporator active zone so that the true interface temperature on the evaporator side of the junction is determined. This is important for the accurate estimation of the thermal resistances which are based on the evaporator interface (i.e. junction) temperature. The temperature of the evaporator wall, condenser wall and compensation chamber were calculated by averaging the temperatures of the thermocouples fixed on their outer zones.

Testing of the mLHP prototype was done in the horizontal configuration with the evaporator and condenser at the same level. Start up of the mLHP was assumed to occur with the rise in temperature of the vapour line and consequent clearing of liquid from the vapour line. For a successful start up at a given heat load the temperature difference between the outlet of the evaporator and inlet of the condenser should be less than or equal to 1°C . For a given heat load, steady state was characterized by constant evaporator temperature. The heat load limit applied to the mLHP was decided by the permissible temperature limit at the heat source which should be within $100\pm 5^\circ\text{C}$.

4.5 Summary

A detailed description of each component of a mLHP with a flat disk shaped evaporator is given. In order to avoid the formation of any Non Condensable Gases (NCGs) inside the mLHP system, it should be charged with deionised, degassed and distilled water. Also, the

system should be leak tight and a proper cleaning procedure on the loop components should be done before assembling the parts. The test procedure to conduct thermal testing of the mLHP is explained in detail in the latter part of the chapter.

The next chapter discusses the results of tests conducted on the mLHP with a disk shaped evaporator.

Chapter 5

mLHP with Disk Shaped Evaporator: Results and Discussion

In this chapter, outcomes of experimentation on the mLHP are discussed in detail. Thermal characteristics of the mLHP with regard to the startup phenomena and steady state operation of the loop system are explained. Factors that can lead to the start up failure of the mLHP are explained with the help of examples. The optimum quantity of the fluid charge for reliable start up and steady state behaviour of the device over a range of applied heat loads was experimentally determined. Also, the effect of the fluid distribution and pre start -up situation inside the mLHP evaporator on the startup characteristics of the device are presented. In order to validate the proposed theoretical model for the designed mLHP, predictions made from the model are compared to the experimentally obtained results. As LHPs are very reliable devices for heat transfer against gravity, the thermal behaviour of the miniature LHP is also studied for the adverse tilt in the gravitational field.

As the current trend of technology is towards dense and high powered microprocessors, so the thermal performance of the mLHP was evaluated with both uniform and non-uniform heating modes. In the non-uniform heating mode only 14% of the evaporator active zone was heated. Recognising the importance of the capillary structure which is the most critical component of the two phase passive system, the effect of the material and physical properties of the wick on the operational characteristics of the loop system was assessed. Performance of the mLHP with monoporous as well as biporous wick configurations was also tested. Detailed investigation has also been carried out on the mLHP to study the effect of Non Condensable Gases (NCGs) on the thermal characteristics of the system. Different approaches to detect and flush out the NCG from the mLHP have been proposed and successfully tested.

5.1 Thermal Characteristics of the mLHP

The operational characteristics of the designed mLHP were tested using a heater of 3.75 cm^2 ($25 \times 15 \text{ mm}^2$) active area. In this case, the heater was able to provide the heat load to approximately 50% of the active area of the evaporator. The device was tested for transferring heat load up to distance of 150 mm while maintaining the evaporator surface temperature below $100 \text{ }^\circ\text{C}$. In this study, a nickel monoporouse wick with average pore size less than $15 \text{ }\mu\text{m}$ and 60% porous volume was used as the capillary pump. The loop was charged with water up to 70 to 80% of its internal volume. Testing was done with the evaporator and condenser at the same horizontal level.

5.1.1 Start-Up Phenomena

Figure 6.1 depicts the startup of the mLHP at 15 W input power. As heat load is applied to the evaporator active zone, steady rise in the evaporator wall temperature is noted. Heat is conducted from the evaporator surface to the capillary structure through the vapour removal channel fins. In the cold state, most of the working fluid is present in the evaporator and compensation chamber due to their large volume compared with the condenser and transport lines. Therefore, heat is also distributed to the capillary structure and evaporator grooves through convection inside the liquid working fluid present in the grooves. Another important factor relates to the high thermal conductivity of the copper housing. Since this property for copper is considerably high (around 380 W/m K) when compared to other materials, heat is better conducted and evenly distributed throughout the evaporation portion. Now, depending on the fluid distribution inside the evaporator grooves, if the free surface of the liquid or the liquid-vapour interface already exists inside the grooves or along the evaporating face of the wick, evaporation of the liquid will occur instantly on the application of heat. Alternatively, if the grooves are predominately occupied by the liquid, then the liquid must be superheated to a certain degree for initiating boiling in the bulk of the liquid. As the liquid working fluid present in the evaporator grooves achieves the required degree of superheat from the evaporator surface, nucleate boiling occurs in the grooves. The resulting vapour pushes the liquid from the evaporator grooves and causes a very sharp rise in temperature of evaporator outlet as shown by the blue line in the graph. This is followed by discharge of the vapour from

the evaporator to the condenser through the vapour line, as indicated by the sharp rise in temperature at the condenser inlet as shown by orange line in the graph.

In accordance with the theoretical conditions for a serviceability of the LHP as discussed in section 3.2.2, it should be noted that to start the fluid circulation inside the loop, the required pressure and temperature difference must be developed across the liquid vapour interfaces in the compensation chamber and the evaporation zone. This pressure and thus temperature difference is required for displacing liquid from the vapour line and filling the liquid line and compensation chamber. In the mLHP evaporator, due to the heat flow through the wetted metal wick and high conductive evaporator wall, part of the heat applied to the evaporator active zone leaks to the compensation chamber. This is evident from the parallel rise in the compensation chamber and evaporator wall temperatures as observed in Figure 6.1.

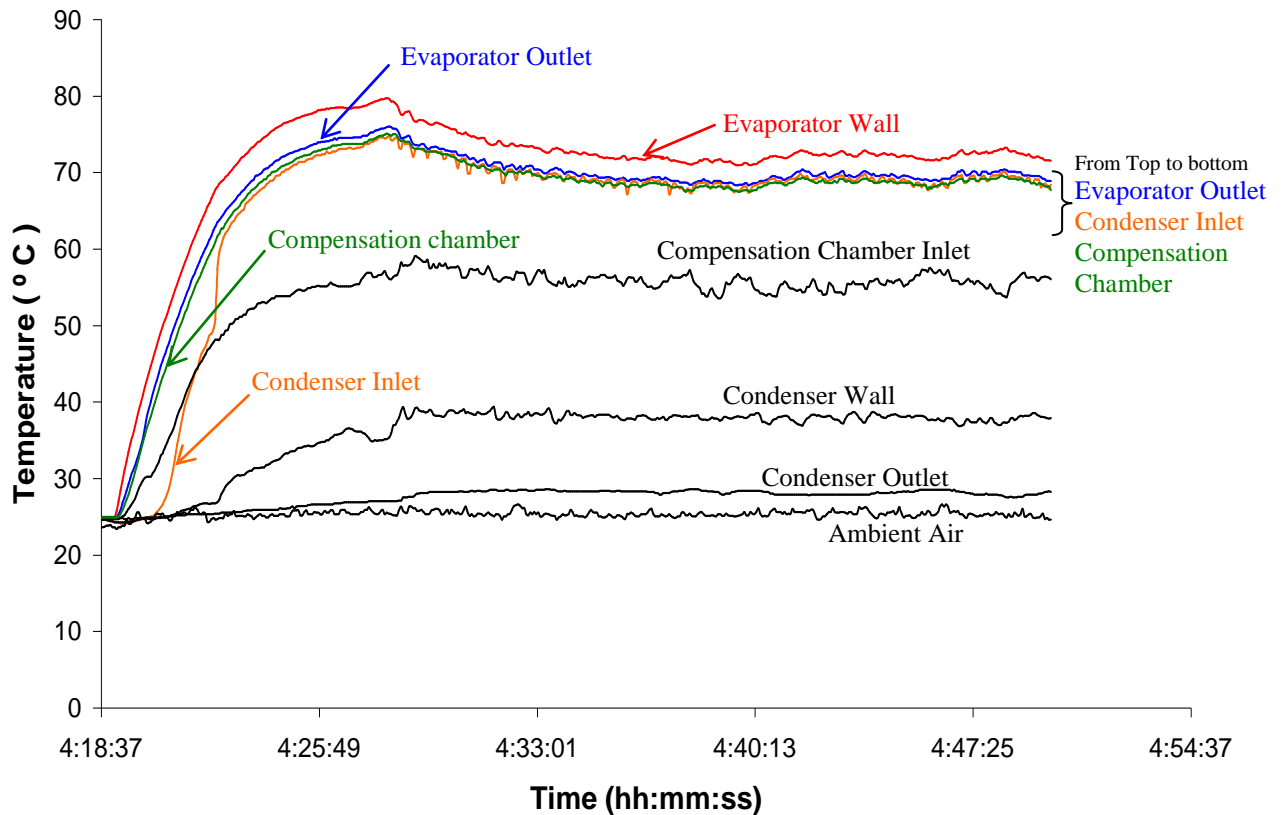


Figure 5.1 Start-up of the mLHP at 15W input power

These heat leaks contribute to increase of the compensation chamber temperature. Due to the void fraction inside the compensation chamber in the cold state, the liquid-vapour interface may be already present inside the chamber even before the heat load is applied to the

evaporator active zone and startup is initiated. Now, due to the closeness of the evaporator wall to the heat source and the thermal resistance of the capillary structure, the associated pressure and temperature of the vapour in the evaporation zone are higher than in the compensation chamber. Here, the function of the wick as a thermal lock manifests itself. Also, the subcooled liquid returning from the condenser to the compensation chamber contributes to lowering the temperature of the chamber. From the graph in Figure 5.1, it is evident that such a temperature difference does exist continuously between the evaporator wall and compensation chamber and helps to instigate fluid circulation and thus reliable start-up of the mLHP. The initiation of fluid circulation inside the loop is well marked by the stabilization of the temperature at the inlet of the compensation chamber which otherwise shows a steady increase due to back flow of heat from the evaporator active zone. In this case, incoming liquid to the compensation chamber takes heat from the compensation chamber wall and exit of the liquid line and thus stabilizes their temperatures. This is why the liquid condensate should be provided with appropriate sub-cooling inside the condenser in order to avoid boiling inside the compensation chamber or in the liquid line. The subcooling helps to keep the temperature of the liquid below the saturation conditions even when including heat from the compensation chamber wall. The excess liquid cleared from the evaporator grooves and vapour line by the vapour is accommodated in the compensation chamber. The evaporating meniscus formed at the wick-wall interface inside the evaporation zone is responsible for developing the capillary pressure to circulate the working fluid continuously around the loop. Successful start up is registered only if the evaporator is able to achieve a prolonged steady state. It has been observed that in some cases even after the initiation of fluid circulation, start-up failure can occur. This is dictated by multiple factors that are discussed in detail later in the section on mLHP failure mode analysis.

5.1.2 Steady State Operation

Figure 5.2 gives the heat load dependence of the evaporator surface temperature. The plot clearly shows that the loop heat pipe is able to automatically regulate its mode of operation with changing heat load.

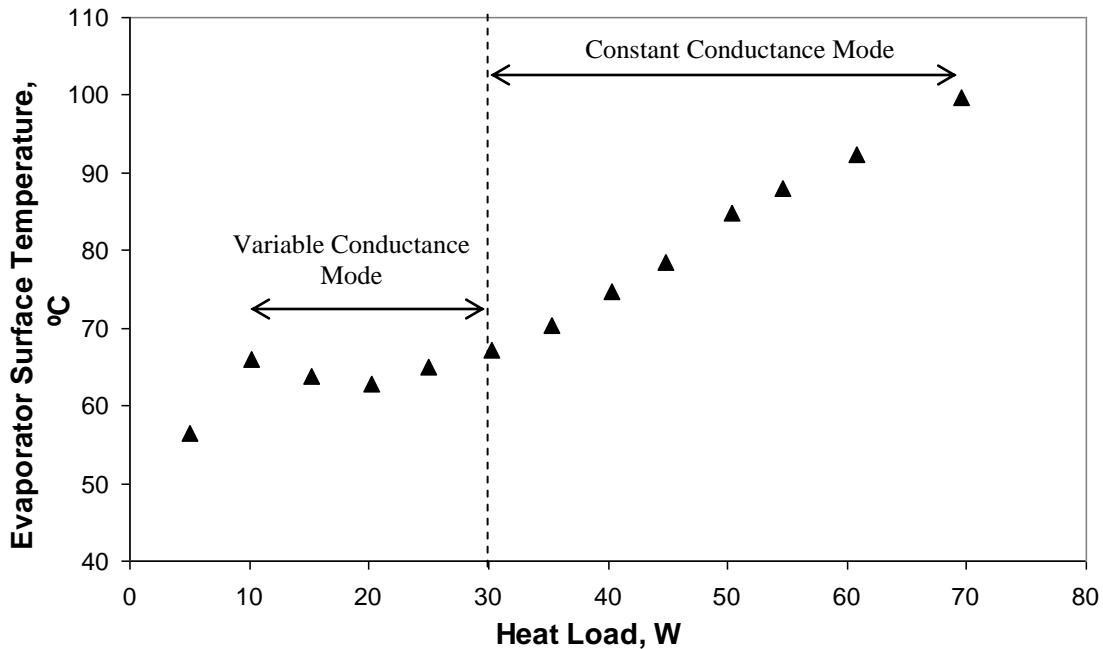


Figure 5.2 Heat load dependence of the evaporator surface temperature

For input power less than 30 W, a variable conductance mode is observed. In this case one can observe that different heat loads may correspond to the same value of temperature. At low heat loads, the mass flow rate of the working fluid is small therefore the compensation chamber and the condenser are partially filled with the liquid. The temperature of the compensation chamber which dictates the saturation condition inside the evaporator is established by the outcome of two main factors. The first one is the amount of parasitic heat flow from the evaporator to the compensation chamber via the capillary structure and the evaporator wall and the second is the liquid redistribution between the condenser and the compensation chamber which take place under changes of head load. With the increase in heat load, the effect of these competitive processes i.e. heat inflow and liquid displaced to the compensation chamber also increase. As a result of this, the compensation chamber and thus evaporator wall temperature is stabilized to some extent enabling the LHP to auto-regulate the source temperature. The variable conductance mode of the LHP continues to the stage when the compensation chamber is completely filled with liquid and the entire condensation surface is utilized for heat removal. It should be noted that in such a mode of operation the thermal resistance of the mLHP decreases with the increasing heat load which is very useful for high powered electronic cooling applications where the permissible thermal resistance is very low. The variable mode of conductance is the unique characteristic of the mLHP that makes it potential replacement alternative to traditional heat pipes. For heat loads more than 30 W, as

presented by Figure 5.2, a constant conductance mode is realized in which the condensation surface is fixed. In this mode, a LHP behaves like conventional heat pipe and shows monotonic temperature trend with changing heat load.

The maximum heat capacity of a mLHP in electronics cooling is mainly decided by the maximum permissible temperature at the heat source which is normally regarded as 100 °C. In case of the designed mLHP, it was able to transfer 70 W maximum heat load while maintaining the temperature of the evaporator below the 100 °C limit. The nominal capacity of the mLHP is the heat load at which the evaporator temperature reaches $80 \pm 1^\circ\text{C}$ and in this case was 45 W. It is evident from the large values for the maximum and nominal capacities that the designed mLHP can handle conditions of non uniform heating without any performance issues. This is attributed to efficient heat exchange in the evaporation zone of the mLHP evaporator. As opposed to the conventional heat pipe in which heat is acquired at the evaporator through the liquid layer inside the wick structure, effective heat exchange is organised in the evaporator of a mLHP by the principle of inverted menisci. In this case, the evaporating surface of the meniscus is present close to the heated wall making it possible to reduce the thermal resistance of the evaporator zone and thus increase the convective heat transfer coefficient.

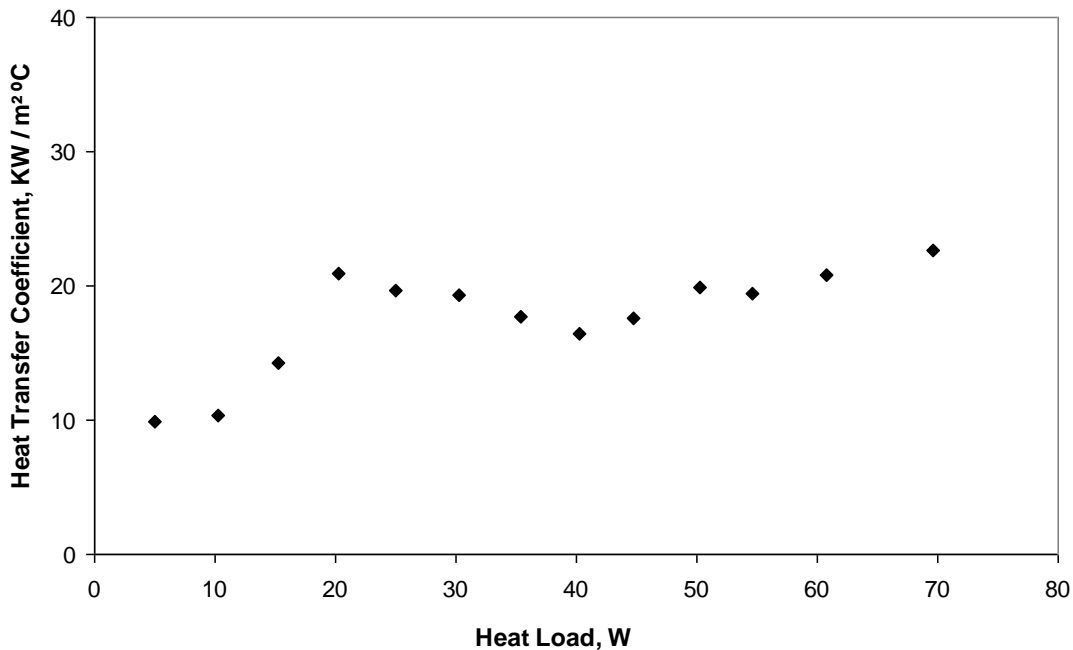


Figure 5.3 Heat transfer coefficient versus applied heat load

For the current mLHP prototype, the effective heat transfer coefficient in the evaporator reaches a maximum value of $22,600 \text{ W/ m}^2 \text{ }^\circ\text{C}$. The plot in Figure 5.3 clearly indicates that high values of the heat transfer coefficient in the evaporator were achieved over the entire range of the applied heat loads. It should be noted that the maximum value of the heat transfer coefficient specified above is limited by the operating temperature limit. For the entire range of heat load, there was no indication of heat transfer crisis phenomena inside the evaporator, for example a sudden rise in the evaporator temperature, hot spots on the evaporator active zone, evidence of back flow of vapour from the evaporation zone to the compensation chamber etc.

In Figure 5.4 the steady decrease in the heat pipe thermal resistance, R_{hp} (evaporator surface to condenser surface) can be observed as input power increases.

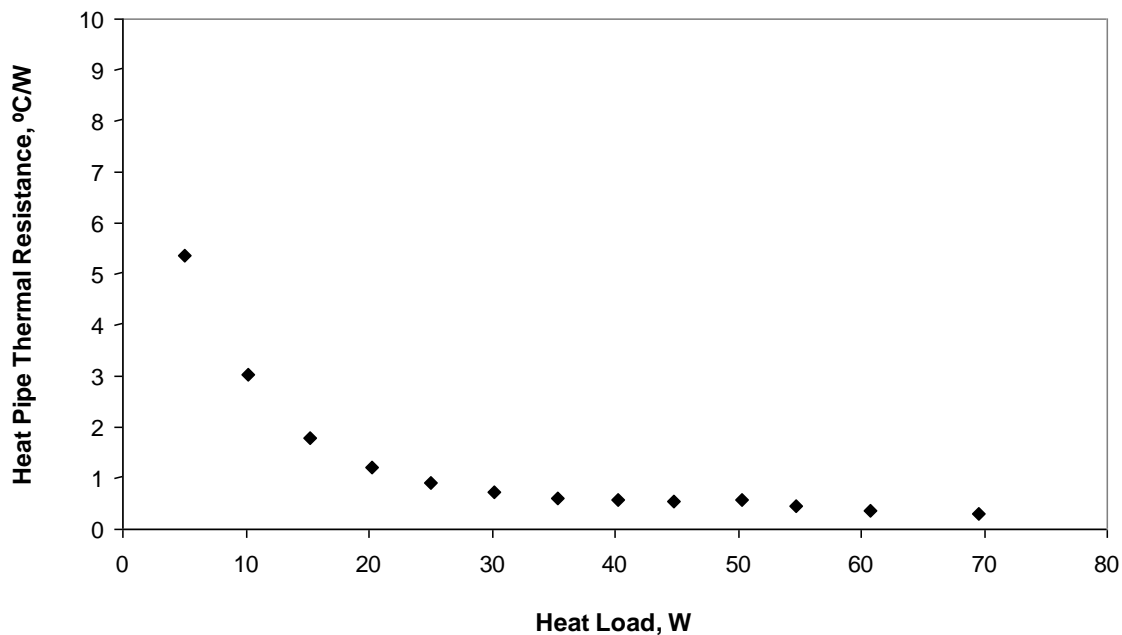


Figure 5.4 Heat pipe thermal resistance versus applied heat load

This is due to the advantages of using water for which the Merit number increases at higher loads. Also, with increase in heat load the quantity of the liquid charge inside the compensation chamber increases and consequently reduces the thermal resistance of the device. The minimum value of the heat pipe thermal resistance is $0.31 \text{ }^\circ\text{C/W}$ at a load of 70 W and an evaporator temperature of $99.6 \text{ }^\circ\text{C}$. For the total thermal resistance - R_t , the heat load dependence is presented in Figure 5.5 and the minimum value of $1.2 \text{ }^\circ\text{C/W}$ was observed at 70

W. The evaporator is the most critical component of the LHP and determines the overall performance of the device. Figure 5.6 presents the plot for evaporator thermal resistance versus heat load. The efficiency of the heat transfer process in the evaporation zone of the LHP is measured on the basis of the evaporator thermal resistance, R_e which is the resistance presented to the heat flow from the evaporator active zone to the evaporation zone.

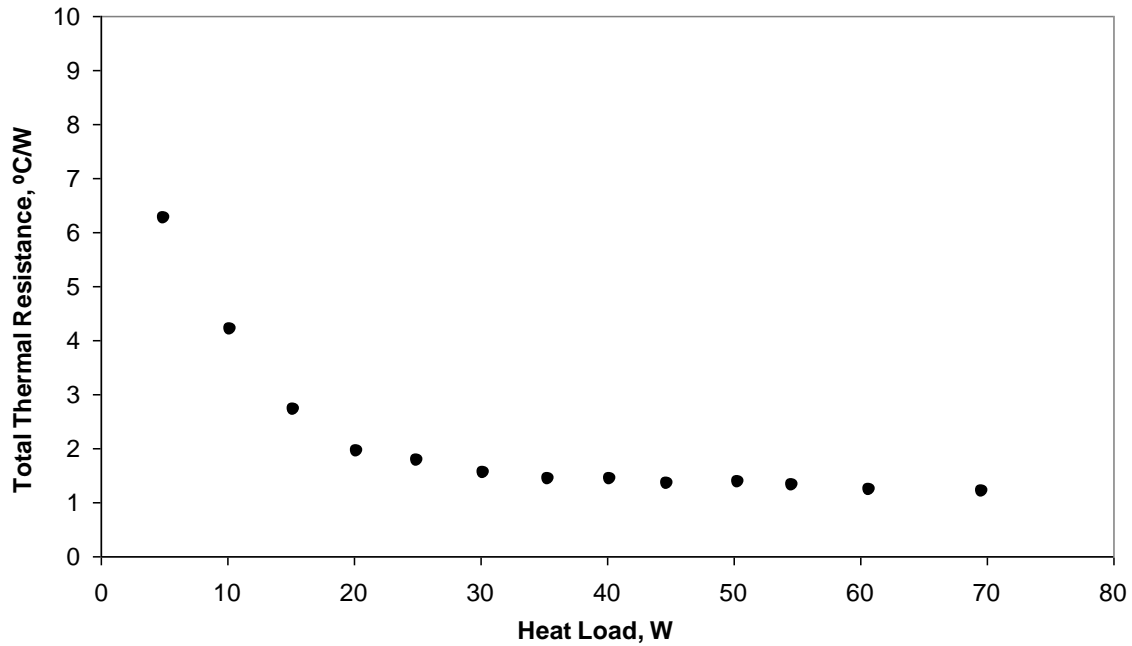


Figure 5.5 Total thermal resistance versus applied heat load

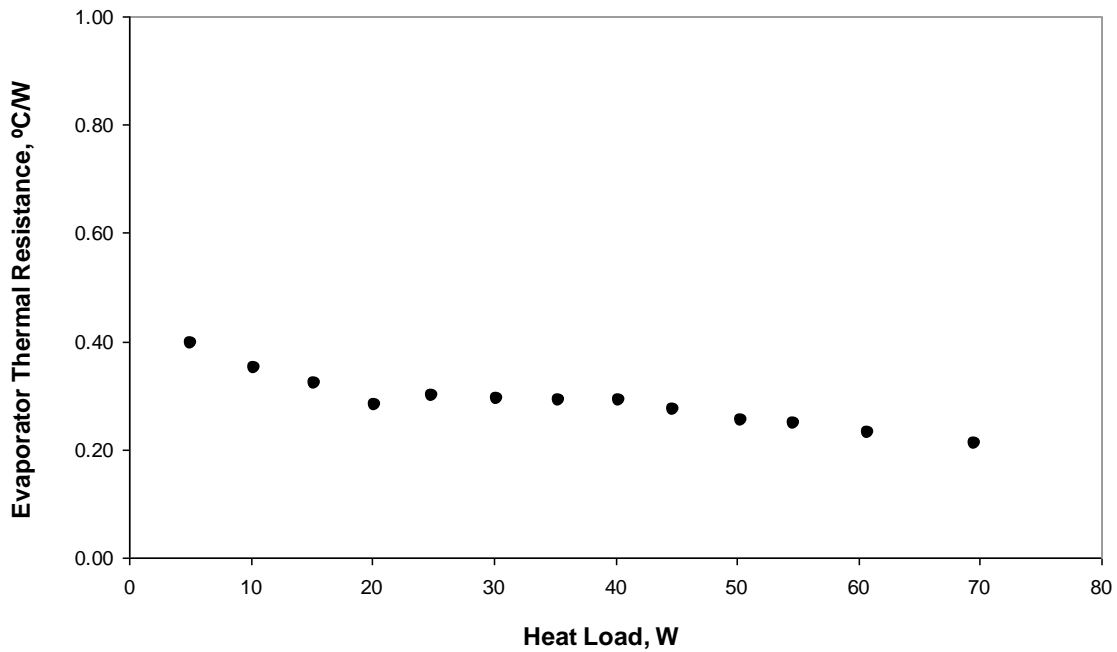


Figure 5.6 Evaporator thermal resistance versus applied heat load

Due to very low spreading and low conductive resistance offered by the evaporator active zone, which was made from copper, very low values of R_e were obtained in the mLHP evaporator, with the minimum value of $0.21 \text{ }^\circ\text{C/W}$ at 70 W . It is seen from the graph that the evaporator thermal resistance decreases with increasing heat load. This is due to the fact that at low heat loads there is more vapour in the evaporator and compensation chamber and thus heat leakage is increased due to the back conduction by the walls and wick resulting in high thermal resistance between the evaporator and compensation chamber (variable conductance). When the LHP is operating at higher heat load levels, there is more liquid in the evaporator wick and compensation chamber and thus the heat leak is reduced, resulting in low thermal resistance (constant conductance).

The thermal resistance from the condenser to surroundings contributes to $0.8 \pm 0.2 \text{ }^\circ\text{C/W}$ and proved to be the main component of the total thermal resistance- R_t . From the above results it can be inferred that the miniature LHP has proved to be a very versatile and promising device for thermal control of electronic devices including personal computers and notebooks.

5.2 mLHP Failure Mode Analysis

LHPs are very reliable two phase heat transfer devices that are known for their robust operation and superior thermal characteristics. Proper care must be taken in cleaning the loop internal volume and leak proof sealing the device to avoid device failure. In some cases, the failure of the device was observed during the startup process. The main cause of start up failure are broadly classified into two main categories which are failure due to the leakage and insufficient charge volume.

5.2.1 Startup Failure due to leakage

Start up failure due to leakage can arise due to improper external sealing or internal sealing. External sealing is done to make the device leak proof against any air entry from the atmosphere into the system, as in this case the system is operating under vacuum conditions. In the case of internal sealing, the wick structure must be properly secured inside the evaporator such that vapour may not bypass the capillary matrix from the evaporation zone to

the compensation chamber. Figures 5.7 and 5.8 presents the startup failure of the mLHP due to external and internal leaks respectively.

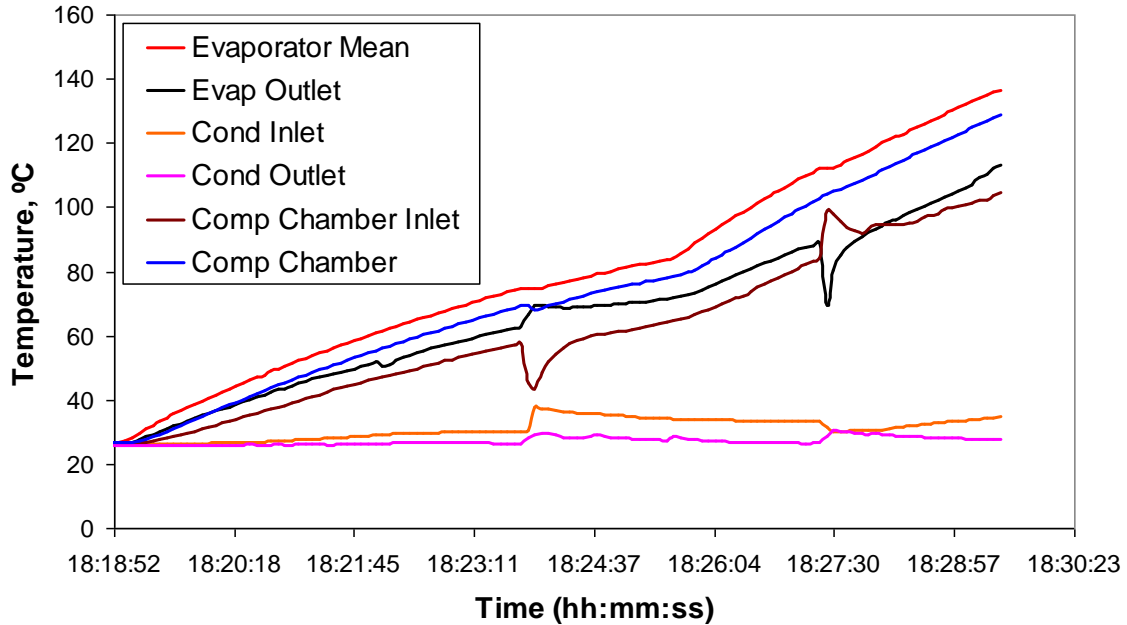


Figure 5.7 Start-up failure due to leakage in external sealing

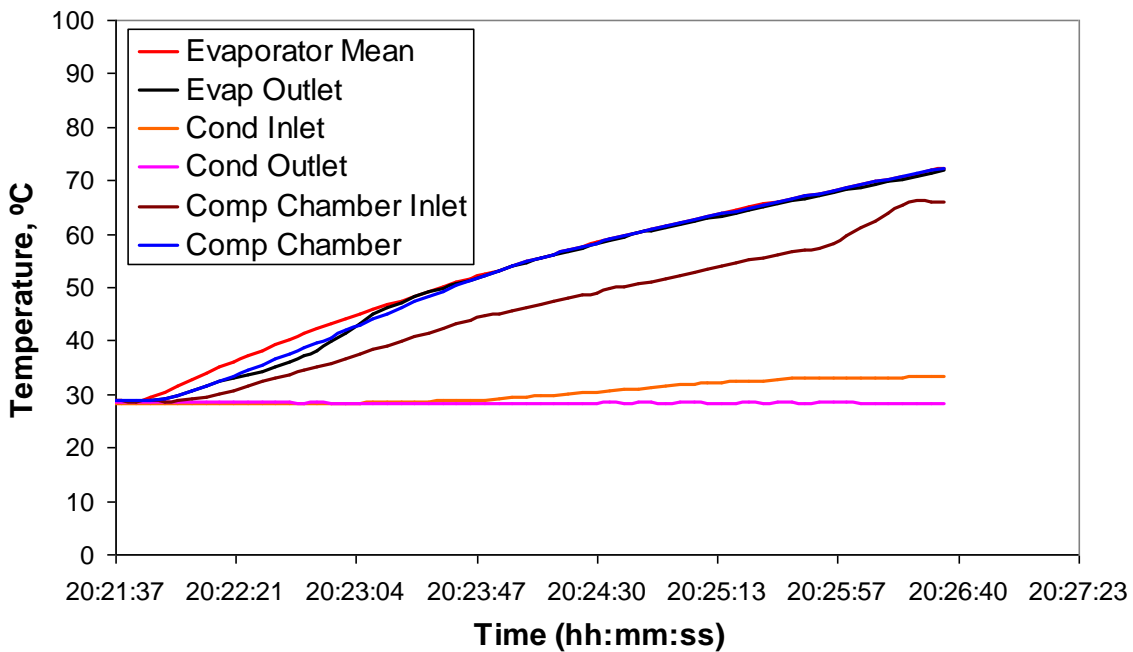


Figure 5.8 Start-up failure due to internal leakage

Here, the failure is evident from the comparison of the evaporator outlet temperature and compensation chamber temperature. In Figure 5.7, the compensation chamber temperature is higher than the evaporator outlet temperature which clearly indicates dry-out of the capillary structure and passage of vapour from the evaporator to the compensation chamber via the wick. Also, the temperatures at the compensation chamber inlet and evaporator outlet confirm the back flow of vapour. During the test, it was observed that the temperature at the condenser inlet and outlet did not increase much due to the absence of vapour flow from the evaporator to the condenser. It is expected that air leaked inside the system, accumulated inside the compensation chamber and blocked the liquid supply to the absorbing face of the wick. This ultimately resulted in dry out of the wick under back heat conducted from the evaporator active zone. Similarly, in Figure 5.8, it is seen that due to the bypass of the vapour around the wick, from the evaporator to the compensation chamber, the temperature at the compensation chamber approaches the evaporator outlet and evaporator surface temperatures. The continuous rise in the compensation chamber inlet temperature indicates that there is no fluid circulation along the loop circuit. The presence of both external and internal leaks were confirmed after the post operation inspection of the mLHP.

5.2.2 Start-up Failure due to Insufficient Fluid Inventory

Startup failure due to the insufficient charge inside the compensation chamber is illustrated in Figures 5.9 and 5.10. The tests were conducted with fluid inventories of 30% and 40% of the total mLHP internal volume respectively. The failure in these cases occurred due to improper wetting of the wick structure inside the mLHP evaporator. It is evident that, in both cases, the vapour line was de-primed successfully. The parallel and continuous rise in the evaporator and compensation chamber temperatures clearly indicates intensive flow of heat from evaporator to compensation chamber. In both the graphs, there is drop in the temperature of the condenser inlet and evaporator outlet with a corresponding peak in the compensation inlet temperature which indicates dry out of the wick and bypass of vapour into the compensation chamber.

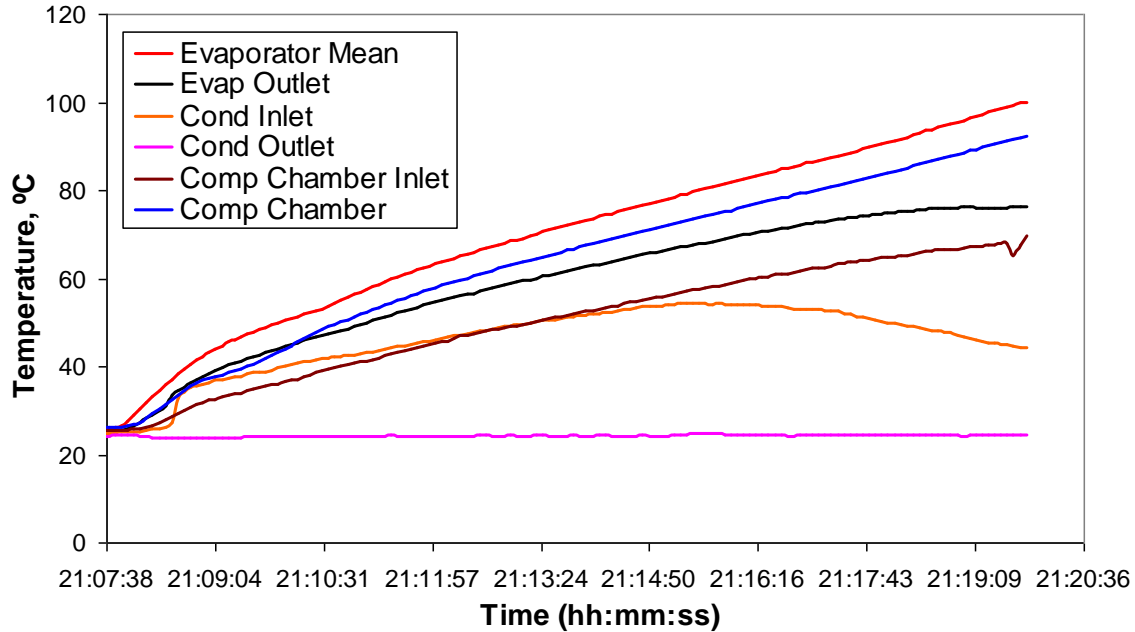


Figure 5.9 Start-up failure of the mLHP under 30% fluid charge

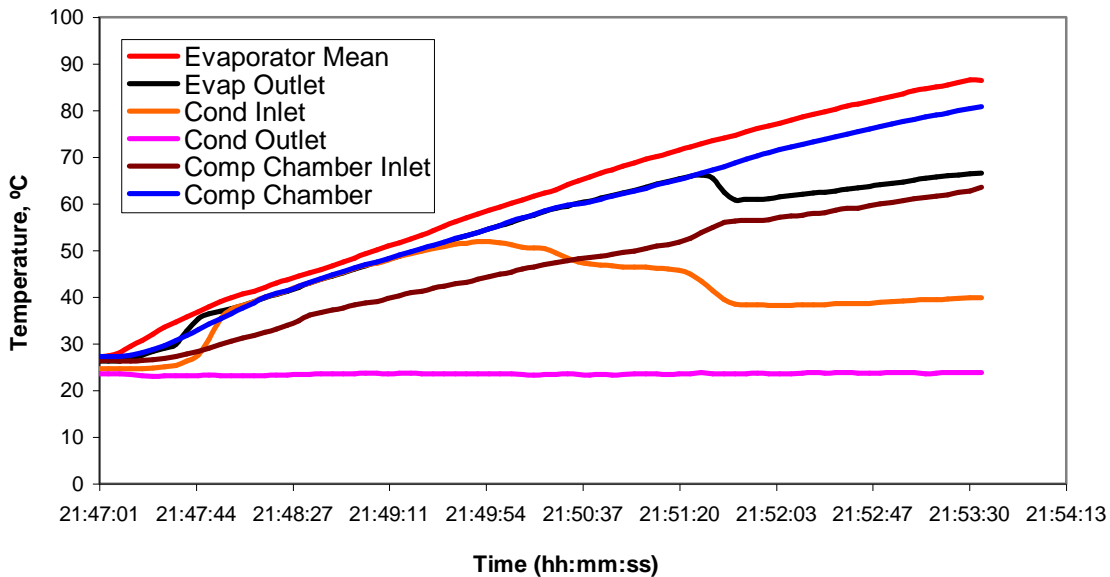


Figure 5.10 Start-up failure of the mLHP under 40% fluid charge

For the mLHP with 40% charge (Figure 5.10) the conditions for the start up of the device are more favorable than for the mLHP with 30% charge (Figure 5.9). This is due to the higher fluid inventory inside the loop in the former case. Apart from the startup failure, the device does not show any indications of failure during transient or steady state operation.

5.3 Startup Trends of the mLHP

Depending on the fluid distribution and pre-startup situation inside the evaporator and in the compensation chamber of the mLHP, different startup trends are seen. In the mLHP, the startup trend of the type shown in Figure 5.11 was commonly observed. In this type of startup, it is expected that there is a ready vapour liquid interface present in the evaporation zone (i.e. wick and wall interface) (Maydanik et al, 1995). As heat is supplied to the evaporator there is an intensive generation of vapour inside the evaporation zone. With the increase in the volume of the vapour phase inside the evaporator, the liquid present in the vapour line is displaced into the compensation chamber. This process is linked with the development of some minimum pressure difference and thus temperature gradient across the evaporating and absorbing face of the capillary structure in accordance with the condition 2 in section 3.2.2. The mLHP temperature will increase until this condition of serviceability is fulfilled as shown in section 1 of the graph in Figure 5.11. The moment of time at which this condition is met corresponds to the temperature stabilization in section 2. This trend indicates very reliable startup of the mLHP at low as well as at high input powers and occurs when the loop is charged with the optimum inventory of the working fluid that guarantees liquid charge inside the compensation chamber while in the cold state.

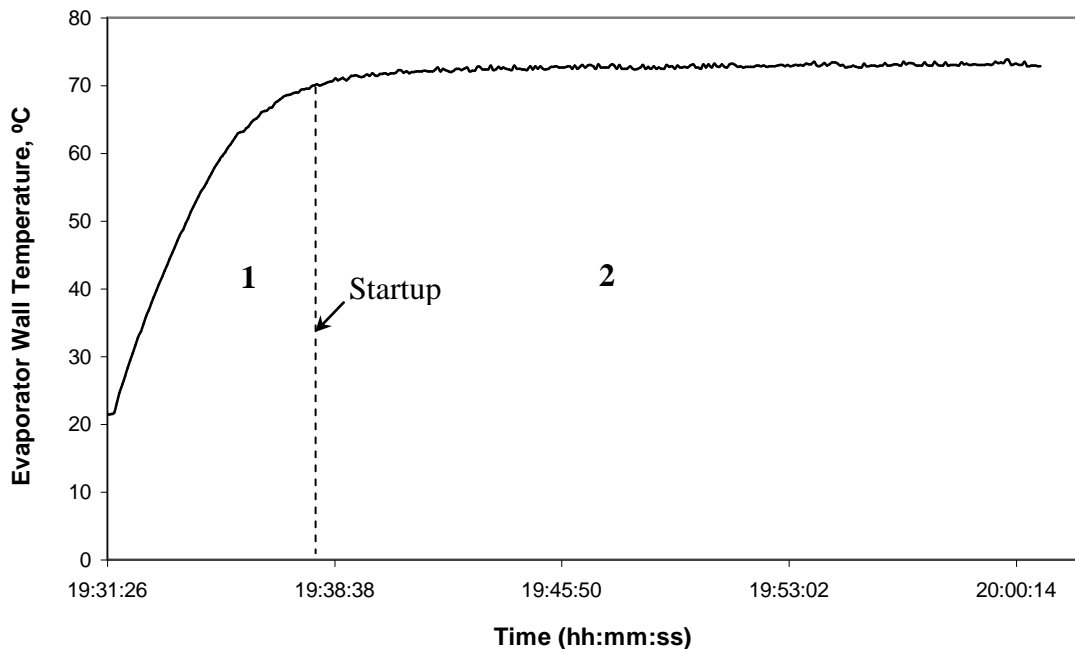


Figure 5.11 Start-up trend shown by the mLHP when the liquid-vapour interface is already present in the evaporator before heat load is applied

The mLHP can also show other startup trends for different fluid charge distribution and pre-startup situation inside the loop before the device is operated. A start up situation similar to Figure 5.12 can result when the vapour removal channels in the evaporator are completely flooded with liquid.

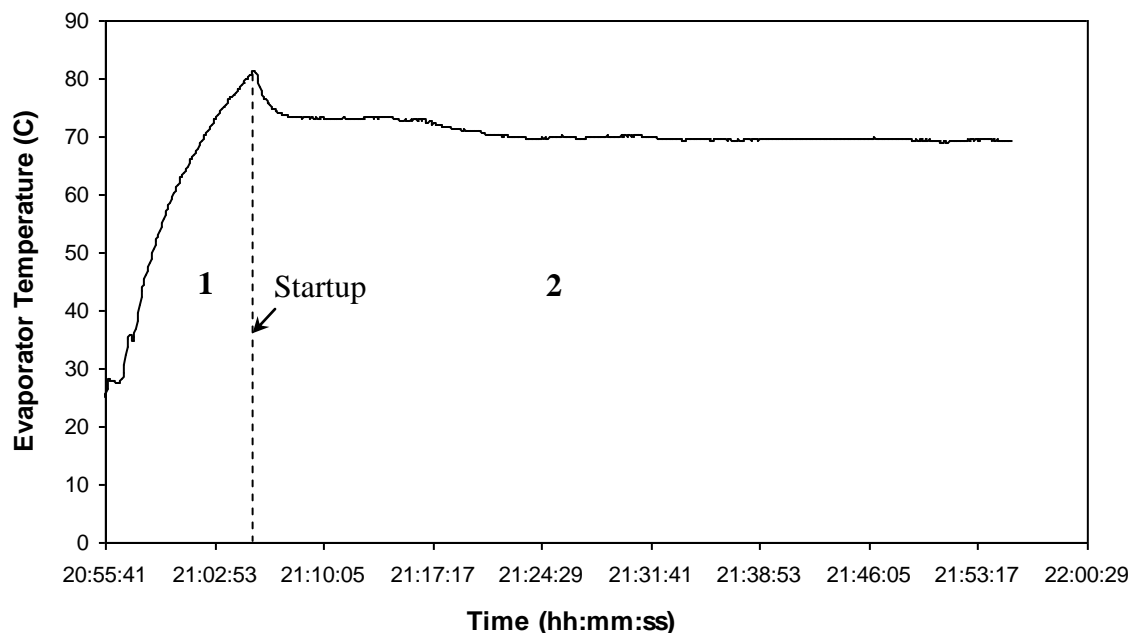


Figure 5.12 Start-up trend shown by the mLHP when in the pre start state the vapour removal channels are completely flooded with liquid

Such a trend can occur if the device is slightly tilted so as to fill the evaporator completely or when the condenser temperature is higher than that of the evaporator before the heat load is applied to the evaporator. In certain cases, this startup situation can also arise when the device is operated for the first time after charging. As the charging is done at the compensation chamber, the possibility of the evaporator becoming flooded by liquid is higher. At the time of startup, in the vapour removal channels one can observe an abrupt boiling of liquid that has been superheated with respect to the loop saturation temperature. The process is accompanied by abrupt clearing of the vapour line and gradual temperature decrease in section 2 (Figure 5.12).

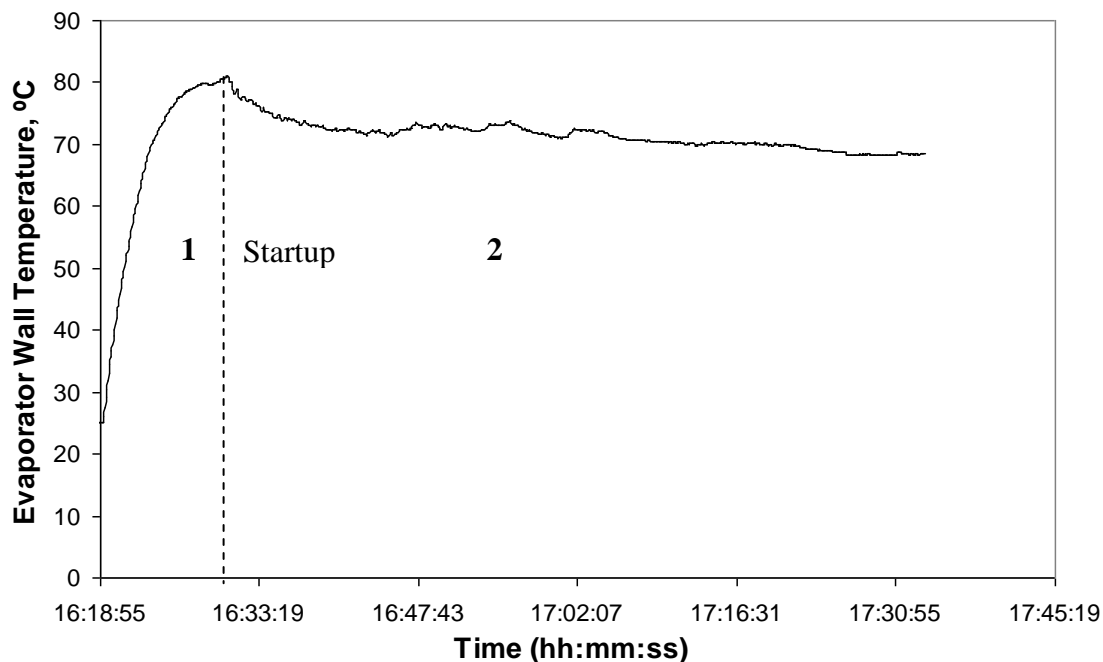


Figure 5.13 Start-up trend shown by the mLHP when in the pre start state insufficient fluid inventory is present in the compensation chamber

A startup situation as presented in Figure 5.13 can result when the liquid quantity present in the compensation chamber is low and a liquid-vapour interface is present in the vapour removal channel. This situation can arise if the mLHP evaporator has low fluid inventory or if the major fluid quantity is distributed elsewhere in the loop. Owing to small charge inside the compensation chamber, void fraction (vapour space) inside the chamber is high. Now as the liquid-vapour interface is almost always present inside the compensation chamber before startup, low liquid charge inside the chamber as well as in the wick results in intensive heat flow into the chamber and increases its temperature. Because of the closeness of the evaporation zone to the heating wall, the quantity of vapour generated in the evaporator is more than in the compensation chamber, which increases the pressure inside the evaporator above that in the compensation chamber. As the pressure in the evaporator rises above that of the compensation chamber, the vapour inside the evaporation zone pushes the liquid from the vapour line into the compensation chamber thereby initiating startup of the device. Decrease in the evaporator temperature as shown in section 2 results from the decrease in the compensation chamber temperature due to fluid flow.

5.4 Comparison of Theoretical and Experimental models.

The theoretical model proposed in Chapter 3 was tested against the current mLHP design using a uniform heating source. To predict the thermal characteristics of the mLHP, the specified loop conditions include the ambient/sink temperature which was kept constant at 24 ± 2 °C and the mode of cooling at the condenser which was forced convection using an air cooling fan with flow area of 5 cm^2 and volumetric flow rate of $0.1\text{ m}^3/\text{min}$. Tests were conducted in the power range of 5 to 70 W and using two types of capillary structures which were made from copper and nickel respectively. All the tests were carried out with the mLHP leveled horizontally such that the evaporator and the condenser lay on the same horizontal plane.

Results are presented by taking the evaporator surface temperature versus the applied heat load for the mLHP. Figure 5.14 presents a comparison between the experimental results and the predictions for the mLHP with the sintered nickel capillary structure.

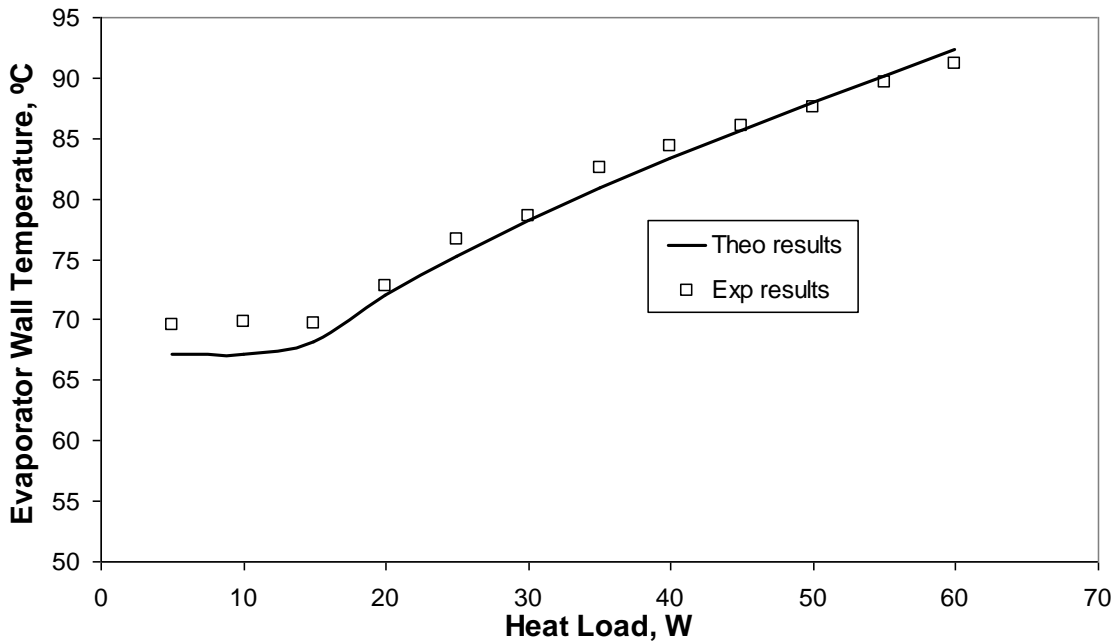


Figure 5.14 Comparison of theoretically predicted and experimentally determined results for the mLHP design with sintered nickel capillary structure

It is evident from the graph that theoretical model was able to predict very closely the typical mLHP thermal behaviour including both the variable and constant conductance modes. The calculated values are within 0.3 to 3.8 % of the experimental measurements. It is seen that for

heat loads above 20 W the agreement between the experimental and predicted values is very close. For low power input (5 to 15 W) the operating temperature predictions are less satisfactory (i.e. within 2.2 to 3.8 % of the experiment values). This can be attributed to the fact that the effect of the heat exchange with the surroundings is more pronounced at low powers. In the present theoretical model, this effect has been neglected to simplify the model and because of the smaller surface area of the compensation chamber exposed to natural convection. At high powers, the energy balance in the compensation chamber is dominated by the liquid return from the condenser rather than by heat exchange with the surroundings. As the heat exchange with the surroundings becomes a smaller fraction of the applied heat, the predictions are better at high powers. Figure 5.15 shows the result of comparison for the sintered copper wick. It is seen that for the mLHP with a copper wick the thermal performance predictions showed larger variations than for the nickel wick but the results are still satisfactory within the limitations imposed by the assumptions that were made in the formulation of the theoretical model.

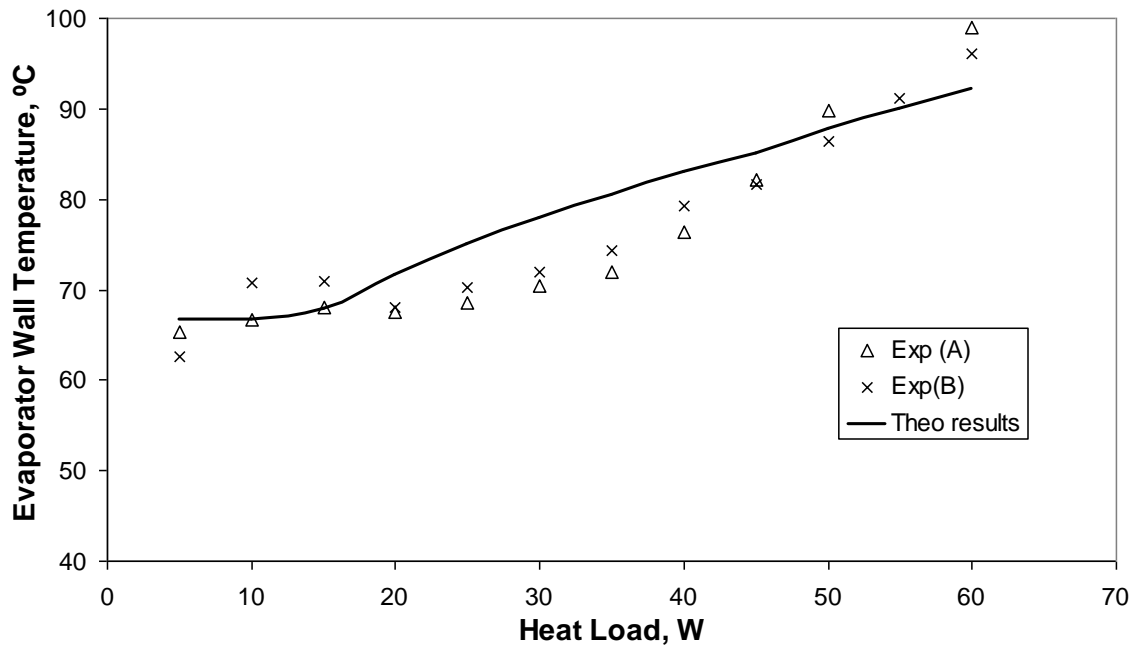


Figure 5.15 Comparison of predicted and experimental results for the mLHP design with sintered copper capillary structure

The discrepancies in the predicted values can arise from the limitation of the theoretical model to take into account critical heat transfer phenomena like the effect of local wick dry-outs and vapour bubble formation on the absorbing face of the wick, which can affect the

thermal performance of the mLHP immensely. The probability of these critical heat transfer limiting phenomena occurring in the case of the copper wick is higher than for the nickel wick due to the very high thermal conductivity of copper material. In Figure 5.15, Exp (A) and Exp (B) are two trial runs carried out on the mLHP experimental prototype.

The maximum heat transfer capacity of the loop heat pipe is limited by the maximum capillary pressure that the wick structure can generate on the working fluid. However, in practice the maximum heat that an LHP can transfer is generally decided by the maximum permissible operating temperature of the source (generally ≤ 100 °C) which is reached much before the capillary limit is achieved. Table 5.1 lists the maximum heat transfer capacity of the mLHP calculated on the basis of the above two approaches as discussed in section 3.4. The difference in the experimental and predicted values calculated on the basis of maximum temperature limit is attributed to the multitudes of unaccountable factors that affect the device performance and are generally difficult to take into account.

Table 5.1 Maximum heat transfer capacity of the mLHP calculated on the basis of theoretical and experimental approaches.

	Theoretical Prediction - Based on Maximum Operating Temperature limit ($T_{max} \leq 100$ C)	Theoretical Prediction - Based on maximum capillary limit of the wick structure ($r_{em} = 10$ μm)	Experimentally determined values ($T_{max} \leq 100$ C)
Q_{max} for Copper Wick (W)	79	244	70
Q_{max} for Nickel Wick (W)	94	244	75

5.5 Effect of the Fluid Inventory on mLHP Thermal Performance

The operational characteristics of the mLHP are influenced by the quantity of the working fluid inventory inside the loop. In particular, the charged inventory should be sufficient to provide proper wetting of the capillary structure before the heat load is applied. Otherwise it may be difficult to achieve filling of the wick after a heat load is applied under rapid heating of a dry evaporator. In order to satisfy the wetting requirement, proper consideration must be given to the compensation chamber volume and the fluid charge inventory. For the compensation chamber volume, it should be large enough to accommodate the liquid charge displaced from the evaporator vapour channels, vapour line and part of the condenser. In the present prototype, the compensation chamber was sized such that its internal volume was approximately equal to the internal volume of the loop. In the LHP, a considerable part of the liquid is present in the unbound state throughout the loop. As the testing was done in the horizontal orientation, it is expected that the fluid was distributed through the entire loop volume. Under such circumstances, it is always desirable to guarantee some minimum quantity of the working fluid inside the compensation chamber to keep the wick saturated with the liquid. In this case, for keeping the wick primed with the liquid, the loop was charged such that in the cold state at least 30-40% of the compensation chamber was occupied by the working fluid. It has been mentioned in the literature (Maydanik and Fershtater, 1997) that LHPs can operate with a relatively wide range of charge and compensation chamber volumes.

Figure 5.16 shows the outcomes of tests conducted on the designed mLHP with fluid inventory equal to 50% and 80% of total volume. The mLHP was able to operate satisfactorily in both cases over the range of input heat loads. However, it should be noted that the thermal performance of the mLHP is better with 80% charge than with 50% charge volume. This is directly related to the fluid distribution inside the loop and the compensation chamber during operation. For the 50% charged inventory, it is expected that approximately 30% of the compensation chamber was occupied with fluid whilst for 80% charge, approximately 50% of the compensation chamber was filled with working fluid. The presence of significant amount of fluid in the compensation chamber helps to absorb part of the back heat conducted from the evaporator and thus decrease the compensation chamber temperature. For the LHP, variables like the room temperature, condenser temperature, evaporator wall

thickness, type of working fluid, geometric characteristics of the transport lines etc affect the steady state evaporator temperature. The design parameters were constant and the room and condenser temperatures were kept the same for all the testing carried on the device. Therefore it can be inferred that the evaporator temperature for any given test is largely dictated by the compensation chamber temperature. Hence, low evaporator temperature was achieved with the 80% charge because there was more liquid in the loop which gave better wetting conditions in the wick as well as a low degree of heating of the compensation chamber. Nonetheless, the mLHP was not able to start up or operate reliably with charges less than 50% or more than 80%.

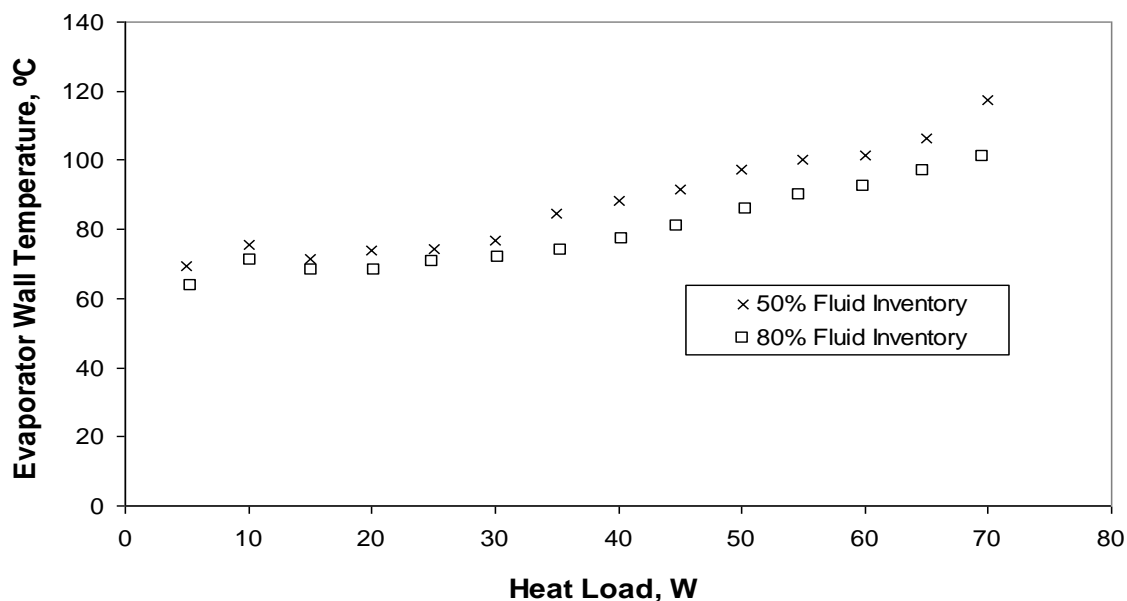


Figure 5.16 Effect of the fluid charge on the evaporator wall temperature for the given range of applied heat loads

For lower charge ($< 50\%$) dry out of the wick occurs due to the insufficient fluid quantity present inside the compensation chamber to keep the wick structure completely wet. On the other hand for large fluid charge ($> 80\%$) the active condensation area of the condenser may decrease, the liquid may occupy the vapour line and part of the vapour removal channels during operation depending upon the quantity of charge. If liquid is present inside the vapour removal passage and evaporation zone due to excess charging, it may also block the capillary pumping action of the wick. These factors ultimately produce instability towards acquiring steady state and thus result in the startup or operational failure of the device. The startup failure of the mLHP due to the insufficient fluid inventory is presented in section 5.2.2 in relation to mLHP failure mode analysis.

5.6 Effect of Tilt on the mLHP Thermal Performance

The primary aim of the current design of mLHP was to effectively transfer waste heat from the microprocessors of laptop computers. As the laptops must operate horizontally, so all the tests on the device were conducted with the evaporator and condenser at the same level i.e. without taking into consideration the effect of the mLHP tilt in the gravity field on its operational performance. However, under certain circumstances the device may be subjected to adverse tilts in the gravity field.

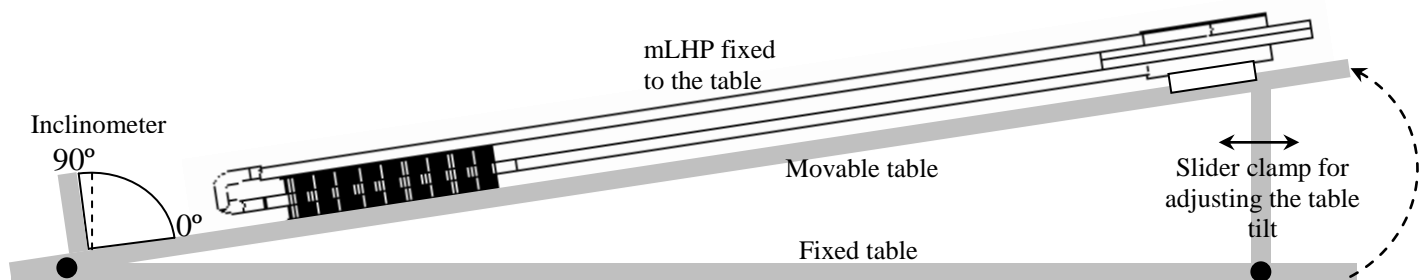


Figure 5.17 Test setup to measure the thermal performance of the mLHP at different tilt angles

In order to satisfy this requirement, the following test was carried out to study the thermal performance of the mLHP at different tilts in the gravity field. A mLHP was installed on a test table as shown in Figure 5.17 that could be adjusted to a fixed inclination (evaporator above condenser) to horizontal. During testing, the inclination was changed in steps of 10° starting from 0° (horizontal) to 90° (vertical) while the device was made to operate at a constant heat load of 25 W.

Figure 5.18 shows the performance of the mLHP at different orientations as a plot of evaporator surface temperature against tilt angle. The curve shows an increase in evaporator temperature with increase in the inclination. For horizontal orientation, the evaporator temperature was steady at 62°C while for the vertical orientation (90°) the evaporator was able to achieve stable state at 111°C . The rise in evaporator temperature can be explained by taking into consideration the natural flow tendencies of the vapour and liquid phases. As the tilt angle increases, more pressure is required to push the vapour out of the evaporator. This is because from the buoyancy effect the vapour tends to flow up against gravity. Because of the prolonged stay of the vapour in the evaporation zone, the vapour acquires extra heat from the

evaporator heated wall and becomes superheated, resulting in increase of the evaporator wall temperature. Contrary to the vapour phase, the liquid phase has a natural tendency to flow down by gravity but in this case, it must be pumped from the condenser to the compensation chamber against gravity. The intended function is provided by the surface tension forces developed in the fine pored sintered wick. However, the flow rate of the liquid to the compensation chamber decreases because of the difficulties encountered by the vapour flow and accumulation of the liquid in the bottom portion of the loop including the condenser.

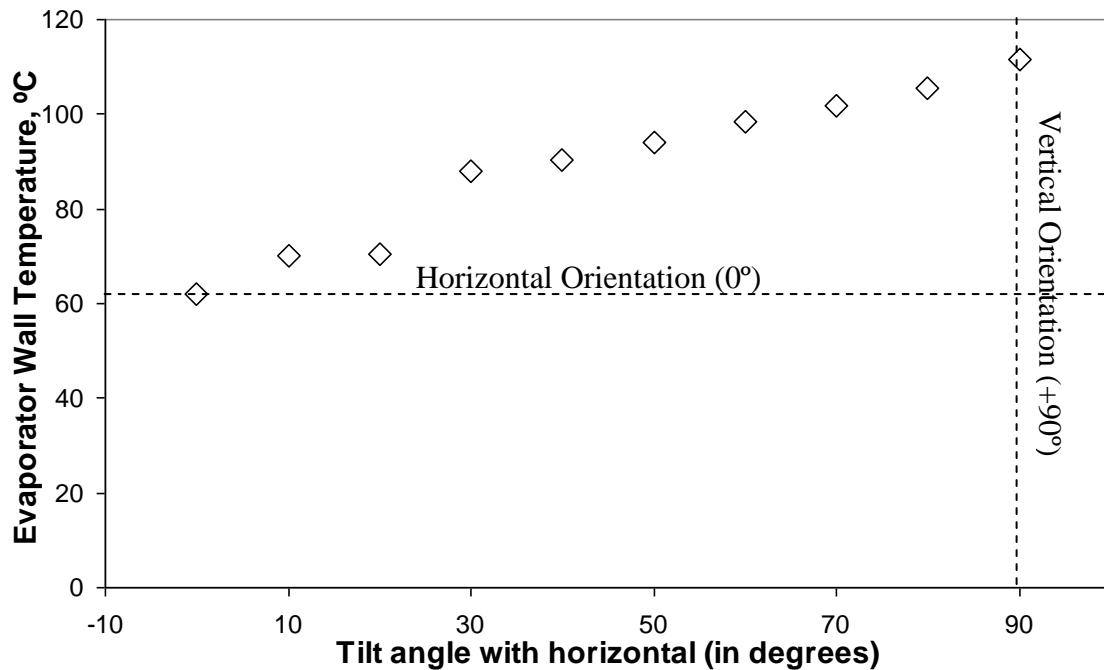


Figure 5.18 Effect of the tilt angle on the thermal performance of the mLHP

The present design of mLHP with a disk shaped evaporator is intended for operation in the horizontal configuration and the relative positions of each component in the loop are fixed. In this case, change in the orientation of the loop affects the fluid distribution inside the loop mainly inside the compensation chamber. As shown in Figure 5.19, this design is very efficient in keeping the wick structure primed with the liquid at all times while in the horizontal orientation. However, with tilt, this design results in the exposure of the absorbing face of the wick inside the compensation chamber to the vapour phase, the extent of this exposure increasing with the tilt angle. This decreases wetting of the capillary structure and

provides a favorable path for back heat flow from the evaporator zone to the compensation chamber. Consequently there is a higher temperature of the evaporator at vertical orientation.

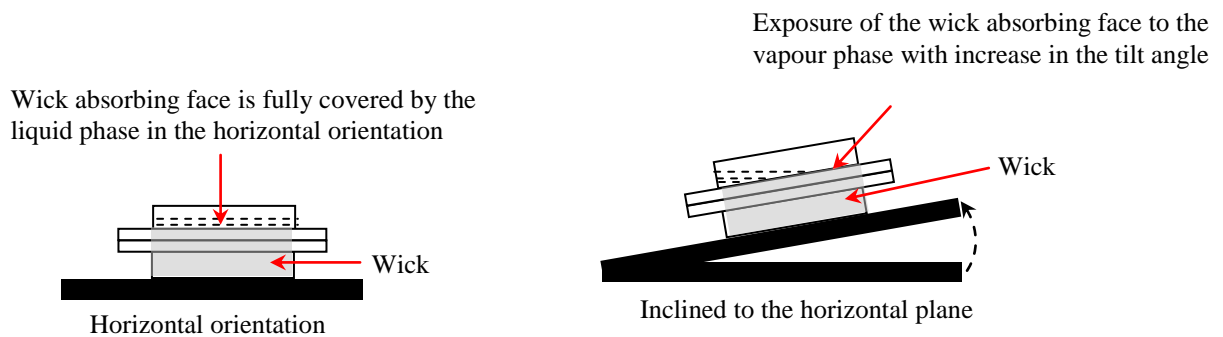


Figure 5.19 Change in the fluid distribution inside the compensation chamber with the increase in the tilt angle

However, the mLHP was able to achieve steady state within a short time period at different elevations and did not show any indications of evaporator failure. Also, the device was able to repeat the same steady conditions at a given tilt angle. The experiment helps to confirm the successful operation of the mLHP device at adverse orientation in the gravity field.

It should be noted for the case of the positive angle influence i.e. the condenser above evaporator configuration, the mLHP will operate more or less like a thermosyphon between the evaporation zone and the condenser. As liquid will be present in the evaporator at all the times, the capillary action of the wick will be completely destroyed. It was observed that the present design of mLHP operated with a high evaporator temperature at such a mode of operation (bottom heat mode). Proper operation at positive slopes is possible with the proper design and location of the evaporator and condenser with respect to each other.

5.7 Thermal Performance of the mLHP under Different Heating Modes

From the literature survey it was seen that the performance of most LHP prototypes is evaluated at uniform heating modes of the evaporator. In this mode heating is provided over the whole of the evaporator active zone i.e. the surface where the capillary structure makes contact with the evaporator wall and there are vapour removal channels. In practice, situations can arise in which only part of the active zone may be heated due to local heating or hot spots on the heat source. For this purpose, the thermal characteristics of the LHP should be studied for a non-uniform heating mode in which only part of the active zone is heated. This second mode of heating is very important from the point of view of microprocessors that can involve local hot spots and irregular surface heating patterns depending on the data processing load of the microprocessor. For these reasons, the present study was conducted to test and compare the thermal performance of the mLHP for thermal control of the microprocessors with both uniformly and non-uniformly heated active zone.

The mLHP was tested under conditions of uniform heating using a heater of 6.25 cm^2 ($25 \times 25 \text{ mm}^2$) area and non uniform heating using a heater of 1 cm^2 ($10 \times 10 \text{ mm}^2$) area. Testing was done using a sintered nickel wick and the optimum charge of 70% to 80% of the loop internal volume in both cases. For non-uniform heating, only part of evaporator active zone was supplied with heat. Here, non uniform heating was provided to approximately 14% of the evaporator active zone. During testing, the heat source was attached symmetrically to the center of the circular heat absorbing face.

Heat load applied to the active zone of the evaporator results in the formation of vapour inside the evaporator grooves followed by clearing of liquid from the grooves and vapour line. The displaced liquid is accommodated inside the compensation chamber and a stable evaporating meniscus is formed at the wall wick interface inside the evaporation zone. Such liquid-vapour interfaces also exist inside the compensation chamber and the condenser. Figures 5.20 and 5.21 show the startup characteristics of the mLHP for uniform heating (using $25 \times 25 \text{ cm}^2$ source) and partial or non-uniform heating (using $10 \times 10 \text{ cm}^2$ source) respectively with 20 W input power.

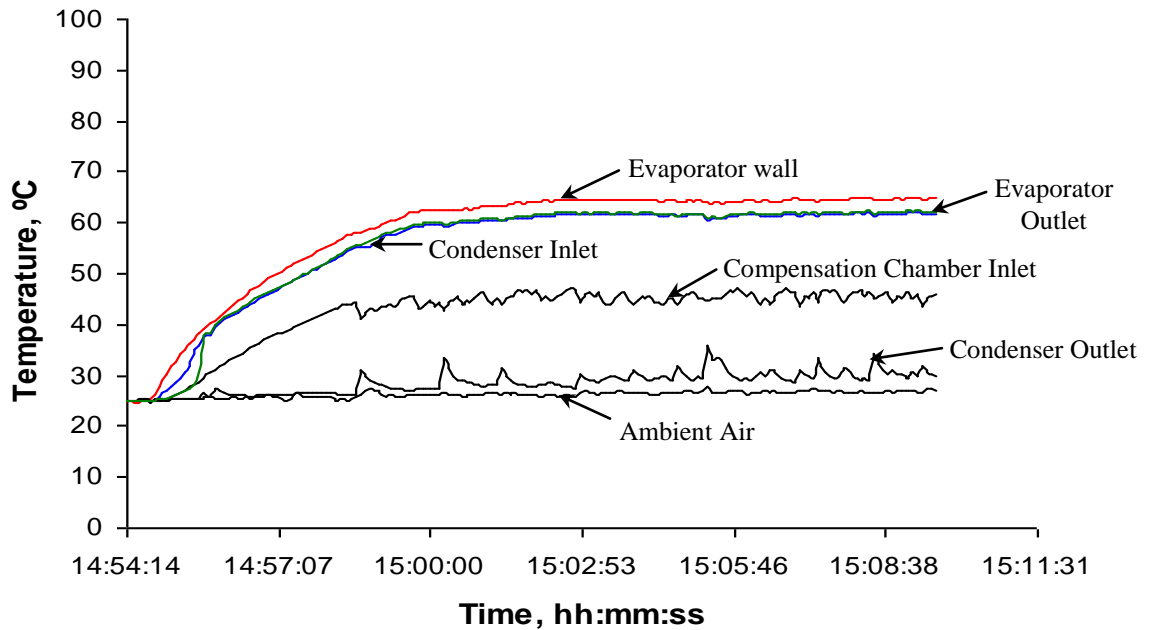


Figure 5.20 Startup of the mLHP with uniform heating of the evaporator active face at input power of 20 W

The designed mLHP registered successful startup with both modes of heating. The startup process was very reliable over the range of applied power and the mLHP evaporator did not show any indication of wick dry-outs.

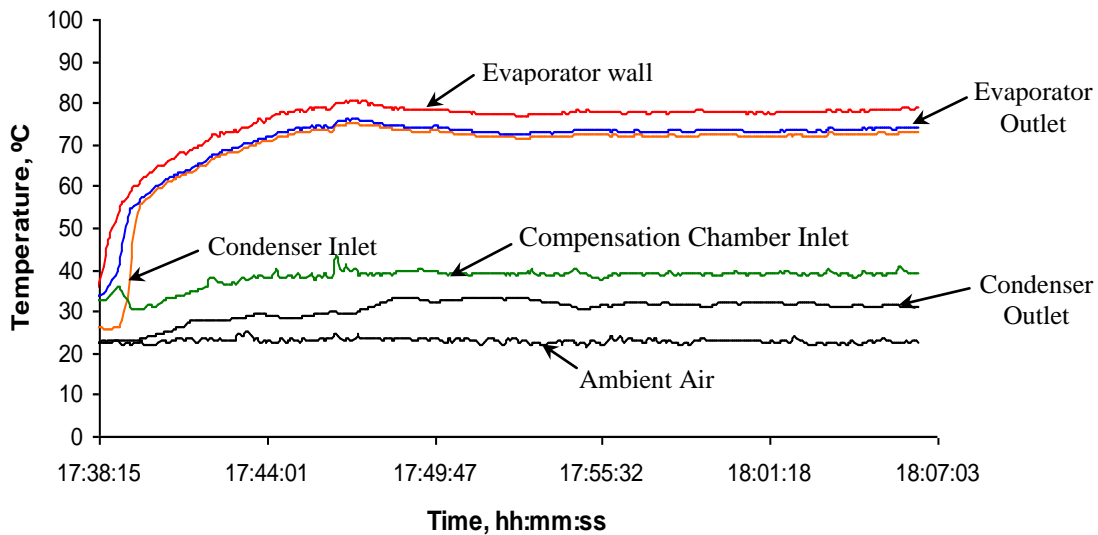


Figure 5.21 Startup of the mLHP with non-uniformly heating of the evaporator active face at input power of 20 W

Figure 5.22 shows the variation of the evaporator wall temperature as a function of the applied heat load for both heating modes. The reduction of the active heating area of the evaporator brings an additional conductive resistance that opposes spreading of heat to the entire heating face. It is evident from the graph in Figure 5.22 that the mLHP was able to handle the conditions of local heating even when only 14% of the evaporator active area was heated. For the range of applied heat load, the evaporator wall temperature with local heating (using 10x10 mm² heater) was between 5 to 15 °C higher than that of the uniform heating case (using 25x25 mm² heater).

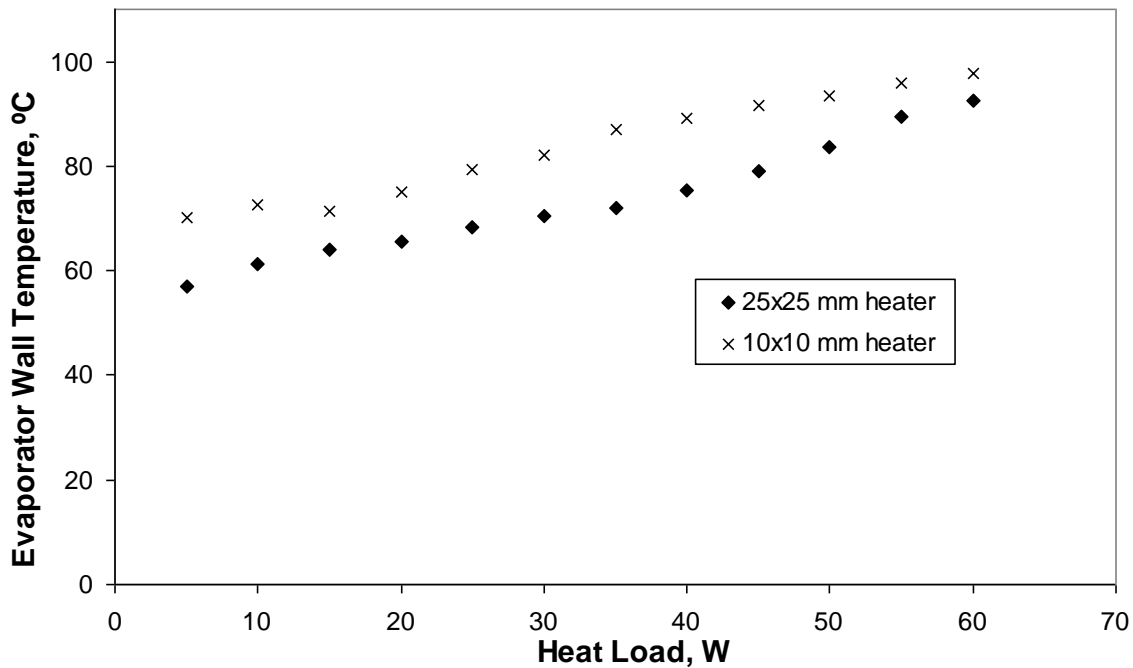


Figure 5.22 Thermal performance (evaporator wall temperature versus applied heat load) of mLHP for uniform as well as non uniform heating modes

This is made possible by the enhanced design of the capillary evaporator that decreases the conductive as well as convective resistance offered to the heat acquisition process. The mLHP evaporator was made from copper, which with its high thermal conductivity decreased the spreading resistance and promoted the efficient transfer of heat from a hot spot without any local overheating of the evaporator surface. For the mLHP prototype, a heat transfer coefficient of the order of 10,000 to 20,000 W/m² K was achieved with both uniform as well as non-uniform heating modes over the range of applied power. The plot for evaporator thermal resistance versus applied heat load for the two heating modes is shown in Figure 5.23.

For uniform heating, R_e lies in the range of 0.18 to 0.24 °C/W whereas for the local heating case R_e values from 0.24 to 0.38 °C/W were obtained. It is clear from the above outcomes that the mLHP evaporator was able to manage the thermal loads of the local heating source effectively.

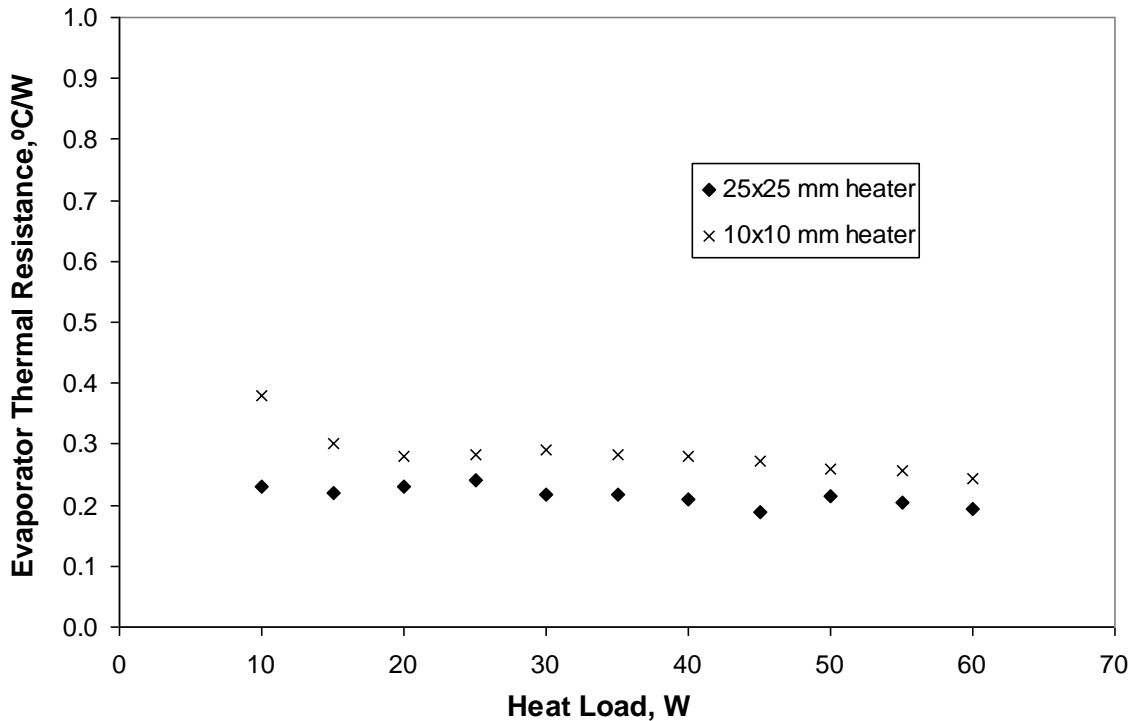


Figure 5.23 Evaporator thermal resistance versus applied heat load for uniform and non uniform heating modes

Figures 5.24 and 5.25 show the trends for the heat pipe thermal resistance, R_{hp} and total thermal resistance, R_t with change in applied heat load. With uniform heating, minimum values of 0.30 °C/W for R_{hp} and 1.11 °C/W for R_t were achieved at 60 W. The corresponding values for the local heating mode are 0.48 °C/W for R_{hp} and 1.20 °C/W for R_t . It is clear that at high heat loads the total thermal resistance of the mLHP with both the heating modes is nearly same. This is because of the increased liquid flow rates and better wick wetting characteristics supported by the presence of sufficient liquid inside the compensation chamber.

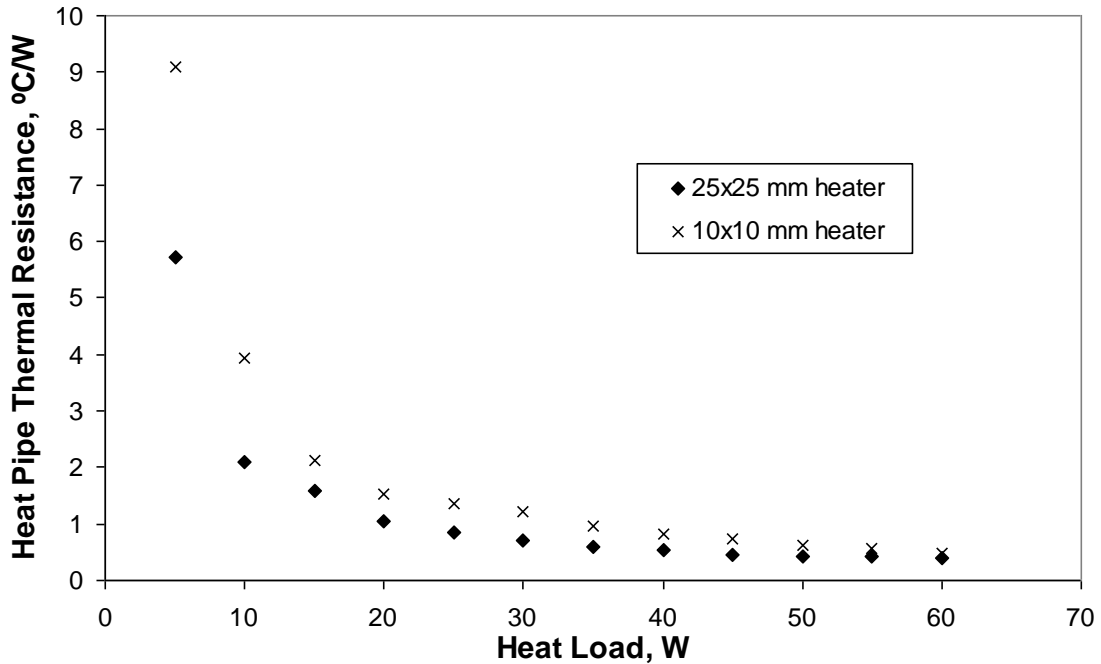


Figure 5.24 Heat pipe thermal resistance versus applied heat load for uniform and non uniform heating modes

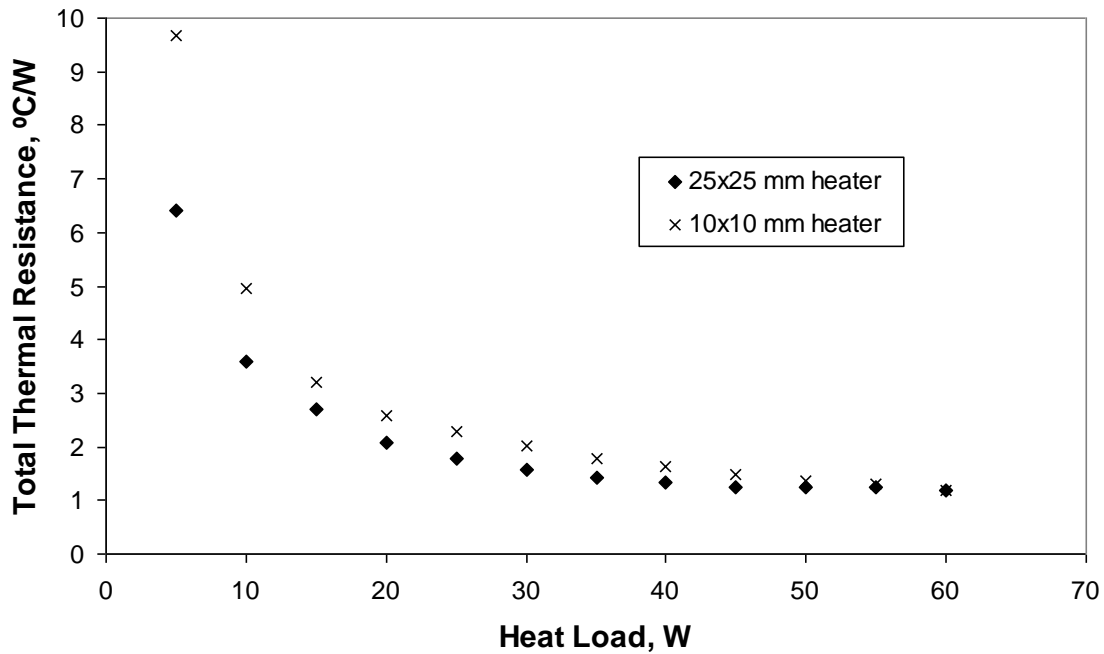


Figure 5.25 Total thermal resistance versus applied heat load for uniform and non uniform heating modes

The results clearly identify the good thermal characteristics of the mLHP and its ability to acquire and transfer waste heat from compact microprocessors and chipsets with local hot spots.

5.8 Thermal performance of the mLHP with different Wick Configurations

The wick is an integral part of the loop heat pipe and provides the necessary capillary forces to the working fluid for its continuous circulation in the loop. The choice of wick material and its physical properties like pore size, porosity and permeability has considerable effect on the operational characteristics of the loop system. As a connecting link between the evaporator and compensation chamber, the wick is also expected to perform as a thermal and hydraulic barrier to minimize back flow of heat and vapour from the evaporation zone to the compensation chamber. The function as a hydraulic or vapour lock is made possible by the introduction of the fine pore capillary structure in the LHP evaporator. In this case, the presence of liquid in these fine pores helps to avoid any vapour migration from the evaporation zone to the compensation chamber via the capillary structure. The problem of back conduction of heat is very critical and to a large extent dictates the thermal behaviour of the LHP. Different methods have already been proposed and tested on large LHPs to counteract or minimize heat flows to the compensation chamber. They include subcooling of the incoming liquid to the compensation chamber, making use of low thermal conductivity material for the wick and increasing thickness of the wick. In mLHPs, this problem of back conduction is compounded by the limited permissible thickness of the wick which is only few millimeters. Additionally, for electronic cooling where use is made of air cooling fans it is not possible to cool the liquid below the ambient temperature which restricts the degree of subcooling given to the condensate. Considering the possible options, appropriate choice of the thermal conductivity and the physical properties of the wick structure can help in the design of a suitable wick configuration for a mLHP. In relation to this consideration, different types and grades of wick structures were developed and tested in the designed mLHP as discussed below.

5.8.1 Effect of the wick material

Sintered metal wicks made from nickel and copper were used to study the effect of the thermal conductivity on the mLHP performance. For the two wick types the physical characteristics were approximately the same with the pore radius less than 15 μm and 45-60% porous volume. The thermal conductivities of the copper material and nickel material used to fabricate these samples were 398 W/m.K and 90.5 W/m.K respectively. Based on the

experimental correlation for the homogeneous wick structure obtained by Alexander (1972), the effective thermal conductivities of the water-saturated copper and nickel wicks were estimated to be 59.6 W/m.K and 21 W/m.K respectively. The thickness of the wick structure was restricted to 3 mm with an absorbing face area of 615 mm². Figure 5.26 shows the heat load dependence of the evaporator surface temperature for the two types of wick material.

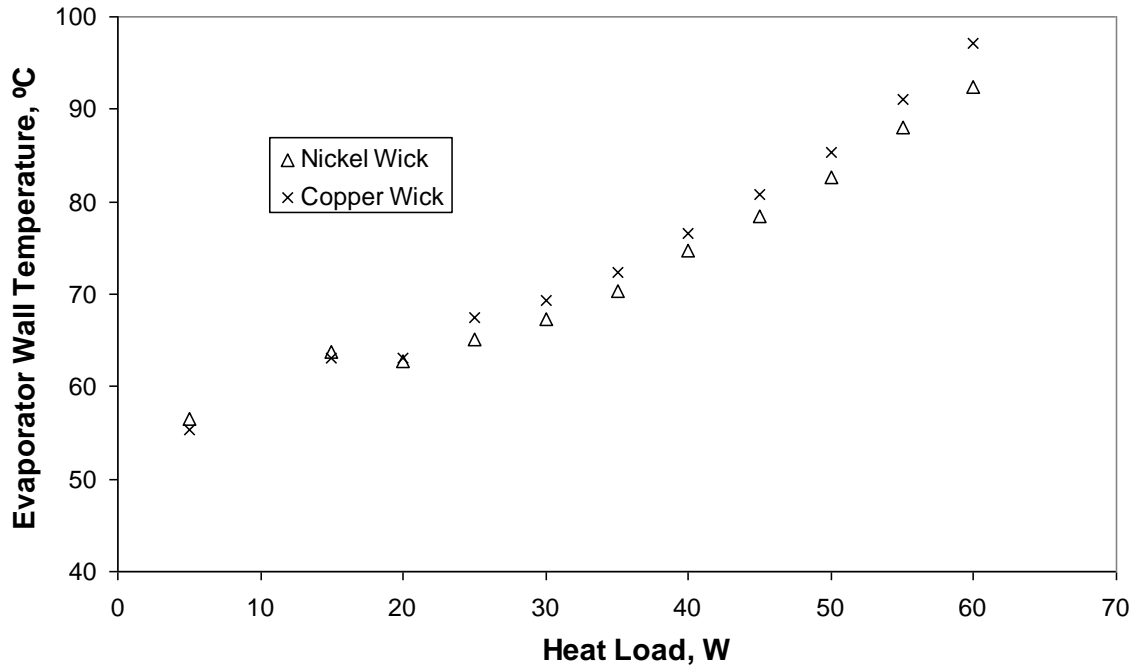


Figure 5.26 Heat load dependence of the evaporator wall temperature with nickel and copper wicks

It can be seen from the graph in Figure 5.26 that for a heat load of less than 20 W, the evaporator temperature for the mLHP with Cu-wick is lower than the Ni-wick mLHP. This is the result of the efficient heat exchange process in the evaporator of the Cu-wick mLHP as shown by Figure 5.27. With a copper wick a heat transfer coefficient as high as 26,200 W/m² K was achieved over the range of input heat load. These higher values of the heat transfer coefficient were obtained because of the high thermal conductivity of copper which helped to transfer heat efficiently to the menisci surfaces in the capillary structure by conduction through the wick skeleton. An abrupt decrease in the heat transfer coefficient with the copper wick was experienced at approximately 35 W, possibly due to the formation of dissociated pores near the heating wall as the heat load increases. Here, the desiccated or dried out pores introduced additional thermal resistance in the evaporation zone as is clearly shown in Figure

5.27 for heat loads greater than 35 W. In the case of the Ni-wick mLHP, the maximum heat transfer coefficient value achieved was 21,000 W/m² K.

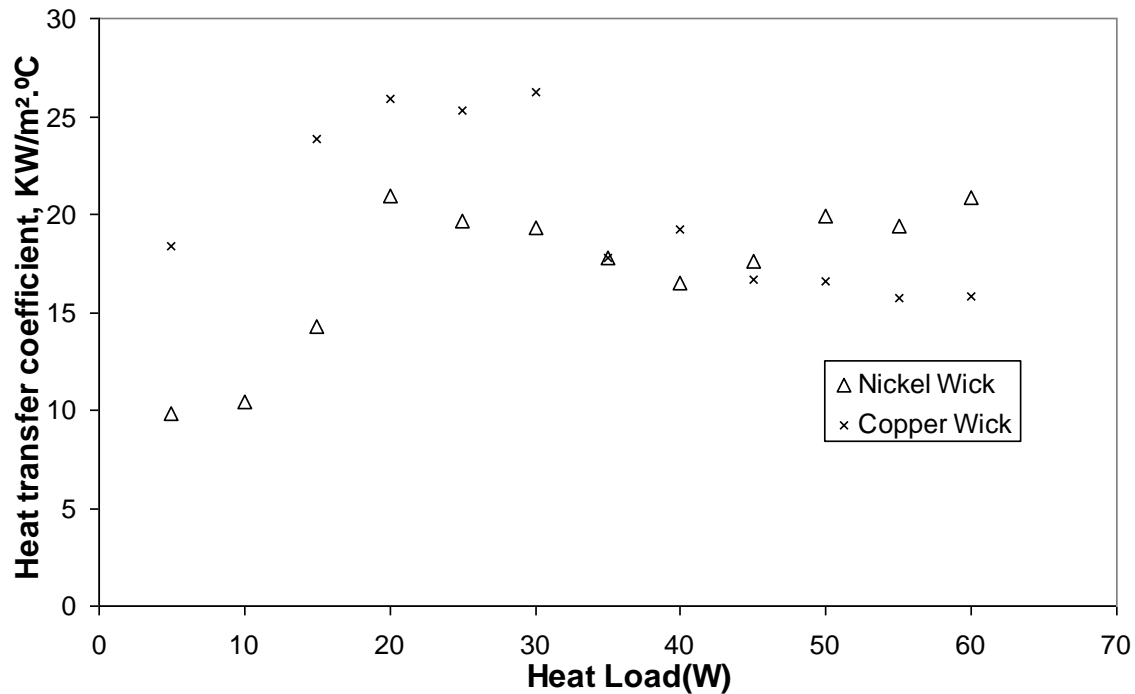


Figure 5.27 Heat load dependence of the evaporator wall temperature for mLHP with nickel and copper wicks

For the Cu-wick mLHP as shown in Figure 5.28, low values of evaporator thermal resistance - R_e lying between 0.20 to 0.24 °C/W were achieved and remained lower than for the Ni-wick mLHP over the entire range of applied heat load. Due to the high thermal conductivity of copper, the thermal resistance of the copper wick was lower than for the nickel wick. It can be inferred from the graph in Figure 5.28 that superior heat exchange can be achieved in the evaporation zone using a copper wick. R_e for the Ni-wick mLHP was found to be between 0.23 to 0.40 °C/W. Referring back to Figure 5.26, it is observed that for input power more than 20 W, the evaporator surface temperature for the mLHP with Cu-wick was slightly higher than that of the Ni-wick mLHP. This can be ascribed to relatively large heat leakage from the evaporator active zone to the compensation chamber at high heat loads owing to the high effective thermal conductivity of the copper wick.

At high heat loads (above 50 W) it is noted that the same incremental rise in the input load produced higher increase in evaporator temperature for both wick structures. Such behaviour of the mLHP indicates either the possibility of occurrence of a heat transfer crisis in the

evaporator or a limit on the heat dissipation capacity of the condenser which does not allow rejection of a higher heat load under the given condition of air cooling.

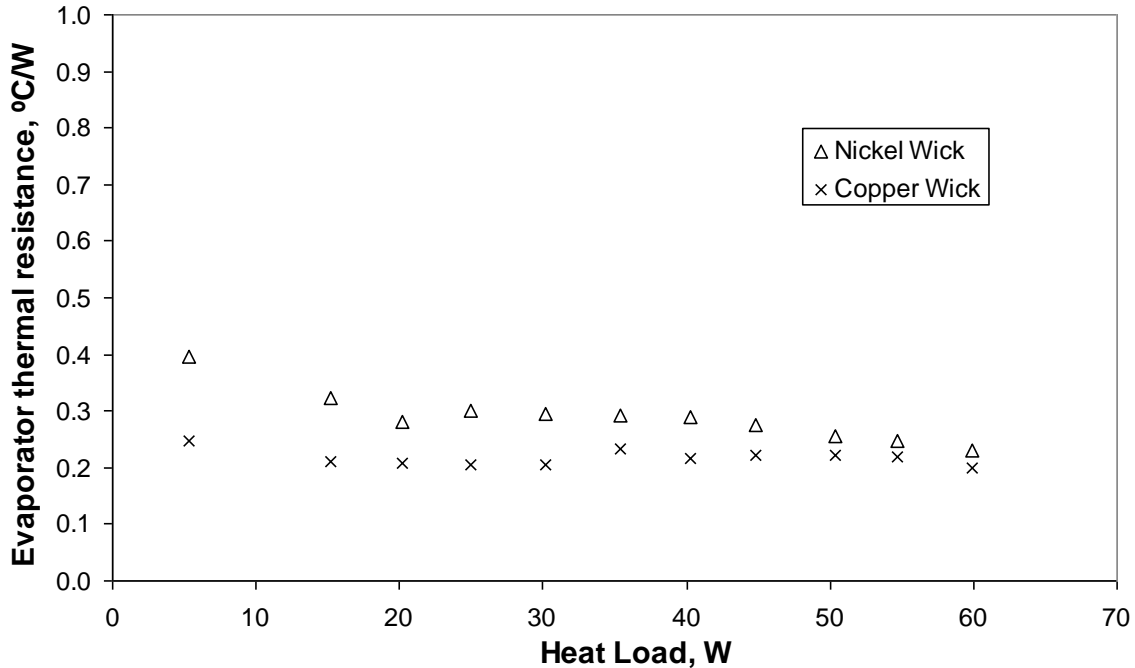


Figure 5.28 Evaporator thermal resistance versus applied heat load for mLHP with nickel and copper wicks

As an outcome of this experiment, it can be concluded that capillary structures made from a highly conductive material like copper can be effectively used in a miniature LHP for thermal control of electronic equipments without any major performance degradation. This is made possible by the use of a fine pore wick with a highly porous matrix that is occupied by working fluid with relatively low thermal conductivity. It has been seen that with the inclusion of the working fluid into the porous volume, the overall thermal conductivity of the capillary structure is much reduced. For example, thermal conductivity of the copper material is 398 W/m.K where as for the copper wick with porosity of 45-50% and saturated with water, the overall thermal conductivity is only 59.6 W/m.K.

5.8.2 Effect of the Physical Properties

Apart from the material characteristics like thermal conductivity, physical properties of the wick structure like porosity, permeability and pore configuration also play an important role in determining its operational characteristics. In order to see the effects of the physical

properties on the operation of a mLHP, two samples of the mono-porous copper wick (i.e. wick structures which are characterized by a single average pore size) with different physical properties were fabricated and tested. The first sample was sintered from copper powder with #100-200 mesh size while in the second sample, powder with mesh size greater than #200 was used. The geometrical properties of these samples were measured using different methods discussed in Appendix C on the measurement of the physical properties of the wick structure and the results are presented in Table 5.2.

Table 5.2 Physical properties of the monoporous copper wick

Property	Sample A	Sample B
Maximum pore radius (μm)	30 – 40	12 – 15
Porosity (%)	42	46
Permeability (m^2)	1.15×10^{-11}	3.74×10^{-12}

The results of the experiment are presented in the Figure 5.29 as a heat load dependence of the evaporator surface temperature for the two samples. It is evident from the graph that the performance of the mLHP with sample B is much better than that with sample A. The physical properties of sample B are optimum from the loop heat pipe design point of view in order to provide proper hydraulic and heat locking from the evaporation zone to the compensation chamber. The maximum capillary pressure provided by the wick structure is decided on the basis of the effective radius of the largest through-pore which is much higher in the case of sample A. At higher heat loads a pore can become dry and vapour can transfer thorough it from the evaporating surface of the wick to the absorbing one. For sample A, the value of the maximum pore radius (≤ 15) was low enough to guarantee vapour locking in the given range of heat load as verified by the loop pressure analysis.

The porosity and permeability of the wick affect the parasitic heat leaks from the evaporator zone to the compensation chamber and thus take part in providing thermal lock. As the effective thermal conductivity of the wick structure is dependent upon the porosity of the capillary structure, sample B had a better heat lock character than sample A.

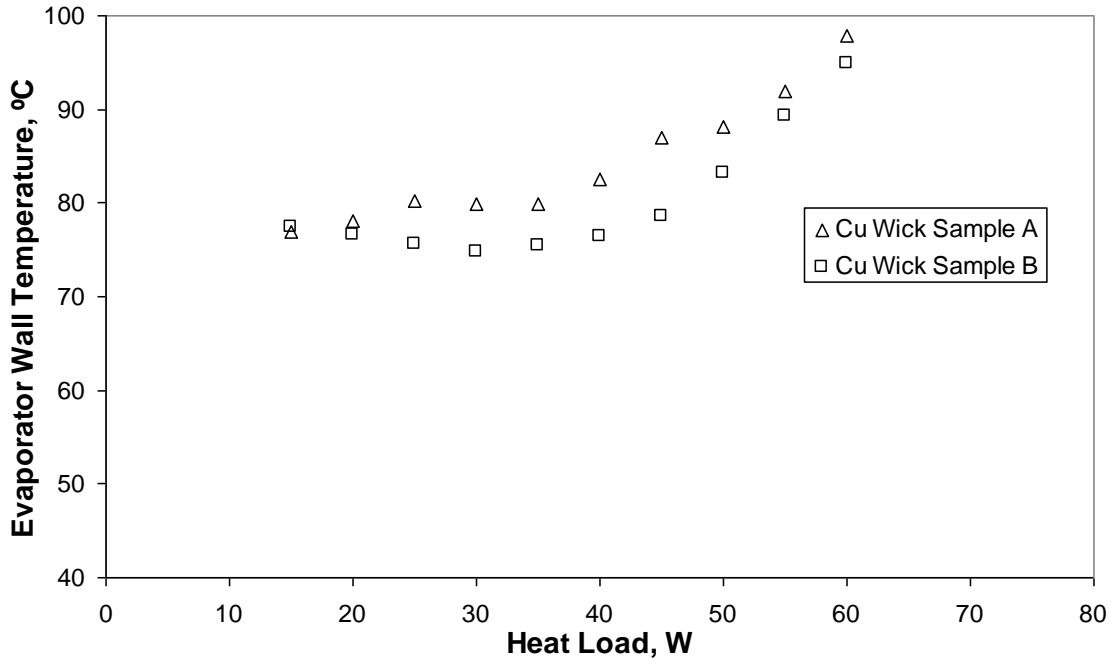


Figure 5.29 Heat load dependence of the evaporator wall temperature for monoporous copper wicks with different physical properties

In the case of a LHP, heat transfer is organized in the evaporation zone on the basis of inverted menisci. Here, the heat and the working fluid flow towards each other. In the wick structure, heat is introduced from the evaporating face while the working fluid enters from the absorbing face. If the flow rate of the working fluid through the wick structure is enhanced by increasing permeability of the capillary structure, the extent of the heat flow from the evaporator to the compensation chamber will automatically decrease which is the case with the sample B.

5.8.3 Effect of the Wick Structure

The wicks used are mostly mono-porous wicks i.e. their pore size distribution is similar to the Poisson distribution and they are characterized by average pore size. In contrast, a biporous wick is a porous medium which has two characteristic capillary pore radii i.e. large ones and small ones. The size of the largest pores in such a material is an order of magnitude greater than in a monoporous one. Thus a biporous wick includes bi-dispersed media which are made from large porous particles which have small pores in/on them as depicted in Figure 5.30.

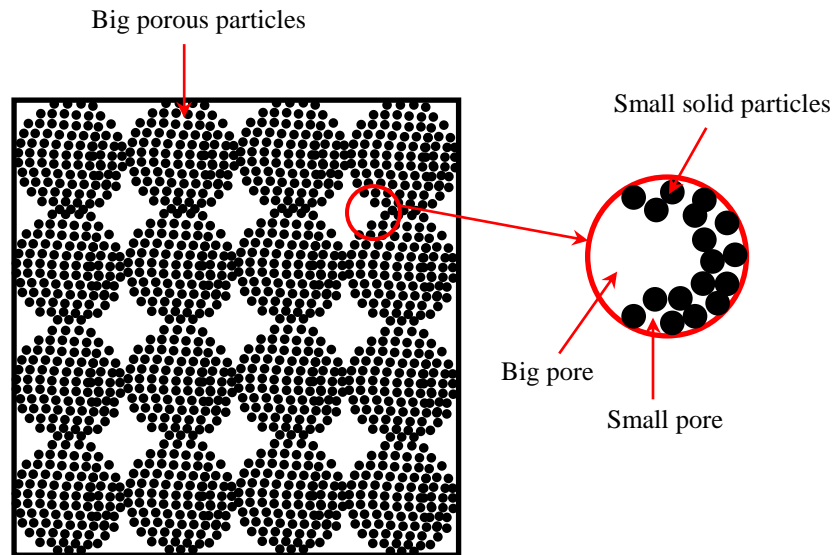
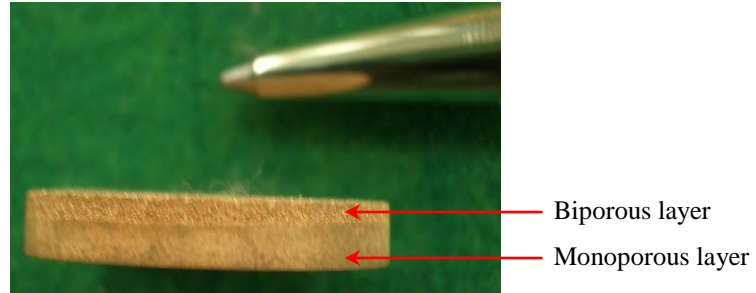


Figure 5.30 Structure of biporous wick

In another experiment, two samples of a sintered copper wick were made. The first sample was a monoporous wick with 46% porosity and made from copper powder of mesh size less than #200. In the second sample, a bi-porous copper wick with 65% porosity and made from powder with granular size in the range of 100-300 μm was used. Due to the possibility of vapour breaking through the large pores of the biporous media into the compensation chamber, an additional locking layer of a monoporous material (the same as that used in the first sample) was applied. The biporous portion of the wick formed the evaporating face while the monoporous portion acted as an absorbing face (Figure 5.31). The total thickness of both the samples was kept the same at 3 mm.

Figure 5.32 presents the outcomes of experimentation with the monoporous and combined wick structure. It is seen from the graph that the combined wick structure presented superior performance to that of the monoporous wick, particularly, for the range of the heat loads between 15 to 40 W. This can be explained by looking into the details of the heat transfer processes with the two types of wick configuration. In the wick with a monoporous pore size distribution, the vapour phase in the capillary structure volume along the heating wall is absent at the low to moderate heat loads, because the liquid superheat is not sufficient for boiling of the working fluid in the pores.



(a) Side View of the combined copper wick



(b) Monoporous layer as an absorbing face of the combined wick



(c) Biporous layer as an evaporating face of the combined wick

Figure 5.31 Combined Copper wick showing monoporous and biporous layers

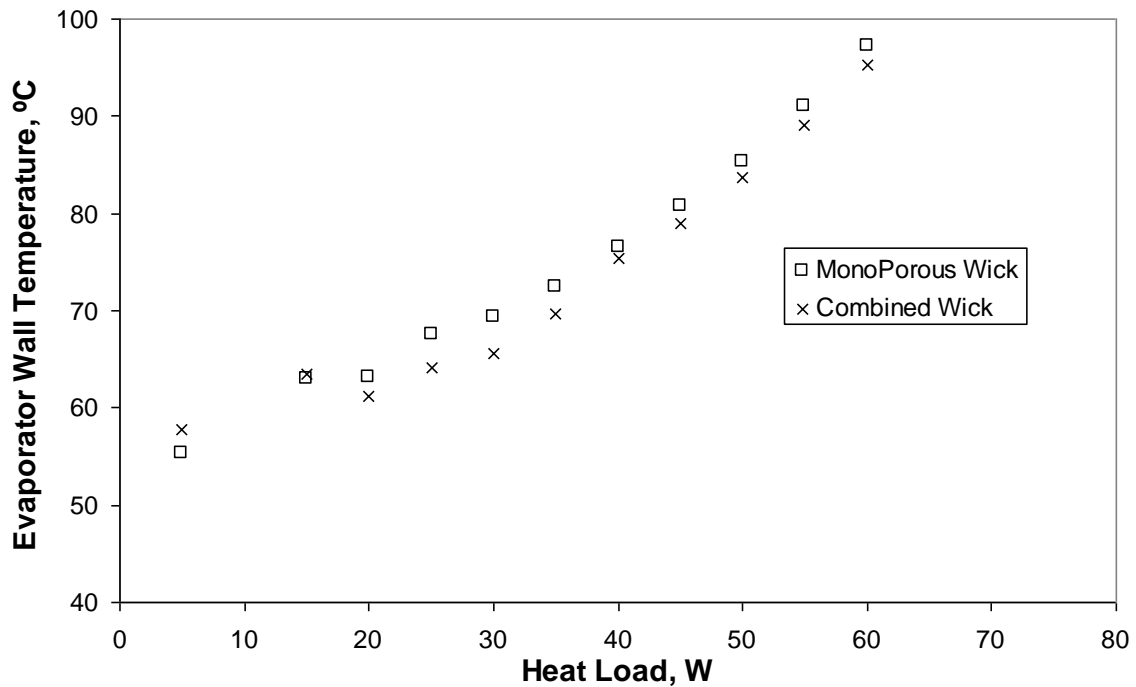


Figure 5.32 Heat load dependence of the evaporator wall temperature for mLHP with monoporous and combined wicks

A different situation arises with a biporous capillary structure where, due to the presence of two characteristic pore sizes, the value of superheat at which one can observe liquid boiling in large pores is smaller than in monoporous wicks. Therefore in the bi-dispersed wick portion heat transfer is enhanced in the nucleate boiling regime by the increasing surface area from which thin film evaporation can take place. The wick also allows the liquid and vapour phases to have separate flow paths, the liquid through the small pores and the vapour through the large pores. Unlike the monoporous wick, this helps to avoid any vapour blanket formation at the heating wall due to desiccation of the pores at high heat fluxes which can introduce additional thermal resistance.

5.9 Effect of Non Condensable Gases on mLHP Thermal Performance

For a mLHP to perform effectively over its life, it is very important to evaluate the potential for non condensable gas (NCG) generation inside the system and its effect on the thermal performance. Numerous experimental investigations conducted on conventional heat pipes have shown that two-phase systems are always vulnerable to some NCG formation over time. Since the materials used in the construction of LHPs are similar to those used for conventional heat pipes like copper-water, aluminum-ammonia, stainless steel-ammonia, loop systems are also susceptible to NCG production.

NCG can be generated in the LHP for various reasons. The most common causes of the NCG formation are those arising due to cleaning issues, and chemical compatibility issues between the working fluid and the loop and wick materials. The working fluid should be chemically compatible with the loop containment and the wick materials. Cleanliness of the working fluid, envelope and wick should be given due consideration while preparing a mLHP for testing. Scientific grade materials and working fluid are used in the loop but impurities from the fabrication and cleaning process can give rise to NCG during loop operation. Although very rare, another potential gas generation mechanism is the breakdown of the heat pipe working fluid. This can occur due to the dissimilar electrolytic potentials of the container and wick material or as a result of induced ionizing radiation from a source.

As part of this investigation, different methods were devised to detect the formation of NCG inside a mLHP. Sensitivity of the mLHP to NCG was tested by comparing its thermal

performance with and without NCG generation. Also, the effect of NCG on the start up and the steady state operation of the loop are presented. For flushing NCG out of the system, appropriate design modification was done to the mLHP. In addition, some of the methods to prevent the formation of the NCG inside the system are also discussed. The effects of NCG on the performance of an mLHP will depend on the location of the gas accumulation. It is likely that the NCG, once formed, may collect at a stagnation zone in the loop which includes the compensation chamber and the condenser. It can be absorbed and circulate with the working fluid around the loop. Furthermore, it can also be absorbed by the mLHP envelope or the wick. In reality, it is expected that all of the above factors contribute to the storage of the generated gas. Any gas that is released in the evaporator is swept to the mLHP condenser by the vapour. In the condenser the vapour will condense but the gas will not. Gas bubbles may be encapsulated by the condensate liquid and moved towards the evaporator where they are collected in the compensation chamber. In other cases, depending on the condenser design, if these gas bubbles are not encapsulated by the condensate and stay at a stagnation point inside the condenser, it is still likely that the gas will be transported back to the evaporator. The temperature in the gas blocked region of the condenser will be lower than the local saturation temperature. Since the total pressure in the condenser is nearly equal to the saturation pressure in the evaporator, the pressure difference between the evaporator and condenser made up by the partial pressure of the gas in the condenser drives the NCG back into the solution. As the liquid returns to the evaporator, the rise in the enthalpy of the liquid tends to liberate the dissolved gas. If the gas is liberated before passing through the wick it will be retained in the compensation chamber otherwise if the gas is released in the evaporator it will be swept away by the vapour back to the condenser and the process repeated (Nikitkin et al, 1998)

In the current design of mLHP, the condenser was made from a smooth walled copper tube with total length of only 50 mm. Due to the absence of any stagnation points inside the condenser, the probability of the gas being retained in the condenser is much reduced. The NCG study on the loop was done by choosing a copper wick along with the copper envelope and water as the working fluid. It should be noted that copper-water is the best known combination in two-phase systems with very strong chemical compatibility. Conservatively, it can be assumed that the gas/metal reaction does not occur and eventually all the gas ends up

in the compensation chamber. In the experiment, potential for NCG formation was created by skipping the water degassing procedure as explained in the section 4.3. It should be noted that the other cleaning and charging procedures were followed as elaborated in the previous chapter.

5.9.1 NCG Detection

To detect the generation of any NCG inside the mLHP, an absolute pressure transducer was installed in the compensation chamber. It is expected that formation of the NCG would result in the increase in absolute pressure inside the mLHP for the same constant ambient temperature maintained in the room during the course of the test period. As the compensation chamber is the most likely location for the accumulation of NCG generated throughout the mLHP, five T-Type thermocouples were fixed to the outer surface of the compensation chamber to sense NCG from the surface temperature profile. Testing was done in the horizontal configuration to avoid any buoyancy effects.

5.9.2 Effect of the NCG on the Steady State Performance of a mLHP

The mLHP was tested on a daily basis over a period of time for the same range of heat loads while the ambient temperature was kept constant. Figure 5.33 presents the results of the experiment as heat load dependence on the evaporator surface temperature. The graph clearly indicates trend of rise in operating temperature of the mLHP. This is predominately due to the production of NCG in the loop as was confirmed from the absolute vacuum readings given by the pressure transducer as in Figure 5.34. The readings from the absolute pressure transducer were recorded every time before operating the mLHP for the same constant surrounding conditions and showed a continuous increase due to the formation of gas with time. It is interesting to note from the transducer readings shown in Figure 5.34 that the generation of NCG was greater for the first few days after which it slowed down or practically ceased. Figure 5.33 also supports this argument where it is clear from the operating temperature trend of the mLHP which showed an initial increase for 2-3 days and then stayed constant with time. In Figure 5.33, the temperature trend for the “Days 1, 2 and 3” shows a clear contrast where as for the “Days 3 and 6” is quite close. It can be inferred from these outcomes that the majority of NCG formation occurred in the initial test runs of the mLHP.

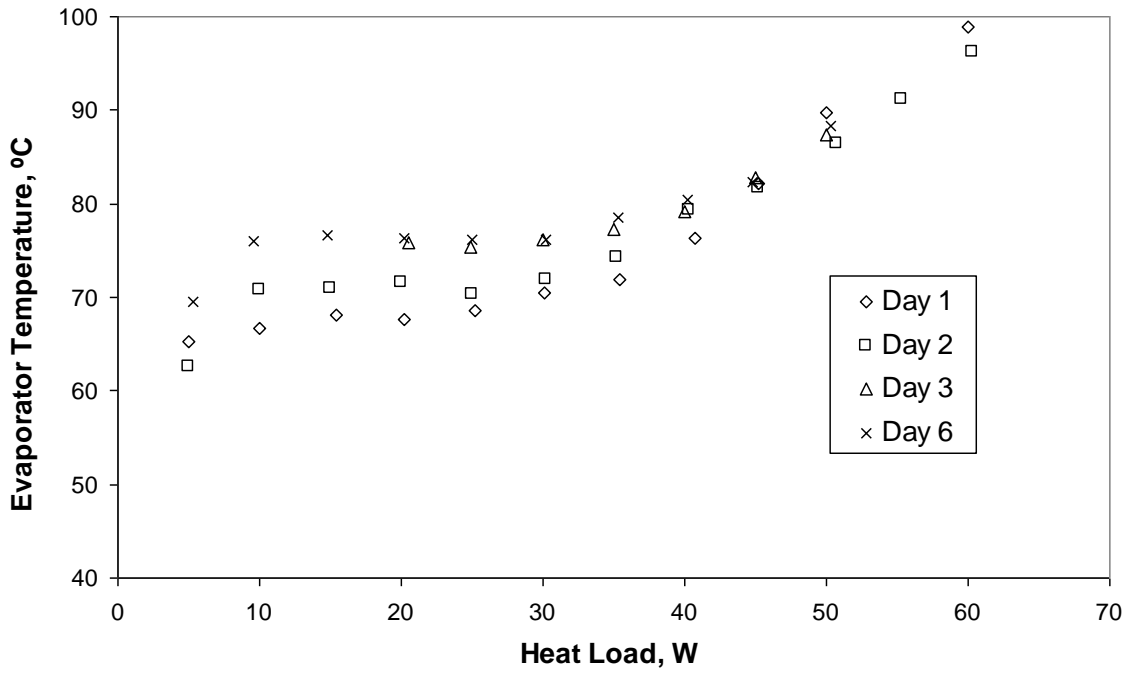


Figure 5.33 Evaporator temperature trend with respect to the applied heat load for the number of trial runs made on the mLHP over a period of time

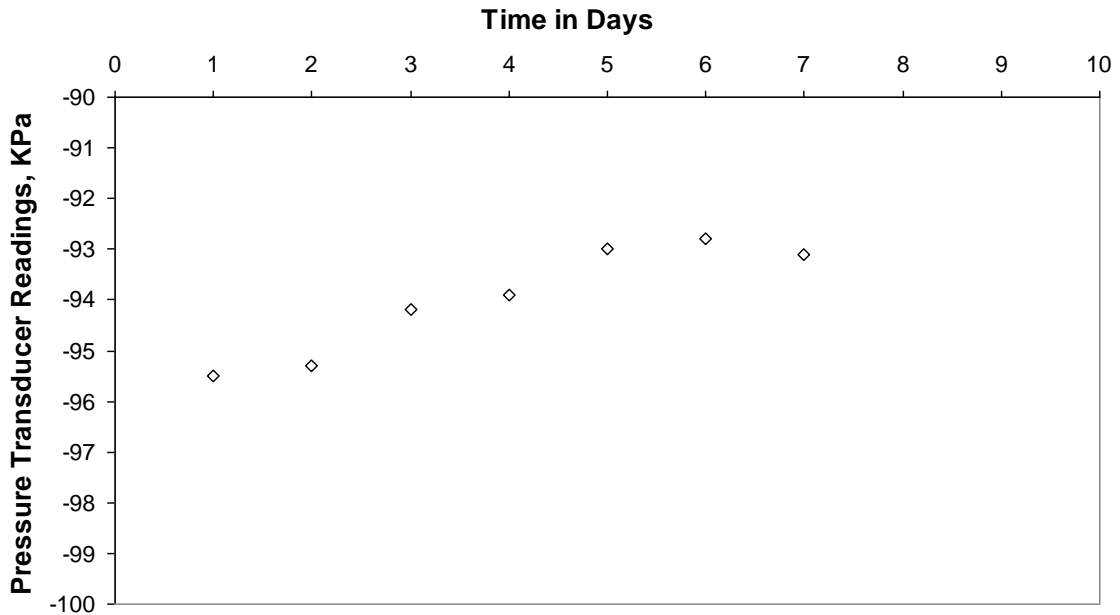


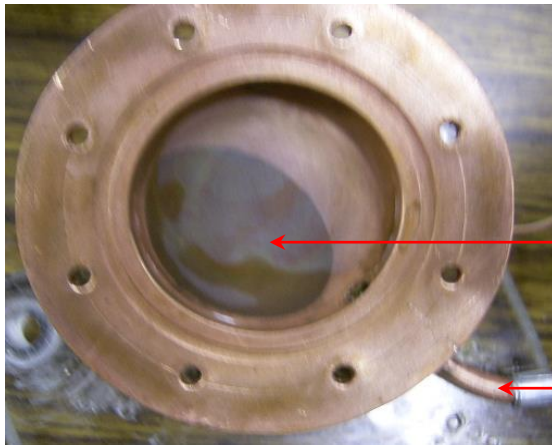
Figure 5.34 Change in the absolute pressure inside the loop due to generation of NCG over a period of time.

The operating temperature of the loop is very much controlled by the temperature of the compensation chamber. From Figure 5.33, it is also clear that the gas accumulates in the compensation chamber which is evident due to the increase in the operating temperature of the mLHP with time.

The compensation chamber temperature is mainly influenced by three heat exchange processes: i.e. heat exchange between: the compensation chamber and evaporator, the compensation chamber and incoming liquid from the condenser, and the compensation chamber and the environment. As gas is accumulated inside the compensation chamber, its partial pressure increases the overall pressure inside the chamber which in turn results in increase of vapour pressure. With the increase in the vapour pressure, heat flow from the evaporator to the compensation chamber and thus its temperature also increase. Since the saturation conditions on the two sides of the wick i.e. evaporating and absorbing faces are related to each other, the increase in the compensation chamber temperature results in a corresponding rise in the operating temperature of the mLHP.

Note that the effect of NCG is more pronounced at low heat loads. This is due to the fact that at high heat loads heat exchange between the compensation chamber and the incoming liquid from the condenser dominates the energy balance in the compensation chamber owing to the increase in the flow rate of the incoming liquid. In this case the additional heat input raises the liquid enthalpy rather than increasing the compensation chamber temperature. Beside this, the increase in pressure inside the loop at high heat loads can also drive the gas, present in the compensation chamber, back into the working fluid which can account for the less profound effect of the NCG at high power. Also, at low heat loads, the quantity of the liquid inside the compensation chamber is less and therefore the NCG or the vapour bubbles present inside the chamber can cover some portion of the absorbing face of the wick which can decrease the filtered quantity of the liquid through the wick and therefore increase the operating temperature of the mLHP. As the power increases, the NCG gas is pushed away to one end of the compensation chamber under the impact of the incoming flow and consequently makes the wick absorbing face more accessible to the incoming liquid. This reasoning was confirmed from the post-operation inspection of the mLHP (Figure 5.35) which clearly shows

the oxidized portion on the inside wall of the compensation chamber as well as on the absorbing face of the wick due to the gas absorbed at these locations. The oxidized portion of the compensation chamber wall is present on one side due to the impact of the incoming flow from the opposite end. The temperature profile on the compensation chamber wall taken with the help of five thermocouples and presented in Figure 5.36 also confirms the accumulation of a major quantity of NCG into the compensation chamber. It is seen from the plot that the temperature trend shown by the No.5 thermocouple is higher than those shown by No. 1 to 4 thermocouples. This is due to the presence of the NCG on the portion of the wall on which probes 1 to 4 were installed which lowers their temperature by a certain amount (in this case approximately by 1°C) than probe No. 5 where there is no NCG.



Oxidised portion of the compensation chamber wall due to NCG accumulation inside it

Compensation chamber inlet

Oxidation of the absorbing face of the wick due to NCG accumulation inside compensation chamber

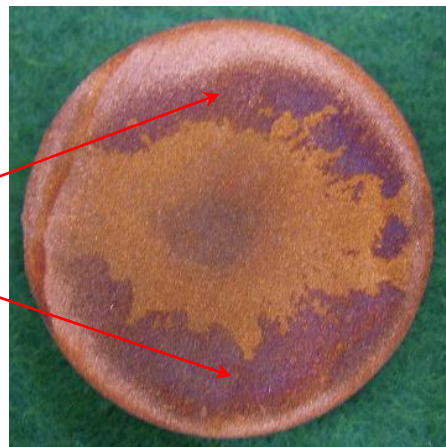


Figure 5.35 Oxidation of the container and wick material due to the reaction and absorption of the NCG gas accumulated inside the compensation chamber

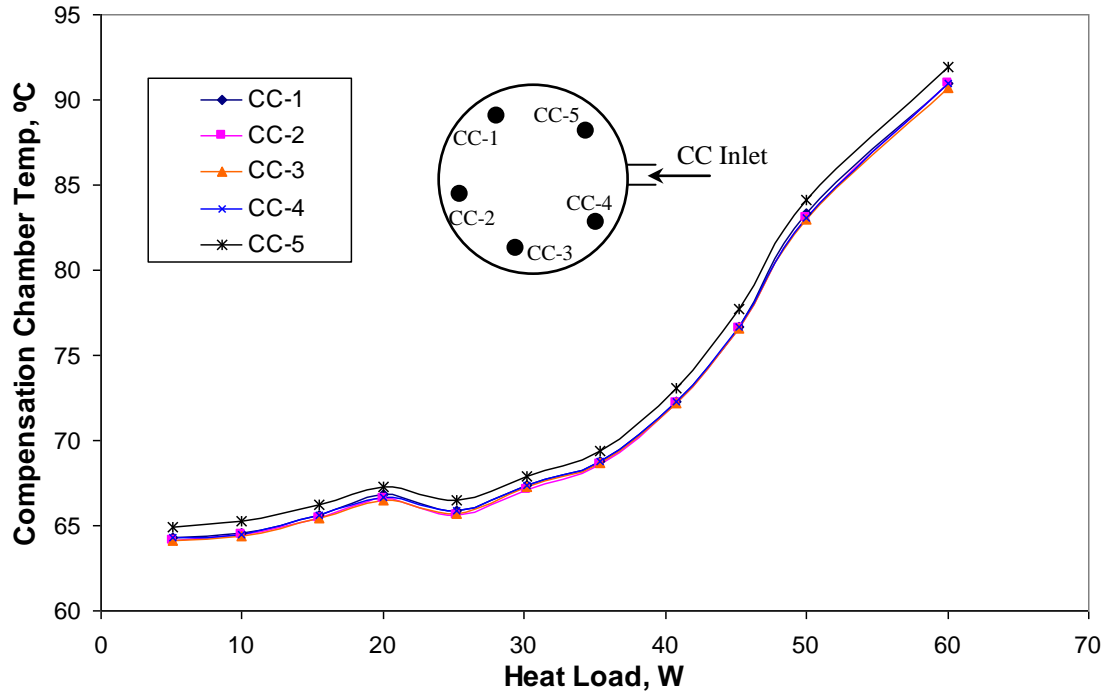


Figure 5.36 Temperature profile on the surface of the compensation chamber taken with the help of five T-Type thermocouples

5.9.3 Effect of the NCG on the Start-up Process

There was some notable increase in the startup time when the performance of the mLHP was evaluated at the end of the test period. In the Figure 5.37, the start up process for the mLHP after charging and at the end of the test period (i.e. 7 days) is depicted. Here, the startup is assumed to occur with the initiation of fluid circulation as is indicated by the increase in the temperature of the vapour line and decrease in the temperature at the compensation chamber inlet. It should be noted that the increase in startup time was only noticeable towards the end of the test period i.e. when the mLHP has presumably its maximum inventory of the gas as validated by the pressure transducer readings. This increase in startup time and operating temperature of the mLHP, as is evident from the Figure 5.37, is related to the presence of the NCG inside the compensation chamber which produced the rise in the overall pressure inside the loop because of the partial pressure exerted by the gas. As some minimum pressure and thus temperature difference are required across the wick faces to start the fluid circulation, gas present in the compensation chamber increases this difference due to its own partial pressure and hence the time to achieve this difference.

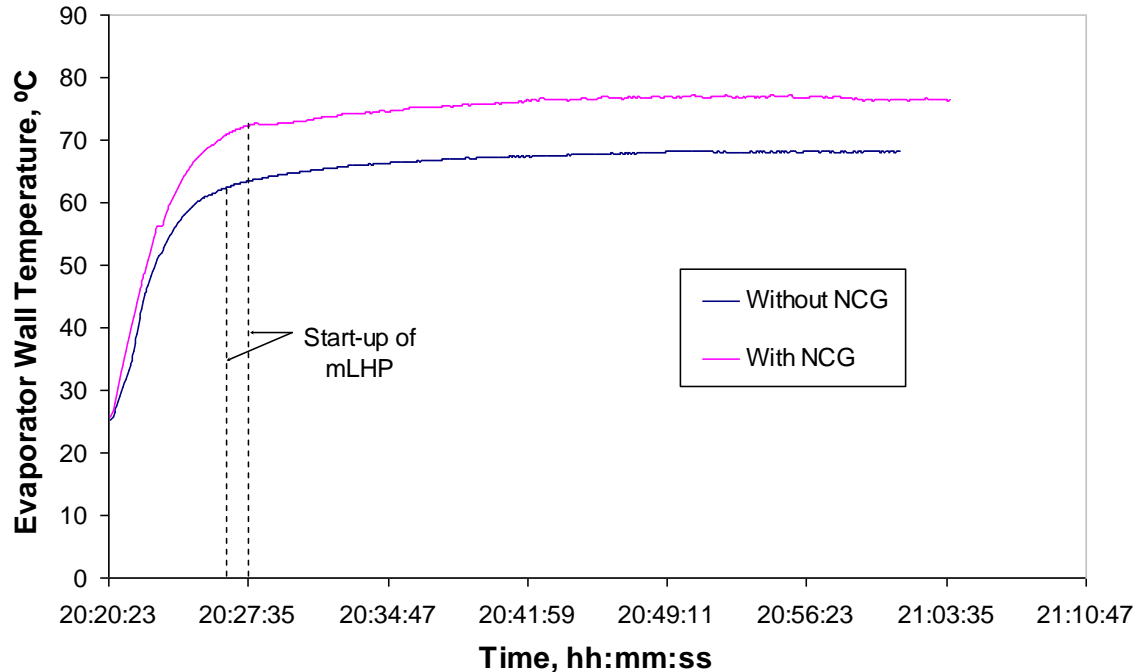


Figure 5.37 Startup trend shown by the mLHP with and without NCG

5.9.4 Purging of NCG from a mLHP

As the generation of some NCG inside the two-phase systems is unavoidable, design arrangement for the flushing out of the NCG from the system should be made. From the above experiment, it can be deduced that the major inventory of NCG is formed during initial testing of the mLHP. Two methods can be used for purging the NCG from the mLHP. In the first method, mLHP is charged with extra working fluid inventory and it is heated in a furnace at 150 °C for 2-3 hours. During this period most of the NCG is generated as a result of left over traces of the cleaning agent and reaction between the loop material and working fluid. The resultant gas is flushed out of the charging line by tilting the mLHP such that most of the gas accumulates in the compensation chamber near the charging line due to buoyancy. While performing the purging operation, care must be taken that only the extra charge escapes the system. For this, mLHP is weighed constantly to keep the required charge inside the loop. This method also helps to clean the wick structure due to the high pressure under which the liquid-vapour mixture escapes from the loop.

In the experiments described, it was not possible to apply this method as EPDM rubber packing was used to seal the system which has a permissible temperature limit of $100\pm 5^\circ\text{C}$.

Beside this, time permitted for the generation of the NCG was very short which can lead to consequences of additional gas generation during the working life of the system. In order to cope with these problems, another method for purging NCG from the designed mLHP was used. Figure 5.38 depicts the design arrangement that comprises of a purging line that is installed in the center of the circular face of the compensation chamber. The purging line was connected to a vacuum pump through two purge valves and one three way valve. For flushing out a certain fixed quantity of fluid (gas + vapour + liquid) from the compensation chamber, first vacuum is established in the line between the two purge valves. To do so valve A is kept closed, while valve B is open and port X is connected to port Y for the three way valve. Next, valves B and C are closed and valve A is slowly opened. NCG will be flushed out from the loop into the purge line. Valve A is closed and valve B is opened to allow the escape of gas by suction from the pump. At the end of the procedure, valve B is also closed. To avoid over flushing of fluid during purging the mLHP is charged with 1-2 cc extra inventory of working fluid. Figure 5.39 shows the experimental set up for purging NCG from the mLHP system.

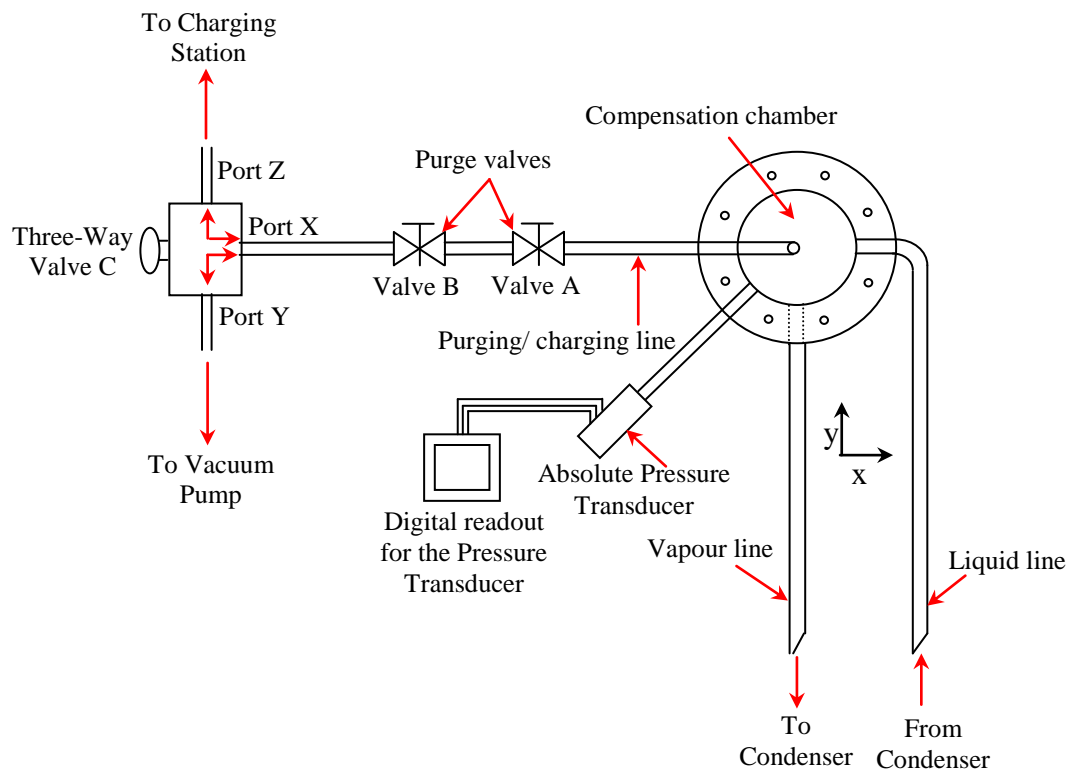


Figure 5.38 Design arrangement for purging the NCG from the mLHP system

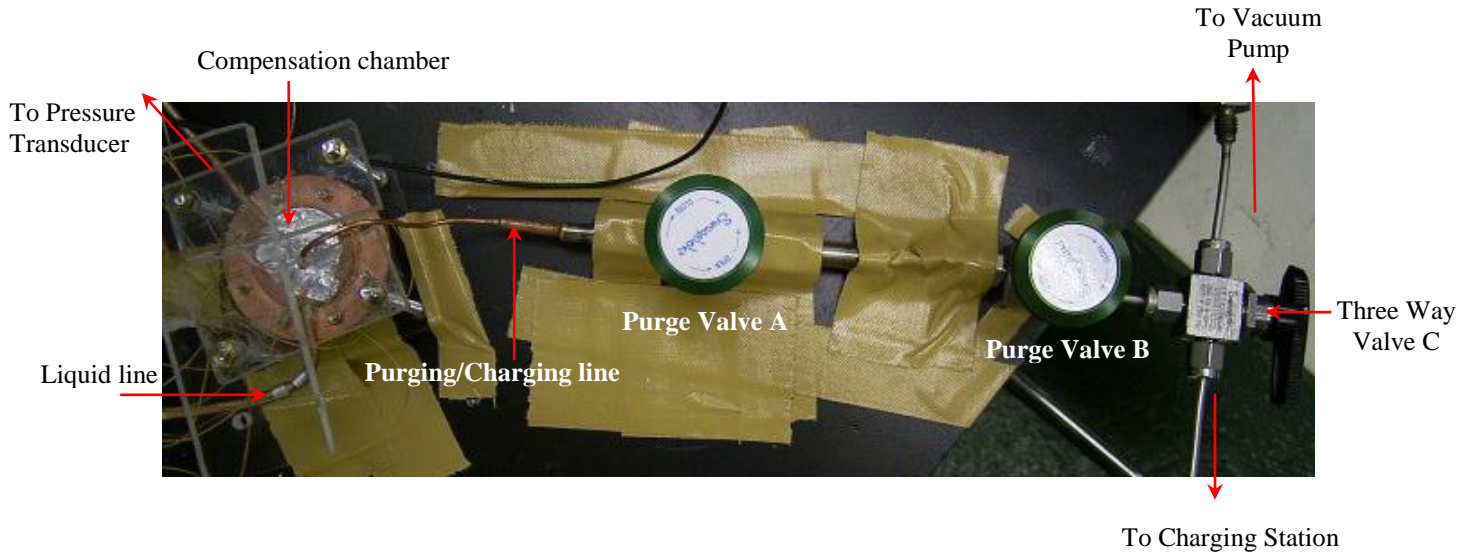


Figure 5.39 Experimental Set-up for purging the NCG from the mLHP system

In Figure 5.40, results of the purging operation performed on the mLHP at the end of the NCG test cycle are presented. The mLHP was tested for NCG generation trend over a period of time as discussed above. At the end of the test duration, the purging process was performed on the system. It is evident from the test results that the designed purging procedure was able to restore the operational characteristics of the mLHP to normal. The results also confirm that the degradation in performance of the mLHP over the test period was due to NCG formation.

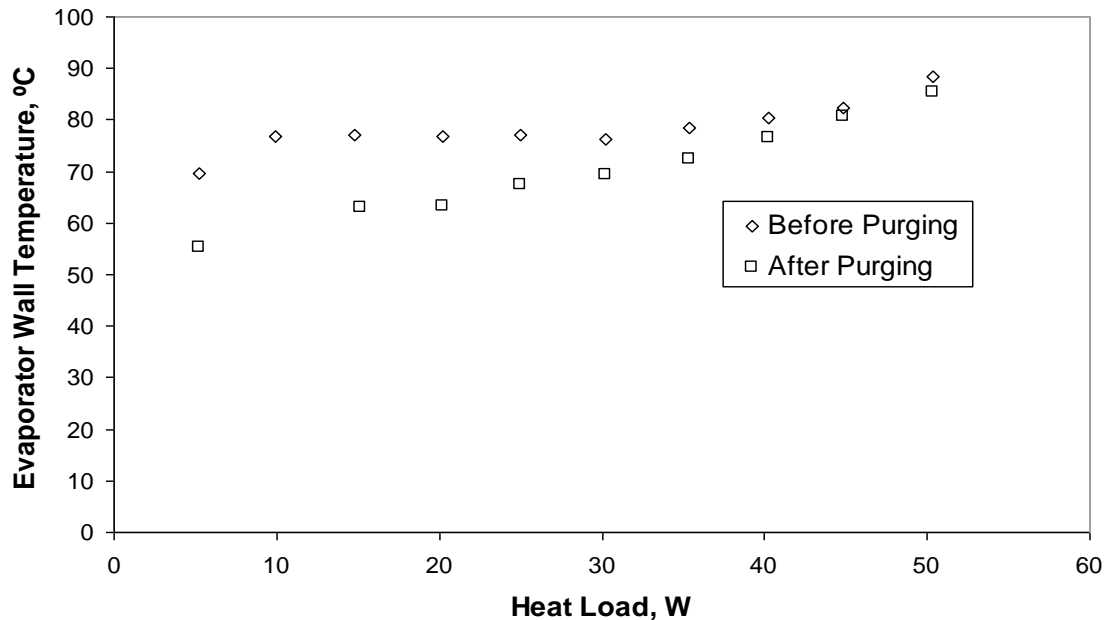


Figure 5.40 Operational Characteristics of the mLHP before and after purging procedure

5.9.5 Methods to Decrease NCG Generation inside a mLHP

An attempt was made to decrease NCG generation inside the mLHP by improving the cleaning process and the fluid charging procedure. In the previous NCG testing, the working fluid was charged into the mLHP without performing any additional purification procedure on it. It is expected that at atmospheric pressure, non condensable gases from the surrounding air are dissolved in the working fluid. As the working fluid is charged into the mLHP, these dissolved gases are released because of the vacuum conditions inside the loop. In order to avoid the intrusion of these gases into the mLHP a degassing procedure on the working fluid before charging is necessary. For degassing liquid water, the charging cylinder is connected to the vacuum pump as explained in section 4.3 on the charging procedure. As the vacuum conditions are maintained above the liquid surface, the dissolved gases are released from the liquid thereby degassing the working fluid. It is very desirable that the amount of working fluid present in the charging cylinder is slightly higher than necessary (approximately 10% more) to account for evaporation inside the cylinder. Figure 5.41 shows results from experimenting on the mLHP with and without using degassed working fluid. It is clear from the outcomes of the testing that the degassing procedure prior to the charging of the working fluid into the mLHP decreases the extent of NCG generation in the system.

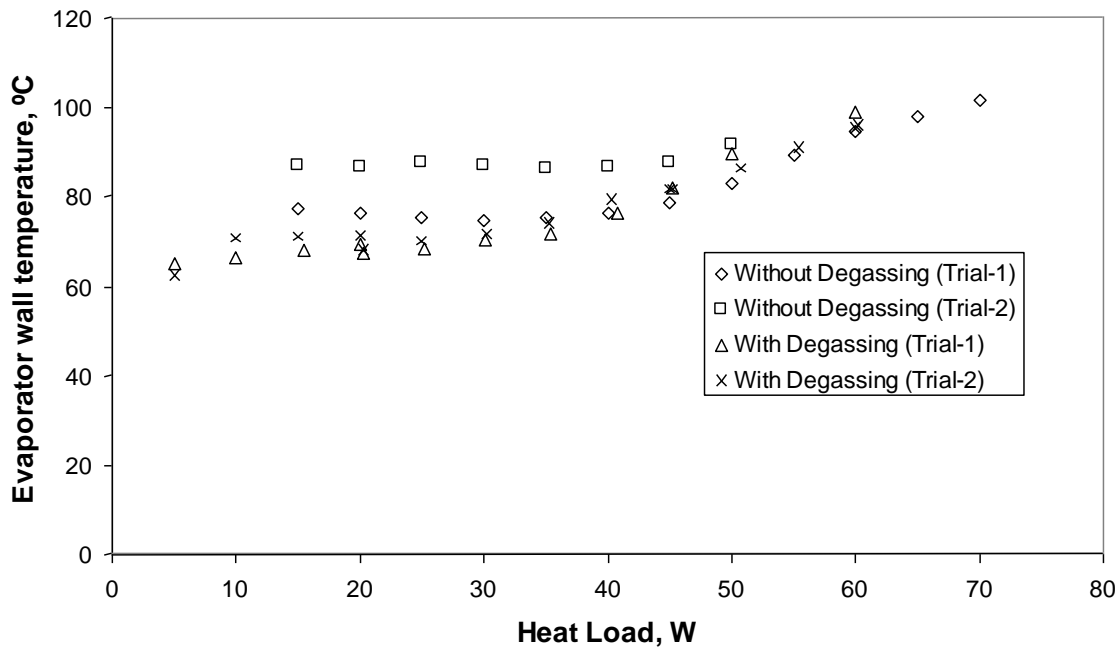


Figure 5.41 Operational Characteristics of the mLHP before and after degassing procedure

It should be noted that the majority of the gas generated inside the two phase system arises from the reaction between the working fluid and the container and wick materials. Therefore, a proper cleaning procedure as explained in section 4.3 should be performed on a mLHP before assembling it for testing. In all of the test results for the mLHP presented, thorough cleaning and charging procedures were strictly followed. It was only in the NCG analysis study that the exhaustive cleaning procedure was not carried out in order to generate the performance trend of the mLHP under the effect of NCGs. It has been established from the experimental studies that unlike conventional heat pipes, mLHPs are not very sensitive to NCG formation inside the system. This is attributed to the inbuilt geometry of the compensation chamber which can contain most of the NCG produced during the operation cycle and thus enable the evaporator to function reliably although with some performance degradation.

Summary

The results of the tests can be summarised as follows:

- The miniature prototype of the LHP with flat disk shaped evaporator has proved to be a very versatile and promising device for thermal control of microprocessors with a high power density and a relatively small thermal footprint. With the current model, heat flux as high as 70 W/cm^2 was successfully removed from a thermal test system and transferred to a remote heat exchanger over a distance of 150 mm. This has helped to validate the feasibility of the LHP concept at miniature scale as a reliable thermal control technology for the next generation high end microprocessors.
- The theoretical model that was designed on the basis of energy balances inside the loop predicted the loop operating temperature very well and within the uncertainties imposed by the modelling assumptions.
- The start up of the mLHP was very reliable over the wide range of heat load applied to the evaporator active zone.
- It was established experimentally that a mLHP can operate satisfactorily within a wide range of working fluid charge quantities.

- The designed mLHP can be used as an effective thermal control technology for transferring heat at different orientations in the gravity field with some loss of performance compared to horizontal operation.
- mLHPs with the current design of evaporator can be used effectively for cooling microprocessors which involve local hot spots and irregular surface heating patterns depending on their data processing load.
- A capillary structure made from high conductivity material like copper can be used in a miniature LHP for thermal control of electronic equipments without any major performance degradation.
- The operational characteristics of a mLHP are largely dependent on the effective thermal conductivity of the wick when saturated with the working fluid and on the physical properties of the wick structure; the most important being pore size, porosity and permeability.
- The heat transfer characteristics of biporous wick structures (i.e. with two characterised pore radii) are better than monoporous wicks (i.e. those characterised by a single average pore radius).
- mLHPs are not very sensitive to the non-condensable gases which are generated inside the system because of impurities present inside the working fluid and the loop material.

In the next chapter, design and results of testing of an innovative model of a mLHP with a flat rectangular evaporator as thin as 5 mm is discussed.

Chapter 6

mLHP with Flat Rectangular Evaporator

In this chapter, the design and results from testing a miniature LHP with a flat rectangular evaporator are explained in detail. The mLHP with rectangular evaporator having thickness as small as 5 mm was designed. To achieve such a small thickness of evaporator, a new design concept is proposed that relocates the position of the compensation chamber from the thickness of the evaporator structure to its sides. The test setup and method to evaluate the performance of the designed mLHP are stated briefly. Thermal performance of the mLHP was studied with respect to the start up process and under steady state operation. Outcomes of the experiments are explained in detail. In the final section, a comparison of the rectangular evaporator mLHP is made with the previously discussed disk shaped evaporator mLHP.

6.1 Introduction

In the design of the heat transfer system for thermal control of compact electronic equipments like laptops a major restriction is imposed on the thickness of the evaporator. Particularly, in thermal management devices like loop heat pipes where the thickness of the evaporator as a rule includes the compensation chamber, the decrease in the evaporator thickness beyond certain minimum limit impairs the performance of the device. This limit is predominately dictated by the minimum thickness of the capillary structure that guarantees its intended functionalities as a thermal and hydraulic lock. In the previous study, a disk shaped evaporator with total thickness of 10 mm was designed that comprised 50% evaporator thickness and 50% compensation chamber thickness. In that case, an optimum design approach for the loop evaporator (i.e. vapour removal channel, wall thickness, compensation chamber volume etc) permitted wick thickness of not more than 3 mm. The device was able to perform efficiently and transfer a maximum of 70 W at a distance of 150 mm while maintaining the source temperature within the allowable limit of 100 ± 5 °C.

It is understood that in the previous design of the disk shaped evaporator mLHP, further decrease in evaporator thickness is only feasible with some possible loss of thermal

performance. This is because the heat locking feature of a wick with the smaller thickness is reduced and may result in increase of heat flow through the wick to the compensation chamber. As the heat exchange processes in the compensation chamber dictate the saturation conditions inside the loop, the aforesaid consequence results in the increase of the operating temperature. By decreasing the evaporator thickness at the expense of the vapour removal channel thickness, the flow resistance and thus the overall pressure losses inside the loop increase. If the overall pressure losses inside the loop exceed the maximum capillary head generated by the wick structure, the mLHP will fail to operate. Such a decrease is also not possible with the thinning of the evaporator wall as this may lead to deformation of the evaporator heating face under the attachment pressure between the evaporator and source face which is required for efficient heat acquisition from the heat source. Any attempt to reduce the compensation chamber thickness will reduce the fluid accumulating capability of the chamber which may result in poor priming of the wick prior to start-up. In addition, the potential for bubble formation inside a compensation chamber of limited thickness may produce flow blockage and consequently flow instabilities inside the loop. It is seen that numerous performance issues are linked to down scaling of the evaporator thickness some of which are discussed above. However, for the proper promotion of the loop system in cooling compact and high end electronic equipment, miniaturization with respect to the evaporator thickness is necessary.

The present study was conducted with the objective of designing and testing a miniature LHP with evaporator thickness as low as 5 mm. It should be noted that such a design of mLHP with low thickness can be successfully implemented inside the limited available space of the laptop PC and thus has more prospects for notebook thermal control compared with the disk shaped mLHP model with a total thickness of 10 mm. The rectangular flat evaporator mLHP with 5 mm thickness was designed to transfer the heat load over a distance of up to 150 mm.

6.2 Description of the mLHP Prototype

The schematic of the miniature LHP, as in Figure 6.1, shows a flat rectangular evaporator and a fin-and-tube condenser which are connected by separate vapour and liquid lines. The mLHP

body and the transport lines were made of copper. Each component of the mLHP is explained in detail in the following sections.

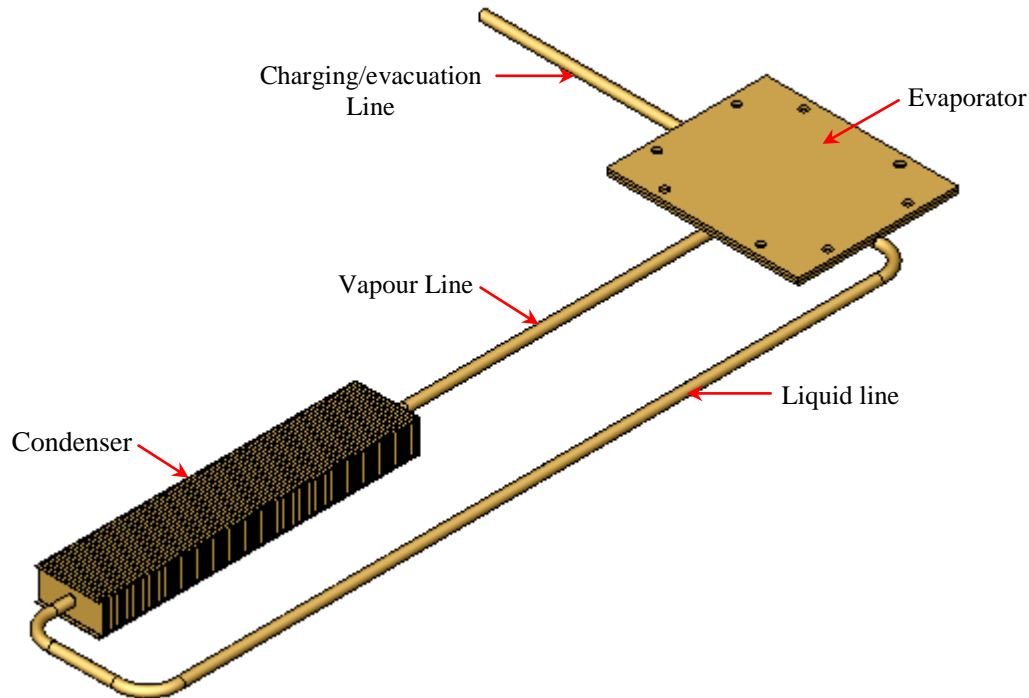


Figure 6.1 Schematic of Flat Rectangular Evaporator mLHP showing the components

The mLHP evaporator is rectangular in shape and consists of a vapour removal channel, wick structure and integrated compensation chamber. The overall dimensions of the evaporator including the sealing flanges were 50×60 mm. The design structure of the evaporator can be well understood from its exploded view as shown in Figure 6.2 which shows the top cover plate of the evaporator, the wick structure, evaporator body and the heat acquisition or active region. The evaporator body basically comprise the evaporator region where the microchannel or heat acquisition portion is placed, and the distributed compensation chamber region. The heat acquisition portion is the evaporator active zone that is made up of the system of vapour removal channels (i.e. microchannels) and the capillary structure. It is to be noted that due to the integration of the evaporator and compensation chamber in one body, the term evaporator is used for the reference to the complete body.

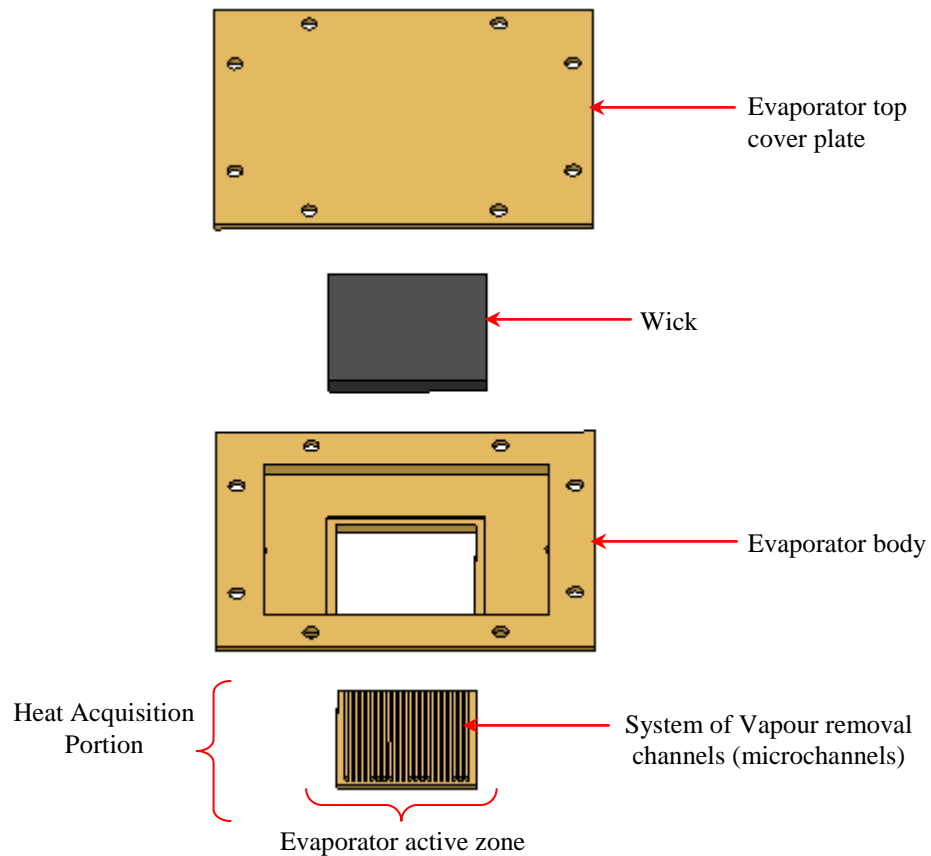


Figure 6.2 Exploded view of the capillary evaporator showing the parts

In order to achieve thickness of 5 mm for the capillary evaporator, the compensation chamber was relocated from the thickness of the evaporator to its sides. As presented in the cross sectional view of the capillary evaporator in Figure 6.3, the evaporator section and the compensation chamber are coplanar with each other. The compensation chamber lies in the same plane as the wick structure with access to three sides of the wick as fluid absorbing faces. Figure 6.4 illustrates the evaporator plan view. The vapour removal channels are located towards the middle of the evaporator body structure and cover an active area of 22×22 mm. It should be noted that the vapour channels are in the same plane as the evaporator wall. The heat acquisition portion or the evaporator active area is represented by these systems of vapour removal passages.

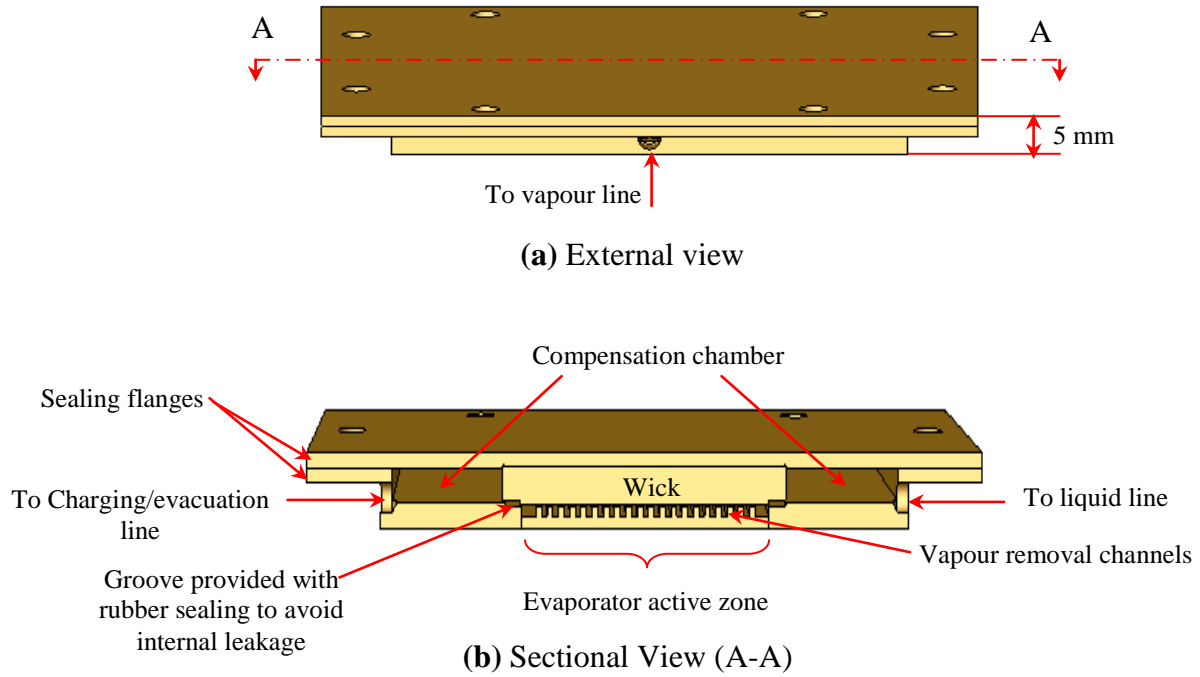


Figure 6.3 mLHP Evaporator

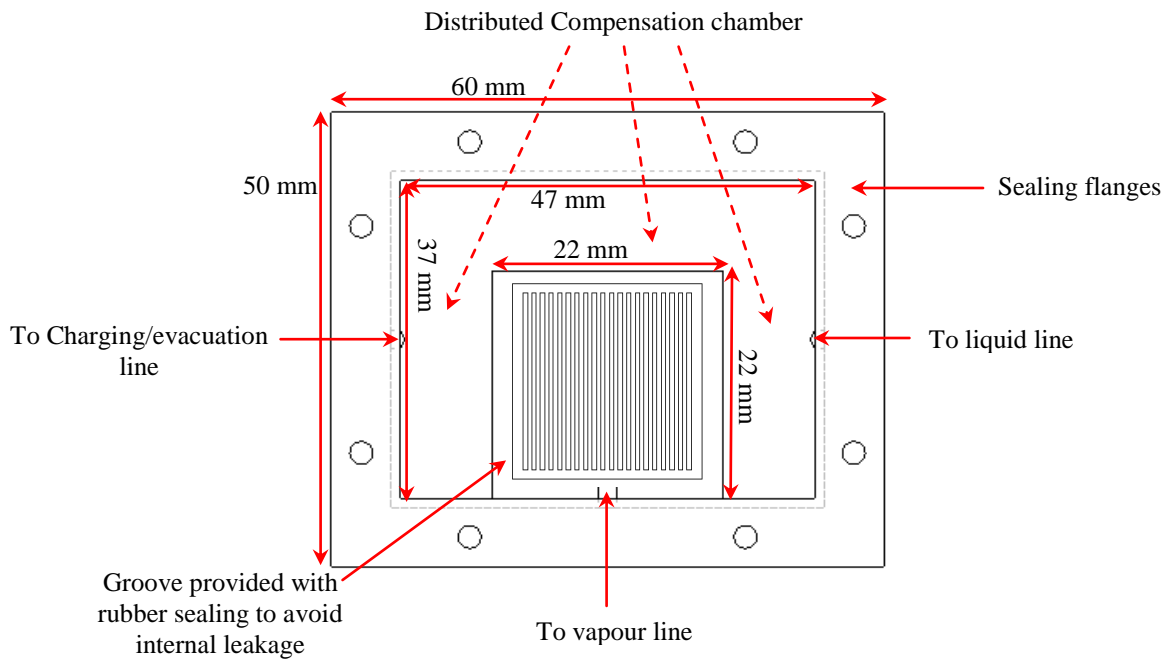


Figure 6.4 Plan view of the evaporator body

The vapour line, 150 mm in length and 2 mm internal diameter, is connected to the active zone of the evaporator and was aligned with the system of vapour removal channels. Beside this, the liquid line with the total length of 290 mm length and 2 mm ID is linked to the compensation chamber. Charging and evacuation of the loop were done with the use of a 100 mm tube also connected to the compensation chamber.

The present architecture of the mLHP evaporator needs special consideration to prevent internal leaks of vapour from the evaporation zone to the compensation chamber. For this reason, a small groove was machined around the evaporator zone as shown in Figures 6.3 & 6.4, and EPDM sheet was provided inside it that helped to seal the gap between the wick and the evaporator inner wall. An EPDM packing is also provided between the sealing flanges for making the system leak-proof against any external leaks.

The evaporator active zone is flat in shape with an area of 22x22 mm. In contrast to the disk shaped mLHP design, the evaporation zone is square shaped and provided with 20 micro vapour removal passages with rectangular cross-section of 0.7 mm depth and 0.5 mm width (Figure 6.5).

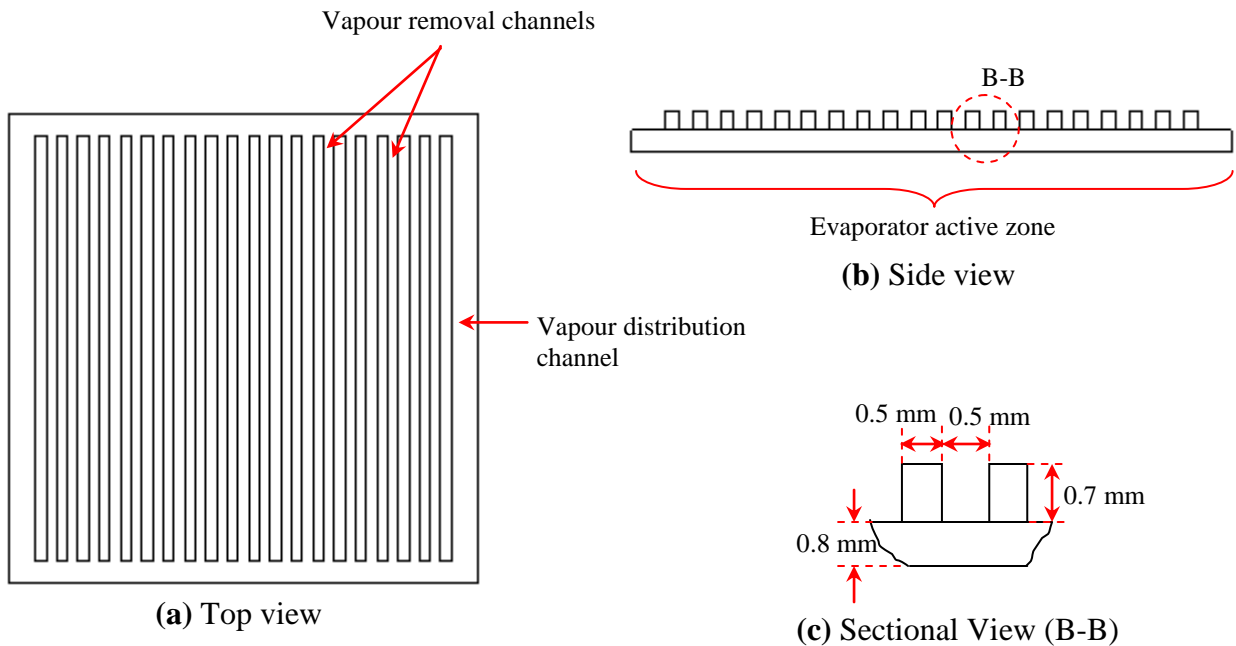


Figure 6.5 Details of vapour removal channels

The wick structure covers all the vapour channels and extends a little further beyond it to provide proper internal sealing with the help of the EPDM packing. A small pad of EPDM rubber was also used on the top face of the wick in order to press the wick against the channel fins for better thermal contact and to provide insulation between the evaporator top plate and the wick structure.

The volume of the compensation chamber was approximately equal to the total volume of the loop so that it should be able to accommodate most of the fluid inventory that is displaced from the evaporator grooves, vapour line and part of condenser during startup of the mLHP.

For the rejection of the latent heat transferred from the evaporator to the surroundings, a fin-and-tube condenser as shown in Figure 6.6 was provided at the exit of the vapour line. The condenser was 50 mm in length and 10 mm high in Z-direction. It was provided with external fins (Figure. 6.6 b & c) measuring 20x10 mm with a thickness of 0.2 mm. Copper fins were joined to the copper line (ID: 2mm, OD: 3 mm) using thermally conductive epoxy resin.

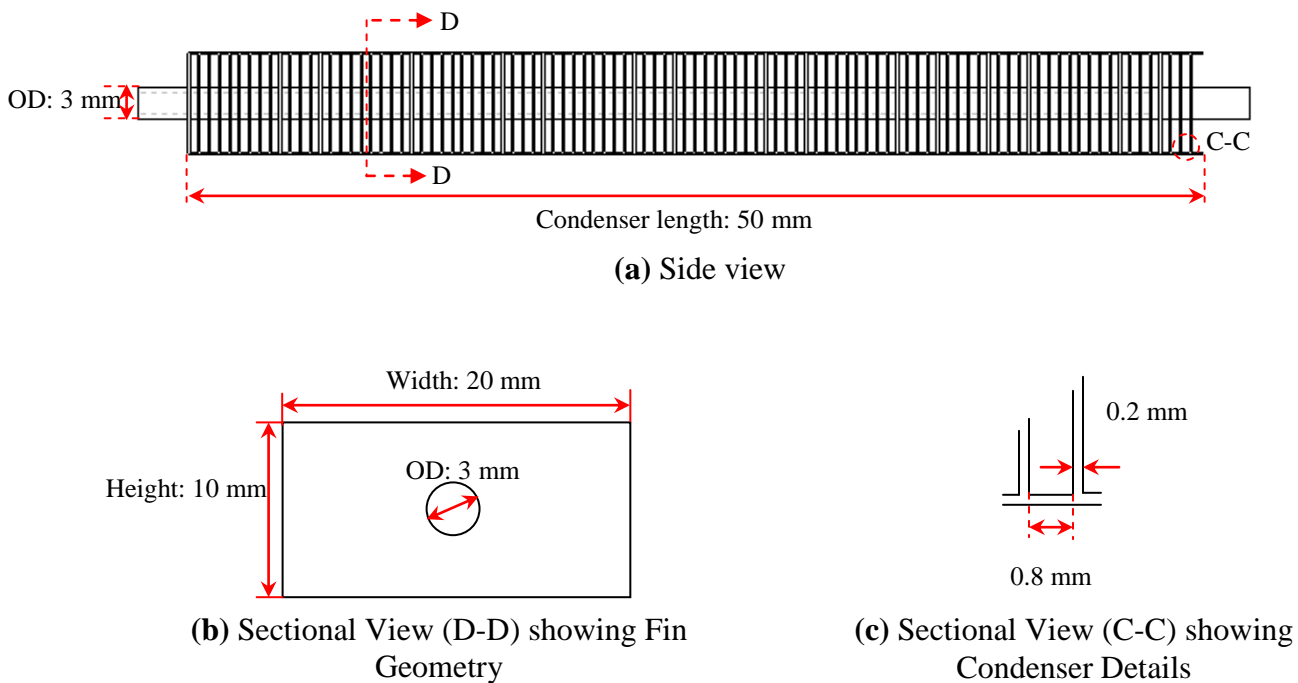


Figure 6.6 Details of Fin-and-Tube Condenser

6.3 Experimental Setup and Testing Method

The thermal characteristics of the mLHP with a rectangular evaporator were evaluated in the horizontal orientation by using a heat load simulator of 10×10 mm. The heater was in the form of a copper block with machined holes into which two cartridge heater were inserted. The condenser cooling was done by forced convection of ambient air with a temperature of $24 \pm 2^\circ\text{C}$ that was provided by an air cooling fan with volumetric flow rate of $0.1 \text{ m}^3/\text{min}$. The capillary structure was made by sintering nickel powder in order to perform the function of a passive pump to circulate the working fluid around the loop. The loop was charged with the optimum liquid inventory that guaranteed at least 50% working fluid in the compensation chamber for proper wetting of the wick structure at all the times. Thermal performance of the mLHP was studied in the range of heat load that assured a source temperature below $100 \pm 5^\circ\text{C}$. Input power was tuned using a digital power meter. Figure 6.7 shows the experimental set up including locations of temperature measurement points. T-type thermocouples with an accuracy of $\pm 0.5^\circ\text{C}$ were used to test the performance of the loop.

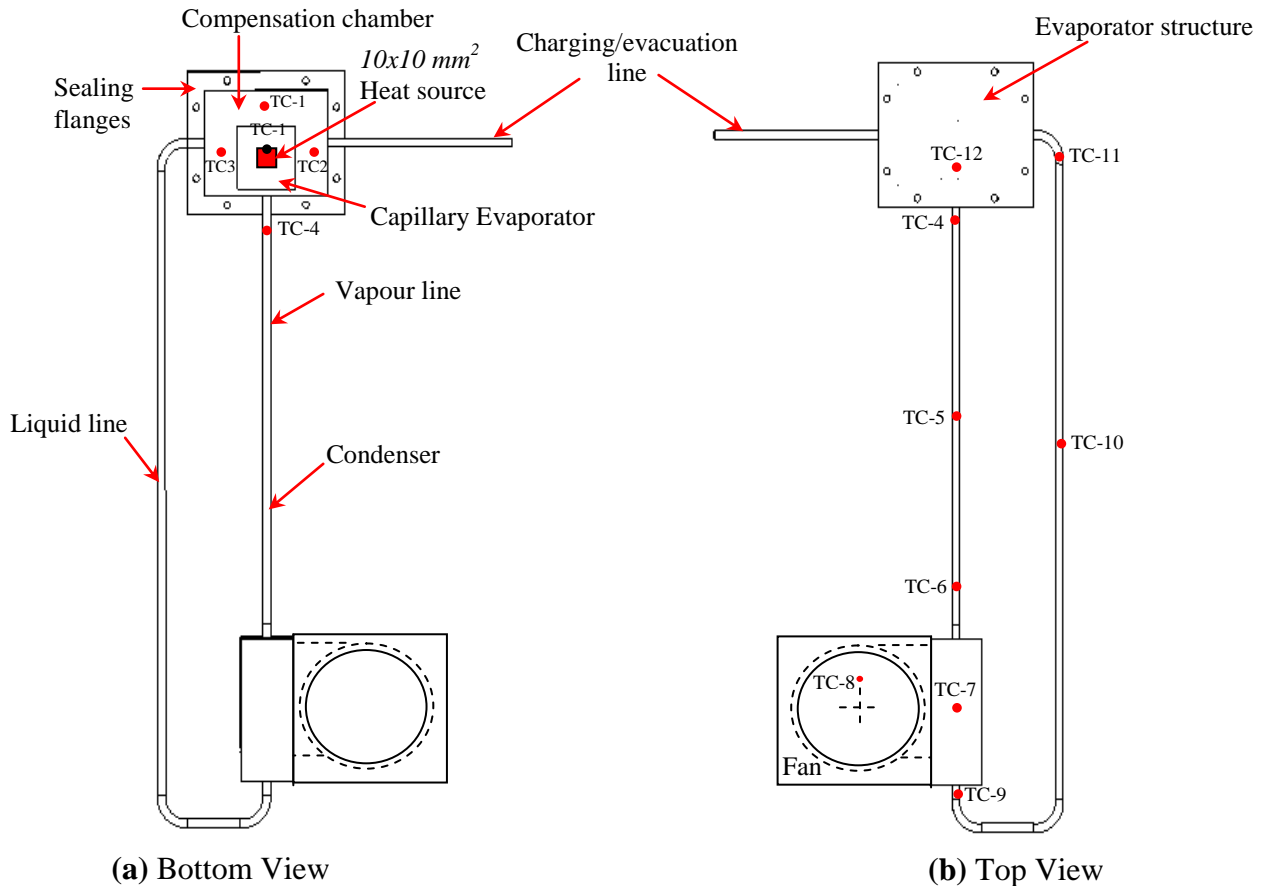


Figure 6.7 Experimental set up for testing the flat rectangular evaporator mLHP

The efficiency of the mLHP was measured on the basis of the evaporator temperature, maximum heat capacity, evaporator thermal resistance and total thermal resistance of the device.

6.4 Results and Discussion

Heat was applied to the active zone of the evaporator under a condition of non uniform heating using a heater with $10 \times 10 \text{ mm}^2$ heating face area. In this case, heating was applied to approximately 20% of the evaporator active zone. The device was tested to transfer heat up to a distance of 150 mm under the given mode of condenser cooling while operating in a horizontal configuration. For these tests, a sintered nickel wick was used as the capillary structure inside the evaporator and the loop was charged with 70-80% of its internal volume with water as working fluid.

6.4.1 Thermal Characteristics of the Flat Rectangular Evaporator mLHP

Figure 6.8 presents the start-up phenomena of the mLHP under 20 W input power. It is seen from the temperature trends that start-up of the mLHP is very reliable at these heat loads.

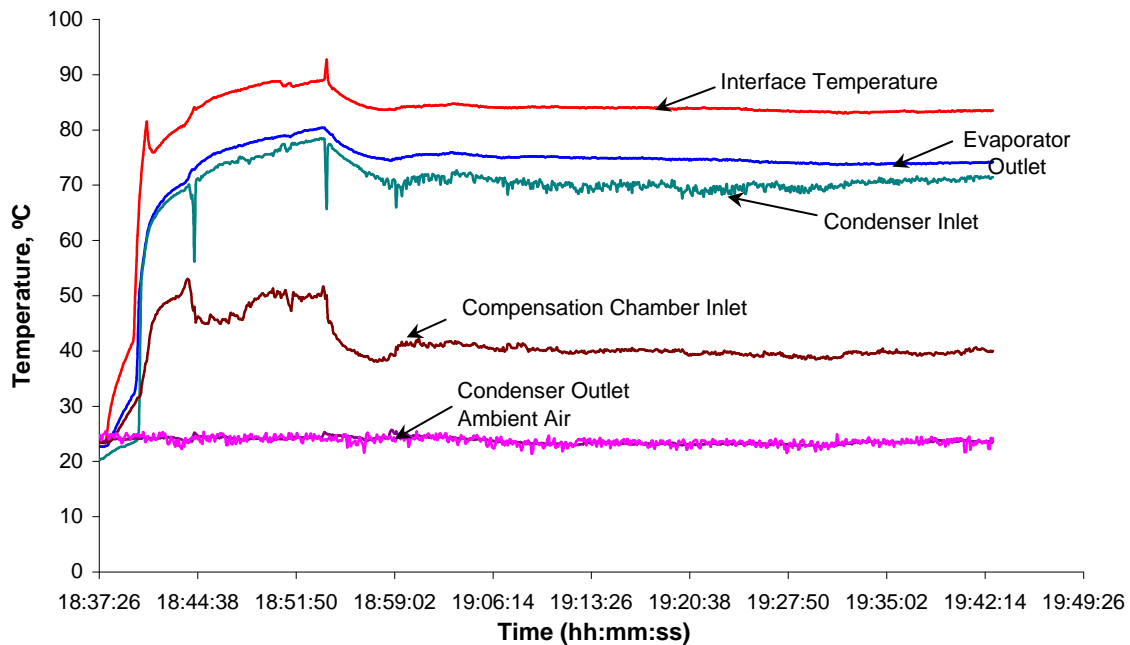


Figure 6.8 Startup of the rectangular evaporator mLHP at 20 W input power

As the heat load is applied to the evaporator active zone, the evaporator temperature start rising rapidly which results in the formation of vapour in the evaporation zone as a result of the evaporation/boiling process and depending upon the pre start fluid distribution inside the evaporator. This is followed by the clearing of the liquid from the vapour line and filling it to the fluid accumulator or compensation chamber which is indicated by the drop in the temperature at the compensation chamber inlet as fluid circulation commences. As the heater-evaporator interface temperature achieved steady state, successful start-up of the device was registered.

Figure 6.9 depicts the heat load dependence of the evaporator temperature for 10 to 50 W input power. It is clear from the graph that the mLHP showed a monotonic linear trend with the applied heat load. The loop was able to transfer a maximum heat load of 50 W while maintaining the heat source temperature and interface temperature within 100 ± 5 °C.

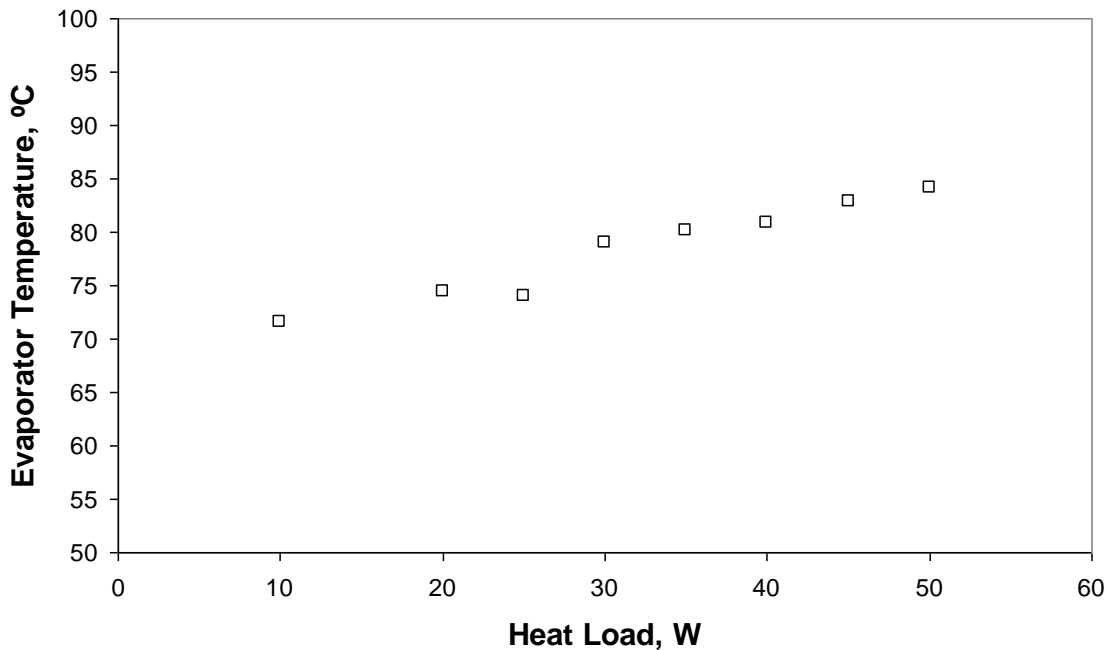


Figure 6.9 Heat load dependence of the rectangular evaporator mLHP evaporator temperature

In the given test range the mLHP was able to achieve steady state without any failure indication which could have manifest itself as evaporator temperature overshoot or back flow of vapour from the evaporator to the compensating chamber due to wick dry out. Figure 6.10 presents the variation of the evaporator thermal resistance, R_e with respect to the applied heat load. R_e lies between 0.28 to 0.38 °C/W for 10 to 50 W input heat load.

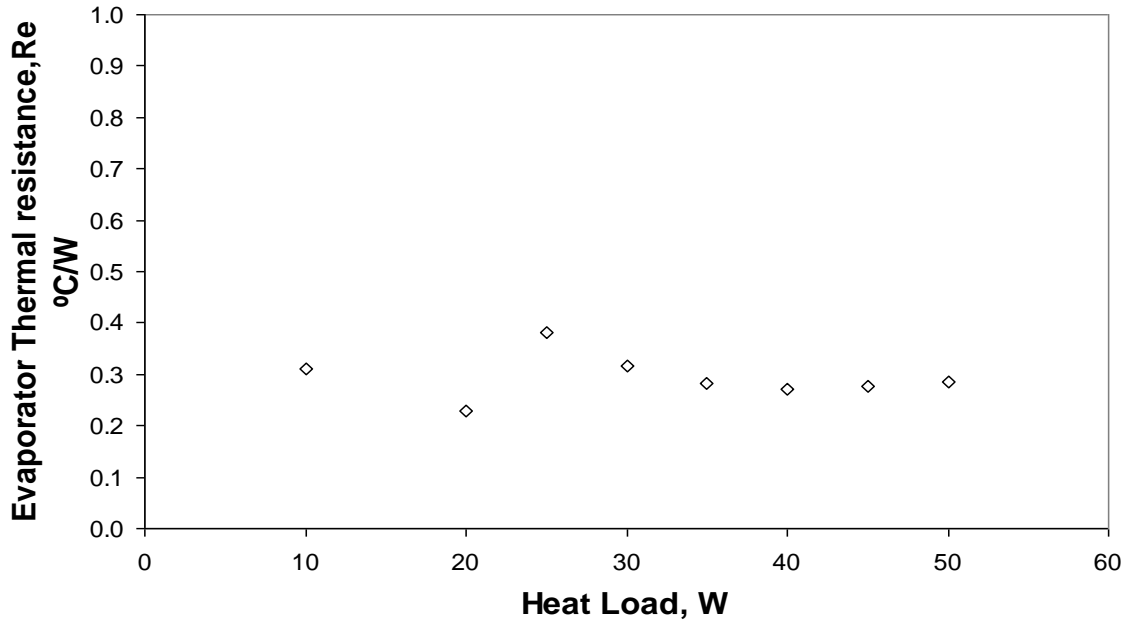


Figure 6.10 Evaporator thermal resistance versus applied heat load for the rectangular evaporator mLHP

Figure 6.11 shows the variation in total thermal resistance - R_t of the mLHP (calculated on the basis of the interface and ambient temperatures) with the applied heat load. R_t lies in the range of 1.51 to 3.62 °C/W for input power between 10 to 50 W. For R_t the minimum value of 1.51 °C/W was achieved at a maximum heat load of 50 W corresponding to an interface temperature of 98.5 °C.

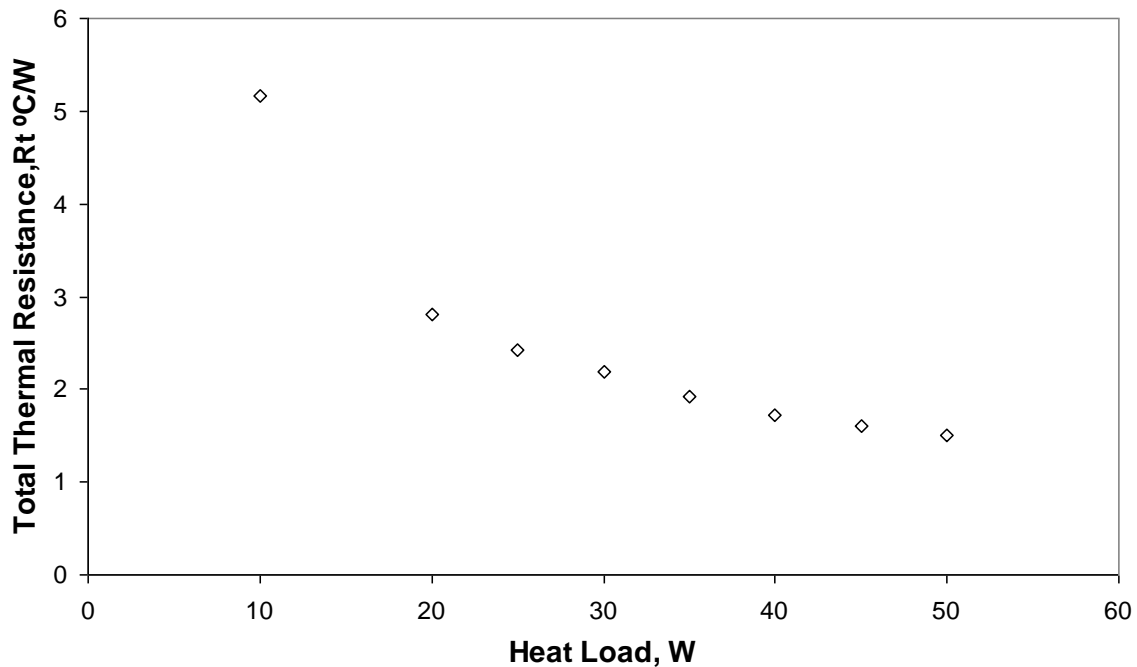


Figure 6.11 Total thermal resistance versus applied heat load for the rectangular evaporator mLHP

6.5 Comparison of the Thermal Performance of the Disk Shaped and Rectangular Shaped Evaporators

Tests were conducted on the two types of mLHP design i.e. disk shaped evaporator and rectangular evaporator under the same experimental conditions to compare their thermal performances. Figure 6.12 and 6.13 compares the operational performance of the mLHP with disk shaped evaporator and rectangular evaporator on the basis of the evaporator and heater/interface temperature respectively.

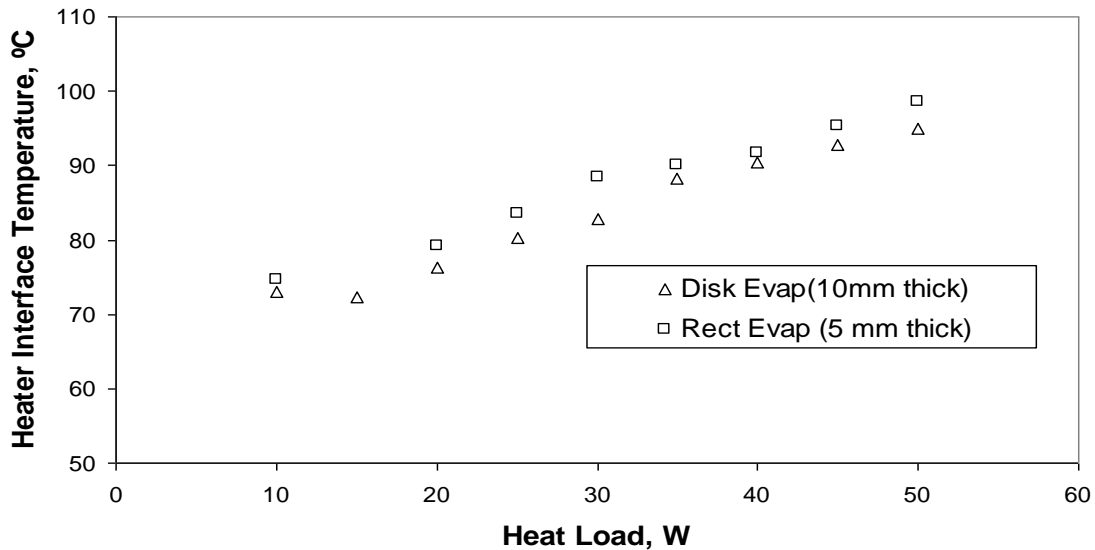


Figure 6.12 Comparison of the interface temperature for the disk shaped evaporator mLHP and rectangular evaporator mLHP at the same range of input heat loads.

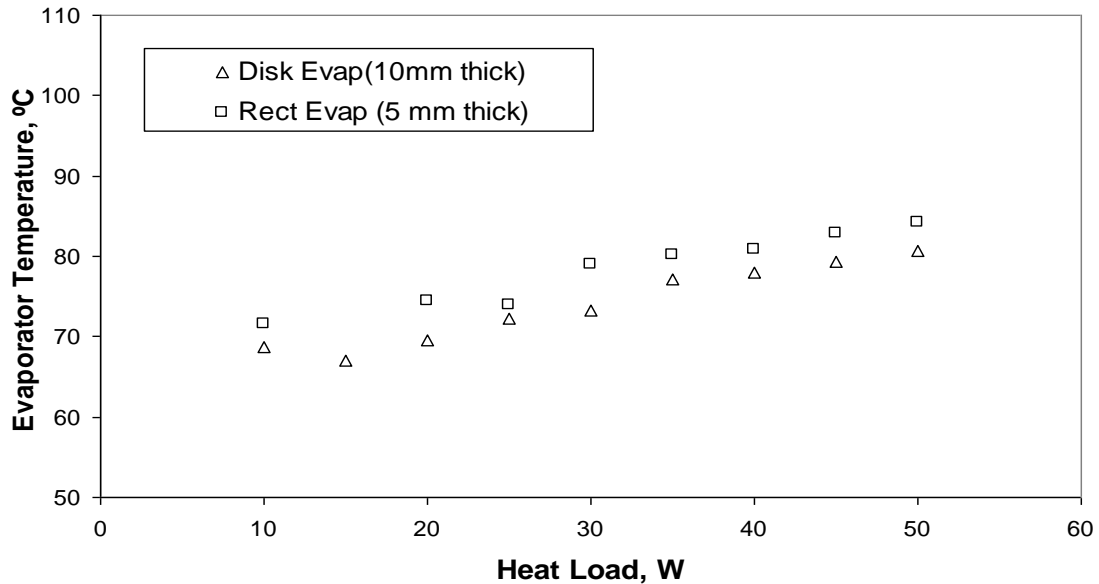


Figure 6.13 Comparison of the evaporator temperature for the disk shaped evaporator mLHP and rectangular evaporator mLHP at the same range of input heat loads.

It is evident from the comparison plots that the thermal performance of the disk shaped evaporator is somewhat better than that of the rectangular evaporator. In the current design of the flat rectangular evaporator, reduced thickness of 5 mm has been obtained at the expense of some performance sacrifice. Factors that can contribute to this can be the change in the orientation of the wick with respect to the compensation chamber and reduction in the area of the fluid absorbing face of the wick. In the disk shaped evaporator which obeys the customary design of a LHP, the direction of the fluid and heat flow in the capillary structure are towards each other. The opposite faces of the disk shaped wick behave as evaporating and absorbing faces. Figure 6.14 and 6.15 presents the internal cross section of the two evaporator designs that shows the liquid and heat flow directions inside them.

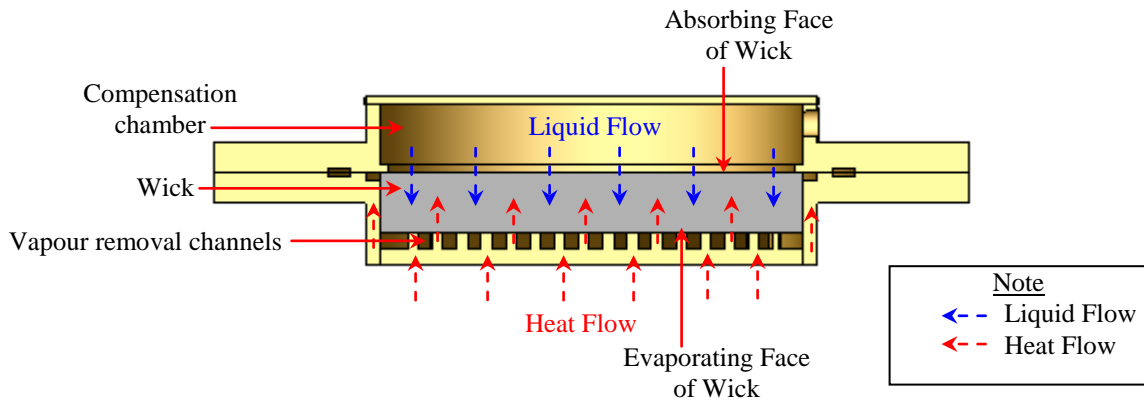


Figure 6.14 Cross section of the disk shaped evaporator showing internal structures and directions of the liquid and heat flows relative to each other

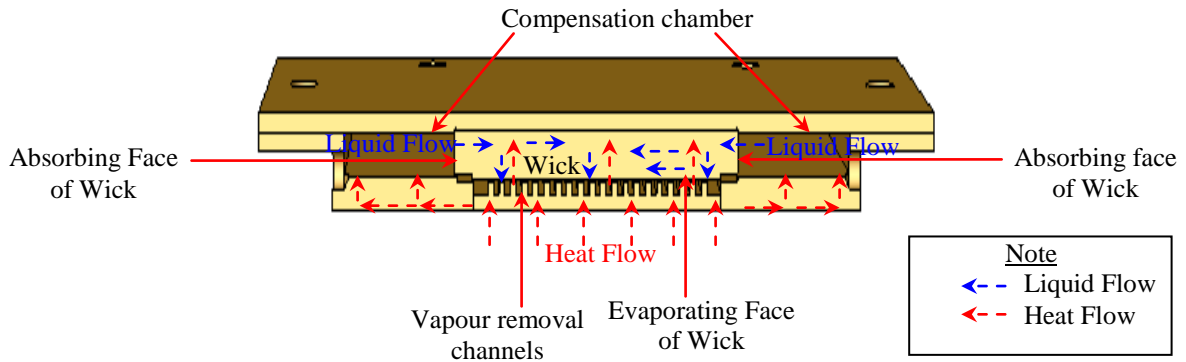


Figure 6.15 Cross section of the rectangular shaped evaporator showing internal structures and directions of the liquid and heat flows relative to each other

In the disk shaped evaporator the compensation chamber is contained in the thickness of the evaporator structure and linked to the evaporator through the capillary structure. Conversely, in the flat rectangular evaporator the compensation chamber is distributed on the sides of the capillary structure and lies in its plane. On one hand, this results in a decrease of the liquid absorbing area of the capillary structure while on the other hand this alters the liquid and heat flow directions which become perpendicular to each other. As the heat exchange between the fluid and the solid surface is dependent on the direction of fluid and heat flow relative to each other, back heat flow to the compensation chamber in the rectangular case increases to some extent. Apart from this, as a result of the modified structure of the evaporator the liquid filtration path inside the capillary structure also increases which produces additional pressure losses. From Figure 6.15 it can be seen that there is no liquid wetting the top part of the wick which also contributes to increasing the evaporator temperature. In the same way, as liquid returns to the compensation chamber from one side only, wetting and thus cooling efficiency of the compensation chamber/wick is impaired. Perhaps more efficient liquid return to the compensation chamber and the presence of a gap between the wick top part and the cover plate would reduce the evaporator temperature.

Another factor that leads to increase in the extent of the back heat conduction from the evaporator active zone to the compensation chamber, in the case of the rectangular evaporator, is the coplanar location of the evaporation zone with respect to the compensation chamber. As explained above, in the case of disk evaporator the compensation chamber constitutes the thickness of the evaporator structure. Here, the heat flow from the evaporation zone to the compensation chamber takes place through the liquid saturated wick structure and evaporator walls. Also due to the inherent structure of the disk shaped evaporator the majority of the liquid present in the compensation chamber makes contact with the wick absorbing face rather than the container walls. Since the thermal conductivity of the liquid saturated wick structure is much lower than the bulk material conductivity, the extent of the back heat flow is lower. In contrast to this, for the rectangular design heat flow from the active zone to the compensation chamber take place through the high thermally conductive evaporator wall made of copper. Also, the bulk liquid in the compensation chamber makes contact with the high temperature coplanar evaporator wall. Therefore in this case, the rate of heat flow to the chamber increases.

As the compensation chamber temperature dictates the loop saturation conditions, the operating temperature in the rectangular evaporator is higher than in the disk shaped evaporator mLHP.

However it is worth mentioning that with the rectangular evaporator design, thickness as low as 5 mm which is half of the thickness of the disk shaped evaporator was achieved and the evaporator showed satisfactory performance characteristics in the test range of applied heat load.

In both evaporators, the designs of the heat acquisition region i.e. system of vapour removal channel and the evaporation zone are similar. For that reason the evaporator thermal resistance, R_e for both the design, as shown in Figure 6.16, lies in the same range.

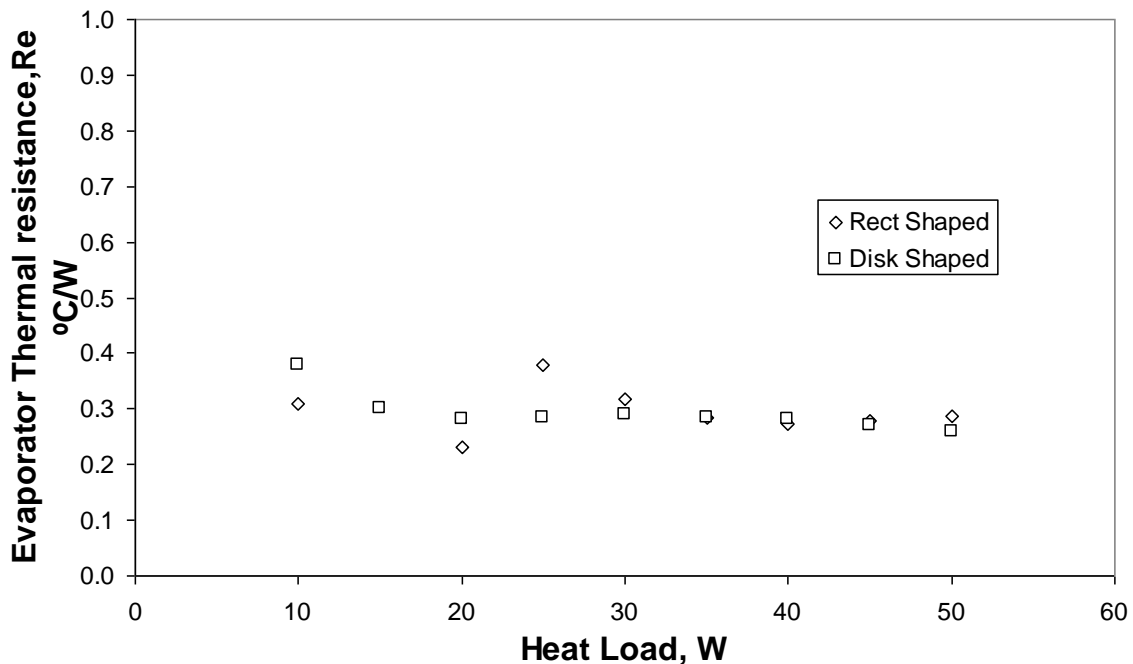


Figure 6.16 Evaporator thermal resistance for the disk shaped evaporator mLHP and rectangular evaporator mLHP at the same range of input heat loads.

Figure 6.17 presents a comparison between the total thermal resistance, R_t of the two type of evaporator for the same range of heat load. It is seen from the plot that the mLHP with a rectangular evaporator was able to achieve the cooling of the high density heat sources within the thermal constraints imposed by the design requirements.

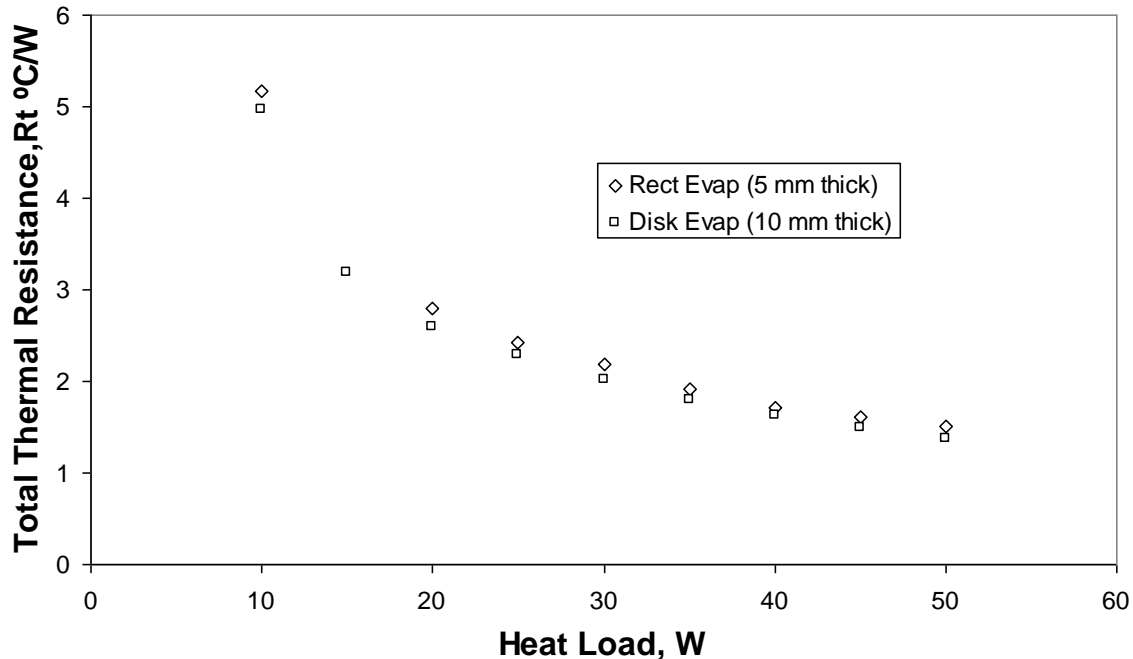


Figure 6.17 Total thermal resistance for the mLHP with disk shaped evaporator and rectangular evaporator at the same range of input heat loads.

As an outcome of the experimentation described it is concluded that the proposed design of a mLHP with a rectangular shaped evaporator was able to operate successfully and authenticate the design concept for the modelling of a compact miniature LHP with reduced thickness. However there remain certain performance issues related to the loop operation that need to be addressed through further research work. Proposals like use of low conductive material for the evaporator body to reduce back heat flow to the compensation chamber and changes in the wick design and shape for proper wetting and efficient liquid filtration though it can be further explored.

6.6 Summary

The chapter can be summarized as follow:

- It is possible to down scale the thickness of the miniature LHP by using a novel concept of relocating the compensation chamber from the thickness of the evaporator to its sides.
- The mLHP evaporator with the compensation chamber distributed on its sides was able to attain a minimum thickness of as low as 5 mm while preserving the functionalities of the capillary structure and efficiency of the heat transfer process inside the evaporation zone.

A mLHP with such a low thickness is easy to install inside a laptop PC with the limited available space compared to the disk shaped mLHP model of 10 mm thickness.

- The prototype was able to transfer extremely high heat flux of 50 W/cm^2 up to a distance of 150 mm while maintaining the source temperature within the permissible limit of $100 \pm 5^\circ\text{C}$.
- In the case of a flat rectangular evaporator mLHP, the total thermal resistance and the interface temperature of the device were higher than for the disk shaped evaporator mLHP.

The next chapter discusses experimental investigation of a liquid cooling system with a microchannel heat sink.

Chapter 7

Liquid Cooling using a Microchannel Heat Sink

In this chapter, the study of a single phase liquid cooled microchannel heat sink for the cooling of electronics microprocessors with extreme heat flux as high as 405 W/cm^2 is reported. To begin with, a complete description related to the design and development of the experimental prototype is given in detail. After this, the experimental setup and test facility to investigate the thermal performance of the heat sink is explained. In addition, the standard equations for analysis of experimental results and available heat transfer correlations to predict the heat transfer inside the channels are also reported. A microchannel heat sink was tested under different conditions of input power and flow rate. Finally, results from the experiments are discussed in detail and compared with the predictions made on the basis of the theoretical relationships.

7.1 Introduction

With the worldwide technology revolution in the development of silicon chips, the well known prediction by Gordon Moore in 1965 (also popularly known as Moore's Law) which states that the number of transistors on a chip doubles about every two years has become a reality. On one hand this has boosted the processing capabilities of microprocessors but at the same time this technology advance has offered new challenges in the design of thermal architecture for cooling the chipsets efficiently. The increase in the number of integrated circuits on a chipset produces an extreme rise in the heat dissipation requirements for the same or reduced size of chip. Also, as a necessary thermal requirement, for the reliable operation of a microprocessor, its temperature must be maintained below 100°C .

Until now, different designs of single phase as well as two-phase cooling systems, as discussed in the literature review, have been proposed and successfully employed for thermal control applications. However looking at the rapid rise in the thermal payload of chipsets these available cooling alternatives will produce diminishing returns. Two phase passive systems including heat pipes and vapour chambers are expected to be the ultimate cooling

solution for the future micro processors. But this will need further in-depth understanding and development of the two phase systems to bring the technology to the level required by advances in the silicon technology. Alternatively, forced convection based single phase cooling systems are also a reliable option to satisfy the thermal needs of the upcoming electronic appliances. At present, liquid cooling can be considered as the most viable solution for thermal control of heat sources with extremely high and concentrated heat fluxes. In the literature survey it is seen that performance of these single phase liquid cooling systems can be greatly improved by using microchannel (or microfins) on the fluid side of the cold plate (or cooling section). In the present investigation, one such microchannel heat sink is designed with an appropriate material and working fluid combination in order to transfer high intensity thermal loads from computer microprocessors.

7.2 Description of Microchannel Heat Sink (MHS) Prototype

The layout of the microchannel heat sink is as shown in Figure 7.1 and includes the bottom plate on which microfins are fabricated and the top cover arrangement for flow management.

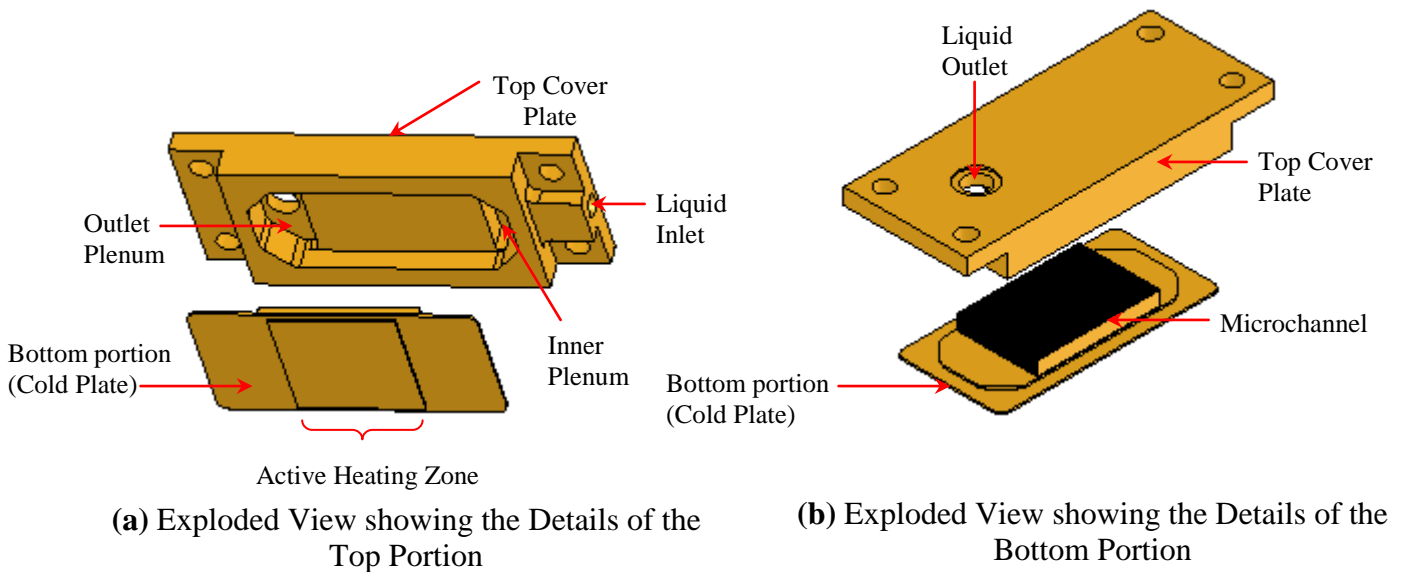
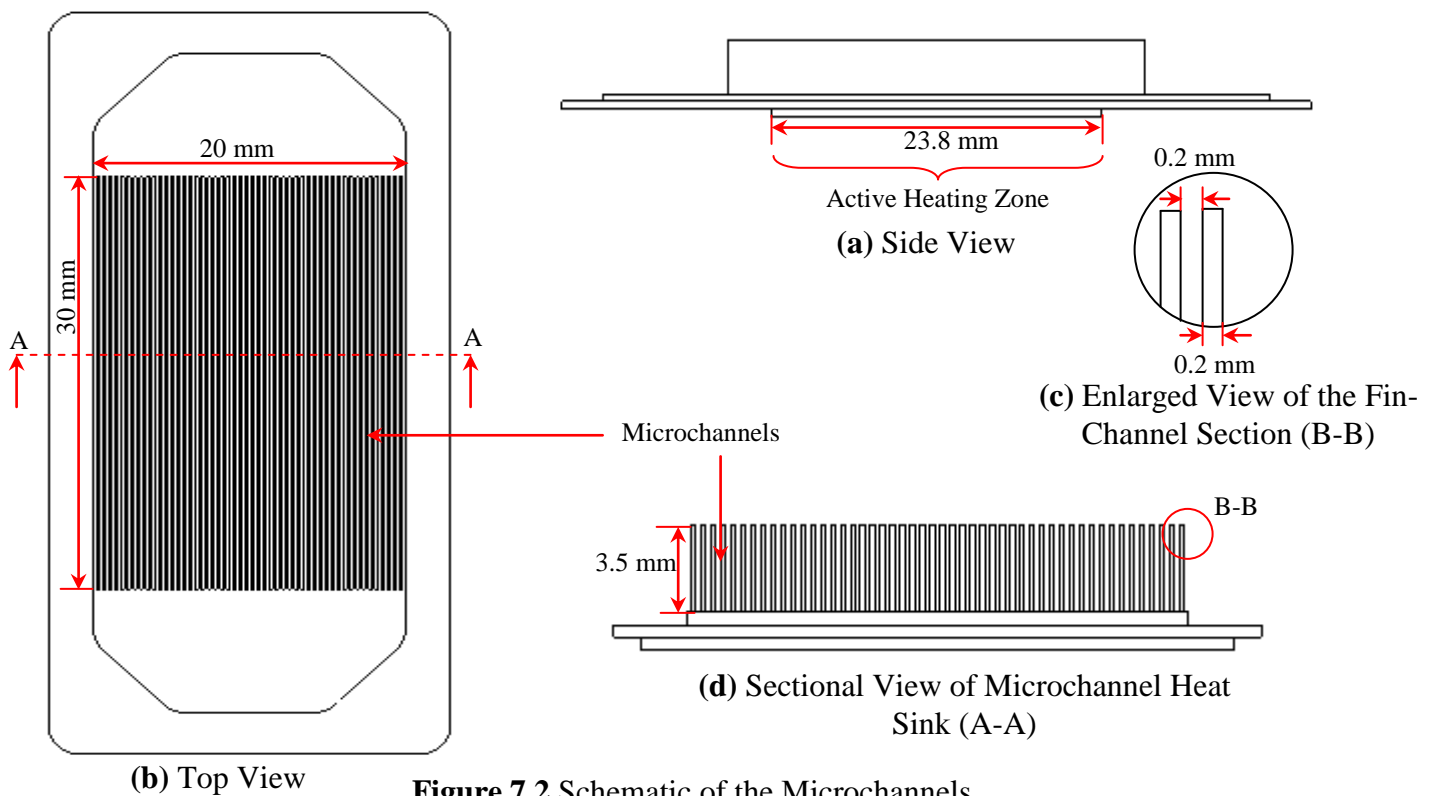


Figure 7.1 Layout of the Microchannel Heat Sink Assembly

Microchannels were fabricated on a copper block of 54 mm (L) x 26 mm (W) x 5 mm (H) by a wire cutting technique. There was a total of 49 channels in the finned area of 30 mm (L) x 20 mm (W), each channel being 0.2 mm wide and 3.5 mm high. Figure 7.2 shows in detail the geometry of the microchannel plate. The large aspect ratio of 17.5 for the channels was

purposely made to enlarge the surface area for heat transfer augmentation. The active heating zone that relates to the micro channelled area was $23.8 \times 23.8 \text{ mm}^2$ as depicted in Figure 7.1b and 7.2. In order to avoid deformation of the heating face under attachment pressure from the heat load simulator, the active zone was approximately 0.5 mm thicker than the rest of the plate. Inlet and the outlet plenums were machined in the top cover portion of the heat sink. These plenums help in achieving efficient fluid distribution through the microchannels. The top cover and the bottom finned plate were brazed to each other to provide proper sealing. During the assembly of the two halves of the heat sink, proper care had to be taken to ensure that there was no gap between the tops of the micro fins and the top plate. Essentially, the contact between the micro fins and the inner machined cavity of the top cover should be perfect. In the case of improper contact, the existing gap will provide the least resistance path to the flow of the fluid which will reduce the quantity of the liquid flowing through the microchannels and thus will severely hamper the performance of the heat sink. One method to guarantee proper contact is to keep positive clearance between the micro fins and the cover plate while brazing the two halves together.



The coolant enters the heat sink from the side and collects in the inlet plenum where it is equally distributed through the microchannels. While flowing through the microchannels, the liquid acquires heat from the large exposed surface of the channel walls (microfins) and rises in temperature. The hot liquid collects in the outlet plenums and exits through the outlet on the top of the cover plate. The flow pattern of the liquid and the internal details of the microchannel heat sink can be well understood from the side and the isometric cross sectional view as shown in Figure 7.3 (a) and (b).

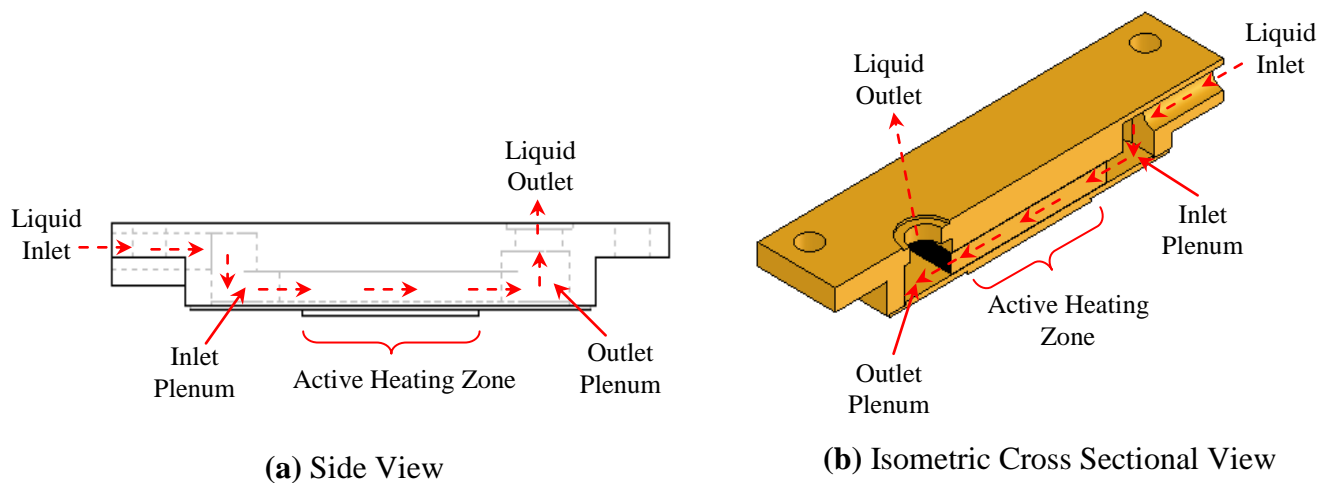


Figure 7.3 Internal details and liquid flow path inside the microchannel heat sink

7.3 Experimental Setup and Test Procedure

Figure 7.4 shows the experimental setup that was used to test the thermal performance of the microchannel heat sink. It consists of microchannel test section, finned heat exchanger and a liquid pump. The heat load simulator (i.e. heater), in the form of a copper block embedded with two cartridge heaters, was tightly secured to the active zone of the test section with the help of a screw-flange arrangement. To provide better thermal contact between the heater and the heat sink active zone, thermal grease was used as the thermal interface material between the bottom of the heat sink and the top surface of the heater/chip. The liquid was pumped directly into the heat sink with the help of an electric pump to transfer the heat applied to the active zone of the test section by forced convection to the coolant flowing through the microchannels. As the present prototype of the microchannel heat sink was designed to handle large heat loads, a collector type finned heat exchanger with well developed external and internal surfaces was used for sensible cooling of the liquid leaving the microchannel heat

sink. The finned heat exchanger incorporated a bottom header that helped to distribute the hot liquid equally among six tubes passing through the heat exchanger. On the other end of the heat exchanger, the top header collected the cold fluid and passed it to the pump for recirculation. The finned heat exchanger was made from copper. The flow of fluid through the microchannel heat sink, bottom header, tubes connecting the headers and top header is clearly shown with the help of the cross sectional view of the cooling unit in Figure 7.5.

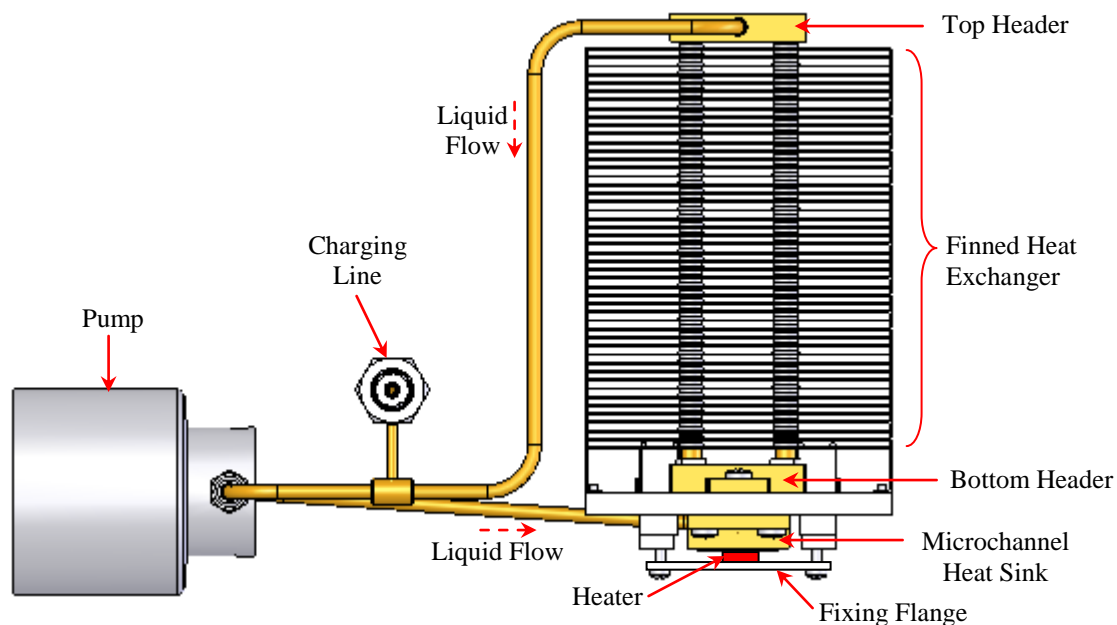


Figure 7.4 Experimental Setup to test microchannel heat sink

The finned heat exchanger was cooled by means of forced air flow by placing it inside wind tunnel as shown in Figure 7.6. Throughout the test period, the room temperature was maintained constant at 22 ± 2 °C. The wind tunnel helped to maintain uniform and well distributed air passage through the heat exchanger section and thereby provide stable conditions to perform the experiment. Sufficient air flow rate was maintained through the heat exchanger to dissipate all the heat input at the microchannel heat sink.

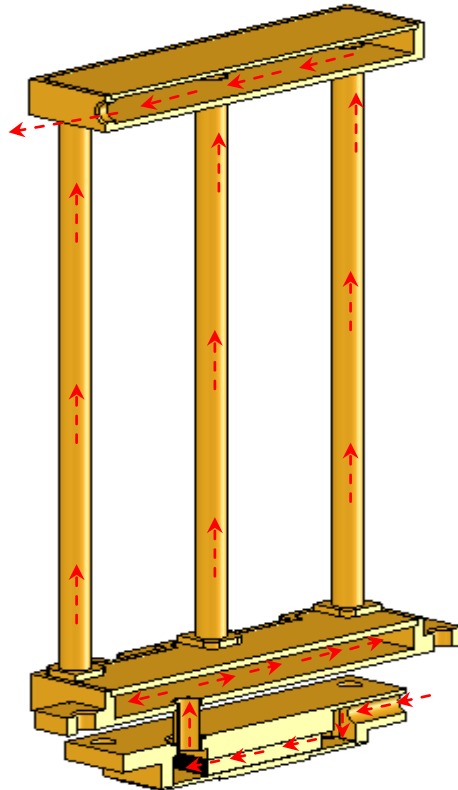


Figure 7.5 Cross sectional view of the microchannel heat sink and distributed finned heat exchanger showing the fluid flow pattern inside the cooling unit.

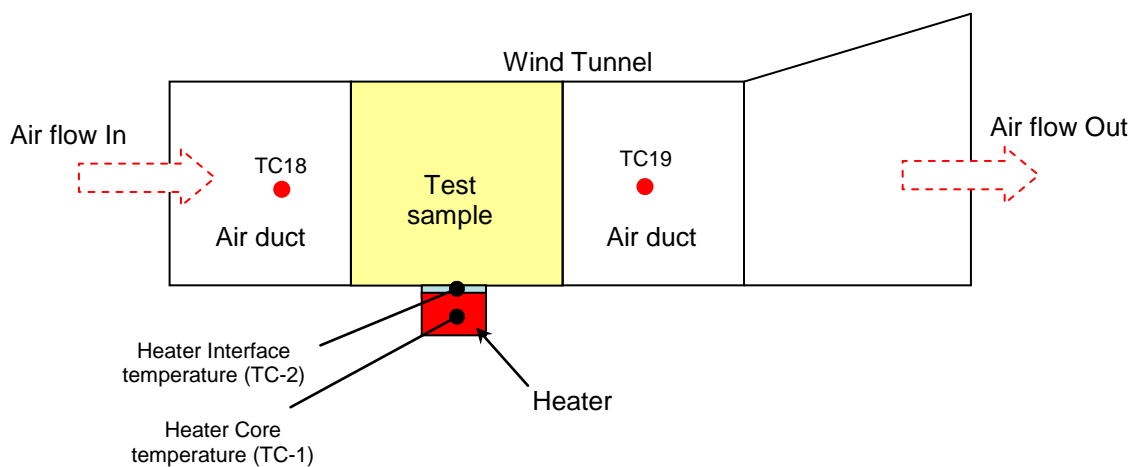


Figure 7.6 Test bed for the Microchannel heat sink

The thermal performance of the cooling unit was tested at different liquid flow rates using either open or closed loop systems. In the open loop system as shown in Figure 7.7, the test unit was connected to the constant temperature water supply from a reservoir and the liquid flow rate through the microchannel section was controlled by using a control valve at the heat

sink inlet. With this arrangement very high flow rates were achievable which was useful for testing the maximum heat capacity of the heat sink.

The temperature of the coolant at the inlet was maintained constant at 14 ± 2 °C. The mass flow rate of coolant through the microchannels was primarily determined by measurement of water mass collected over a fixed time interval. Precise measurements for mass were done using a mass balance of sensitivity 0.01 grams.

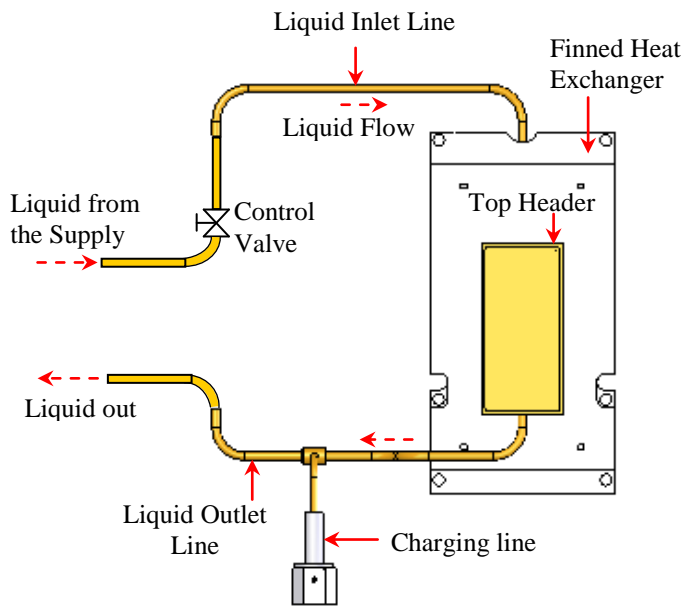


Figure 7.7 Experimental setup for open loop system.

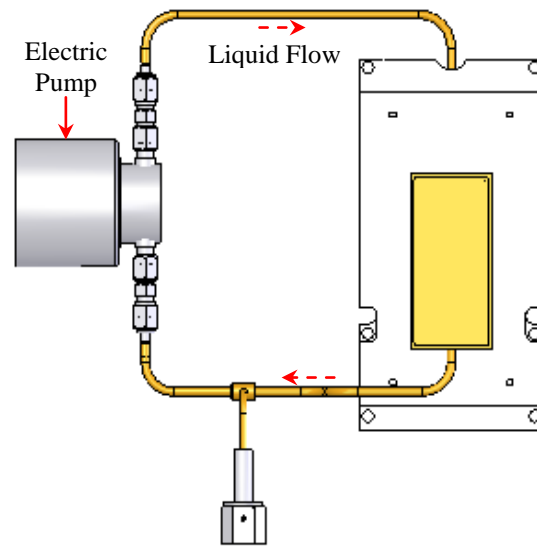


Figure 7.8 Experimental setup for closed loop system.

For the closed loop system, a centrifugal pump made by the SEPA Company with a maximum flow rate of 0.43 l/min under 60 cm water head and operating under max 12 V & 0.2 A was used to circulate liquid through the loop. The location of the electric pump with respect to the test section and the finned heat exchanger arrangement are presented with the help of a top view of the test facility in Figure 7.8. Charging of the closed loop system was done after evacuating the air from the system using a vacuum pump. Pure deionised water was used as the coolant inside the cooling unit. As the mode of the heat transfer in this case is forced convection using single phase (i.e. liquid cooling), the cooling unit was fully charged with the working fluid.

The thermal characteristics of the microchannel heat sink were studied using nineteen T-type thermocouples which were installed at different locations of the cooling unit as depicted in Figures 7.9 and 7.10. The accuracy of the temperature readings was within ± 0.5 °C. Data from the thermocouples was monitored and recorded every 5 seconds by using a Keyence data acquisition system and a computer system.

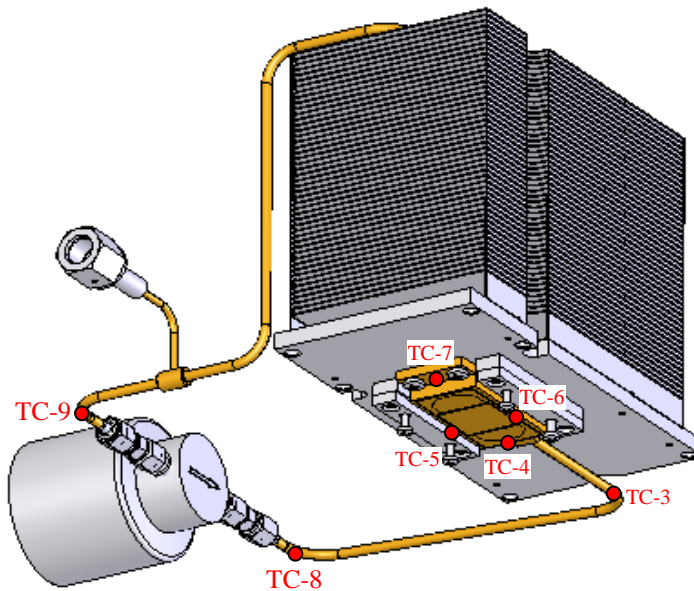


Figure 7.9 Test facility for the heat sink showing the location of the thermocouples on the microchannel heat sink

The temperature at the interface between the heater and the heat sink was recorded with the help of a thermocouple (Figure 7.6) that was fixed inside the groove machined in the centre of the top active heater surface. Four thermocouples (Figure 7.9) were mounted on the outer wall of the microchannel heat sink to measure the mean temperature of the cooling section. In addition, seven thermocouples (Figure 7.10) were installed at different locations on the finned heat exchanger section to measure its mean wall temperature by an averaging technique. The outlet temperature of the hot liquid leaving the microchannel, which assists in the calculation of the cold plate (i.e. cooling section) thermal resistance, was estimated by a thermocouple installed at the external surface of the outer plenum. The inlet fluid temperature was obtained using a thermocouple positioned immediately upstream of the microchannels. Also, the rise in temperature of the cooling air was determined with the help of the two thermocouples at the entrance and exit of the finned heat exchanger respectively as shown in Figures 7.6 and 7.10. A digital wattmeter with an accuracy of ± 0.1 W was used to measure the input power and for

adjusting the input voltage and current in order to control the applied heat flux. Tests were performed in the power range of 5 to 200 W. The input power and the mass flow rate of coolant were used as the primary controlling parameters for the experiment.

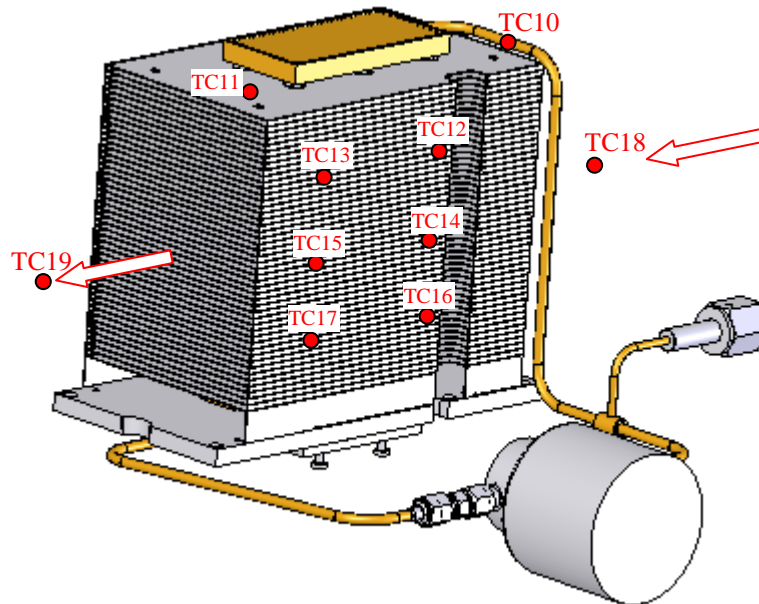


Figure 7.10 Test facility for the heat sink showing the location of the thermocouples on the Finned Heat Exchanger

The following procedure was followed for the conduct of each test. Initially, the fluid circulation through the microchannel was initiated by opening the control valve (for an open loop test) or turning on the electric pump (for a closed loop test). The desired flow rate could be set by adjusting the control valve or changing the input power to the pump. After the flow rate was stabilised, the heater power supply was switched on and maintained at the required level to achieve a steady state. For steady state, the temperature at the cooling section had to be maintained stable within $\pm 0.1^\circ\text{C}$ limit. After steady state was achieved, readings from all the thermocouples were stored using the data recording system.

7.4 Heat Transfer Analysis

For the particular input heat load and mass flow rate (i.e. Reynolds number) of the coolant, thermal characteristics of the heat sink were calculated on the basis of the steady state operating temperature of the cooling section (microchannel heat sink), its maximum heat transfer capability and the mean heat transfer coefficient.

In the analysis, the thermodynamic properties of the fluid are calculated based on the mean fluid temperature, T_{mf} (average of the fluid inlet and outlet temperatures). All the heat is assumed to be dissipated uniformly through the top of the chip (i.e. heat source) to the microchannel heat sink base. Heat losses from the chip through the substrate to the ambient, and through the cover plate to the surrounding air are neglected.

T_{mf} is calculated as follow:

$$T_{mf} = \left(\frac{T_{l,o} + T_{l,i}}{2} \right) \quad (7.1)$$

where $T_{l,o}$ and $T_{l,i}$ are the outlet and the inlet fluid temperatures of the liquid.

The applied heat load, Q_a^\bullet was determined from the measured input voltage, V_e and current, I as follows:

$$Q_a^\bullet = V_e I \quad (7.2)$$

The mean heat transfer coefficient, h_m is determined from:

$$h_m = \frac{Q_a^\bullet}{NA_{ch}(T_{wl} - T_{mf})} \quad (7.3)$$

where, A_{ch} is the area available for convection per channel and is equal to $(L_{ch}(W_{ch} + 2H_{ch}))$, L_{ch} is the length of the channel, W_{ch} is the width of the microchannel and H_{ch} is the height of the microchannel. N is the number of microchannels and T_{wl} is the internal wall temperature of the microchannels.

As direct measurements of the microchannel wall temperature was not available, it was determined by extrapolation from the mean temperature of the heat sink base, T_{hsb} as follow:

$$T_{wl} = T_{hsb} - \frac{Q_a^\bullet t_{hsb}}{A_{hsb} k_{Cu}} \quad (7.4)$$

In Equation 7.4, T_{hsb} , A_{hsb} and t_{hsb} are the temperature, area and thickness of the heat sink base, k_{cu} is the thermal conductivity of copper.

Thermal performance of the heat sink is also determined on the basis of the thermal resistance between different sections as follows:

The efficiency of the heat transfer process from the source to the coolant is very important and calculated on the basis of the cold plate thermal resistance, R_{cp} expressed as:

$$R_{cp} = \frac{(T_j - T_{mf})}{Q_a} \quad (7.5)$$

where, T_j is the junction temperature at the interface between the heat sink base and heat source.

The total thermal resistance, R_t of the device is calculated from the junction or the interface temperature, T_j through to the ambient temperature, T_a as follows:

$$R_t = \frac{(T_j - T_a)}{Q_a} \quad (7.6)$$

The uncertainty in the measurement of the temperature by thermocouples was $\pm 0.5^\circ\text{C}$. For the input heat load, using the Watt meter, uncertainty of ± 0.1 W was introduced. The experimental results revealed that uncertainties in the thermal resistance and convective heat transfer coefficient were $\pm 9.8\%$ and $\pm 18.7\%$ respectively.

7.4.1 Heat Transfer Correlations

The experimental results for the channel heat transfer can be compared with theoretical predictions made on the basis of heat transfer correlations as discussed below. It may be noted that although these correlation equations were originally developed for circular tubes, they have been used for non-circular tubes with substitution of the hydraulic diameter, D_h .

Correlations for the prediction of heat transfer were generally reported in terms of Nusselt number, Nu which is defined as:

$$Nu = \frac{h_m D_h}{k_l} \quad (7.7)$$

in which, D_h is the characteristic hydraulic diameter of the microchannel and given by:

$$D_h = \frac{2W_{ch} H_{ch}}{(W_{ch} + H_{ch})} \quad (7.8)$$

and k_l is the thermal conductivity of the liquid at the mean temperature, T_{mf} .

The heat transfer coefficient can be obtained from the above equation as:

$$h_m = \frac{k_l Nu}{D_h} \quad (7.9)$$

The following conventional correlations are used by a number of researchers for the prediction of channel heat transfer.

Kays and Crawford (1980) proposed a correlation in order to predict the Nusselt number for fully developed laminar ($Re < 2200$) liquid flow through a rectangular microchannel:

$$Nu = 8.235 \left(1 - \frac{1.883}{\alpha} + \frac{3.767}{\alpha^2} - \frac{5.814}{\alpha^3} + \frac{5.361}{\alpha^4} - \frac{2}{\alpha^5} \right) \quad (7.10)$$

in this, $\alpha = \frac{H_{ch}}{W_{ch}}$ is the aspect ratio of the channel.

In the case of liquid flow through a channel both velocity and temperature depend on the axial distance. Two different types of entry length solution can be obtained. The simplest one is based on a fully developed velocity profile and a developing thermal boundary layer. Such a situation would exist if the location at which heat transfer begins was preceded by an unheated starting length. Even in the absence of an unheated starting length, the velocity boundary layer development would occur far more rapidly than thermal boundary layer development and the solution based on the above approximation can be used. In contrast, the combined (thermal and velocity) entry length solution corresponds to the case for which the temperature and velocity profiles develop simultaneously.

For the combined or simultaneously developing entry lengths, a suitable correlation, due to Sieder and Tate (Incropera and DeWitt, 2001), for flow inside a circular tube is of the form:

$$Nu = 1.86 \left(\frac{Re Pr}{L / D_h} \right)^{1/3} \left(\frac{\mu_l}{\mu_{wl}} \right)^{0.14} \quad (7.11)$$

The correlation is valid for the following conditions:

$$\left[\begin{array}{l} T_{wl} = \text{constant} \\ 0.48 < Pr < 16,700 \\ 0.0044 < \left(\frac{\mu_l}{\mu_{wl}} \right) < 9.75 \end{array} \right] \quad (7.12)$$

where the Reynolds number, Re is defined as $Re = \frac{\rho_l u D_h}{\mu_l}$ (9.13)

and Prandtl number is $Pr = \frac{c_{pl} \mu_l}{k_l}$ (9.14)

ρ_l , μ_l and c_{pl} are the liquid density, viscosity and specific heat capacity at the mean temperature respectively, μ_{wl} is the liquid viscosity at the wall temperature, u is the flow velocity and T_{wl} is the surface or wall temperature of the cooling section.

Stephan and PreuBer (Lee et al, 2005) proposed correlations for simultaneously developing boundary layers at constant wall temperature and constant wall heat flux conditions for liquid flow inside circular tubes:

$$Nu = 3.657 + \frac{0.0677(Re Pr(D_h / L))^{1.33}}{1 + 0.1Pr(Re(D_h / L))^{0.3}} \quad (7.15)$$

Valid for surface temperature, $T_{wl} = \text{constant}$, $0.7 < Pr < 7$ or $RePr(D/L) < 33$ for $Pr > 7$.

$$Nu = 4.364 + \frac{0.086(Re Pr(D_h / L))^{1.33}}{1 + 0.1Pr(Re(D_h / L))^{0.83}} \quad (7.16)$$

Valid for surface heat flux, $q_{wl} = \text{constant}$, $0.7 < Pr < 7$ or $RePr(D/L) < 33$ for $Pr > 7$.

For a thermally developing laminar boundary layer and a fully developed velocity profile inside a circular tube, the following correlations are reported by Hausen (Incropera & DeWitt, 2001) and Shah & London (1978) for constant surface temperature and constant wall heat flux conditions respectively:

$$Nu = 3.66 + \frac{0.19(Re Pr(D_h / L))^{0.8}}{1 + 0.117(Re Pr(D_h / L))^{0.467}} \quad (\text{Hausen Correlation}) \quad (7.17)$$

Valid for surface temperature, $T_{wl} = \text{constant}$, $Re < 2200$

$$Nu = \begin{cases} 1.953(\text{Re Pr}(D_h / L))^{1/3} & (\text{Re Pr} \frac{D_h}{L} \geq 33.3 \\ 4.364 + 0.0722(\text{Re Pr}(D_h / L)) & (\text{Re Pr} \frac{D_h}{L} < 33.3 \end{cases} \quad (\text{Shah \& London, 1978}) \quad (7.18)$$

Valid for surface heat flux, $q_{wl} = \text{constant}$, $Re < 2200$

Different heat transfer correlations for the transitional and fully developed turbulent flow through circular tubes have also been proposed in the literature by Hausen, Dittus-Boelter, Petukhov and Gnielinski (Incropera & DeWitt, 2001, Lee et al, 2005).

The Dittus-Boelter Correlation for the calculation of heat transfer characteristics for fully developed turbulent flow of liquid inside a circular tube is given as:

$$Nu = 0.023 \text{Re}^{4/5} \text{Pr}^{1/3} \quad (7.19)$$

In addition, new and modified correlations have been proposed by Choi et al (1991), Yu et al (1995), Peng et al (1994), Adams et al (1998) and others researchers (Lee et al, 2005) to establish better agreement with, and close predictions of, the experimentally obtained results. Several of the above correlations have been used for the prediction of the heat transfer rate inside the microchannel.

7.5 Result and Discussion

7.5.1 Thermal Characteristics of the MHS using 11x13 mm² Heat Source

Figure 7.11 shows the heat load dependence of the heat sink interface temperature. In this test, a heat load simulator with an active area of 1.43 cm² (i.e. 11 mm x 13 mm) was used to provide heating to approximately 25% of the active portion i.e. the region of the heat sink where the microchannels are present. This results in extremely high heat flux of 140 W/cm² at a maximum power dissipation capacity of 200 W from the heat source. The interface temperature showed a linear rise with the increase in input heat load. For input power in the range of 25 to 200 W, the interface temperature lay between 26.6 to 63.9 °C.

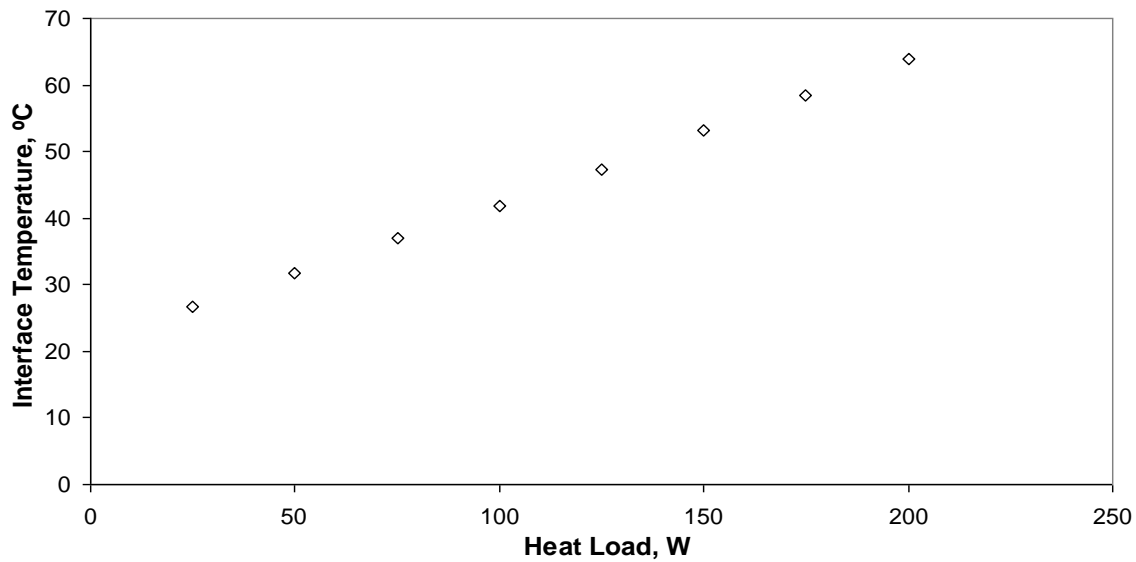


Figure 7.11 Heat load dependence of the Interface temperature of the microchannel heat sink with the 11mm x 13mm heat source

It is seen from Figure 7.12 that the power inputs considered here do not have an observable effect on the thermal resistances of the cooling section and the overall device.

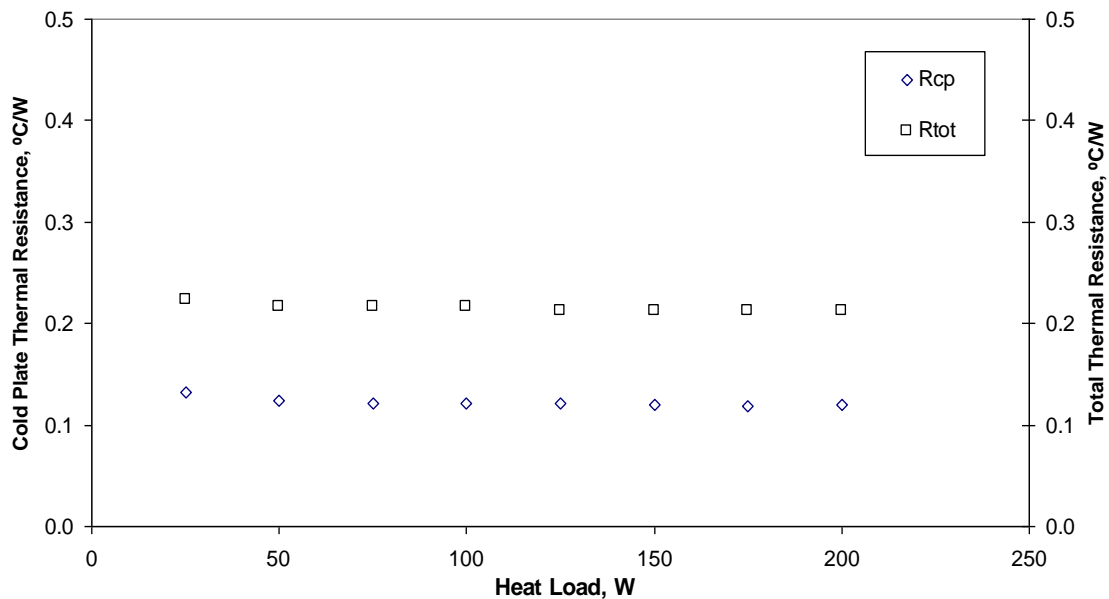


Figure 7.12 Cold plate thermal resistance and total thermal resistance of the microchannel heat sink with respect to the applied heat load using 11mmx13mm heat source

7.5.2 Thermal Performance of MHS with Different Heater Sizes

For even higher heat flux characterization of the designed liquid cooled microchannel heat sink, a heat source with a active footprint as low as 0.49 cm^2 was used to test its performance. Such a concentrated heat source supplies a local heat density to approximately 8.7% of the active face of the cooling section. Here it contributes to the ultra high heat flux of 408 W/cm^2 which can imitate a local hot spot on the high-end chipsets.

In Figure 7.13 the heat load dependence of the temperature at the interface of the heat sink and the $7 \times 7 \text{ mm}^2$ source (0.49 cm^2 heater) is plotted and compared to that of the $11 \times 13 \text{ mm}^2$ source (1.43 cm^2 heater) for the same cooling conditions at the condenser.

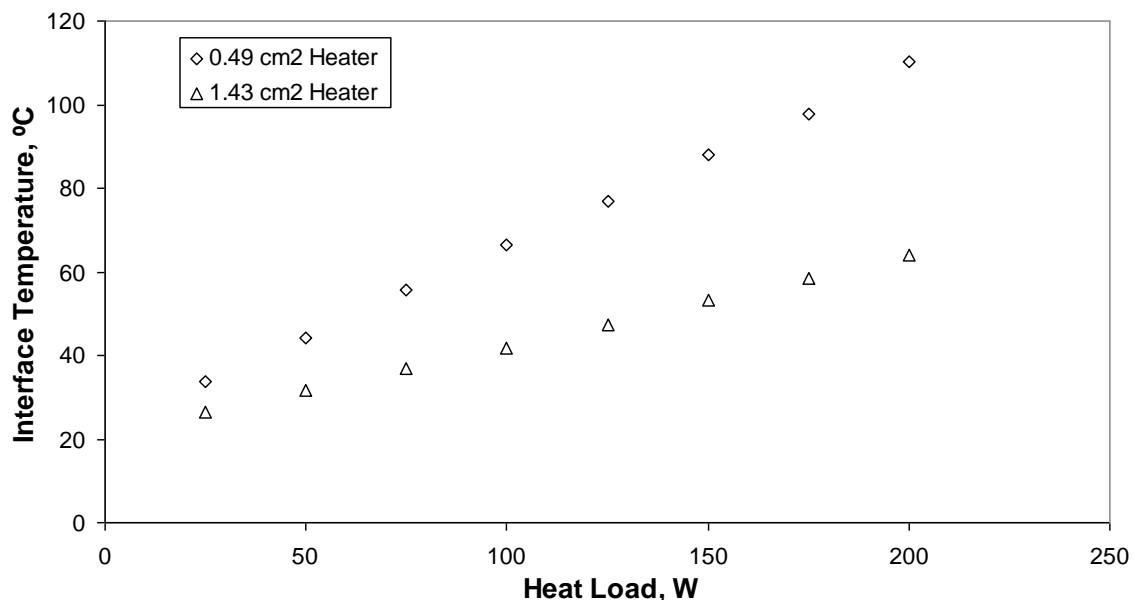


Figure 7.13 Heat load dependence of the Interface temperature of the microchannel heat sink with different heater sizes ($7 \times 7 \text{ mm}^2$, $11 \times 13 \text{ mm}^2$)

Due to the smaller size of the 0.49 cm^2 heater, the steady state interface temperature achieved in this case was higher than for the 1.43 cm^2 heater. For example at 100 W input load, the interface temperature with the 0.49 cm^2 heater was approximately 37% of that of the 1.43 cm^2 heater. This is predominately due to the addition of the metallic resistance offered to the distribution of the heat from the heater footprint to the active section of the cooling plate and the microchannels. Due to the concentration of the heat load in a smaller area, the microchannels are not heated uniformly which decreases the sensible heat gain by the coolant

from the fins. As a result, the wall or interface temperature of the cooling section increases as experienced in the present case. For input power from 25 to 200 W, the junction/interface temperature for the 0.49 cm² source ranged from 33.6 to 110.4 °C.

Figures 7.14 and 7.15 present the results for the cold plate thermal resistance and total thermal resistance with changing heat load. The thermal resistance of the cold plate with the high flux chipset (i.e. 0.49 cm² heater) is 0.33 °C/W compared to 0.09 °C/W for the 1.43 cm² heater while the total thermal resistance is 0.44 °C/W compared to 0.18 °C/W for 1.43 cm² heater source.

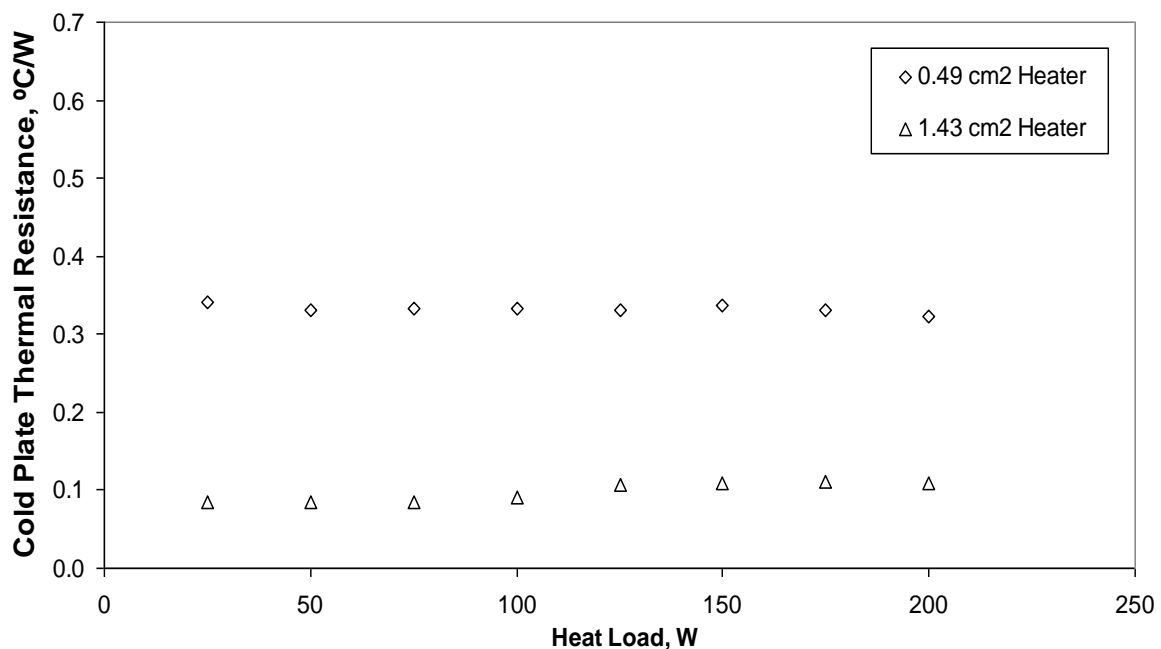


Figure 7.14 Variation of the cold plate thermal resistance of the microchannel heat sink with the applied heat load with different heater sizes (7 x7 mm², 11 x13 mm²)

It is also noted from the plotted results that the thermal resistances remains fairly constant (within ± 0.1 °C/W) over the entire test range of input heat loads. For the 0.49 cm² source, the value of the heat transfer coefficient for the forced flow of liquid through the microchannels lies between 3500 to 4100 W/m²K while for the 1.43 cm² source, it varies in the range of 3800 to 5100 W/m²K. The cause of the slightly low value of the heat transfer coefficient with high heat flux source can be possibly due to the unequal temperature gradient observed on the microchannel walls which were heated more in the centre than at the sides. As the micro fins were not heated equally along the entire length of the channel, therefore the heat gain by the

fluid decreased which decreased the overall heat transfer coefficient. Contrary to this, due to the larger active area of the second source (1.43 cm^2 heater), heat spreading on the micro fins and channel walls was better. Hence improvements in the heat transfer coefficient occurred.

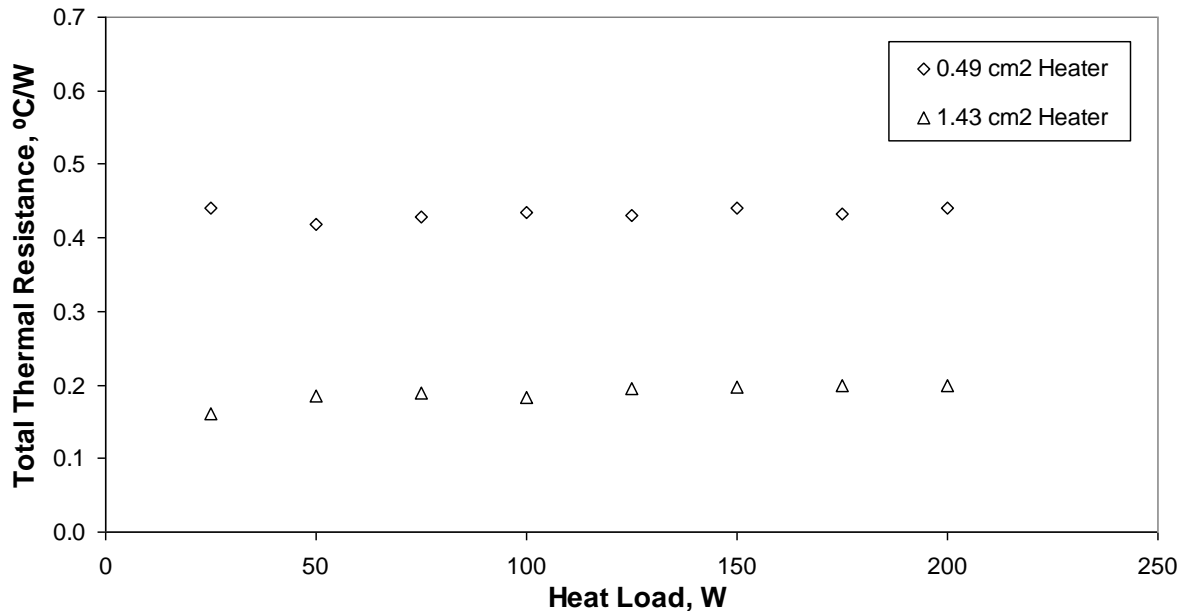


Figure 7.15 Variation of the total thermal resistance of the microchannel heat sink with the applied heat load for different heater sizes ($7 \times 7 \text{ mm}^2$, $11 \times 13 \text{ mm}^2$)

7.5.3 Thermal Performance of MHS with Different Flow Rates

In the present investigation, the thermal characteristics of the microchannel heat sink were studied by varying the flow rate of the coolant from 0.1 to 0.9 l/min (or 1.7 to 15 cc/sec). As the electric pump used in the previous testing was capable of providing a maximum rate of 0.43 l/min, the current tests were conducted using an open loop system as discussed above. The coolant temperature at the inlet to the heat sink was maintained constant at $14 \pm 2 \text{ }^\circ\text{C}$. Testing was done with the high heat flux chipset of $7 \times 7 \text{ mm}^2$ thermal footprint.

The measured chip interface temperature and cold plate thermal resistance at different flow rates are shown in Figures 7.16 and 7.17 as functions of the applied heat load. As expected, when the flow rate increased the chip temperature and the thermal resistance decreased. With increasing flow rates, the interface temperature decreased rapidly at first and then at a slower rate. It is further seen that, at a given heat load, for high flow rates (above 0.58 l/min) the interface temperature was almost constant and showed little decrease with increase of the flow

rate. It should be noted that flow rates beyond 0.9 l/min were not possible with the current setup due to the limited fluid supply pressure available at the inlet to the heat sink.

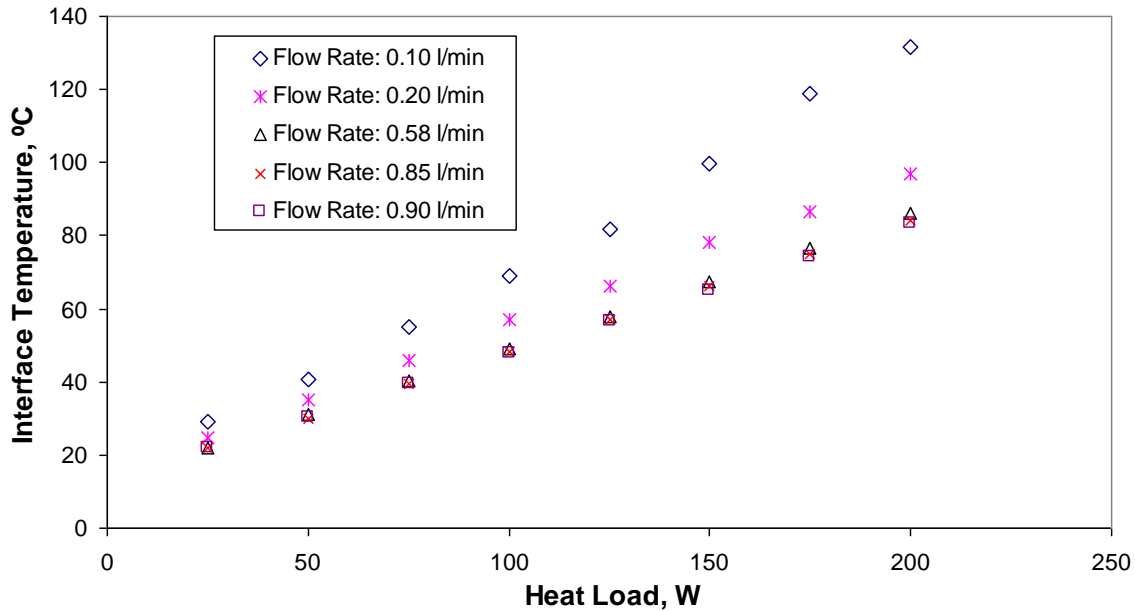


Figure 7.16 Heat load dependence of the interface temperature for the microchannel heat sink for different flow rates

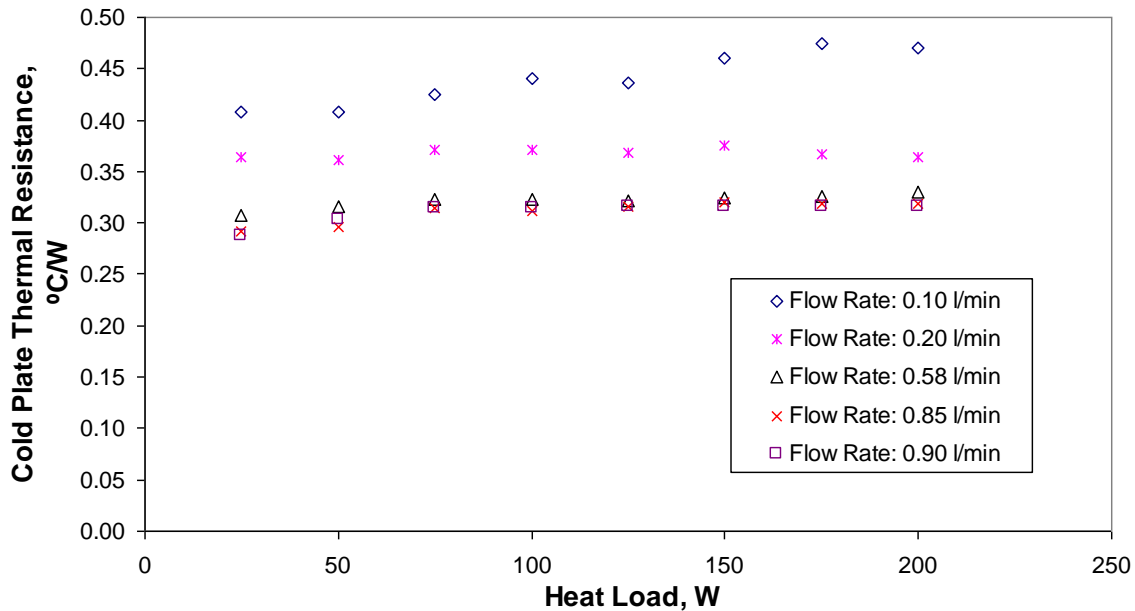


Figure 7.17 Cold plate thermal resistance of the microchannel heat sink with respect to the applied heat load for different flow rates

The same trend is noted for the cold plate thermal resistance. The initial increase in the flow rate corresponded to a notable decrease in the thermal resistance which then became nearly

constant for any further increase in the flow rate beyond 0.58 l/min at a given input power. For example at 100 W, the thermal resistance decreased from 0.44 to 0.32 °C/W as the flow rate increased from 0.10 to 0.58 l/min, whereas for the same power, the thermal resistance decreased from 0.323 to 0.315 °C/W for increase of flow rate from 0.58 to 0.90 l/min. This can be explained by considering the total thermal resistance through which heat has to pass starting from the heater top to the liquid. The total thermal resistance in this case is composed of a conductive resistance to spread heat in the metallic wall of the heat sink and the convective resistance to heat transfer from the channel inner wall to the coolant. Here, the conductive resistance is fixed by the physical properties and dimensions of the heat sink wall. With the initial increase in the flow rate, a considerable decrease in thermal resistance due to the enhancement of convective heat transfer from the channel wall to the liquid takes place. However, a point is reached when maximum possible decrease in the convective resistance is attained at a particular coolant flow rate. Beyond this, no further decrease is expected in the resistance which is now mainly of conductive nature. The effect of increase in the flow rate on the enhancement of the overall heat transfer coefficient is clear from the plot in Figure 7.18. For an input power of 100 W to the cooling section, as the coolant flow rate is increased from a low value of 0.1 l/min to high value of 0.9 l/min, the heat transfer coefficient increases from 1198 to 5246 W/m²K.

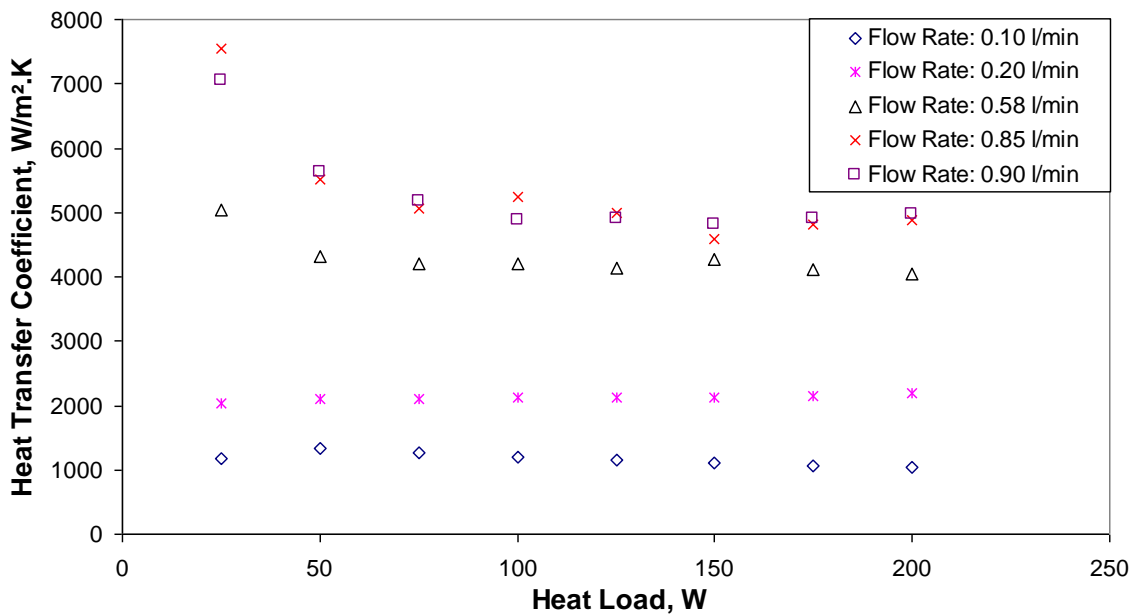


Figure 7.18 Heat transfer coefficient of the microchannel heat sink with respect to the applied heat load for different flow rates

7.6 Comparison of Experimental and Predicted Results

The experimental results are compared to the predictions obtained on the basis of the correlations formulated in Equations (7.10) – (7.19). Figure 7.19 presents the results of the comparison on the basis of the heat transfer coefficient versus applied heat load. The inlet conditions for the range of the flow rates pertain to the laminar regime. It is seen that the predictions made by the laminar flow correlations, that are based on different entry length conditions, always considerably over predict the heat transfer rate inside the microchannels. However, results predicted from the Dittus-Boelter correlation for the fully developed turbulent flow inside the channel gave good agreement with the experimental results.

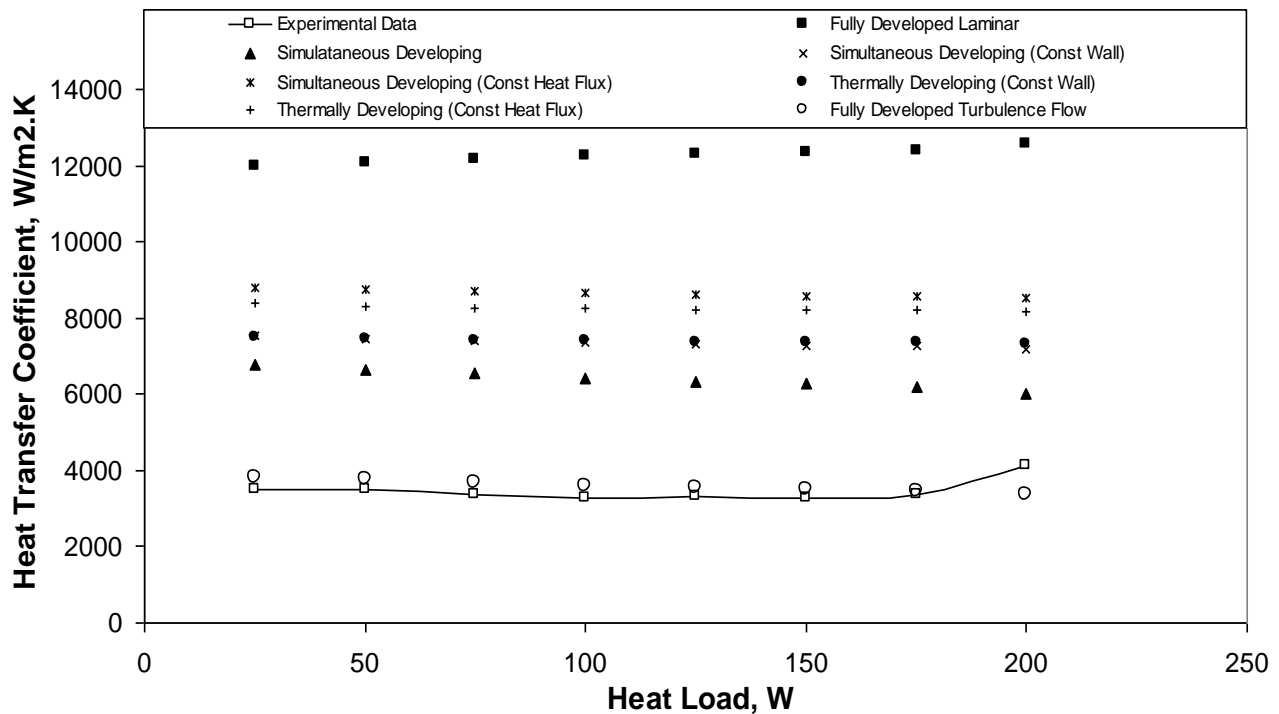


Figure 7.19 Variation of the heat transfer coefficient with applied heat load: Comparison of the experimental and the predicted results by using different entry length conditions and flow regimes

Basically, the heat transfer coefficient is highly associated with the flow conditions inside the channels. On account of the extremely small channels in the heat sink, the heating creates a sudden and large change in the liquid temperature. As a consequence, the thermophysical properties of the flowing liquid change dramatically. It has been reported by Wang & Peng (1994) that the Reynolds number for the experiments using the microchanneled structure was

usually approximately 500-1000 at the inlet and approximately 1800-2500 or larger at the outlet for the range of water flow velocities and other experimental conditions. This means that for water flow, the Reynolds number could be possibly doubled over the length of the microchannel due to change in viscosity with increasing temperature. For the fluids flowing through the microchannels, Wu & Little (1983) found transition to turbulence at a much lower Reynolds number than for conventional sized channels.

Results from the heat transfer experiments are compared to predicted values for a range of flow rates by taking dimensionless parameters (i.e. Reynolds number versus Nusselt number) as in Figure 7.20. In this situation also, the predicted results obtained by the laminar flow correlations over predict the heat transfer coefficient. With the fully developed turbulence correlation, agreement between the experiment and predictions is quite close. It is noted that at low Reynolds number, the experimental results match the predictions. As the Reynolds number increases the experimental results depart from the predictions.

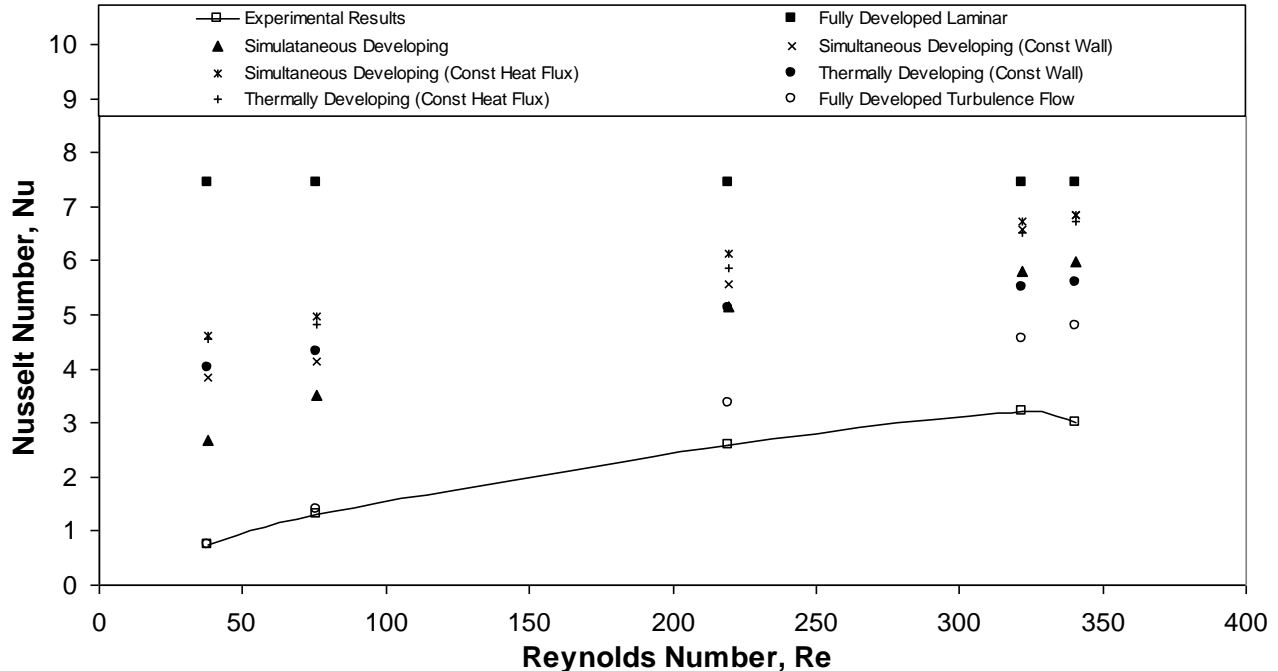


Figure 7.20 Variation of the Nusselt number with Reynolds number: Comparison of the experimental and the predicted results by using different entry length conditions and flow regimes

Various other reasons for these deviations (Morini, 2004) of the microchannel behaviour compared with convectional channels have been proposed by involving rarefaction, compressibility, viscous dissipation effects, surface conditions (roughness), property variation with temperature (as discussed above), electro-osmotic effect (electric Double Layer) etc. Reasons for this disparity (Lee et al, 2005) may also include uncertainties in channel geometry and temperature measurement in the experiments as well as a mismatch in the conditions for which the convectional correlations were proposed (circular tubes, different entrance and boundary conditions etc). It is critical therefore, that appropriate correlations which faithfully represent the geometry as well as the thermal and inlet boundary conditions in the experiments are selected for comparison. Different modified and dedicated correlations have been developed for the microchannels by researchers worldwide to give better agreement with the experimental obtained values (Lee et al, 2005).

It should be noted that the comparison study undertaken above does not take into account all the available correlations (for laminar and turbulent flow regime) from the literature for the prediction of heat transfer in the channels. As an outcome of the above study, it can be recommended that complete evaluation of validity of the conventional correlations (for large channels) for the prediction of the microchannel heat transfer could be done as an eminent contribution to heat transfer science.

7.7 Summary

A liquid cooled microchannel heat sink has been developed and characterized for thermal control of high heat flux electronic packages with water as coolant. The microchannel heat sink, made of copper and with a high aspect ratio of 17.5, has been tested under different power inputs (25 to 200 W) and flow rates (0.1 to 0.9 l/min). Two heat load simulators of different sizes, 7mm x 7mm and 11mm x 13 mm were evaluated as thermal test vehicles. With the 11x13 mm² chip, junction to mean fluid thermal resistances, R_{cp} were measured to be 0.08 to 0.11 °C/W and the overall thermal resistance, R_t for the assembly with the heat sink was 0.16 to 0.20 °C/W. while for the 7x7 mm² chip the corresponding values for the R_{cp} and R_t were 0.32 to 0.34 °C/W and 0.42 to 0.44 °C/W. The higher value of the 7x7 mm² chip thermal resistance compared to that for the 11x13 mm² chip is mainly attributed to the additional

spreading resistance at the heat sink base due to the miniature size of the former. Predictions of the heat transfer inside the micro channel were carried out on the basis of various correlations for the laminar and turbulent flow. The predicted results are compared to the experimental results and reasonably close agreement has been achieved by employing the turbulent flow correlation.

The next chapter discusses the potential of the liquid cooling based system with a sintered porous heat sink.

Chapter 8

Liquid Cooling using a Sintered Porous Heat Sink

The study of a sintered porous heat sink for the thermal control of the electronic microprocessors with extensive processing capabilities and miniature design has been carried out. Initially, a description of the heat sink prototype with body and wick structure made of copper has been given in detail. Then the experimental setup and the procedure followed to conduct the testing of the sample have been elaborated. The thermal performance of the sintered porous heat sink was assessed at different coolant flow rates (0.05 to 0.25 l/min) and thermal load inputs (10 to 150 W). The criterion that the maximum permissible temperature of the heat source should be within the 100 ± 5 °C range was used to determine the maximum heat load capability of the heat sink. Also, a comparison is made between the microchannel heat sink and sintered porous heat sink.

8.1 Introduction

Porous structures are effective and capable candidates for the thermal management of electronic devices. Wick structures made from plastic and metal powders are widely used as capillary pumping sources in two phase heat transfer systems. In single phase cooling applications, porous heat sinks made from metal foams, packed beds, and sintered metal powders provide an efficient heat transfer augmentation technique. Here, the capability of the porous media to increase the surface area in contact with the coolant and to intensify the fluid flow mixing helps to enhance the convective heat transfer between the fluid and the porous matrix. In the following section, an experimental investigation of a heat sink made from sintered copper powder has been carried out with the appropriate material as copper and working fluid as water in order to transfer high intensity thermal loads from computer microprocessors. The outcomes of the present experiment are aimed at finding a reliable thermal design for the thermal control of a desktop microprocessor with an extremely high heat flux (e.g 400 W/cm^2).

8.2 Description of the Sintered Porous Heat Sink Prototype

The layout of the sintered porous heat sink is shown in Figure 8.1 and consists of the bottom portion or the cold plate on which the porous structure is attached and the top cover arrangement for flow management.

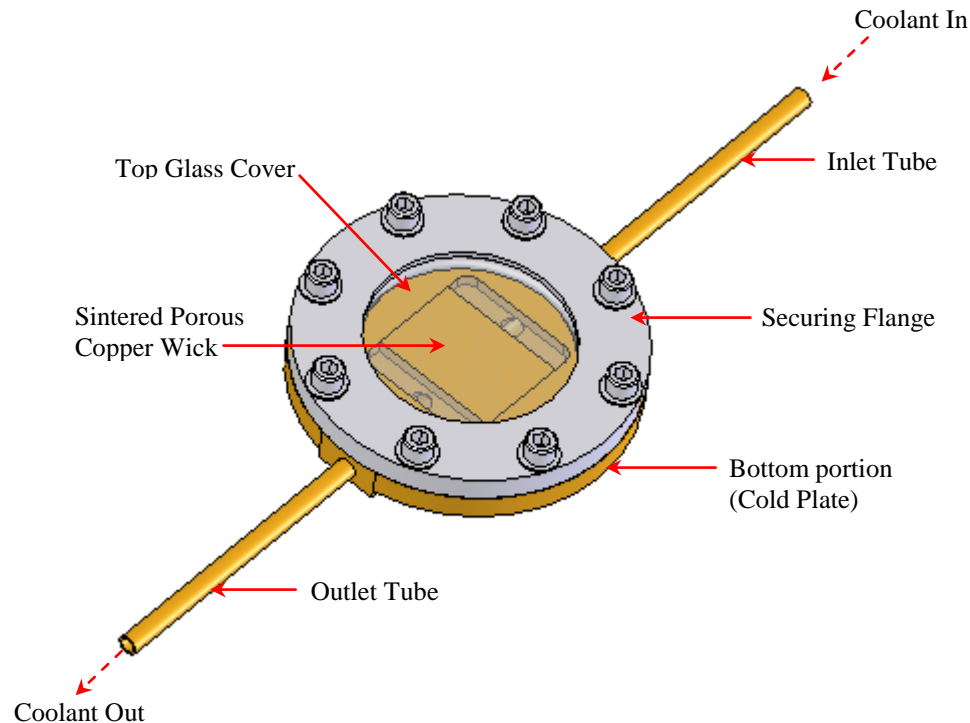


Figure 8.1 Layout of Sintered Porous Heat Sink

The bottom portion or lower housing block consists of a circular copper block of 50 mm diameter and 4 mm thickness. On the top face of the lower block, a rectangular section of 22mm (L) x 20mm (W) x 2 mm (D) was milled in which the porous structure of 14mm (L) x 20mm (W) x 2mm (H) was inserted such that it occupied the entire cross section of the channel as shown in Figure 8.2. On the diametrically opposite ends of the circular block, holes of 3.2 mm diameter were drilled that open into the inlet and outlet plenums located on either side of the porous insert in the form of ports. Inlet and outlet tubes were fixed into the drilled holes to provide coolant flow to the sintered porous heat sink. The inlet and outlet plenums also help in even distribution and proper streaming of the liquid through the porous matrix. Figure 8.3 shows a picture of the cold plate with the porous medium inserted inside the machined rectangular channel.

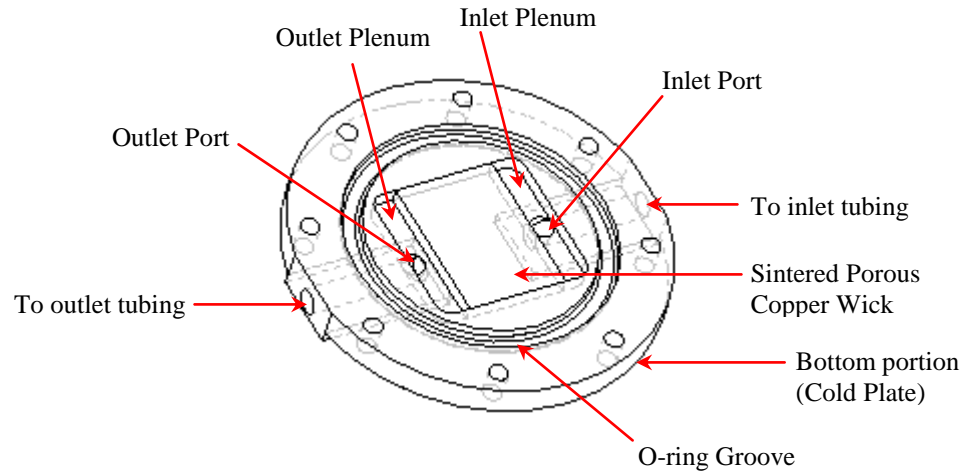


Figure 8.2 Internal structure of the Sintered Porous Heat Sink

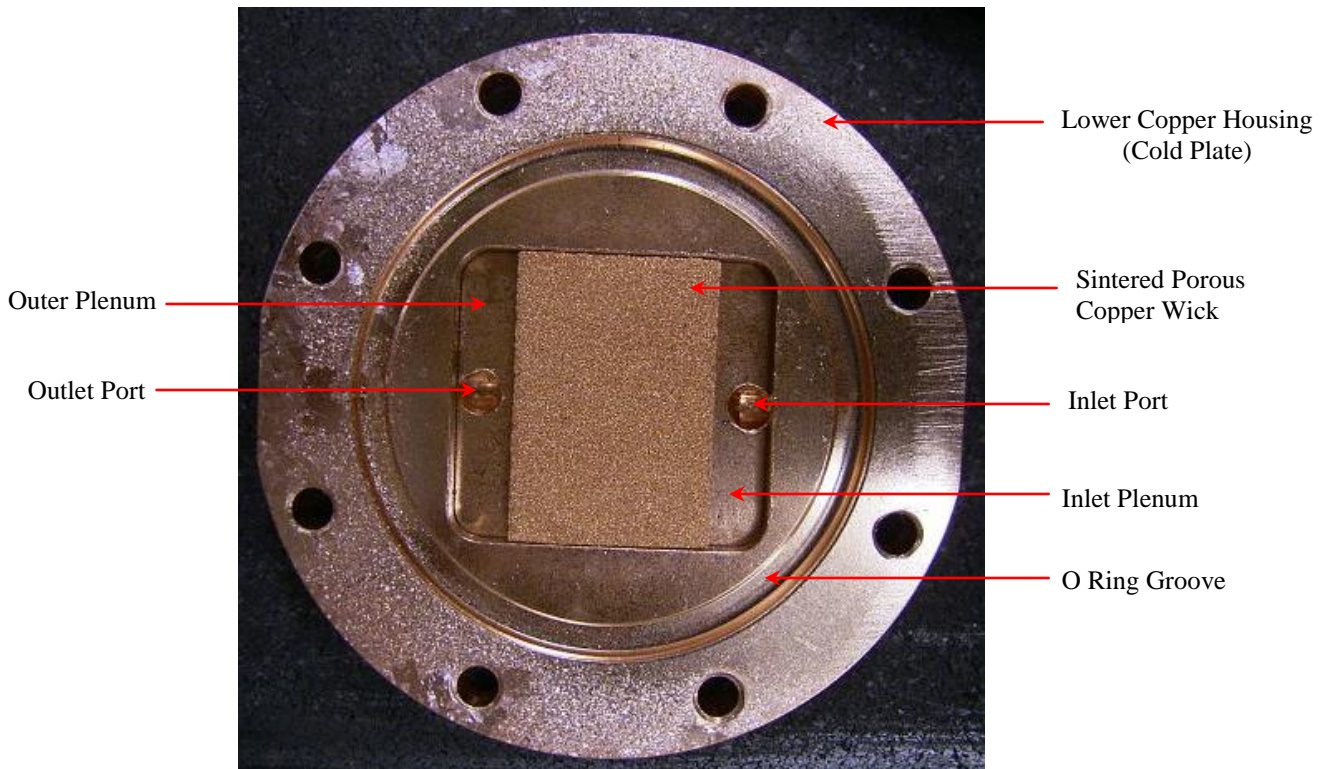


Figure 8.3 Picture of the cooling section showing the Porous Insert inside the machined rectangular channel

Figure 8.4 illustrates the main components of the sintered porous heat sink including an exploded view of the cooling section assembly. In order to direct the liquid flow through the porous matrix, it is enclosed from the top with a circular glass sheet which is kept in place with the help of a flange and nuts arrangement.

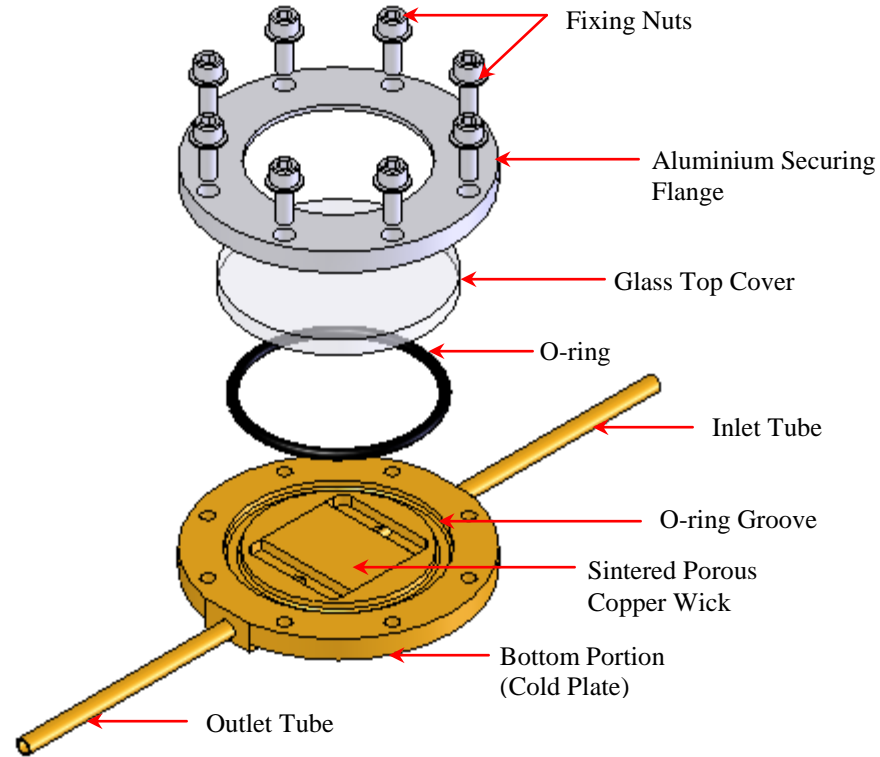


Figure 8.4 Exploded View of the Sintered Porous Heat Sink

The top of the wick should be perfectly flat and levelled with the glass cover to avoid any leakage of the coolant along the contact surface between the sintered porous plate and the glass cover. In the present model, a thin layer of Ethylene Propylene Diene Monomer (EPDM) rubber gasket (not shown in the Figure) was also placed on top of the porous plate for sealing the liquid flow. To prevent any external leakage of the liquid from the interface between the lower copper housing (bottom portion) and the top glass cover, a silicone O-ring seal was provided between them.

Sintered copper material was used as the porous medium in the model of the heat sink. The porous medium was manufactured by using copper granules of # 100-200 mesh size. The copper powders used in the porous sample had rounded irregular shaped particles that were sintered at a temperature slightly less than the melting point of copper in order to fuse and interlock the particles to form a porous matrix. The structure of the sintered porous material is presented in Figure 8.5. Physical properties like permeability, porosity, and maximum pore size of the porous medium were determined by the experimental techniques discussed in the Appendix C. Table 8.1 lists these flow properties of the sintered copper wick.

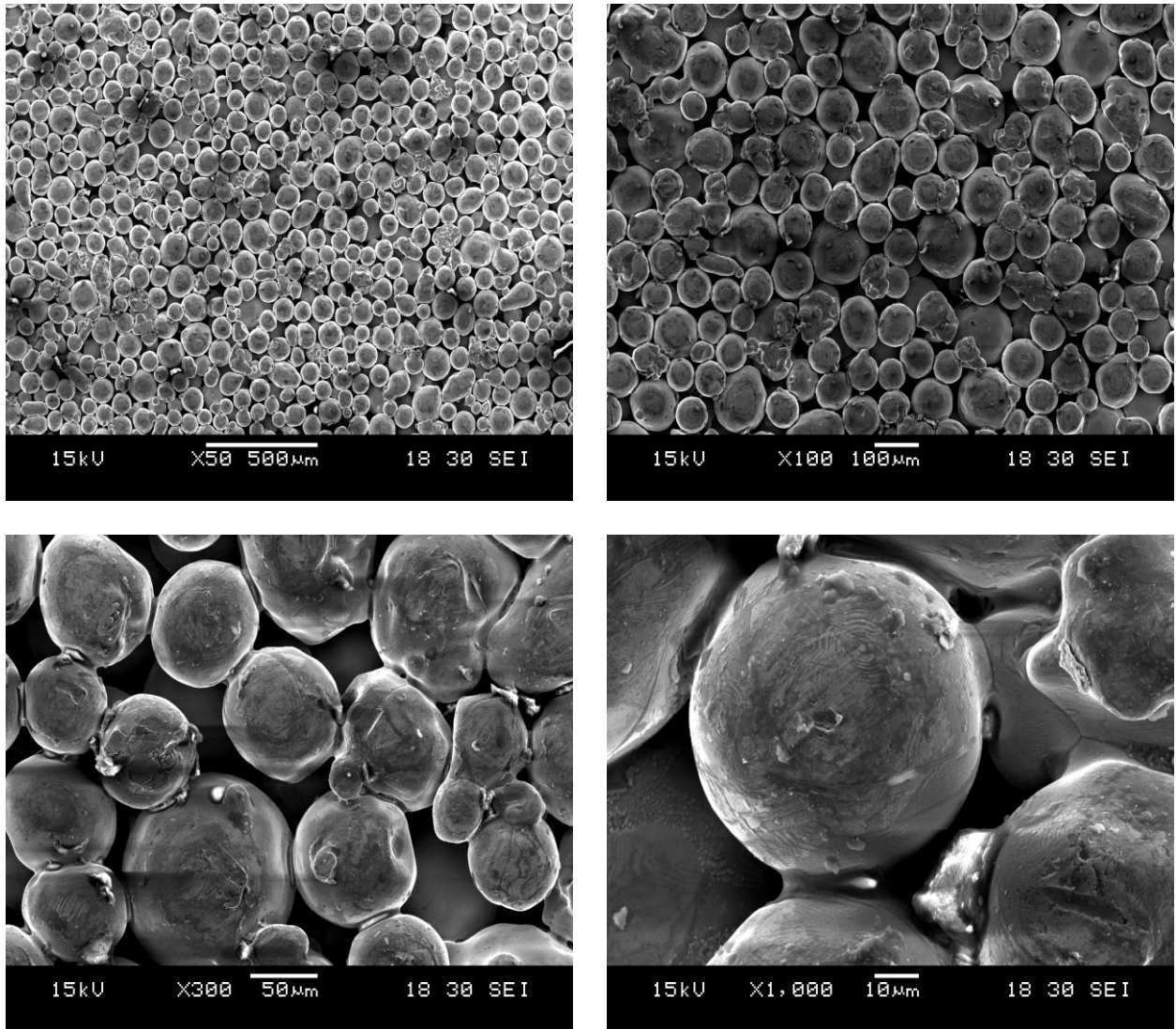


Figure 8.5 Sample of the sintered porous material at different magnifications showing rounded irregular copper granular particles fused together as the result of the sintering process

Table 8.1 Physical properties of copper wick (# 100-200 mesh size)

Physical Property	Value
Pore radius	< 30 μm
Porosity	40%
Permeability	$1.44 \times 10^{-11} \text{ m}^2$

The active area of the cooling section corresponds to the region on the cold plate which is occupied by the porous material and equals the area span by the liquid flow through the wick

i.e. 14mm (L) x 20mm (W). The coolant enters into the heat sink via the inlet tube, passes through the porous structure where it absorbs the heat conducted from the heat source attached at the bottom of the cold plate. After absorbing heat from the porous medium by convection, the coolant exits the heat sink through the outlet tube.

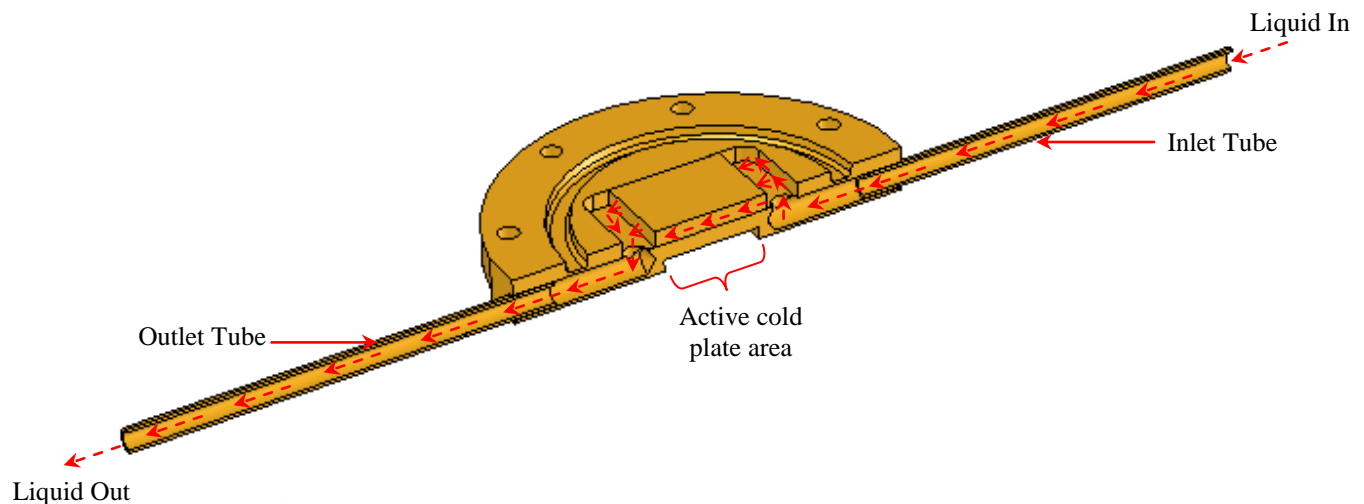


Figure 8.6 Cross Sectional view of the sintered porous heat sink showing the liquid flow pattern inside the cooling section

8.3 Experimental Setup and Test Procedure

The experimental system used to investigate forced convection heat transfer of liquid in porous media is shown schematically in Figure 8.7. The thermal performance of the heat sink was tested under a condition of non-uniform heating of the cooling section active zone using a 7mm x 7mm (0.49 cm²) heat source. In this case, heating was done on approximately 17.5% of the heat sink active zone. The heat load simulator was fabricated from a copper block with two embedded cartridge heater rods. It was symmetrically attached to the active zone at the bottom of the lower housing. Thermal insulation of the heat source was provided by a bakelite plate provided at the heater base. For proper thermal contact between the heater and the heat sink active zone, the required attachment pressure was provided by the base plate with the help of screw bolt arrangement. A layer of heat conducting grease was also applied on the active face of the heater to reduce the thermal resistance.

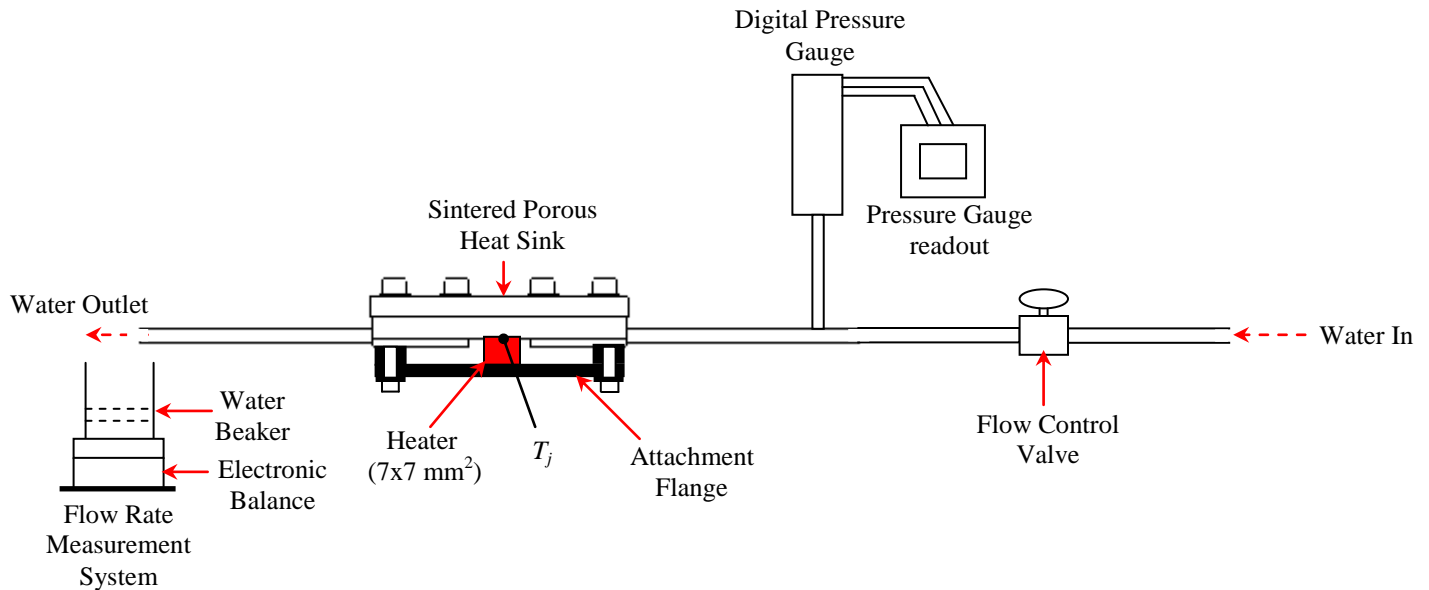


Figure 8.7 Experimental Setup of the Sintered Porous Heat Sink

The parameters measured in the experiment included the temperatures, pressure at the inlet to the heat sink, mass flow rate of the coolant and the input power to the heater. Eight T-type thermocouples with an accuracy of $\pm 0.5^\circ\text{C}$ were used to measure the temperature at different locations in the test facility as shown in Figure 8.8. To measure the interface temperature T_j at the heater-cold plate junction, a thermocouple was fixed in the groove that was machined in the center of the heater face. The external surface temperature of the active zone was determined by taking the weighted mean of readings of the three thermocouples attached to the lower housing. Two thermocouples were installed at the inlet and the outlet of the heat sink to measure the coolant liquid temperature at those points. To monitor and record the temperature at different points of the porous heat sink during testing, the thermocouples were connected to an Agilent HP34970A data acquisition system. The mass flow rate of the liquid was measured by weighing the liquid flowing out of the heat sink in a given time interval using an electronic balance. To set and measure the input power to the heater, a digital power meter with an accuracy of ± 0.1 W was used. The electrical power input to the heat was calculated from the input voltage and current. Water was used as the coolant in the experimental tests.

To conduct each test on the heat sink, the flow rate, input power and the inlet liquid temperature were fixed. All the measurements for temperature were made at steady state

conditions. Each experiment was run for several minutes until the fluid and thermal regimes inside the porous structure became stable. Steady state was assumed to occur when the fluctuations in the heat sink junction and wall temperatures were within ± 1 °C. The experiments were carried out in the range of average volume flow rate of 0.05 to 0.25 l/min in the channel with the porous insert and heat load in the range of 10 to 150 W. The inlet temperature of the liquid was maintained at 20 ± 2 °C.

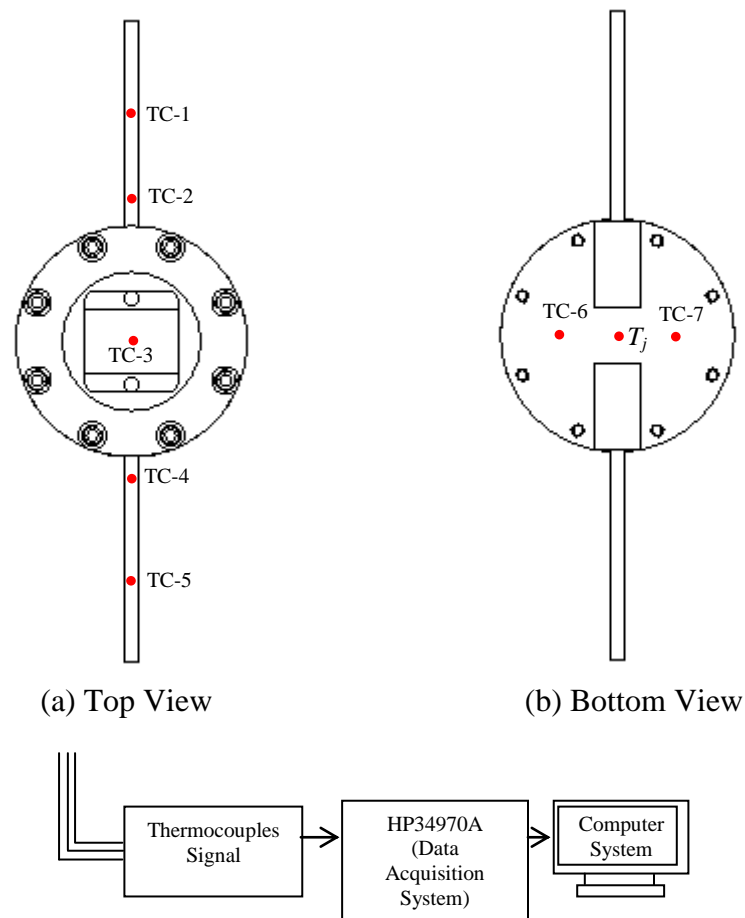


Figure 8.8 Test Facility for the Sintered Porous Heat Sink showing the location of the thermocouple points

8.4 Data Reduction

The measured temperatures at different points were used to calculate the thermal performance of the sintered porous heat sink on the basis of the interface/junction temperature, overall heat

transfer coefficient and cold plate (interface temperature to fluid mean temperature) thermal resistance.

The overall heat transfer coefficient from external wall to liquid is defined as:

$$h_o = \frac{Q_a^\bullet}{A_{pb}(T_{wl} - T_{mf})} \quad (8.1)$$

where, Q_a^\bullet is the heat load applied to the surface of the heater adjacent to the porous sample. The heat losses from the heater surface and bottom surface of the heat sink to the ambient are considered negligible due to the small size of the relevant areas. A_{pb} is the area of the porous block attached to the channel inside the lower housing of the heat sink. T_{wl} is the external weighted mean wall temperature of the heat sink measured by the thermocouples on the external surface of the heat sink and T_{mf} is the average liquid temperature calculated as the mean of the inlet and the outlet temperatures of the liquid in the test section.

The thermal resistance of the test section R_{cp} was calculated on the basis of the junction or interface temperature, T_j and the liquid mean temperature T_{mf} as follow:

$$R_{cp} = \frac{(T_j - T_{mf})}{Q_a^\bullet} \quad (8.2)$$

The flow rate of the water was controlled by adjusting the flow control valve and was measured by the weighing method. The temperatures at the inlet, outlet and wall of the heat sink were measured by K-type thermocouples with an uncertainty of ± 0.1 °C. For the measurement of the input power, the uncertainty of the power meter reading was ± 0.1 W. The error in determining the overall heat transfer coefficient h_o , according to Equation (8.1) is formed from an estimation of the measurement error of the following values: Q^\bullet - input heat load, $T_{f,i}$ and $T_{f,o}$ - average of the input and the outlet temperatures of the liquid coolant, $T_{wl} - T_{mf}$ - difference between the average value of the wall and liquid temperatures. The uncertainty of h_o was estimated to be within $\pm 17.7\%$. For the thermal resistance the uncertainty was estimated to be $\pm 7.9\%$.

8.5 Results and Discussion

8.5.1 Pressure Drop

Figure 8.9 shows the pressure drop through the sintered porous matrix as a function of the volume flow rate of the coolant. The pressure drop in the porous medium significantly increased with increasing flow rate. It is clear from the graph that even for smaller flow rates, large pressure drops are encountered. This is due to the micro porous structure of the wick which has a pore radius of order less than $30\ \mu\text{m}$. As the characteristic hydraulic diameter of flow channels (i.e. micro pores) is very small there occurs an increase in the flow resistance. In addition, the contact area between the coolant and the porous matrix is very high which produce high flow resistance losses.

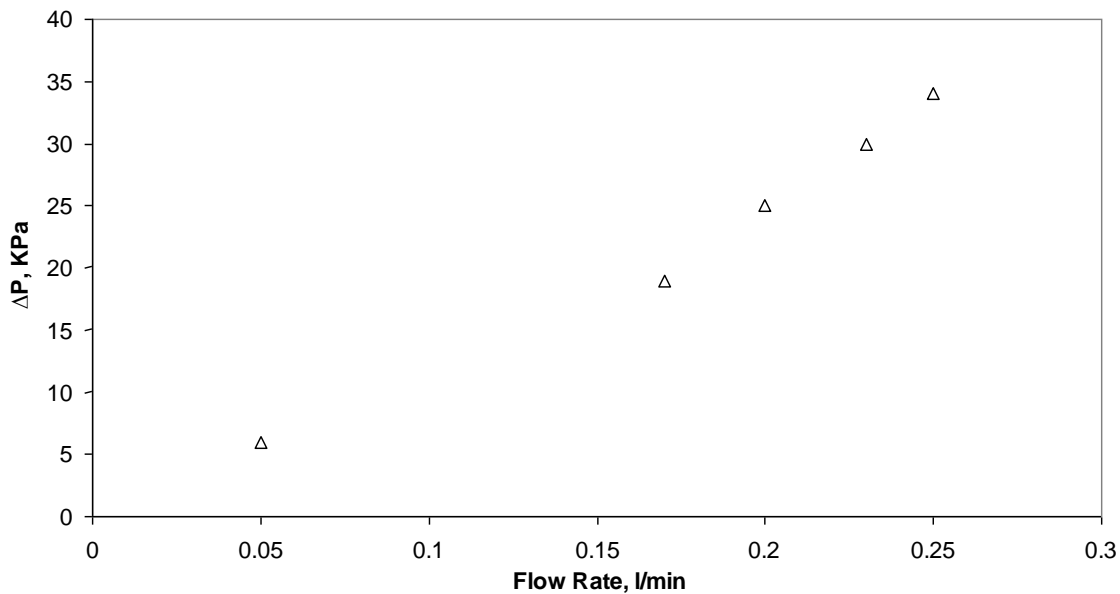


Figure 8.9 Pressure drop versus flow rate for the Sintered Porous Heat Sink

8.5.1 Heat Transfer

Dependence of the interface temperature on the flow rate of the coolant for 100 W input heat load is presented in Figure 8.10. The temperature at the heater-heat sink junction shows a decrease with increase in fluid flow rate. For example, as the flow rate increases from 0.2 to 0.25 l/min, the interface temperature reduces by $17.9\ ^\circ\text{C}$. Figure 8.11 shows the relationship between the interface temperature and the applied heat load for different flow rates from 0.05 to 0.25 l/min. It is noted that the trend between the interface temperature and heat load at a given flow rate presents a monotonic variation. The heat sink was able to transfer a maximum heat load of 140 W at 0.25 l/min while maintaining the interface temperature below $100\ ^\circ\text{C}$. In

this study, the sink was not tested for flow rates beyond 0.25 l/min due to the limitation on the maximum available water supply pressure at the inlet of the cooling section.

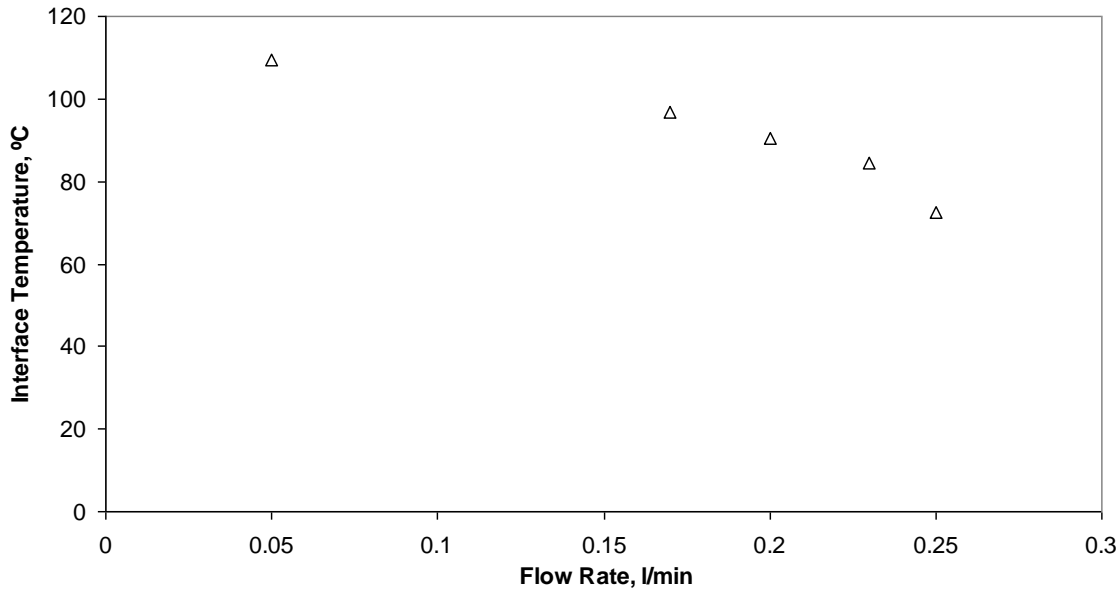


Figure 8.10 Interface temperature versus flow rate for applied heat load of 100 W

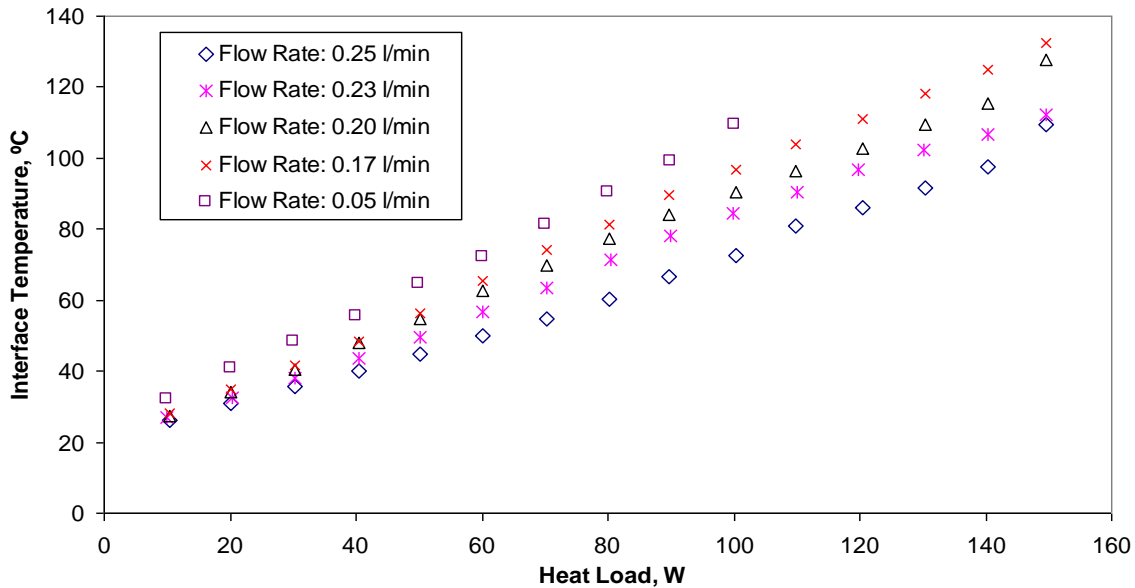


Figure 8.11 Relationship between the interface temperature and the applied heat load for different flow rates

Similar trends were observed for the heat transfer coefficient h_o of the sintered porous heat sink as depicted in Figure 8.12. For the given flow rates and over the range of applied heat loads (10 to 150 W), constant values were achieved for h_o . It should be noted that the magnitude of h_o has a strong dependence on the area involved in heat transfer. In the present

case, the area used to calculate h_o is the external active zone of the heat sink i.e. the area where sintered structure is present.

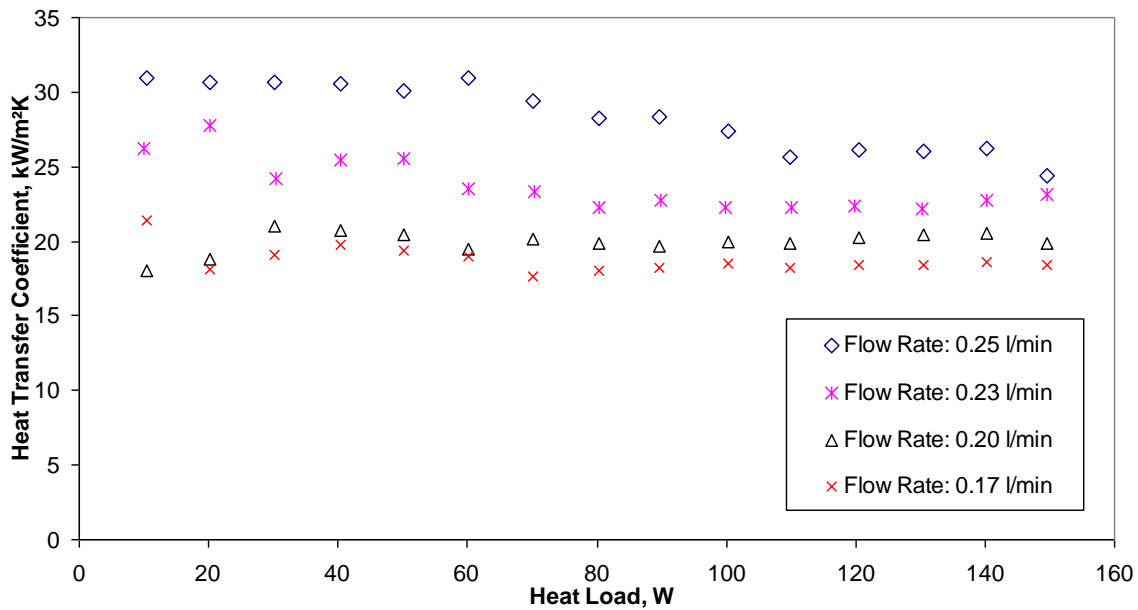


Figure 8.12 Heat transfer coefficient versus applied heat load for different flow rates

Figure 8.13 shows the cold plate thermal resistance “calculated on the basis of the interface temperature and the mean liquid temperature” of the sintered porous heat sink. For the applied heat load (10 to 150 W) and the given flow rate, near constant values of R_{cp} were obtained. For example, at flow rate of 0.25 ml/min, R_{cp} was approximately 0.48 °C/W whereas for 0.20 l/min, R_{cp} values of 0.71 °C/W were obtained.

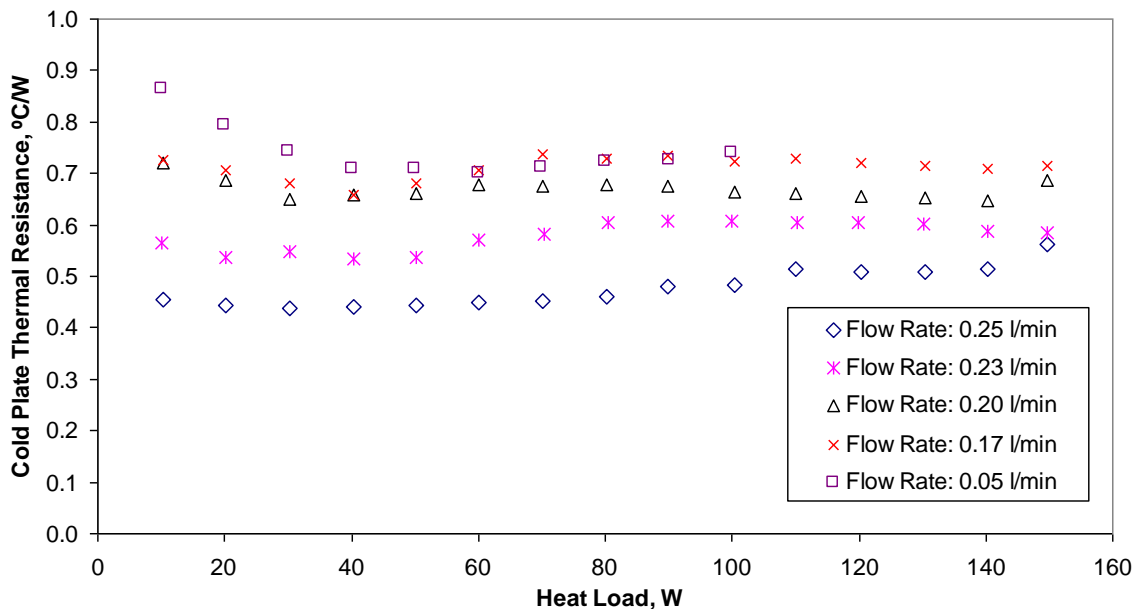


Figure 8.13 Cold plate thermal resistance versus applied heat load for different flow rates

To study the variation of the cold plate thermal resistance with respect to the flow rate of the coolant, Figure 8.14 is used. It is noted that for the given change in the coolant flow rate, the reduction in the cold plate thermal resistance is much higher at high flow rates than compared to the lower flow rates. As an example, a change in flow rate from 0.17 to 0.23 l/min produces a decrease of 0.06 °C/W in R_{cp} whereas for the change of 0.23 to 0.25 l/min in flow rate the corresponding decrease in the R_{cp} is 0.13 °C/W, which is nearly double the previous case. This can be to the dominant viscous pressure losses inside the porous heat sink at low flow rate. As the flow rate increases, the viscous losses are counterbalanced and the flow is properly channeled through the bulk of the porous matrix.

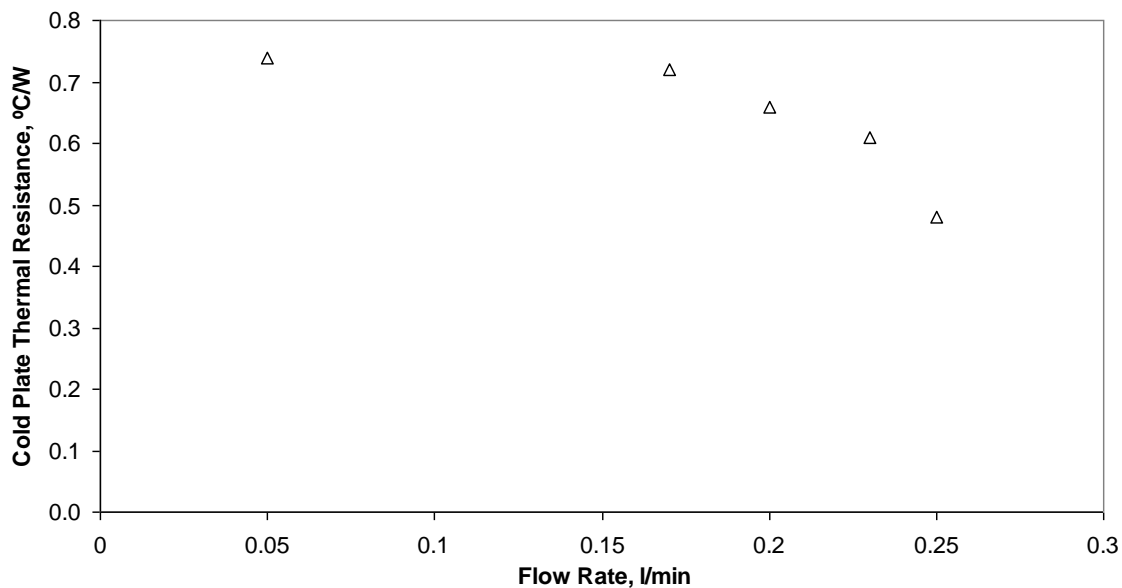


Figure 8.14 Cold plate thermal resistance versus flow rate for applied heat load of 100 W

8.6 Comparison of Thermal Performance of Microchannel and Sintered Porous Heat Sinks

The thermal performance of the two types of the heat sink i.e. the Microchannel Heat Sink (MHS) and the Sintered Porous Sink Heat (SPHS) is compared at different flow rates with the help of Figure 8.15. It is noted from the figure that the cold plate thermal resistance of the microchannel heat sink is lower than that of the sintered porous heat sink for the same condition of heating using the 7mm x 7mm (i.e. 0.49 cm²) heat source. For the same volumetric flow rate of the coolant (0.2 l/min) and same cross sectional area of liquid flow, the R_{cp} for the porous heat sink is nearly two times that of the microchannel heat sink. Even

for higher flow rates through the porous sink (around 0.25 l/min), its R_{cp} values are still higher than the microchannel sink with a flow rate as low as 0.10 l/min. This difference in the thermal performance of the two heat sinks can be explained by taking into consideration the structural design and the thermal conductivity of the two heat sinks.

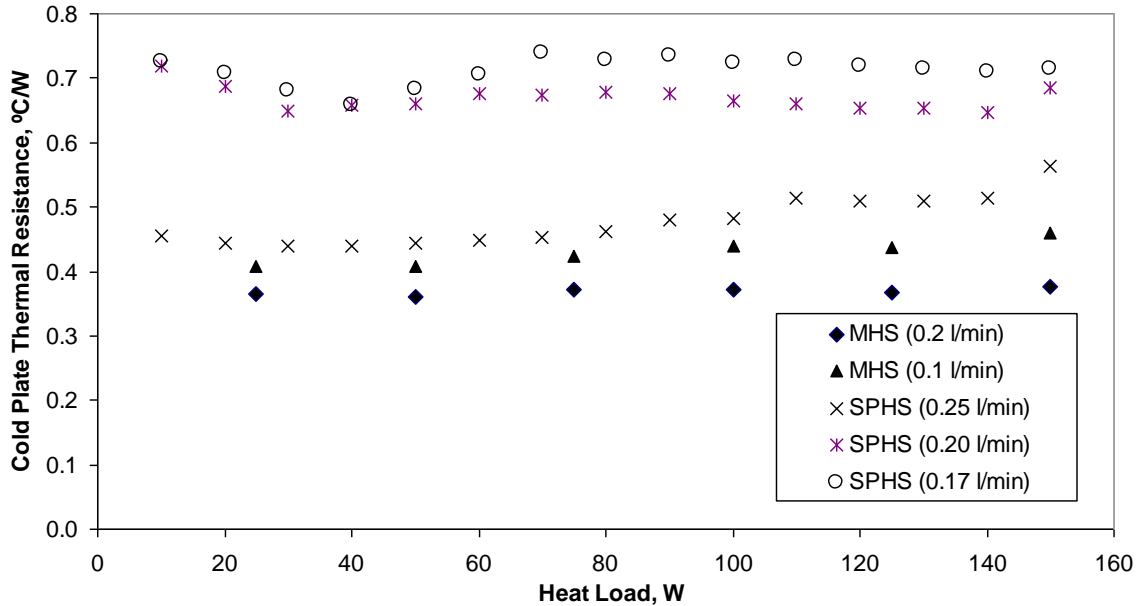


Figure 8.15 Comparison of the cold plate thermal resistance for Microchannel and Sintered Porous Heat Sinks

Even though the porous matrix used in the sintered heat sink is made from high conductivity copper, the effective thermal conductivity of the matrix is lower than the heat conductivity of the bulk material making up the porous structure. Due to high porosity (around 40% in the present case) of the wick structure, the total contact area between the two adjacent layers in the same horizontal plane of the sintered structure is small which increases the resistance of the porous matrix. It was experimentally determined (as explained in Appendix C) that the effective thermal conductivity of the copper wick saturated with water is as low as 32 W/m.K compared to the high value of 380 W/m.K for the thermal conductivity of copper from which the wick structure is made. In the case of the microchannels, the heat is transferred to the liquid from the heated channel walls. As the channel walls or microfins are machined directly on the cold plate and form an integral part of the heat sink, their resistance is lower than that of the porous structure. Another thing to note is that the attachment of the porous heat sink to the machined channel is achieved by a heating or sintering process. Here, the surface attachment between the two largely dictates the heat transfer performance of the heat sink. In

the case of poor attachment, the heat sink can suffer from vapour bubble formation on the heated active zone. Also, at higher heat fluxes the probability of vapour bubble formation inside the porous structure arises more from the higher flow resistance and torturous path followed by the liquid through the wick matrix. The internal pore volume of the porous structure can also contain dead and closed spaces inside the matrix which can instigate vapour bubble formation which can eventually increase resistance and hence increase the cold plate (i.e. cooling section) temperatures.

The thermal performances of each of the heat sinks are also compared on the basis of the overall heat transfer coefficient, h_o that is calculated on the basis of the applied heat load Q^* , heater footprint area A_h and difference in the heater junction temperature, T_j and fluid mean temperature, T_f at the inlet and outlet as follow:

$$h_o = \frac{Q^*}{A_h (T_j - T_{mf})} \quad (8.3)$$

Figure 8.16 shows comparison of the relationships between the overall heat transfer coefficient and applied heat load for different flow rates.

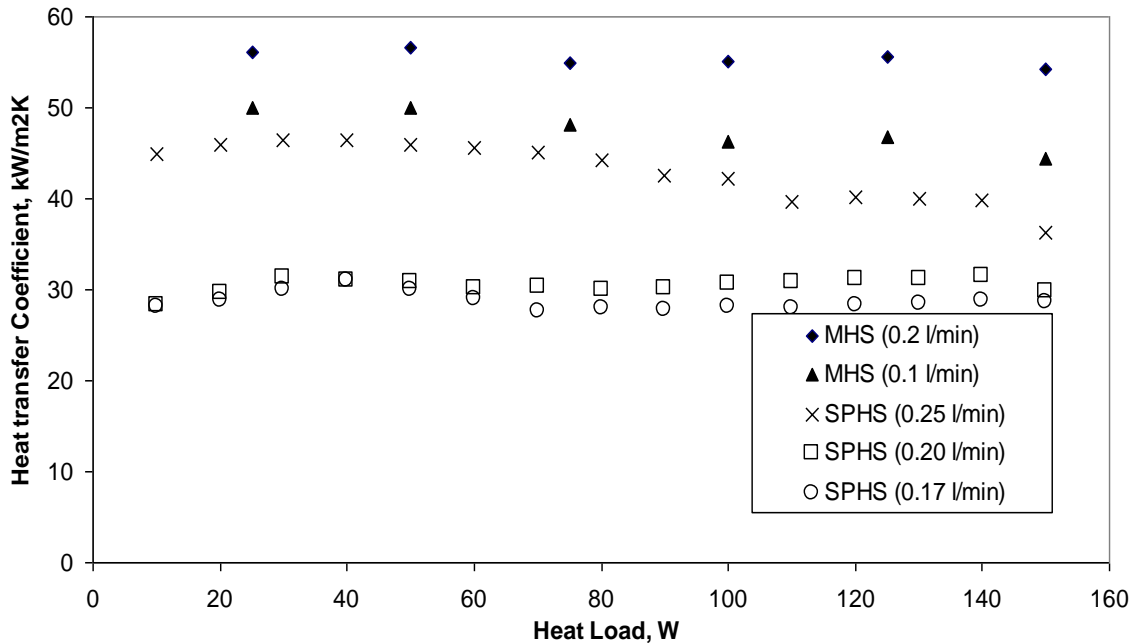


Figure 8.16 Comparison of the overall heat transfer coefficient (based on the heater active face area) for Microchannel and Sintered Porous Heat Sinks

It is evident from the graph that the overall heat transfer coefficient of the microchannel heat sink is quite high (nearly 1.8 times) compared to that of the sintered porous heat sink. Clearly, the performance characteristics of the microchannel heat sink is superior to that of the sintered porous heat sink over the entire range of the applied heat load.

Figure 8.17 shows a comparison of the two types of heat sinks on the basis of pressure drop across the heat sink versus flow rate. It is obvious from the graph that for a given flow rate, the pressure drop across the microchannel heat sink is very low as compared to that of the microporous heat sink. This is due to the very small radius of the pores ($< 30 \mu\text{m}$) and the tortuous path followed by the liquid in the porous structure which increases the hydraulic pressure losses.

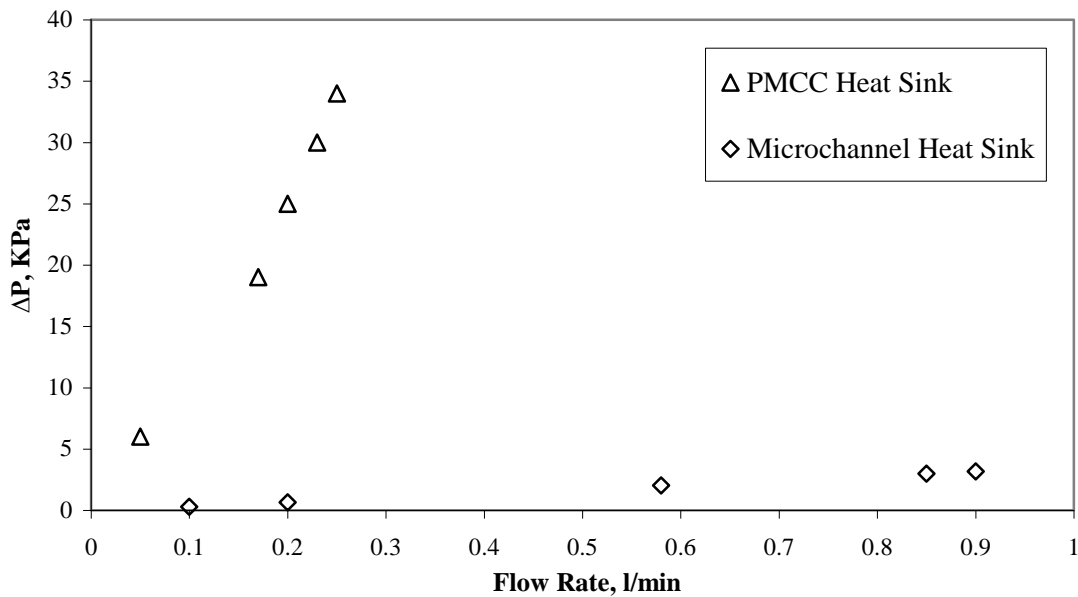


Figure 8.17 Comparison of the pressure drop across the heat sink versus flow rate for Microchannel and Sintered Porous Heat Sink

It should be noted that the comparison is made on the basis of single configurations of the microchannels and porous material and therefore provides a limited comparison of the two types of heat sinks. In order to draw more general conclusions an exhaustive study could be done of the microchannel heat sink with different aspect ratios (fin height/fin width) and porous structures with different flow properties (porosity, permeability and pore size). Such a study is recommended to comprehend the overall potential of two types of heat sink.

8.7 Summary

A heat sink based on a porous copper wick for cooling high powered microprocessors was investigated experimentally. Heat fluxes of up to 2.8 MW/m^2 were removed by using forced liquid cooling via a porous sample with a porosity of 40% and pore radius less than $30 \text{ }\mu\text{m}$ while maintaining the interface temperature within the permissible limit of $100 \pm 5 \text{ }^\circ\text{C}$. An estimate of the thermal performance of the sintered porous heat sink showed a cold plate thermal resistance, R_{cp} of $0.48 \text{ }^\circ\text{C/W}$ at flow rate of 0.25 ml/min and input power of 150 W . It has been noted that effective heat transfer in the sintered porous heat sink is accomplished by a drastic increase in the pumping power. This means that the principle of using the sintered porous heat sinks can be justified in micro electronics of high power if there are no limitations on pumping power. Also, a comparison of the sintered porous heat sink was done with the microchannel heat sink which showed the superior performance of the latter over the former.

In the next chapter, comparative study has been carried out between two-phase systems based on a heat pipe module and single phase cooling systems based on the microchannel based liquid cooling.

Chapter 9

Comparative Study: Two-Phase Vs Liquid Cooling

In the present chapter, a comparative study has been carried out for two-phase and single-phase cooling systems. Two prototypes; one with a heat pipe module and the second with microchannel based liquid cooling were developed to carry out the investigation. Description of both cooling units is given in detail. The thermal performance of each cooling unit was assessed and compared on the basis of a single heat source as well as multiple heat sources.

9.1 Introduction

It has been predicted by chip manufacturers that the heat dissipation requirements of chipsets will continue to increase in future due to the increase in their processing speed and addition of new capabilities to the electronic systems. In the previous chapters, comprehensive investigation of various thermal designs for the cooling of electronic devices particularly computer systems has been done. The main aim of the study was to devise potential cooling devices that can serve the cooling requirements of the new generation high powered microprocessors as well as providing reliable thermal management for future systems. Different prototypes that were developed were based on two-phase or single phase heat transfer. It is established from the experimental outcomes that two-phase systems based on capillary pumping of the heat transfer fluid acts as very reliable thermal control devices. These devices were able to handle heat fluxes up to 50 W/cm^2 given out by the laptop microprocessors and can be favorably accommodated in the limited available space. Nonetheless, the heat transfer capability of these systems is limited by their reliance on inactive fluid circulation and associated low mass flow rates. For handling extremely high heat fluxes, liquid cooling systems that are based on forced convection heat transfer can be considered as a viable option. With these pumped systems extremely high heat fluxes can be removed and transferred. In the study, single phase liquid cooling systems were able to handle extremely high heat flux up to 4 MW/m^2 . As the current research work is focused on the thermal capabilities of the two-phase and single-phase cooling methods, it can be consider as a fruitful contribution to the body of knowledge to compare the thermal

performance of these two types of technology.

All of the investigated thermal designs were intended to handle heat load dissipated by a single heat source. As processing and graphic capabilities in computers are being enhanced, more processing units with high heat dissipating capacity are being added to the main board. As an example, in new laptop computers with enhanced graphic and high data processing potential, the graphics and the memory tasks are separated from the Central Processing Unit (CPU) and assigned to dedicated chipsets which are known as Graphical Processing Unit (GPU) and Memory Processing Unit (MPU) respectively. This has given rise to the problem of cooling multiple heat sources. In the light of the above discussion, a brief study has been conducted to compare the thermal performance of two-phase and single phase heat transfer in cooling of single and multiple heat sources. It should be noted that the thermal modules used in this comparative test i.e. heat pipe module and microchannel heat sink module are standard thermal products developed by Fujikura Ltd. Japan. The main objective of this study is to compare and point out advantages and disadvantages of these two methods of cooling.

9.2 Experimental Setup and Test Procedure

In order to carry out the intended objective, two investigative prototypes of thermal module were built. The first prototype was based on the two phase cooling and consisted of a heat pipe module as a passive operating heat transfer device. In the second sample, thermal control was accomplished by means of liquid cooling using a microchannel structure.

9.2.1 Heat Pipe Cooling Unit (Two-Phase Heat Transfer System)

The unit as shows in Figure 9.1 consists of a flattened heat pipe with fibre composite wick, fin heat exchangers and centrifugal fans. The heat pipe which is initially made in cylindrical form is flattened by pressing it so as to accommodate it in the available thickness and to provide better contact with the heat source active footprint. In the unit, the heat pipe is attached to the copper die-cast plate by soldering. Two finned condensers are installed on each end of the heat pipe. For better surface contact, thermally conductive epoxy is used between the fins and heat pipe surface. The cooling of the condensers is accomplished by means of forced air convection using two centrifugal fans each with a flow rate of $0.1 \text{ m}^3/\text{min}$ (at 5 V, 0.1 A).

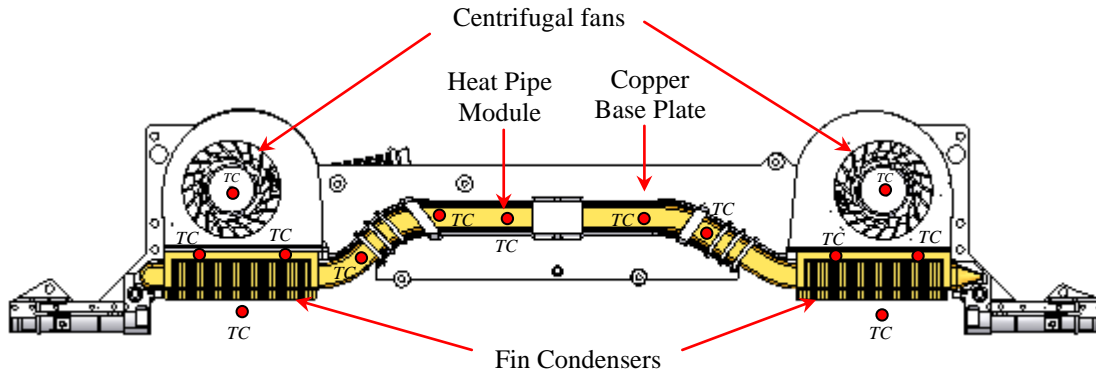


Figure 9.1 Heat Pipe Cooling Unit
 Note: TC denoted thermocouple location

The heat pipe as shown in the Figure 9.2 was made of copper with composite fibre wick structure. The heat pipe prototype had rectangular cross section (2 mm x 8 mm) and total length of 300 mm. In this case, the shape of the heat pipe was restricted by the location of the three heat sources and heat sink. The so called composite fibre wick (FB-G) consisted of very fine axial grooves on the internal wall of the heat pipe and a bundle of copper fibres (Figure 9.3).

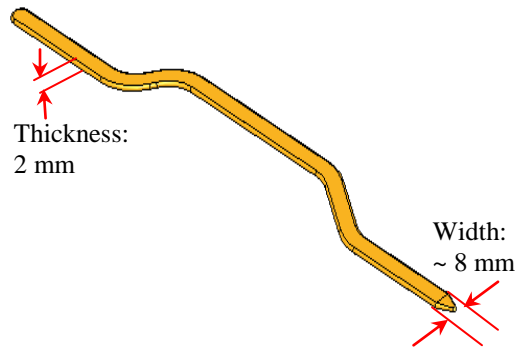


Figure 9.2 Heat Pipe Module

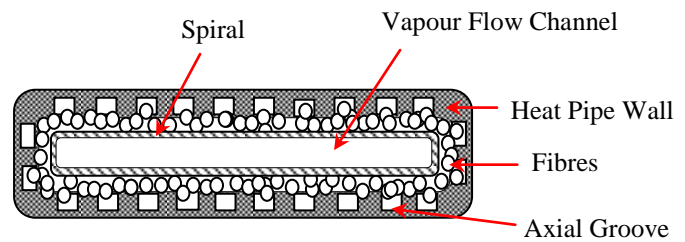


Figure 9.3 Cross Section of the Heat Pipe showing internal configuration

For the best performance of the heat pipe, the wick structure should have high capillary limit and permeability. Capillary forces are required for continuous circulation of the working fluid inside the heat pipe whereas high permeability is needed for better heat transfer capabilities. In contrast to the traditional heat pipes with only a groove wick or fibre wick, a composite fibre wick (FB-G) helped to provide an optimum combination of capillary head using the fibre wick and permeability using the axial grooves. The fibre bundle which was uniformly distributed around the internal circumference of the heat pipe was kept in good thermal

contact with the wall using a spiral retainer as shown in Figure 9.3. Internal voids between fibres acted as micro pores and provided capillary pumping of the working fluid from the cold end of the heat pipe to the hot end. The main dimensions of the miniature heat pipe are listed in Table 9.1.

Table 9.1 Geometrical Dimensions of the Heat Pipe Prototype

Parameter	Dimension (mm)
<i>Heat Pipe Thickness</i>	2
<i>Heat Pipe Width</i>	8
<i>Heat Pipe Extended Length</i>	300
<i>Wall thickness</i>	0.24
<i>Groove Thickness</i>	0.075
<i>Fibre diameter</i>	0.05

It is worth mentioning that non-condensable gases degrade the performance of the heat pipe significantly. Proper cleaning and degassing of the heat pipe was done before charging. Heat transfer capacity of the miniature heat pipe depends more critically on the volume of the working fluid (Faghri, 1995) than with a conventional heat pipe. After vacuuming, 20-25 % of the internal volume of the heat pipe was charged with pure deionised water.

For the proper working of a heat pipe, the net capillary pressure generated by the porous structure, in this case axial grooves and fibre wick, should be greater than the total pressure losses taking place inside the system, this includes vapour pressure losses inside the evaporator and adiabatic region (ΔP_v) and liquid pressure losses inside the condenser and wick structure (ΔP_l). The design criterion can be summarized by relation below:

$$(\Delta P_{cap})_{max} > \Delta P_v + P_l \quad (9.1)$$

In this case, there are three heat sources that need to be cooled by the heat pipe module. Copper plates with dimensions equal to the active footprints of the respective heaters were soldered at the evaporator sections of the heat pipe (Figure 9.4) which helped to provide reliable thermal interface with the heat sources. A thermally conducting grease was also used between the evaporator-heater junction for better heat transfer. An attachment pressure was

applied on each of the heat sources to avoid any air gaps in the interface (Figure 9.5) and to provide metal to metal contact between heater and evaporator plate. The three heat load simulators had active thermal footprints of $25 \times 25 \text{ mm}^2$ (MPU), $25 \times 25 \text{ mm}^2$ (GPU) and $10 \times 10 \text{ mm}^2$ (CPU). The maximum heat dissipation capacity of the three heat load simulators were 40 W for CPU, 25 W for GPU and 25 W for the MPU unit. Each of the heat sources was made from a copper block embedded with two cartridge heaters.

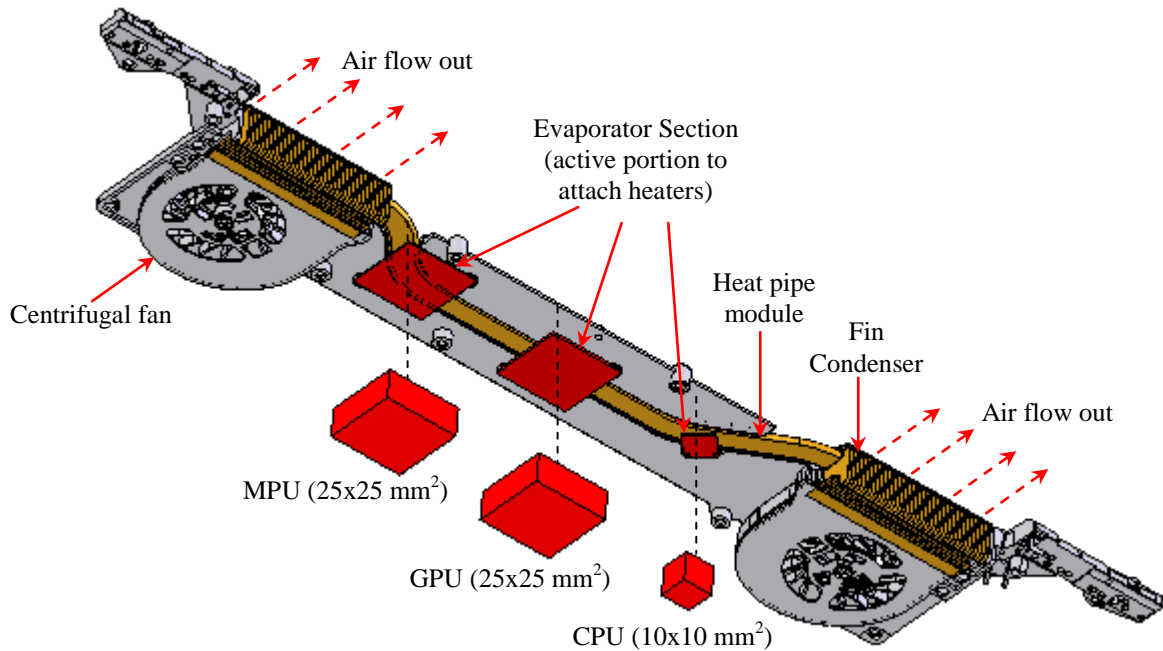


Figure 9.4 Bottom perspective view of the Heat Pipe Cooling Unit showing the evaporator sections and related components.

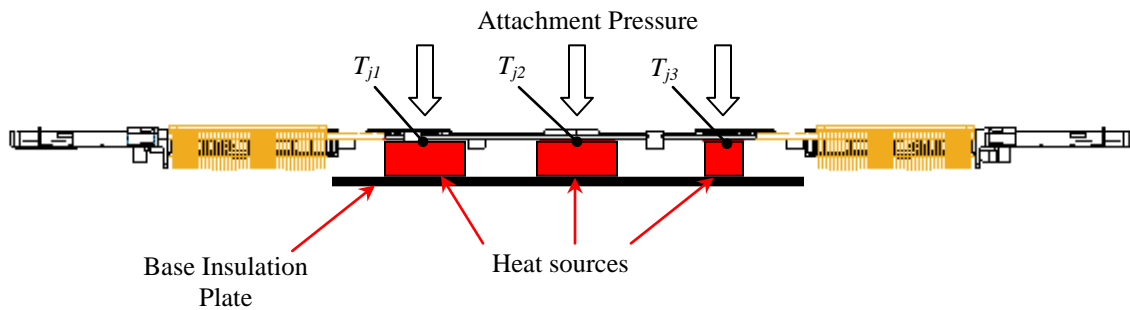


Figure 9.5 Side View of the Heat Pipe Cooling Unit showing the heater locations

9.2.2 Liquid Cooling Unit (Single Phase Heat Transfer System)

In the single phase cooling unit, a rectangular channel was machined all along the periphery of the copper base plate (Figure 9.6). The inlet and outlet to the liquid channel were connected to a centrifugal pump by copper tubes. The centrifugal pump made by SEPA Company with maximum flow rate of 0.43 l/min under 60 cm water head and operating under max 12 V & 0.2 A was used to circulate liquid through the loop. Two finned heat exchangers were installed on the outer surface of the channel and soldered to the base plate. For cooling the heat exchanger, two centrifugal fans, each with air flow rate of $0.1 \text{ m}^3/\text{min}$ (at 5 V, 0.1 A), were used. Figure 9.6 shows a schematic of the liquid cooling unit. The outlet of the pump line was connected with the main module and charging/evacuating line with the help of a three way connector.

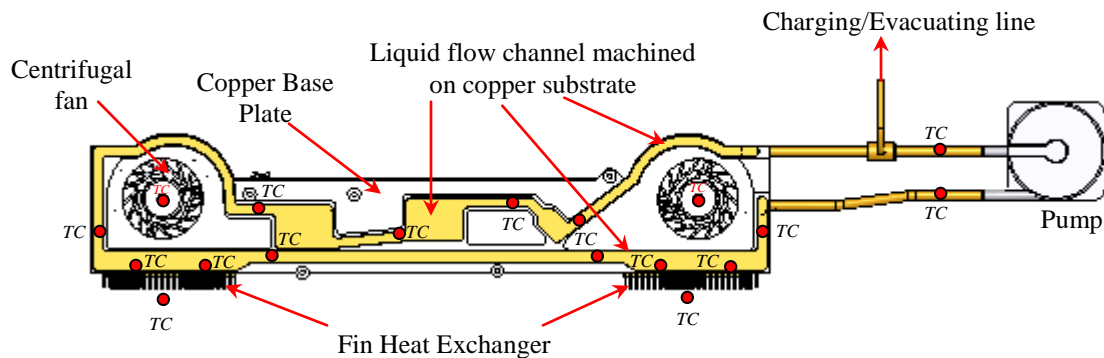


Figure 9.6 Liquid Cooling Unit
Note: TC denotes thermocouple location

At each of the heat source sites, a microchannel heat sink was installed and fixed in place by brazing. The maximum heat dissipation capacities of the three heat load simulators were 40 W for CPU, 25 W for GPU and 25 W for the MPU unit. The corresponding sizes of the heat sources were as discussed before (i.e. $10 \times 10 \text{ mm}^2$ for CPU chip and $25 \times 25 \text{ mm}^2$ for each GPU/MPU chips). Due to the high heat flux (maximum value of 40 W/cm^2) output by CPU, microchannel with high density was used in the CPU cooling section, as compared to the GPU/MPU sections. For the GPU and MPU, the microchannels used were of the same description. Figure 9.7 and 9.8 shows a schematic of two types of microchannels. Table 9.2 gives the specifications of the microchannels used in each cooling section. The heat load simulators that were in the form of a copper block with two embedded cartridge heater were fixed to the microchannel external base (active zone of the heat sink) by using attachment

plates on the top of the cooling unit and bottom of the heater block. Figures 9.9 and 9.10 presents the bottom perspective view and side view of the cooling unit showing the location of the heaters and related components.

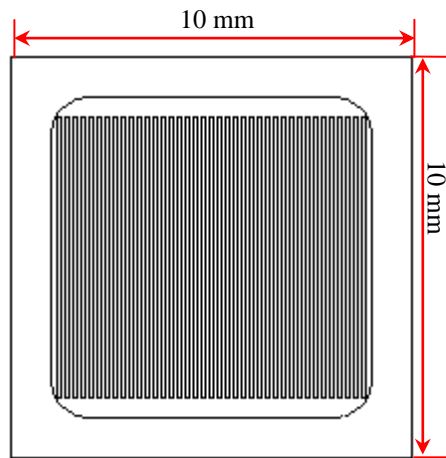


Figure 9.7 Microchannel for CPU size heater

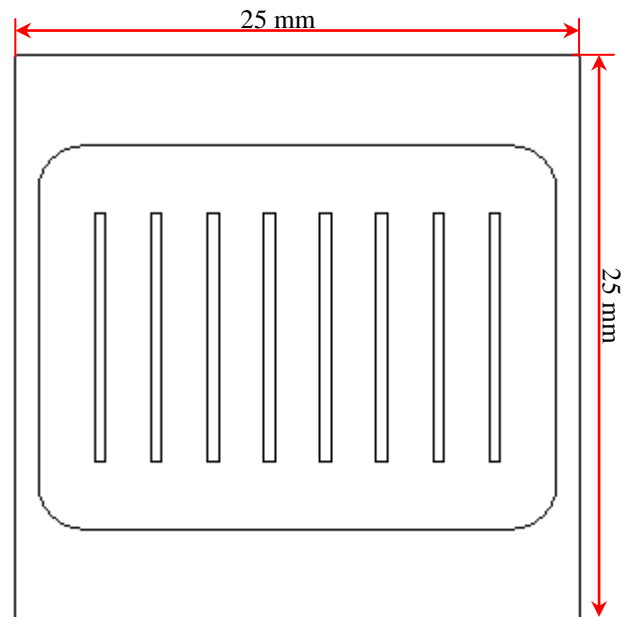


Figure 9.8 Microchannel for MPU/GPU size heater

Table 9.2 Specifications of the Microchannels

Parameter	CPU Microchannel	GPU/MPU Microchannel
Channel Geometry	Rectangular	Rectangular
Channel height	1.3 mm	1.3 mm
Channel Width	0.1 mm	2 mm
Inter-channel Distance	0.1 mm	0.5 mm
Channel Length	7 mm	11
No of Channels	39	8

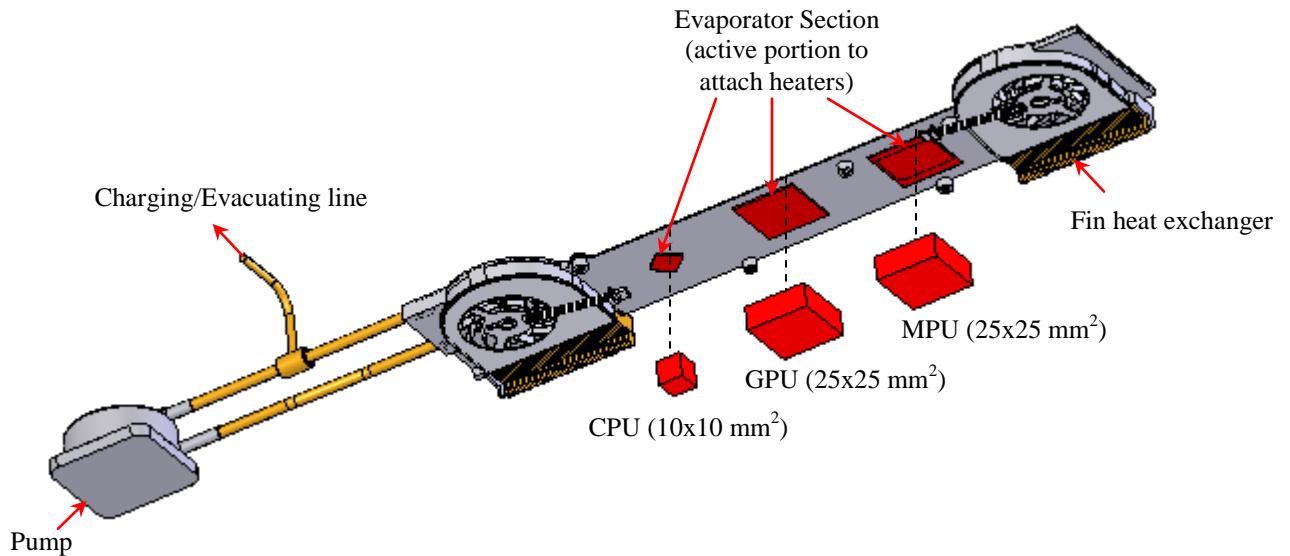


Figure 9.9 Bottom perspective view of the liquid cooling unit showing the evaporator sections and related components.

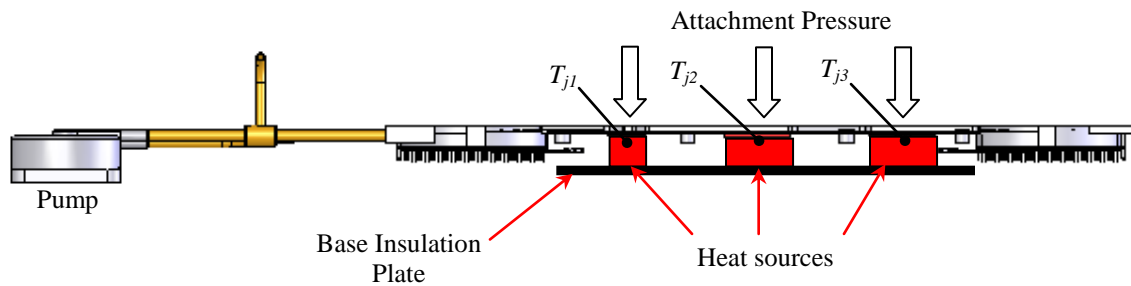


Figure 9.10 Side View of the liquid cooling unit showing the heater locations

Figure 9.11 shows the liquid flow pattern inside the loop and the location of each of the three microchannels.

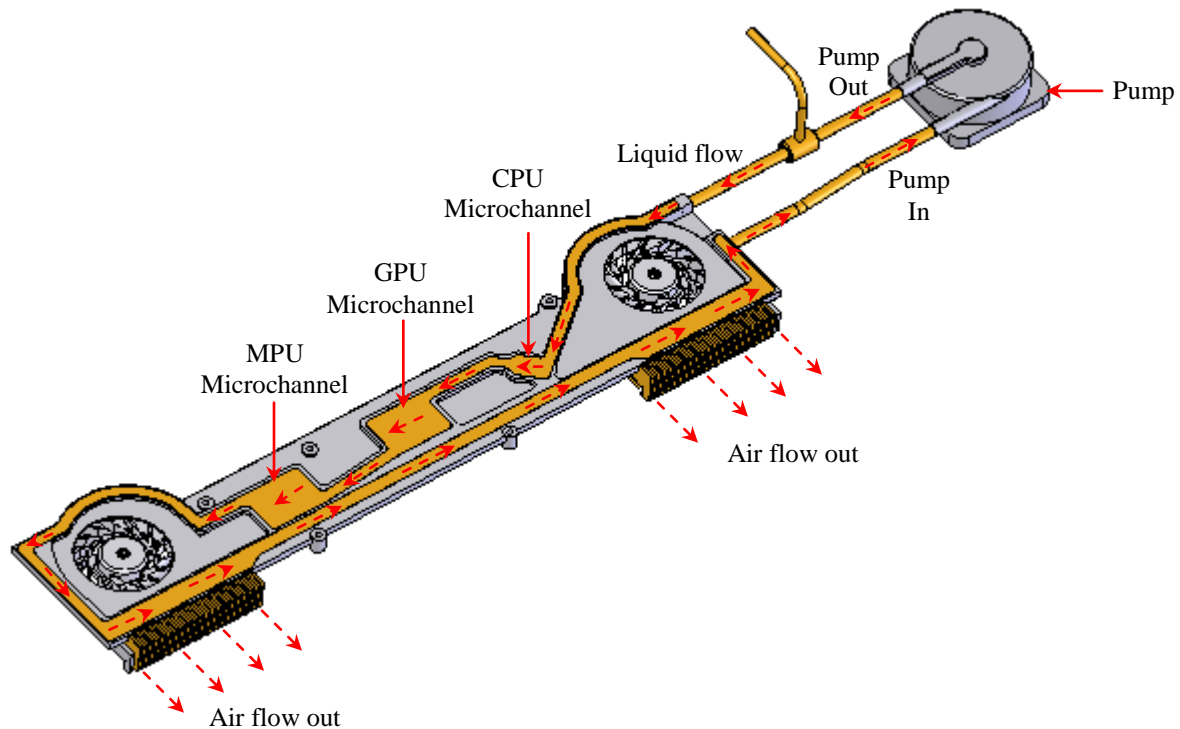


Figure 9.11 Perspective view of the liquid cooling unit showing the fluid flow pattern inside the loop and location of each microchannel section.

The procedure that was used for testing both the heat pipe and liquid cooling unit is as follows; First, both the units were tested with a single heat source and then the tests for the thermal control of three heat sources were conducted. Due to the high heat flux given out by the CPU chip, it was chosen for the single heat source testing. In the multiple heat source testing, different combinations of heat load in the range of 0/0/0 W to 40/20/20 W (CPU/GPU/MPU) were delivered to the three chipsets. During testing, the heat load was increased in increments of 5 W. In both units, the centrifugal fans were run from a 5 V, 0.1 A power supply. For liquid cooling, the pump was run at 12 V, 0.2 A throughout the test period. Testing was done at the steady ambient temperature of $24 \pm 2^\circ\text{C}$ for both units. To run each test, first the fans (and pump) were turned on and then power was applied to the heater.

9.3 Results and Discussion

Heat Pipe Cooling Unit: As the power to a heater is turned on, the temperature of the evaporator rises and results in vaporization of the working fluid. This is followed by rise in temperature of the heat transport section (i.e. adiabatic section) and then the condenser section which registers the start up of the heat pipe. The vapour formed in the evaporator section is condensed in the condenser section and the condensate returns to the evaporator section by capillary pumping provided by the composite fibre wick of the heat pipe. Steady state is reached after a certain time period depending upon the applied heat load.

Liquid Cooling Unit: Once the fluid circulation inside the loop is stabilized, the power to the heater is turned on. The heat from the heater will be conducted to the active zone of the cooling section and then to the walls of the microchannels. This heat will be convected to the liquid coolant flowing through the microchannels thereby heating the fluid which is then cooled by the fin heat exchanger.

9.3.1 Single Heat Source Cooling

Figure 9.12 plots and compares results of testing on the two cooling units with the single heat source (i.e. CPU) turned on. In the range of applied power (from 0 to 40 W), the interface temperature for the heat pipe unit lay within 34 to 140 °C while for the liquid cooling unit, lower values of the interface temperature were obtained, within 31 to 81.5 °C. It is observed from Figure 9.12 that for a heat load below 20 W, the interface temperature at the heat pipe lay closer to that achieved by the liquid cooling unit and showed a linear trend with respect to the applied power. As the heat load increases beyond 20 W, the heat pipe interface temperature registered a more rapid increase. This clearly indicates the heat transfer crisis phenomenon in the form of initiation of dry out inside the heat pipe evaporator. It can be explained as follow: With the increase in heat load, the quantity of the vapour and the associated flow rate inside the heat pipe increases. This increase the overall pressure losses that are comprised of vapour pressure loss inside the empty channel of the heat pipe and liquid pressure loss inside the capillary wick. As the pressure losses inside the system reach the maximum capillary pressure that the wick can generate, the condensate liquid is no longer able to reach the evaporator and this results in the dry out inside the evaporator. The interface

temperature of the microchannel heat sink remain linear with the increase in applied power even for input heat load higher than 40 W.

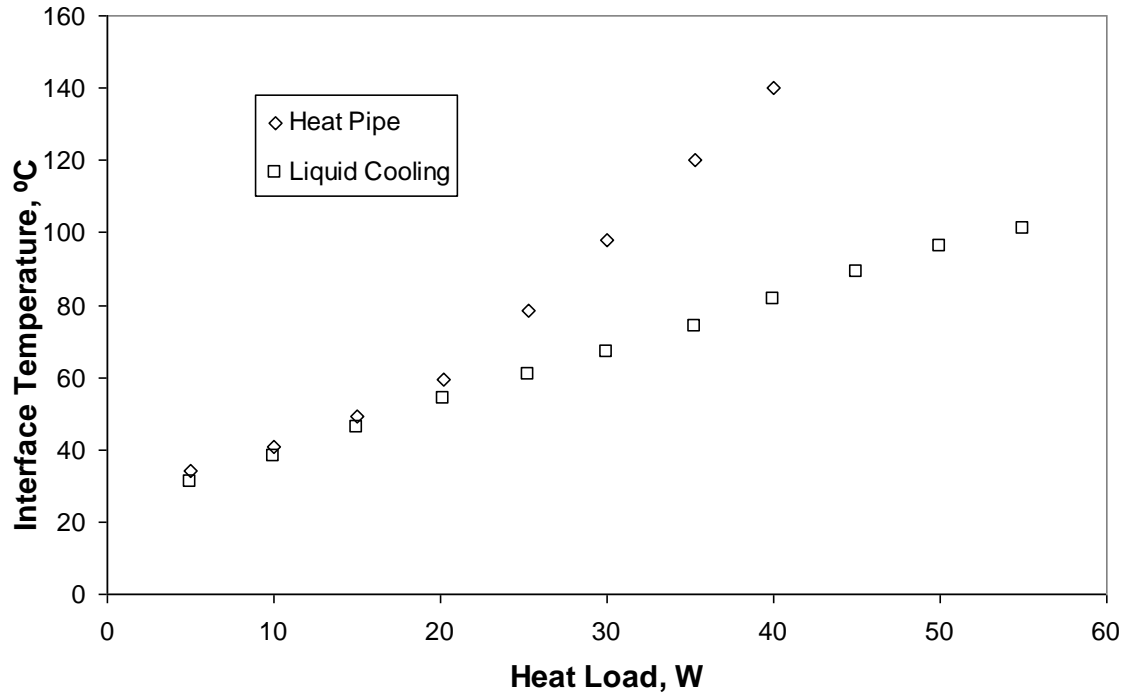


Figure 9.12 Heat load dependence of the interface temperature for the heat pipe and liquid cooling unit

The total thermal resistance, R_t of the each unit was calculated on the basis of the interface/junction temperature, T_j and the ambient temperature, T_a as follows:

$$R_t = \frac{(T_j - T_a)}{Q_a} \quad (9.2)$$

As shown in Figure 9.13, the total thermal resistance of the heat pipe clearly confirms the occurrence of the dry out inside the heat pipe evaporator for heat loads greater than 20 W. The overall thermal resistance with liquid cooling remains constant at approximately 1.35 °C/W.

It is noted from the above study that within the heat transfer capability of the designed two phase system which is determined by the system configuration (working fluid, container material, wick characteristics, transport line dimensions etc) and specifications (input heat load, heat transfer length, etc), the thermal performance is similar to that of the single phase

heat transfer system. In addition, the two phase systems are more reliable and independent of any active control element (e.g. the pump in the single phase systems). However, single phase systems are able to manage heat loads of higher intensity due to the active pumping component in the system that can provide high flow rates of coolant fluid. In the capillary pumped system, the physical or flow properties of the wick, including pore size, permeability and porosity dictate the performance of the device at high heat loads. Further development of these devices will need wick pumps with enhanced flow properties i.e. very fine pore size with high porosity and permeability values.

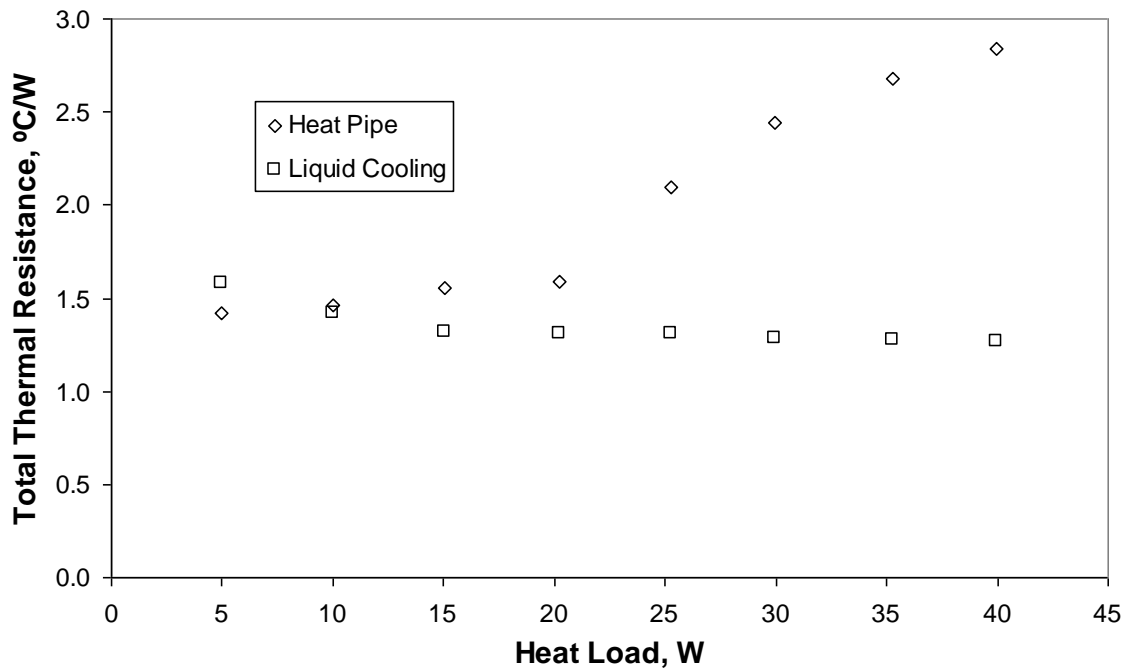


Figure 9.13 Total thermal resistance versus applied heat load for the heat pipe and liquid cooling unit

9.3.2 Multiple Heat Source Cooling

Testing of the cooling units for multiple heat source cooling was done by fixing the constant heat load at the GPU and MPU chips and varying the heat input to the CPU chipset. Figure 9.14 shows the results for the heat pipe cooling unit as a dependence of the CPU interface temperature on its input heat load for specified power inputs to GPU and MPU units. It is very interesting to note from the graph that as the heat inputs to the GPU and MPU chips are increased, the thermal performance of the heat pipe module increases. It is expected that such behaviour of the heat pipe can occur as a result of the increased vapour flow rate and

turbulence effect created by the vapour flow coming from the secondary low powered chips (GPU and MPU). The net effect of the vapour flow over the heated section of the CPU evaporator is to enhance its heat transfer coefficient and induce convective heat transfer from evaporator section to the incoming vapour. It is noted from the graph that such an enhancement is more evident at high heat loads when the vapour flow inside the heat pipe is expected to increase. In the single heat source condition, the major liquid inventory lies away from the CPU evaporator section and can be bound inside the wick or in the remote condenser. As the three heat sources are operated, the central segment of the heat pipe is heated entirely which provide more or less uniform distribution of the fluid inside the pipe. This can result in better liquid supply to the CPU evaporator from the nearby condenser. The performance of the heat pipe can be greatly increased through the capillary structure and by optimizing the fluid charge for the given application. Wick structures with high permeability, high porosity and small pore sizes are preferred.

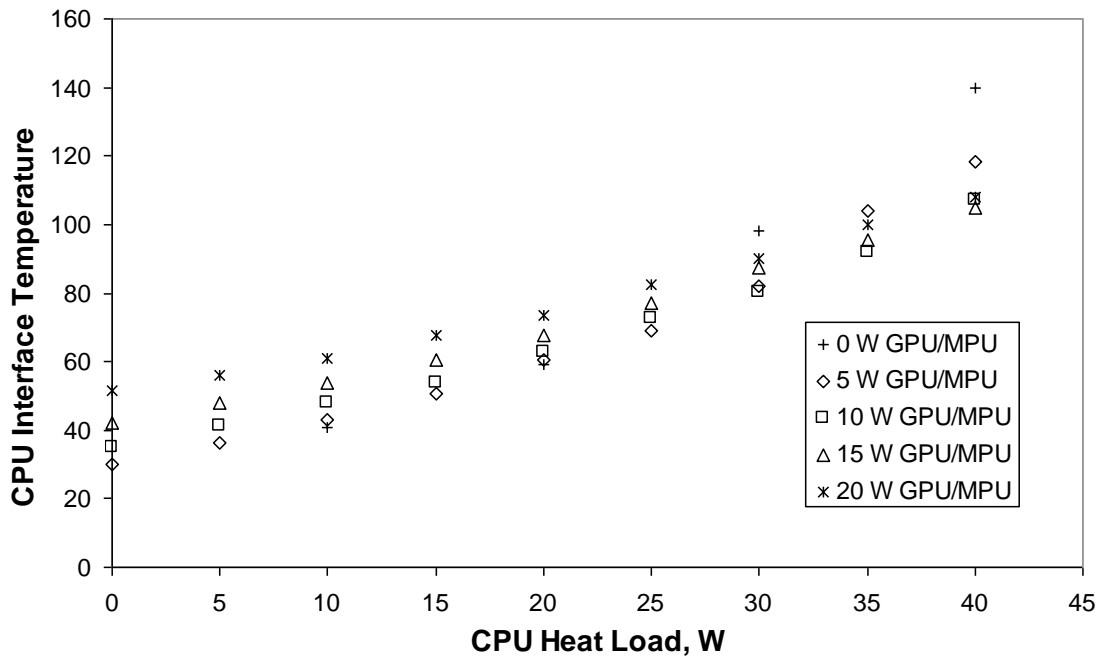


Figure 9.14 CPU Interface temperature versus CPU applied heat load for different power inputs to the GPU and MPU units (Heat pipe cooling unit)

Figure 9.15 shows the results of multiple heat sources cooling using the liquid cooling unit. As expected, the unit performs very efficiently over the entire range of input power. Figure 9.16 presents the results of comparison between the two-phase and single phase systems for

cooling multiple heat sources. It is clear from the graph that efficiency of the liquid cooling was higher than with the two-phase cooling only at high heat loads. For CPU input power less than 20 W, the difference in their performance was similar.

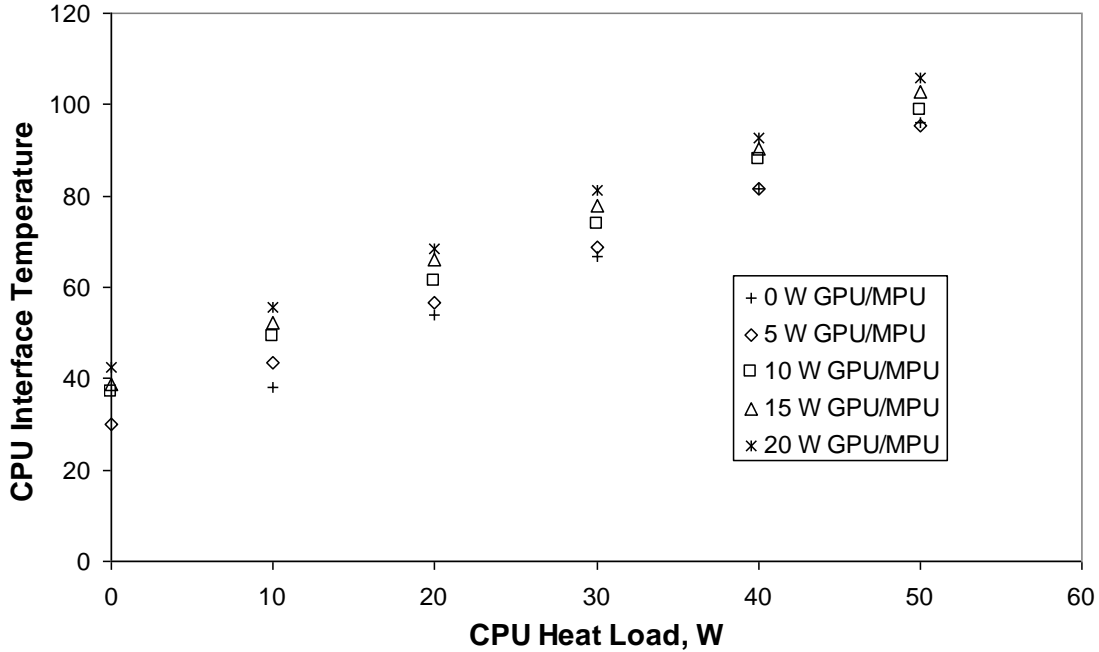


Figure 9.15 CPU Interface temperature versus CPU applied heat load for different power inputs to the GPU and MPU units (Liquid cooling unit)

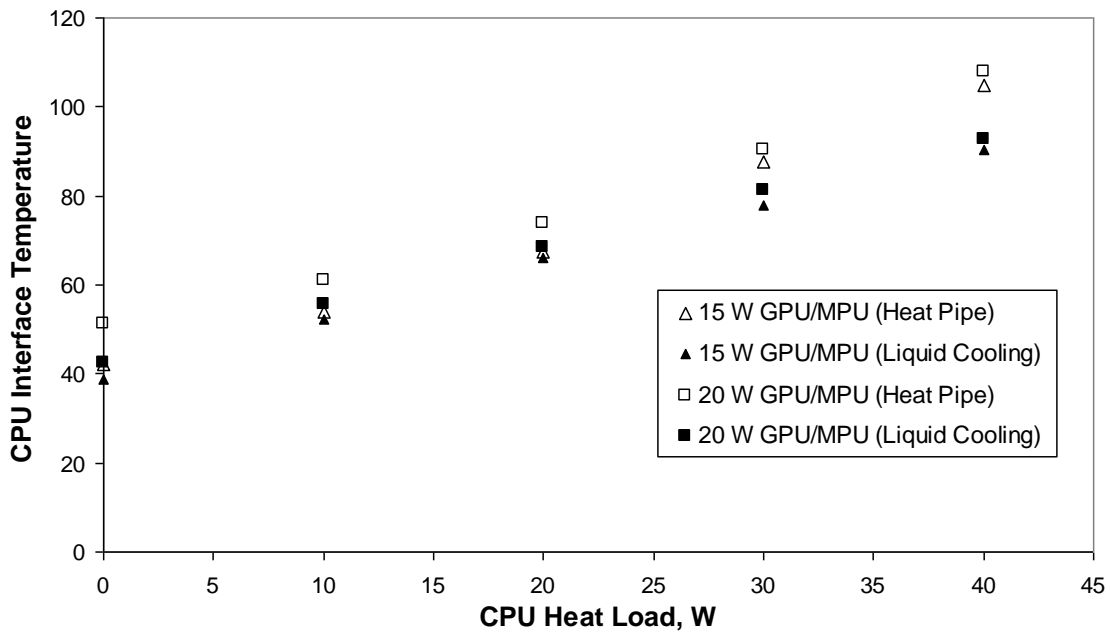


Figure 9.16 CPU Interface temperature versus CPU applied heat load for different power inputs to the GPU and MPU units : Comparison between Heat pipe cooling unit and liquid cooling unit

9.4 Summary

A comparative study has been carried out between the two-phase and single-phase heat transfer system for thermal control of single as well as multiple (in this case three) heat sources. The two phase cooling system was in the form of a flattened copper heat pipe with water as the working fluid while for the single phase cooling system, a microchannel based heat sink based on the forced convection of water was developed. As an outcome of the experimental investigation, it was found that for low to moderate heat fluxes, the thermal performance of the two-phase cooling unit was the same as that of the single phase system. For high heat fluxes, the performance of the two-phase systems degrades due to the limitation imposed by the maximum capillary pressure generated by the wick and associated low liquid flow rates. Both two phase and single phase cooling systems have potential for the thermal management of multiple heat sources of high thermal outputs.

In the next chapter, conclusions of the complete research work are listed.

Chapter 10

Conclusions and Recommendations

In the present research work, exhaustive investigation of cooling systems for the thermal management of microprocessors for laptops and desktop computers has been carried out. For this purpose, different thermal designs based on two-phase and single-phase heat transfer technology were designed and tested. Conclusions drawn from the current study are presented in the following section for each of the designs and the related technology. For convenience, the conclusions are divided into two sections, as is the main body of the thesis. The first section discusses the results of two-phase cooling using capillary driven loop systems while in the second section outcomes of single-phase cooling using forced liquid convection are outlined.

10.1 Concluding Remarks

- Two-phase cooling systems using miniature loop heat pipes can be effectively used in the thermal management of laptop microprocessors with high heat flux chipsets (up to 50 W/cm^2) and limited available space for accommodating the heat removal device.
- Liquid cooling using forced convection through microstructures (i.e. microchannels, microporous wicks) is a viable approach for the thermal control of high-powered (e.g. 3.6 MW/m^2) next generation computer microprocessors
- Two phase cooling systems that are capillary driven (i.e. passive operation) are more reliable than pump driven single phase cooling systems because of the absence of any power operated active component. Also, two-phase systems can transfer high heat loads with relatively low mass flow rates compared to single phase systems by making use of the latent heat of the evaporation of liquid working fluid. However, single phase systems are able to provide a better solution to thermal control of high powered miniature chipsets with ultra high heat fluxes. This is due to high mass flow rates that can be achieved by using active pumping devices and enhanced microstructural designs of the heat sink. Nonetheless, liquid cooling systems when compared to two phase systems are structurally more complex and vulnerable to failure during the normal life cycle due to potentially

unreliable active components (i.e. pump). In the long run, two phase systems are the ultimate thermal solutions for future electronics due to their reliable nature and high thermal control potential. There is a need for further research and development in wick pumps and thermal design of these devices in order to enhance their heat transfer capabilities and help them to meet the thermal requirements of the new generation high end electronic systems.

10.2 Conclusions from the study of two-phase cooling systems

In order to examine the heat transfer capabilities of two-phase systems for thermal control of microprocessors, two investigative prototypes of miniature loop heat pipe with flat evaporator were developed. One of the prototypes had a flat disk shaped evaporator with 30 mm diameter and 10 mm characteristic thickness while the second prototype had a flat rectangular shaped evaporator with 37x47 mm² planar area and 5 mm thickness. Before proceeding on experimentation on the miniature loop system, a medium scale prototype of the capillary pumped loop was built to assess the operation of the capillary driven loop system and to explore the unique and different capabilities of CPLs in contrast to LHPs. The complete study is summarized in discrete sections as follow:

10.2.1 Miniature Loop Heat Pipe with a flat disk shaped evaporator

- The miniature prototype of a LHP with a flat disk shaped evaporator has proved to be a very versatile and promising device for thermal control of microprocessors with high power density and a relatively small thermal footprint. With the current model, heat flux as high as 70 W/cm² was successfully removed from a thermal test vehicle (TTV) and transferred to a remote heat exchanger over a distance of 150 mm. This has helped to validate the feasibility of the LHP concept at miniature scale as a reliable thermal control technology for the next generation of high end microprocessors.
- The theoretical model that was designed on the basis of energy balance between different loop components predicted the loop operating temperature very well and within the uncertainties imposed by the underlying assumptions.
- In the present design, the flat disk shape evaporator acts as an optimum design. The flat evaporator provides an easy interface with the heat source without the need for an

additional thermal interface attachment, which creates additional thermal resistance in the case of cylindrical evaporators.

- The start up of the mLHP was reliable over the wide range of heat loads applied to the evaporator active zone. In the mLHP, the inherent location of the compensation chamber with respect to the capillary structure provides proper wetting of the latter at all times and thus a successful start up of the device under different conditions. It was revealed that the start up trend of the mLHP depends on the total fluid charge and pre start-up fluid distribution inside the evaporator grooves, wick structure and compensation chamber. For a reliable start-up at low heat loads, it was inferred that a pre start-up situation with the ready vapour-liquid interface inside the evaporation zone is required.
- It was established experimentally that a mLHP can operate satisfactorily within a wide range of working fluid charge. Here, the foremost condition is to accomplish the proper wetting of the porous structure. However, it was noted that the thermal performance of the mLHP was better when the loop was operated with the highest fluid charge volume within the given range. Contrary to this, the mLHP presented some pressure and temperature oscillations for high fluid charge ratio. For that reason, it is recommended to operate a mLHP at an optimum charge that is decided by the sum of wick porous volume, liquid line and compensation chamber volume such that in the cold state, 50% of the interval volume of compensation chamber is occupied by the liquid working fluid.
- The designed mLHP can be used as an effective thermal control device to transfer heat at different orientations in the gravity field. Even for adverse tilts in the gravity field (i.e. evaporator above condenser configuration), the loop was able to operate suitably and sustained continuous fluid circulation, in this case against the natural flow tendencies of the vapour and liquid phases. However, there was a notable increase in the thermal resistance of the loop with increase in slope. This was due to the accumulation of the fluid in the bottom portion of the loop including the condenser which reduced the liquid charge inside the compensation chamber and thus produced massive heat flow to the chamber.
- mLHPs with the current design of evaporator can be effectively used for the cooling of microprocessors that involve local hot spots and irregular surface heating patterns depending on their data processing load. In the trial runs conducted with different heat density, it was shown that a mLHP was able to handle the conditions of local heating even

when only 14% of the evaporator active area was being heated. The results clearly identify the superior thermal characteristics of the mLHP and its ability to acquire and transfer waste heat from compact microprocessors and chipsets with local hot spots.

- A capillary structure made from a highly conductive material like copper can be used in the miniature LHP for thermal control of electronic equipment without any major performance degradation. In the mLHP, wick structure with low thermal conductivity is preferred so that the heat conducted back to the compensation chamber can be minimized. However it has been found that a highly conductive wick structure like the one made from copper performs very efficiently to improve the heat exchange process in the evaporation zone. Furthermore due to the complete saturation of the wick structure with the low conductive working fluid, the effective thermal conductivity of the wick decreases appreciably and does not present much concerns regarding back conduction.
- The operational characteristics of the mLHP are largely dependent on the effective thermal conductivity of the wick saturated with the working fluid and physical properties of the wick structure, the most important being the pore size, porosity and permeability. The porosity and permeability of the wick affect the parasitic heat leaks from the evaporator zone to the compensation chamber and thus take part in providing a thermal lock. For the pore size, it should be small enough to generate enough capillary pressure to continue fluid circulation and at the same time guarantee vapour locking in the range of applied heat load.
- The heat transfer characteristics of biporous wick structures (i.e. wicks with two characterised pore radii) are better than monoporous wicks (i.e. wicks characterised by single average pore radius). In the biporous wick, the presence of the two characteristic pore sizes (i.e. large pores and small pores) increases evaporative heat transfer from the two phase thermal layer (i.e. wick wall interface) and at the same time provides separate flow paths for the liquid (through small pores) and vapour (through large pores).
- mLHPs are not very sensitive to the Non Condensable Gases (NCGs) that are generated inside the system due to impurities present inside the working fluid and the loop material. It was found that major inventory of non condensable gas was generated during the first few initial runs of the device and accumulated inside the compensation chamber due to the low fluid velocity profile inside the chamber. The net effect of the generated NCG is to

produce an overall rise in the loop operating temperature which is more pronounced at low heat loads. Also, the NCGs produce an increase in the start up time of the loop. It was experimentally established that the majority of NCG is produced because of contamination and dissolved gases present inside the working fluid. Notable improvements were achieved by enhancing the fluid charging procedure.

10.2.2 Miniature Loop Heat Pipe with a flat rectangular shaped evaporator

- It is possible to downscale the thickness of the miniature LHP by using a novel concept of relocating the compensation chamber from the thickness of the evaporator to its sides.
- The mLHP evaporator with the compensation chamber distributed on its sides was able to attain a minimum thickness of as low as 5 mm while preserving the functionalities of the capillary structure and efficiency of the heat transfer process inside the evaporation zone.
- The proposed design of the mLHP with the rectangular evaporator was able to operate successfully and authenticate the design concept for the modeling of a compact miniature LHP with reduced thickness. Such a mLHP design with low thickness of 5 mm has more prospects and is easy to install inside a laptop with limited height when compared to the disk shaped mLHP model with 10 mm thickness. The prototype was able to transfer extremely high heat flux of 50 W/cm^2 up to a distance of 150 mm while maintaining the source temperature within the permissible limit of $100 \pm 5^\circ\text{C}$.
- In the case of the flat rectangular mLHP, the total thermal resistance and the interface temperature of the device were higher than for the disk shaped mLHP. This is explained by the increased quantity of heat leakage to the compensation chamber of the rectangular mLHP. The heat flow in this case has two different paths i.e. through the wick structure and through the coplanar compensation chamber wall that is in line with the evaporator active zone. In addition, liquid and heat flow through the wick are not directed towards each other and the area of the liquid absorbing face of the wick is reduced. The net effect of these factors causes a larger fraction of heat flow to the compensation chamber and produces high thermal resistance.

10.2.3 Capillary pumped loop with a cylindrical evaporator (as discussed in the Appendix B)

- A model of a medium scale capillary pumped loop with a cylindrical evaporator was developed during this case study and proved to be a very efficient two-phase heat transfer device. The unique thermal characteristics of capillary driven two-phase loops were revealed during the tests. The apparatus was able to remove high heat loads (210 W) from a thermal payload and transport them successfully over long distances (one meter) with minimal temperature drops (as small as 0.29 – 0.46 °C) between heat source and heat sink.
- With CPL very precise control (within ± 3 °C) of the heat source temperature was achievable by setting the temperature and thus the saturation conditions inside the remotely located reservoir with the help of an active thermal controlling device attached to it. It was found that the temperature control capability of the CPL depend on the reservoir temperature and heat load applied to the evaporator.
- For reliable startup of the CPL, the capillary evaporator must be pressure primed by pre-heating the reservoir. Attempts to start the loop from a cold state and without enough time for proper conditioning of the capillary pump resulted in start up failures or high thermal resistances. By maintaining constant temperature of the reservoir for 6-7 hours it was possible to ensure complete wetting of the wick structure.
- Although the CPL provided effective control over the operating temperature with changing input heat load, it was found from the experiments that start-up of the device is very unreliable and relies heavily on proper pre-conditioning of the capillary structure. Beside this, the presence of the thermal element on the reservoir and need for the pre-start up preparations does not justify them as a thermal control devices for the future computer electronics. These limitations are addressed better by LHPs which are highly reliable and do not require any active element in the loop.

10.3 Conclusions from the study on single phase cooling systems

With the rapid rise in heat dissipation capacity of microprocessors, new innovative thermal solutions are needed to address the problem of efficient thermal management of electronic devices. Two investigative prototypes of single-phase cooling system were developed to study the potential and heat transfer characteristics of forced convection of liquid through

microstructural heat sinks. In the first prototype, the active cooling section of the heat sink consisted of microchannels with high aspect ratio of 17.5 while for the second sample, a sintered porous structure with a pore radius less than 30 μm and 40% porosity was used as the heat acquisition component in the heat sink. The outcomes of the study can be summarized as follow:

10.3.1 Liquid cooling using a microchannel heat sink

- The thermal performance of the liquid cooling system was intensified by using microchannels on the fluid side of the cooling section. In this case, extreme heat fluxes of more than 3.6 MW/m^2 were removed successfully from the microprocessor source while keeping the chip temperature within $100 \pm 5^\circ\text{C}$.
- It was found that thermal resistance of the chipset with smaller thermal footprint is higher than the one with relatively large heat conducting surface. This is predominately due to the addition of the metallic resistance offered to the distribution of the heat from the smaller heater footprint to the active section of the cooling plate and the micro fins.
- The flow rate of the coolant has a notable effect on the thermal resistance of the heat sink. It was confirmed that the increase in the flow rate produces a corresponding decrease in the interface temperature of the heat source and heat sink.
- The predicted results obtained by laminar flow correlations over predict the heat transfer coefficient. With the fully developed turbulence correlation, the agreement between the experiment and predictions is quite close.

10.3.2 Liquid Cooling using a Sintered Porous Heat Sink

- The heat sink with a sintered porous microstructure provides an effective heat transfer augmentation technique. With the designed prototype, heat flux up to 2.8 MW/m^2 was removed by using a porous sample with porosity 40% and pore radius $< 30 \mu\text{m}$ while maintaining the interface temperature within the permissible limit of $100 \pm 5^\circ\text{C}$.
- With the porous heat sink, large pressure losses are experienced even for the smaller flow rates of the working fluid.
- Increasing the flow rate is a very important option to enhance the heat transfer capability of the sintered porous heat sink.

- For the sintered porous heat sink convective heat transfer between the fluid and the porous matrix was of superior character due to the large heat transfer area and proper fluid flow mixing inside it. However, it has been noted that the efficient heat transfer process is accompanied by a drastic increase in the pumping power. It can be inferred that the principal use of the sintered porous heat sink can be for micro-electronics of high power with no limitation on pumping power.
- The thermal performance of the microchannel heat sink is better than that of the sintered porous heat sink. Factors that might have contributed to the better performance of the microchannel heat sink are better structural design and higher thermal conductivity of the cooling section along the thickness.

10.4 Conclusions on measurement of properties of porous structures (as discussed in the Appendix C)

- The specific permeability calculated from the experimental tests that were conducted at high flow rates of the working fluid showed close agreement with the permeability values provided by the manufacturer. This is due to the fact that viscous forces in the micro pores are overcome at high pressure and flow is properly channelled through the micro pores which otherwise retard the flow at low pressure.
- In the measurement of the pore size of the wick, the method that makes use of steady height achieved by the fluid under a capillary head gave reliable measurement of the mean pore size of the wick. The bubble point testing method gave the largest pore radius in the test sample.
- For the porosity of the wick, the density method showed better results than the soaking method due to the problems of incomplete wetting of the wick by the fluid or presence of close spaces and dead ends in the porous media.

10.5 Recommendations for Future Work

Refinement of the mLHP theoretical model: The current theoretical model makes use of a number of assumptions and approximations for the prediction of the mLHP thermal performance. It is suggested that the model should be further refined by taking into account these factors: heat exchange between the porous matrix wall and the fluid filtering through the

porous structure, heat losses to the surrounding, two phase flow inside the condenser and more detailed thermal analysis of the condenser.

Further design and development of miniature LHP: In the case of the flat rectangular mLHP, there are still certain performance issues related to the high thermal resistance and longer startup time that need to be addressed. Proposals like the use of low conductive materials for the evaporator body to reduce back heat flow to the compensation chamber, and changes in the wick design and shape for proper wetting and efficient liquid filtration though it should be explored through further research work.

Computational Fluid Dynamic (CFD) Analysis: It is strongly recommended that CFD analysis of the different thermal designs discussed in the thesis should be done. Such an analysis will be very helpful in the modeling and understanding the fluid and heat interactions inside the porous structures that were used in the thermal design of the mLHP capillary evaporator and the sintered porous heat sink.

Evaluation of Heat Transfer Correlations for Microchannels: The analysis of the microchannel heat sink does not take into account all of the available heat transfer correlations (for laminar and turbulent flow regimes) for the prediction of the heat transfer coefficient inside the channels. It is therefore recommended that complete evaluation should be made of the conventional correlations (for large channels) to assess their validity for the prediction of the microchannel heat transfer.

Further Development of Single Phase Cooling Systems: As potential candidates for the cooling of the next generation computer microprocessors, single phase cooling systems should be further investigated. It is recommended that an exhaustive study should be done on the microchannel heat sinks with different aspect ratios (fin height/fin width) and sintered porous heat sinks with different properties of the wick structure including porosity, permeability, pore size and effective thermal conductivity, which are important from the thermal performance point of view. Such a study is recommended to rationalize the overall potential of these types of heat sinks.

References

- Adams, TM, Abdel-Khalik, SI, Jeter, SM & Qureshi, ZH 1998, ‘*An Experimental Investigation of Single-Phase Forced Convection in Microchannels*’, *International Journal of Heat Mass Transfer*, Vol. 41, pp. 851-857.
- Adkins, DR & Moss, T 1990, ‘Measuring Flow Properties of Wicks for Heat Pipe Solar Receivers’, *in Proceedings of the ASME International Solar Energy Conference, Miami, Florida, April 1-4, 1990*.
- Alexander, EG 1972, ‘Structure-Property Relationships in Heat Pipe Wicking Materials’ PhD Dissertation, North Carolina State University, Department of Chemical Engineering, 1972.
- Baumann, J, Cullimore, B, Kroliczek, E, & Bugby, D 1998, ‘Development of the Cryogenic Capillary Pumped Loop’, *Paper No. IECEC-98-1137, in 33rd Intersociety Engineering Conference on Energy Conversion, Colorado Springs, CO, August 2-6, 1998*.
- Baumann, J, & Rawal, S 2001, Viability of loop heat pipes for space solar power applications, *American Institute of Aeronautics and Astronautics, SAE Paper No. 2001-3078, 2001*.
- Bazzo E., Riehl R.R. 2003, ‘Operation Characteristics of a Small-Scale Capillary Pumped Loop’, *Applied Thermal Engineering*, Vol.23, pp. 217-220.
- Bienert, WB, Krotiuk, WJ, & Nikitkin, MN 1999, ‘Thermal Control with Low Power, Miniature Loop Heat Pipes’, *SAE. Paper No. 1999-01-2008*
- Boo, JH, & Chung, WB 2005, ‘Thermal Performance of a Loop Heat Pipe having Propylene Wick in a Flat Evaporator’, *in Proceedings of the ASME Heat Transfer Conference, San Francisco CA, USA, July 17-22, 2005*.
- Boo, JH, & Chung, WB 2004, ‘Thermal Performance of a Small Scale Loop Heat Pipe with PP Wick’, *in Proceedings of the 13th International Heat Pipe Conference, Shanghai, China, September 21-25, 2004*.
- Cengel, Y.A. & Turner, RH 2001, ‘*Fundamentals of Thermal-Fluid Sciences*’, McGraw Hill, New York.

- Chen, PC & Lin, WK 2001, 'The Application of Capillary Pumped Loop for Cooling of Electronic Components', *Applied Thermal Engineering*, Vol.21, pp. 1739-1754.
- Chernysheva, MA, Maydanik, YF, & Vershinin, SV 1999, 'Heat Exchange in the Evaporator of a Loop Heat Pipe with a Biporous Capillary Structure', in *Proceedings of the 11th International Heat Pipe Conference, Tokyo, Japan, 1999*.
- Chernysheva, MA, Vershinin, SV, & Maydanik YF 2002, 'Development and Test results of Loop Heat Pipes with a Flat Evaporator', in *Proceedings of 12th International Heat Pipe Conference, Moscow Russia, 2002*, pp. 134-138.
- Choi, SB, Barron, RF & Warrington, RO 1991, 'Fluid Flow and Heat Transfer in Microtubes', *Micromesh. Sensors Actuation Systems ASME DSC 3*, pp. 123-134.
- Delil, AAM, Baturkin, V, Fridrichson, Y, Khmelev, Y & Zhuk, S 2002, 'Experimental Results of Heat Transfer Phenomena in a Miniature Loop Heat Pipe with a Flat Evaporator', in *Proceedings of the 12th International Heat Pipe Conference, Moscow, Russia, 2002*, pp.126-133.
- Dickey, JT & Peterson, GP 1994, 'Experimental and Analytical Investigation of a Capillary Pumped Loop', *Journal of Thermophysics and Heat Transfer*, Vol.8, no.3, pp. 602-607.
- Dunbar, N, et al, 1997, 'Design, Development and Testing of a Miniature Capillary Pumped Loop', in *Proceedings of the 6th European Symposium on Space Environmental Control Systems, Noordwijk, 1997*, pp.365-370.
- Dunn, PD, & Reay, DA 1994, '*Heat Pipes*', Pergamon Press, Great Britain, 1994.
- Faghri, A 1995, *Heat Pipe Science and Technology*, Taylor & Francis, London, 1995.
- Garzon, et al 2002, 'Next Step in Miniaturizing the LHP Technology', in *Proceedings of the International Two Phase Thermal Control Technology Workshop, Mitchellville, 2002*.
- Gerhart, C & Gluck, D 1999, 'Summary of Operating Characteristics of a Dual Compensation Chamber Loop Heat Pipe in Gravity', in *Proceedings of the 11th International Heat Pipe Conference, September 12-16, 1999, Tokyo, Japan*.
- Gherlone, JA, Jr. 1998, 'Operating Characteristics of a Propylene Charged Loop Heat Pipe with Potential Spacecraft Applications', Masters Dissertation, Report No. A628403, Naval Postgraduate School, Monterey, CA.

- Hambir, S & Jog, JP 2000, 'Sintering of Ultra High Molecular Weight Polyethylene, *Bulletin of Material Sciences, Indian Academy of Sciences*, Vol.23, no. 3, pp. 221-226.
- Hetsroni, G, Gurevich, M, & Rozenblit, R 2005, 'Sintered Porous Medium Heat Sink for Cooling of High-Power Mini-Devices', *International Journal of Heat and Fluid Flow*, Vol.27, no.2, pp. 259-266.
- Hsieh, WH, Wu, JY, Shih, WH & Chiu, WC 2004, 'Experimental Investigation of Heat-Transfer Characteristics of Aluminum-Foam Heat Sinks, *International Journal of Heat and Mass Transfer*, Vol. 47, pp. 5149-5157.
- Huang, BJ 2004, 'Development of a Low Cost LHP for Commercial Application', in *Proceedings of the 13th International Heat Pipe Conference, Shanghai, China, September 21-25, 2004*.
- Incropera, FP & DeWitt, DP 2001, '*Fundamentals of Heat and Mass Transfer*', John Wiley and Sons, New York, 2001.
- Jeigarnik, UA, Ivanov, FP & Ikranikov, NP 1991, 'Experimental Data on Heat Transfer and Hydraulic Resistance in Unregulated Porous Structures', *Teploenergetika*, Vol.2, pp. 33-38 (in Russian).
- Jiang, PX, Meng, L, Lu, TJ, Yu, L, & Ren, ZP 2004, 'Experimental Research on Convection Heat Transfer in Sintered Porous Plate Channels', *International Journal of Heat and Mass Transfer*, Vol. 47, pp. 2085-2096.
- Kandlikar, SG, Joshi, S, & Tian, S 2001, 'Effect of Channel Roughness on Heat Transfer and Fluid Flow Characteristics at Low Reynolds Numbers in Small Diameter Tubes, in *Proceedings of the 35th National Heat Transfer Conference, Anaheim, CA, USA*, paper No. 12134.
- Kays, WM & Crawford, ME 1980, '*Convective Heat and Mass Transfer*', McGraw-Hill, New York, 1980.
- Khrustalev, D & Semenov, S 2003, 'Advances in Low Temperature Cryogenic and Miniature Loop Heat Pipes', in *Proceedings of the 14th Spacecraft Thermal Control Workshop, El Segundo*, 2003.
- Kobayashi, T, Ogushi, T, Haga, S, Ozaki, E, & Fujii, M 2003, 'Heat Transfer Performance of a Flexible Looped Heat Pipe Using R134a as a Working Fluid:

- Proposal for a Method to Predict the Maximum Heat Transfer Rate of FLHP', *Heat Transfer-Asian Research*, Vol.32, no.4, pp.306-318.
- Ku, J 1999, 'Operation characteristics of Loop Heat Pipes', in *Proceedings of the International Conference on Environmental Systems, Denver, CO, July, 1999*, Paper # 1999-01-2007.
 - Ku, J & Birur, G 2001, 'An Experimental Study of Operating Temperature in an LHP with Two Evaporators and Condensers', in *Proceedings of the International Two Phase Thermal Control Technology Workshop, El Segundo, CA, USA, 2001*.
 - Lago, M & Araujo, M 2001, 'Capillary rise in porous media', *Physica A*, 2001 Vol. 289, pp. 1-17.
 - Lage, JL, Weinert, AK, Price, DC & Weber, RM 1996, 'Numerical Study of a Low Permeability Microporous Heat Sink for Cooling Phased-Array Radar Systems', *International Journal of Heat Mass Transfer*, Vol. 39, No.17, pp. 3633-3647.
 - Lee, PS, Garimella, SV & Liu, D 2005, 'Investigation of Heat Transfer in Rectangular Microchannels', *International Journal of Heat Mass Transfer*, Vol. 48, pp. 1688-1704.
 - Li, Q & Xuan, Y 2003, 'Development of High Performance Sintered Wicks for CPLs', in *Proceedings of the 7th International Heat Pipe Symposium, South Korea, October, Jeju, 2003*.
 - Lin, WK, Wong, PL, Wong, PC, Cheng, PC & Wang HP 1994, 'A Design and Performance Test of the Visualization within a Capillary Pumped Loop', *IL NUOVO CIMENTO*, Vol.16D, no.7, pp. 883-893.
 - Maydanik, YF 2005, 'Loop Heat Pipes', *Applied Thermal Engineering*, Vol. 25, no. 5-6, pp. 635-657.
 - Maydanik, YF 2004, 'Miniature Loop Heat Pipes', in *Proceedings of the 13th International Heat Pipe Conference, Shanghai, China, September 21-25, 2004*, pp.24-37.
 - Maydanik, YF, 1999, 'State-of-the-Art of CPL and LHP Technology', in *Proceedings of the 11th International Heat Pipe Conference, Tokyo, Japan, 1999*, pp. 19-30.
 - Maydanik, YF, et al, 1990, 'Development, Analytical and Experimental Investigation of Loop Heat Pipes', in *Proceedings of the 8th International Heat Pipe Conference, Minsk, Russia, Paper No: D21P*.

- Maydanik, YF & Fershtater, YG 1997, 'Theoretical Basis and Classification of Loop Heat Pipes and Capillary Pumped Loops', in *Proceedings of the 10th International Heat Pipe Conference, Stuttgart, Germany, September 21-25, 1997*.
- Maydanik, YF, Fershtater, YG & Pastukhov, VG 1992, 'Development and Investigation of Two Phase Loops with High Pressure Capillary Pumps for Space Applications', in *Proceedings of the 8th International Heat Pipe Conference, Beijing, China, 1992*.
- Maydanik, YF, Solodovnik, N and Fershtater, Y 1995, 'Investigation of Dynamic and Stationary Characteristics of a Loop Heat Pipe', in *Proceedings of the 9th International Heat Pipe Conference, Albuquerque, USA, 1995*, pp.1002-1006.
- Maydanik, YF & Pastukhov, VG 1999, 'Loop Heat Pipes-Recent Development Test Results and Applications', *SAE Pap No. 1999-01-2530*.
- Maydanik, YF, Vershinin, SV & Fershtater, YG 1997, 'Heat Transfer Enhancement in a Loop Heat Pipe Evaporator', in *Proceedings of the 10th International Heat Pipe Conference, Stuttgart, Germany, September 21-25, 1997*.
- Maydanik, YF, Vershinin, SV, Korukov, MA & Ochterbeck, JM 2005, 'Miniature Loop Heat Pipes – A Promising Means for Cooling Electronics', *IEEE Transactions on Components and Packaging Technologies*, Vol. 28, no.2, pp-290-296.
- Miao, J, Chenghui, S & Shun, G 2002, 'Experimental Study of a Capillary Pumped Loop Engineering Model', in *Proceedings of the 12th International Heat Pipe Conference, Russia, 2002*, pp. 77-81.
- Mochizuki, M, Saito, Y, Nguyen, T, Wuttijumnong, V, Wu, X & Nguyen, T 2005, 'Revolution in Fan Heat Sink Cooling Technology to Extend and Maximize Air Cooling for High Performance Processors in Laptop/Desktop/Server Application', *ASME paper # IPACK-73286, 2005*.
- Moore, GE 1965, 'Cramming More Components Onto Integrated Circuits', *Electronics*, Vol. 38, No. 8, April 19, 1965.
- Morini, GL 2004, 'Single-Phase Convective Heat Transfer in Microchannels: A Review of Experimental Results', *International Journal of Thermal Sciences*, Vol. 43, pp. 631-651

- Mulholland, G, Gerhart, C, Gluck, D, & Stanley, S 1999, 'Comparison Between Analytical Predictions and Experimental Data for a Loop Heat Pipe', in *Proceedings of AIP Conference*, Vol. 458, no.1, pp.805-810.
- Nickerson, R 1998, 'Plasma Surface Modification for Cleaning and Adhesion', in *Proceedings of the TAPPI Conference*, 1998.
- Nikitkin, MN, Bienert, WB & Goncharov, KA 1998, 'Non Condensable Gases and Loop Heat Pipe Operation', in *Proceedings of the International Conference on Environmental Systems, Denver, CO, July, 1998*, Paper # 981584.
- North, MT, Sarraf, DB & Rosenfeld, IH 1997, 'High Heat Flux Loop Heat Pipes, Space Technology and Applications', *International Forum (STAIF-97), Albuquerque, N.M. USA, January 26-30, 1997*.
- Pastukhov, VG, Maydanik, YF & Chernyshova, MA 1999, 'Development and Investigation of Miniature Loop Heat Pipes', in *Proceedings of the 29th International Conference on Environmental Systems, Denver, 1999*, Paper 1999-01-1983
- Pastukhov, VG, Maydanik, YF & Vershinin, SV 2003, 'Miniature Loop Heat Pipes for Electronic Cooling', *Applied Thermal Engineering*, Vol. 23, pp-1125-1135.
- Peng, XF, Peterson, GP & Wang, BX 1994, 'Frictional Flow Characteristics of Water Flowing through Microchannels', *Exp. Heat Transfer*, Vol. 7, pp. 249-264.
- Peng, XF, Peterson, GP & Wang, BX 1994, 'Heat Transfer Characteristics of Water Flowing through Microchannels', *Exp. Heat Transfer*, Vol. 7, pp. 265-283.
- Qu, W, Mala, GM & Li, D 2000, 'Heat Transfer for Water Flow in Trapezoidal Silicon Microchannels', *International Journal of Heat Mass Transfer*, Vol. 43, pp. 3925-3936.
- Rahman, MM 2000, 'Measurements of Heat Transfer in Microchannel Heat Sinks', *International Communication of Heat Mass Transfer*, Vol. 27, No.4, pp. 495-506.
- Reimbrecht, EG, Fredel, MC, Bazoo, E, & Pereira, FM 1999, 'Manufacturing and Microstructural Characterization of Sintered Nickel Wicks for Capillary Pumps', *Materials Research*, Vol.2, no.3, pp.225-229.
- Riehl, RR 2004, 'Evaluating the Behaviour of Loop Heat Pipe with Different Compensation Chamber Configurations', in *Proceedings of the 13th International Heat Pipe Conference, Shanghai, China, September 21-25, 2004*.

- Riehl, RR & Dutra, T 2005, 'Development of an Experimental Loop Heat Pipe for Application in Future Space Missions', *Applied Thermal Engineering*, Vol. 25, pp.101-112.
- Riehl, RR, Reimbrecht, EG, Camargo, HVR & Bazzo, E 2002, 'Ground Testing and Thermodynamic behaviour of a Capillary Pumped Two-Phase Loop', in *Proceedings of the 12th International Heat Pipe Conference, Russia, 2002*, pp. 96-101.
- Roukis, JG, Kosson, RL & Westell, JR 1975, 'Self Filling Arterial Heat Pipe', US Patent No. 3, 913, 664, October, 1975.
- Saucius, I, Prasher, R, Chang, JY, Erturk, H, Chrysler, G, Chiu, CP & Mahajan, R 2005, 'Thermal Performance and Key Challenges for Future CPU Cooling Technologies', in *Proceedings of the ASME InterPACK2005 Conference, San Francisco, CA, USA, July 17-22, 2005*.
- Scheidegger, AE 1974, *The Physics of Flow through Porous Media*, University of Toronto Press, Great Britain, 1974.
- Shah, RK & London, AL 1978, *Laminar Flow Forced Convection in Ducts*, Suppl. 1, Advance Heat Transfer, 1978.
- Shlosinger, A 1970, 'Multiple-Chamber Controllable Heat Pipe', US Parent No. 3, 543, 839, December, 1970.
- Sims, JJ 1998, 'Start-up Transients of a Capillary Pumped Loop Operating in Reflux Mode', M.S. Dissertation, University of Akron, Ohio, May 1998.
- Singh, R, Akbarzadeh, A, Dixon, C & Mochizuki, M 2004, 'Experimental Determination of the Physical Properties of a Porous Plastic Wick Useful for Capillary Pumped Loop Applications', in *Proceedings of the 13th International Heat Pipe Conference, Shanghai, China, September 21-25, 2004*.
- Stenger, FJ 1996, 'Experimental Feasibility Study of Water Filled Capillary Pumped Heat-Transfer Loops', NASA TM-X-1310, NASA Lewis Research Center, Cleveland, Ohio, 1966.
- Sudakov, RG, Maydanik, YF, Ochterbeck, JM & Choi, SW 2002, 'Development and Investigation of an Ammonia Reversible Loop Heat Pipe', in *Proceedings of 12th International Heat Pipe Conference, Moscow Russia, May 19-24, 2002*, pp. 177-182.

- Tomlinson, BJ 1997, 'Steady State Analysis of a Capillary Pumped Loop', M.S. Dissertation, The University of Texas at El Paso, Department of Mechanical and Industrial Engineering, May 1997.
- Tuckerman, DB & Pease, RFW 1981, 'High Performance Heat Sinking for VLSI', *IEEE Electron Device Letters*, Vol.2, no.5, pp. 126-129.
- Tzeng, SC, Jeng, TM & Wang, YC 2006, 'Experimental Study of Forced Convection in Asymmetrically Heated Sintered Porous Channels With/Without Periodic Baffles', *International Journal of Heat and Mass Transfer*, Vol. 49, no.1-2, pp. 78-88.
- Tzeng, SC, Jywe, WY, Lin, CW & Wang, YC 2005, 'Mixed Convective Heat-Transfers in a Porous Channel with Sintered Copper Beads', *Applied Energy*, Vol. 81, pp. 19-31.
- Wang, BX & Peng, XF 1994, 'Experimental Investigation on Liquid Forced Convection Heat Transfer through Microchannels', *International Journal of Heat and Mass Transfer*, Vol. 37, suppl.1, pp. 73-82
- Wang, J & Catton, I 2004, 'Vaporization Heat Transfer in Biporous Wicks of Heat Pipe Evaporators', in *Proceedings of International Heat Pipe Conference, Shanghai, China, September 21-25, 2004*.
- Wu, HY & Cheng, P 2003, 'An Experimental Study of Convective Heat Transfer in Silicon Microchannels with Different Surface Conditions', *International Journal of Heat and Mass Transfer*, Vol. 46, pp. 2547-2556.
- Wu, PY & Little, WA 1983, 'Measurement of Friction Factor for the Flow of Gases in very Fine Channels used for Microminiature Joule Thompson Refrigerators', *Cryogenics*, Vol.24, No.8, pp. 273-277.
- Yu, D, Warrington, R, Barron, R & Ameel, T 1995, 'An Experimental and Theoretical Investigation of Fluid Flow and Heat Transfer in Microtubes', in *Proceedings of ASME/JSME Thermal Eng. Joint Conference, 1995*, pp. 523-530.
- Zhang, HY, Pinjala, D, Wong, TN, Toh, KC & Joshi, YK 2005, 'Single-Phase Liquid Cooled Microchannel Heat Sink for Electronic Packages', *Applied Thermal Engineering*, Vol. 25, pp. 1472-1487.
- Zhmud, BV, Tiberg, F & Hallstenson, K 2000, 'Dynamics of Capillary Rise', *Journal of Colloid and Interface Science*, Vol. 228, pp. 263-269.

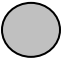
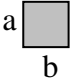
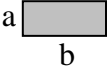
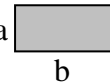
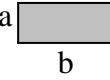
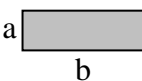
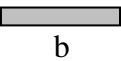
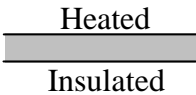


Appendix A

mLHP Modelling Data

Table A.1: Coefficients for the fifth order polynomials for different thermodynamic properties with respect to saturation temperature, for water as working fluid

<i>Coefficient</i> ↓ <i>Property</i>	<i>a</i>	<i>b</i>	<i>c</i>	<i>d</i>	<i>e</i>	<i>f</i>
Pressure, P	1.7957E+02	1.1894E+04	-.6815E+02	8.9801E-01	-2.1493E-03	1.9476E-06
Latent Heat, h_{lv}	7.4603E+02	4.4916E+04	-.3599E+02	1.0736E+00	1.07368E-03	1.0393E-06
Liquid Density, ρ_l	1.0419E-01	6.9020E+00	2.2600E-03	-1.1721E-04	3.0898E-07	-2.5330E-10
Vapour Density, ρ_v	5.9052E-04	3.9113E-02	-5.7848E-04	3.2354E-06	-8.1189E-09	7.7200E-12
Liquid Viscosity, μ_l	1.8713E+01	1.2395E+03	-.3595E+01	5.6007E-02	-1.0256E-04	7.0378E-08
Vapour Viscosity, μ_v	-1.1316E-03	-7.4958E-02	1.1477E-03	-4.8921E-06	9.5964E-09	-7.1464E-12
Surface Tension, σ_l	-1.1607E-02	-7.6878E-01	1.7629E-02	-9.2985E-05	1.9650E-07	-1.5029E-10
Liquid Specific Heat, c_{pl}	2.1857E+00	1.44780E+02	-.3100E+00	5.1015E-03	-9.1976E-06	6.3383E-09
Liquid Thermal Conductivity, k_l	1.3938E-01	9.2324E+00	-9.3063E-02	4.5596E-04	-9.8138E-07	7.6438E-10

Table A.2: Nusselt numbers and friction factors for fully developed laminar flow in tubes of different cross section. (Incropera and DeWitt, Page-496, Table 8.1)

Cross Section	$\frac{b}{a}$	$Nu_D = \frac{hD_h}{k}$		$f Re_{Dh}$
		Uniform q_s''	Uniform T_s	
	—	4.36	3.66	64
	1.0	3.61	2.98	57
	1.43	3.73	3.08	59
	2.0	4.12	3.39	62
	3.0	4.79	3.96	69
	4.0	5.33	4.44	73
	8.0	6.49	5.60	82
	∞	8.23	7.54	96
	∞	5.39	4.86	96
	—	3.11	2.47	53

Appendix B

Case Study: Design and Evaluation of a Capillary Pumped Loop (CPL) with Cylindrical Evaporator

In order to better understand and learn how to design capillary driven two-phase loops, a medium scale capillary pumped loop (CPL) was designed and built. This task was performed to better comprehend the constraints involved when designing such systems as well as gaining the experience of testing and integrating all parts. The study also explored the unique characteristics of capillary pumped loops.

A capillary pumped loop is a two phase heat transfer device for thermal control of electronics, satellites and other space applications. In this chapter, the design and setup of a capillary driven loop for thermal management of up to 210 W at the source and heat transfer over distance of 1 m are discussed. Setting up the experimental test bed and procedure to operate it are elaborated in detail. Results of tests on the designed CPL for heat load in the range of 30-210 W are also been presented.

B.1 Introduction

Capillary Pumped Loop (CPL) is another type of two-phase loop heat transfer system that is based on the same basic principle of closed evaporation-condensation cycle maintained at the expense of capillary forces. The concept of a capillary pumped loop first appeared thirty years ago during the initial development phases of traditional heat pipes. A CPL is a two-phase thermal management system which was first proposed by Stenger in 1966 at the NASA Lewis Research Center. It has the potential to transfer large heat loads over long distances with small temperature differential and no external power requirements except for the power control of the reservoir. Development of CPLs has been primarily focused on thermal control for space applications (Maydanik, 1999) including cooling of electronics (Chen and Lin, 2001) and satellite thermal control (Riehl et al, 2002). A CPL is composed of the following major components: Evaporator (heat acquisition device), Condenser (heat dissipating device),

Reservoir (temperature control device), Liquid and Vapour Transport Lines. A schematic of a CPL is shown in Figure B.1. It uses capillary forces, generated in a porous structure present in the evaporator section, to pump working fluid from the heat acquisition system to the heat dissipating devices.

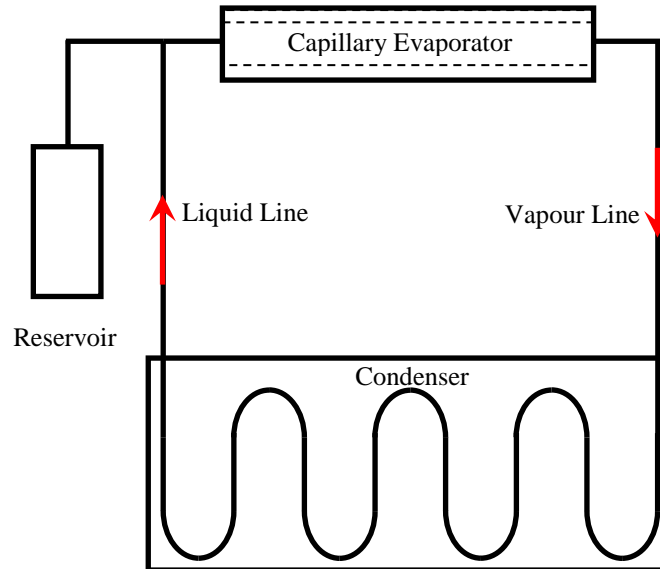


Figure B.1 Schematic of CPL

Like LHPs, in a CPL, the wick structure is present only in the evaporator. This allows the remainder of the tubing in the system to be smooth walled and reduces the frictional pressure drop in the system. Also, vapour and liquid flow passages are completely separated from each other. Due to these design enhancements the thermal transport capacity of the CPL is an order of magnitude greater than that of conventional heat pipes.

As discussed before, the primary difference between a CPL and LHP is the location of the reservoir that physically differentiates these two types of loop, and provides them with their unique operating characteristics. CPLs are provided with a remotely located reservoir connected to the liquid line while a LHP reservoir, also called a compensation chamber, is thermally and hydraulically combined with the evaporator in one body. Due to the remote location of the reservoir or fluid accumulator in the CPL the tendency of wick depriming during startup is more than in the LHP. For that reason, a CPL need an active control like a starter pump or pre-heater on the reservoir to flood the evaporator, particularly the evaporator

wick with liquid prior to startup and to set the operating temperature of the loop during steady state. A CPL is structurally more complex than a LHP but as a benefit of the distant location of the reservoir it provides effective control over the operating temperature with changing input power. A CPL allows active control of the evaporator temperature with the help of the controllable thermal action of the reservoir. Such thermal action may be positive or negative, and its value does not usually exceed 5-10% of the heat load transferred by the CPL. Therefore with CPLs, very precise temperature can be achieved for the heat source that can be set remotely by tuning (i.e. actively controlling) the temperature and thus the saturation conditions inside the reservoir with the help of a heater attached to it.

Theoretical and experimental studies of CPL models have been conducted by different investigators including Dickey and Peterson (1994), Lin et al. (1994) and Miao et al. (2002) using ammonia as the working fluid. Sims (1998) studied in detail the start-up behaviour of the loop in reflux mode. Tomlinson (1997) presented his results on steady state operation and performance of a CPL. A description of the operating characteristics of a small scale capillary pumped loop was given by Bazzo and Riehl (2003). The current study is conducted to design and analyse a medium scale CPL as a heat transfer device using acetone as the working fluid. In this investigation the temperature control capability of the capillary pumped loop is explored in detail. Thermal characteristics of the CPL with respect to the start-up phenomena and steady state behaviour have been studied. As the start-up process in the loop systems is very critical, methods for the reliable start-up for capillary pump loops in particular are discussed.

B.2 Objective of Study

The main objective of this experimental investigation is to gain an understanding of the capillary driven two phase loop system at medium scale before proceeding to the miniature model investigation and to study the unique operational characteristics of the capillary pumped loop including the temperature control capability using an active thermal device on the reservoir, and start-up process through pressure priming of the capillary evaporator.

B.3 Description of Capillary Pumped Loop (CPL) Prototype

The medium scale CPL was designed to achieve thermal management of up to 210 W which was the estimated heat load which was required to be removed from the heat source (in this case the dashboard of a car) and transferred to a remotely located heat sink at a distance of 1 m. The dashboard of the car was receiving radiant heat transfer from the engine. It should be noted that the present model was one of the preliminary models that was designed to get familiar with the CPL working which was also expected to provide guidelines in the design of more profound cooling system for the car dashboard. The design and dimensions of the CPL model were based on pressure loss criteria such that the total pressure loss inside the system is less than or equal to the capillary pressure generated by the wick structure. Also, the prototype design was inspired by the work of Bazzo and Riehl (2003). Figure B.2 shows the layout of the capillary pumped loop showing various components of the model. A resistive tape heater was used as heat source for the capillary evaporator while an air cooled condenser was used as the heat dissipating device. The CPL test bed was placed in a horizontal position to avoid any effect of gravity. Design characteristics of various CPL components are as follows:

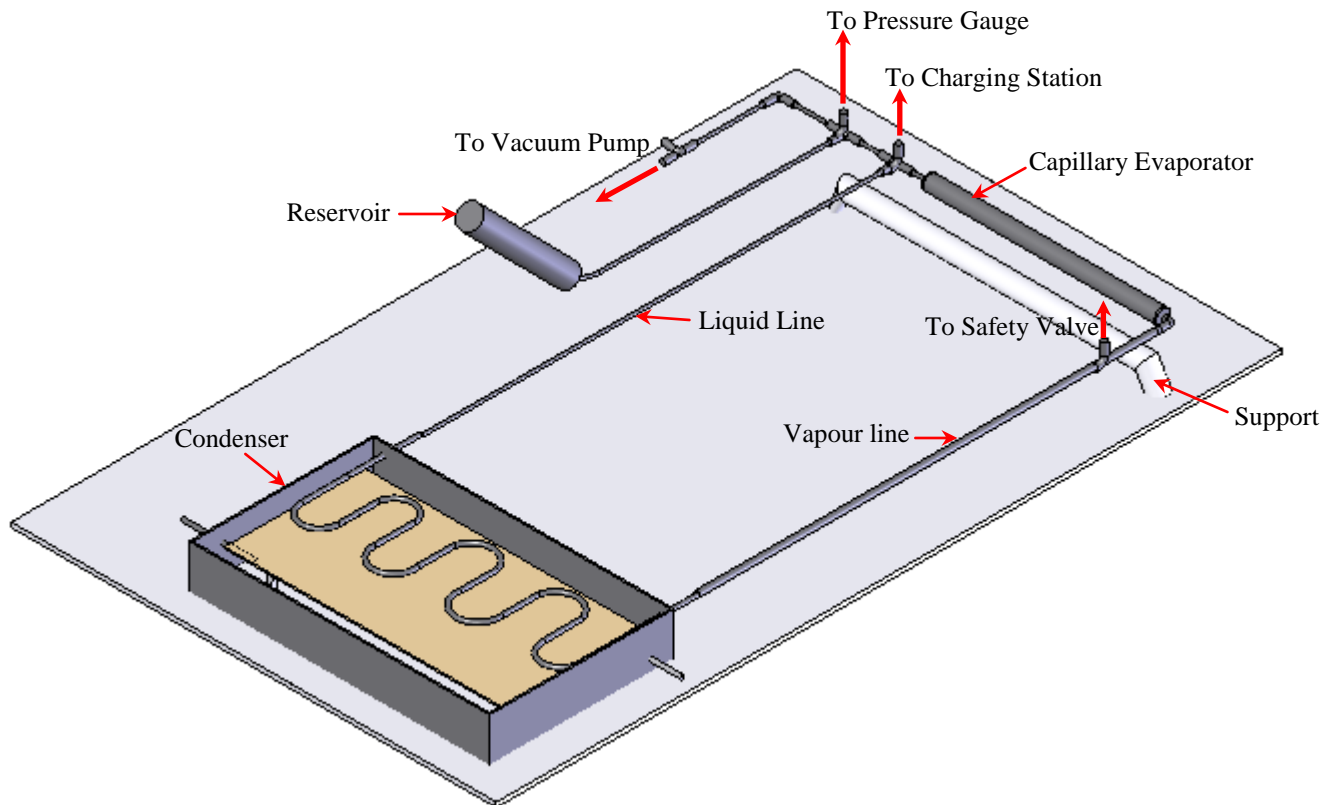


Figure B.2 Layout of the Capillary Pumped Loop Experimental Model

B.3.1 Evaporator Structure

The capillary evaporator consisted of an axially grooved, extruded aluminium (A6063-T5) tube which was force fitted on the inside with a porous Ultra High Molecular Weight (UHMW) polyethylene wick. In this case, aluminium was chosen as evaporator material due to its light weight which was a requirement of the design. It should be noted that dimensions of the evaporator structure including the inner/outer diameter and active length were dictated by the wick geometry which was chosen from the standard products of Pneumotronic Ltd, Brazil. In the case of the internally grooved aluminium tube the total length was 500 mm with 31.5 mm OD and 28.5 mm ID. It consists of 24 axial grooves, the width of the groove top and base was 1.5 and 2 mm respectively and the depth of the groove was 2 mm (Figure B.3). Figure B.4 presents an exploded view of the capillary evaporator showing the internal details.

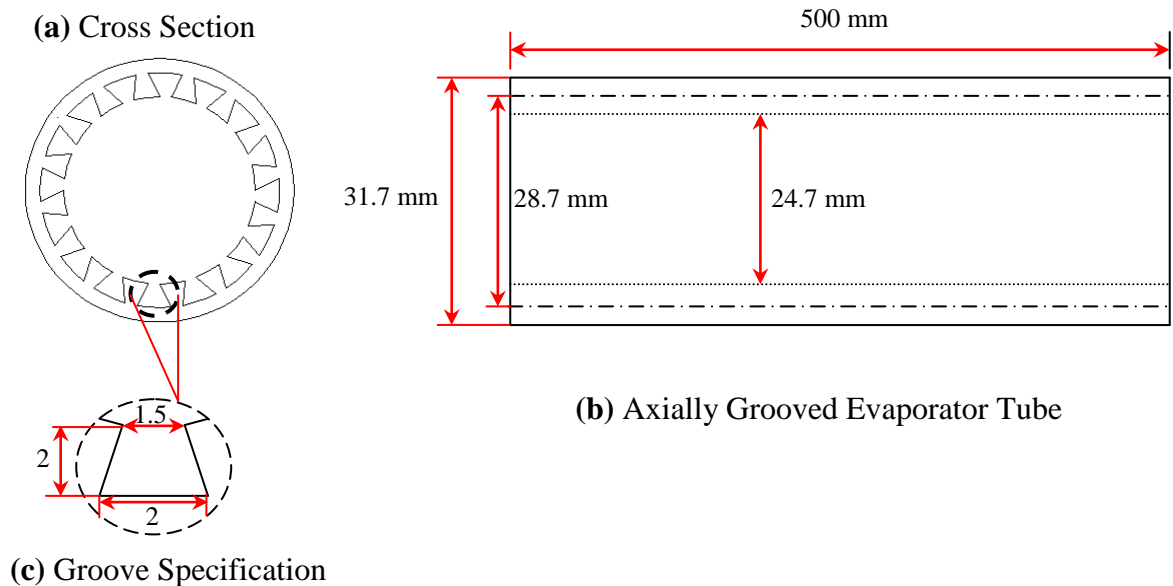


Figure B.3 Design and detail of the axially grooved evaporator tube

The porous tube which was tightly fitted inside the grooved aluminium tube was 440 mm in length, 25 mm OD and 12 mm ID. The wick structure was 50% porous with effective pore radius of 20 μm and permeability of approximately 10^{-12} m^2 . To prevent any internal leakage of vapour from the vapour removal channels to the inside of the evaporator core the ends of the cylindrical wick tube was sealed with the help of two tightly fitted Teflon plugs on each end. A bayonet tube which is the extension of the liquid line was inserted through a hole drilled in one of the plugs to allow liquid flow inside the evaporator core.

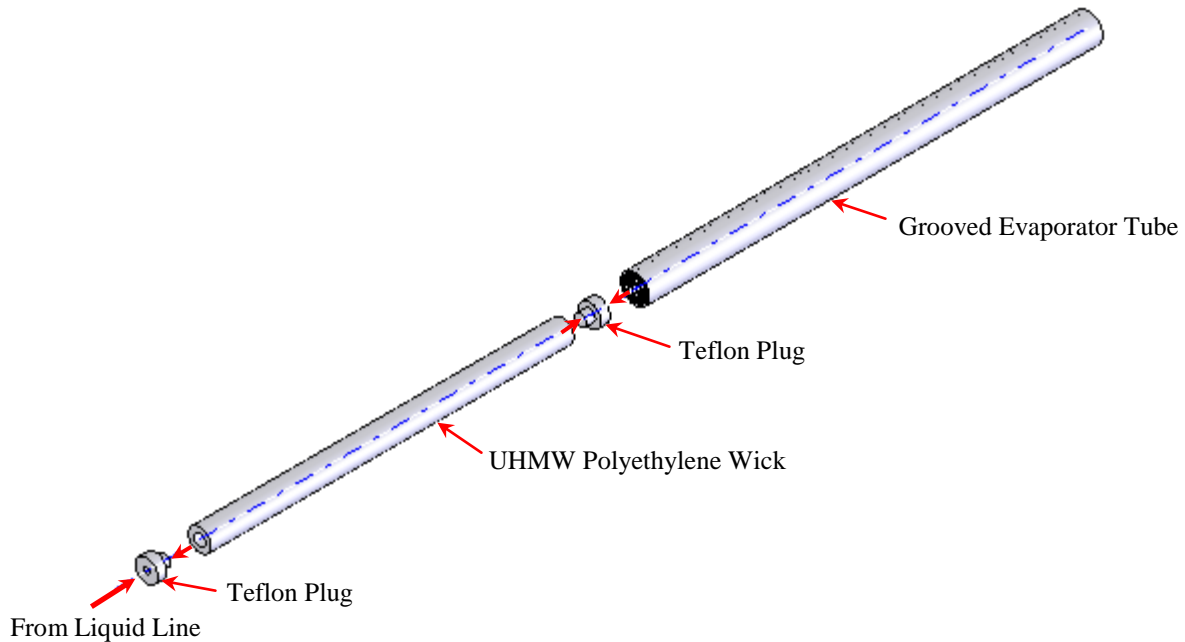


Figure B.4 Exploded view of the Capillary Evaporator

The details of the CPL evaporator are also shown with the help of a side view and cross sectional view in Figure B.5. The bayonet tube extends to the middle of the wick and helps to ensure that its entire length is properly primed with the liquid at all times.

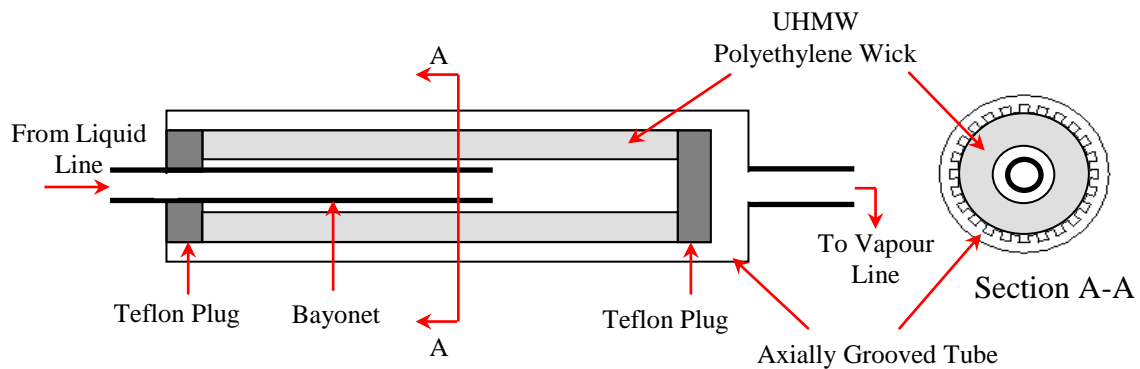


Figure B.5 Schematic of CPL Evaporator

The liquid and heat flow inside the capillary evaporator are depicted in Figure B.6. The liquid enters the evaporator core through the bayonet tube. Here the evaporator core behaves as an embedded reservoir to accumulate and supply liquid to the capillary structure. The liquid is filtered through the wick and forms evaporating menisci at the liquid-vapour interface in the evaporation zone. Like LHPs, heat flow through the wall of the cylindrical evaporator and

liquid flow through the wick structure are projected towards each other. This helps to form an efficient evaporation zone by the principle of inverted menisci. The vapour formed as a result of the evaporation process flows along the heated wall and exits to the vapour line.

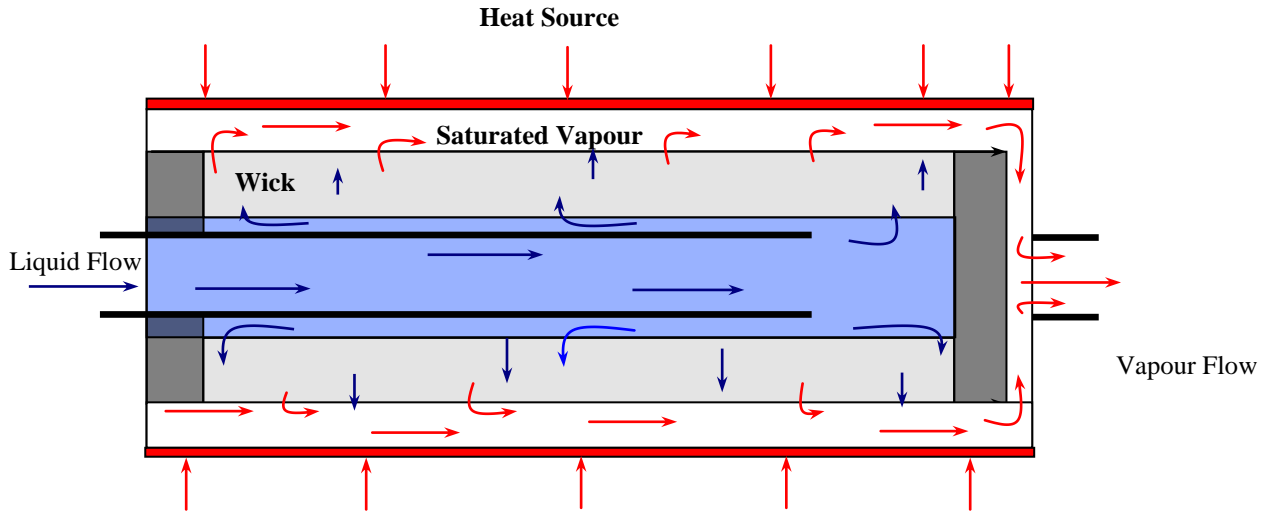


Figure B.6 Heat and Fluid flow inside the capillary evaporator

B.3.2 Condenser

The condenser consists of stainless steel (316L) tube, 4.3 m in length, 6.4 mm OD and 4.5 mm ID, bent in the form of coil and fixed on a copper plate. Depending upon the applied heat load, cooling of the condenser can be performed by natural or forced air convection using a fan. The condenser was designed such that it was able to dissipate all the heat input at the evaporator which has been transported to the condenser and further subcool the liquid going to the liquid line. Liquid subcooling was required to avoid bubble generation inside the evaporator core due to conduction of heat through the evaporator end fittings and back conduction through the porous wick.

B.3.3 Liquid and Vapour Transport Lines

Liquid and vapour transport lines were made of stainless steel (314L) tube, each 1 m long, 6.4 mm OD and 4.5 mm ID. Subcooled liquid flows through the liquid line while saturated or slightly superheated vapour flows through the vapour line. The length of liquid/vapour line denotes the heat transport distance of the CPL with the given configuration and operating under maximum heat load.

B.3.4 Reservoir

The primary functions of the reservoir were pressure priming of the evaporator wick during start-up, to precisely control temperature at the source and to act as an accumulator for liquid inventory. The two phase reservoir was made of a stainless steel (304L) cylinder of 0.75 L capacity. The volume of the reservoir was sized large enough to contain the overall liquid inventory in the CPL loop. To ensure that only liquid and no vapour bubbles would flow from the reservoir to the evaporator core, the reservoir was inclined at 45° to the horizontal. The reservoir was connected to the main loop with the help of stainless steel (314L) tube 0.5 m in length.

B.4 Loop Pressure Analysis

The pressure analysis of the CPL was done on the same basis as that of the LHP, discussed in Chapter 3. According to the first condition of serviceability of the loop system, the total pressure drop in the fluid loop must not exceed the maximum capillary pressure generated by the porous structure on the working fluid which is given by Young-Laplace equation (Dunn & Reay, 1994) as:

$$(\Delta P_{cap})_{\max} = \frac{2\sigma_l}{r_{me}} \quad (\text{B.1})$$

The total pressure drop in the loop, ΔP_t , is the sum of the pressure losses due to vapour flow, ΔP_v , liquid flow ΔP_l , and hydrostatic pressure loss due to the orientation of the device in the gravity field, ΔP_{gr} .

$$\Delta P_t = \Delta P_v + \Delta P_l + \Delta P_{gr} \quad (\text{4.2})$$

The above equation can be further broken down to include the pressure losses in the different sections of the loop. Making use of the terminology used in Chapter 3, the Equation (4.2) can be summarized as:

$$\Delta P_t = \Delta P_{v,vl} + \Delta P_{v,e} + \Delta P_{l,ll} + \Delta P_{v,c} + \Delta P_{l,w} + \Delta P_{gr} \quad (\text{B.3})$$

By substituting the values of the parameters into Equation (B.3) as discussed in Chapter 3, the maximum heat load that can be transferred by the CPL can be calculated. In the case of the designed CPL the values for maximum power along with different pressure losses as calculated on the basis of the above approach are shown in Table B.1.

Table B.1 Major parameters for the CPL

Parameter	Value	Units
Maximum Heat Load, Q_{\max}^{\bullet}	250	W
Evaporator Temperature, T_e	55	°C
Maximum Capillary Pressure, $(\Delta P_{cap})_{max}$	1925	Pa
Evaporative Pressure Loss, ΔP_e	124	Pa
Vapour Line Pressure Loss, $(\Delta P_{v,vl} + \Delta P_{v,c})$	1632	Pa
Liquid Pressure Loss, $\Delta P_{l,ll}$	90	Pa

B.5. Experimental Setup

Figure B.7 shows the placement of the thermocouples (TC) and other instrumentation on the CPL test bed. Temperatures at twenty different points of the CPL were measured with T-type thermocouples with an error of $\pm 0.5^{\circ}\text{C}$.

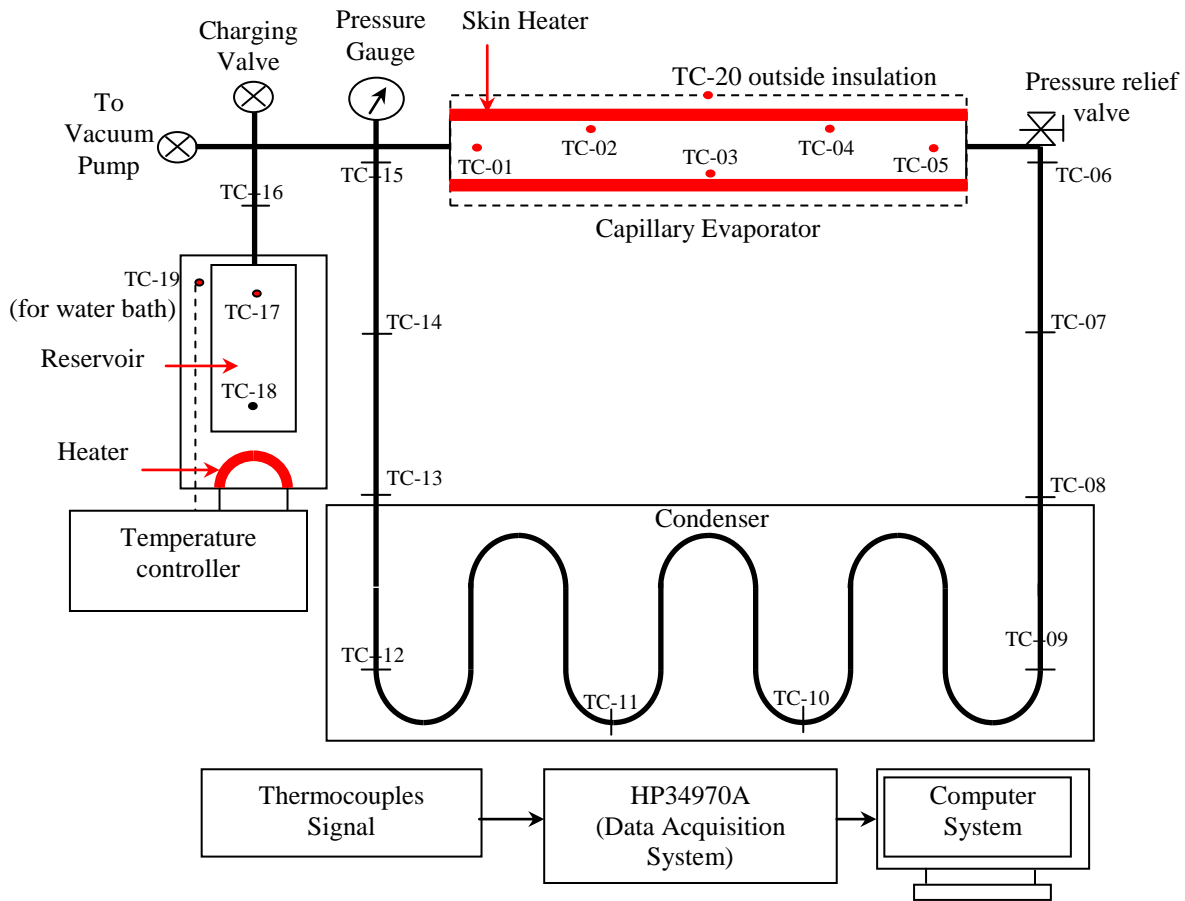


Figure B.7 CPL Experimental Setup

Data from these thermocouples was acquired every 10 s by an HP34970A data acquisition system. The system was connected to a computer in order to visually monitor temperatures throughout the CPL. A compound pressure gauge with a range of -100 – 10,000 kPa was used to ensure proper vacuum before charging and to monitor the pressure inside the loop during operation. To provide safer working conditions and avoid over pressurization of the system, a R3A series pressure relief valve was installed on the vapour line. In order to deliver the required heat load to the capillary evaporator, an electrical resistive heater (1.5 m x 2.5 cm) of rated wattage 225 W was wrapped around the evaporator cylinder. To minimise heat losses to the environment the capillary evaporator was insulated using fibre glass insulation. An AC Step-down transformer was used to vary the wattage of the heater. The power input to the evaporator heater was measured using an AC multimeter which was connected to the output of the transformer. Thermocouples were placed at four different locations along the length of the evaporator to determine its mean temperature. Heat removal at the condenser was provided by a cooling fan. In order to maintain constant saturation conditions inside the reservoir, it was placed in a constant temperature water bath. The water bath was fitted with an immersion heater which was controlled by a temperature controller with an accuracy of ± 1 °C. The CPL test bed is shown in Figure B.8.

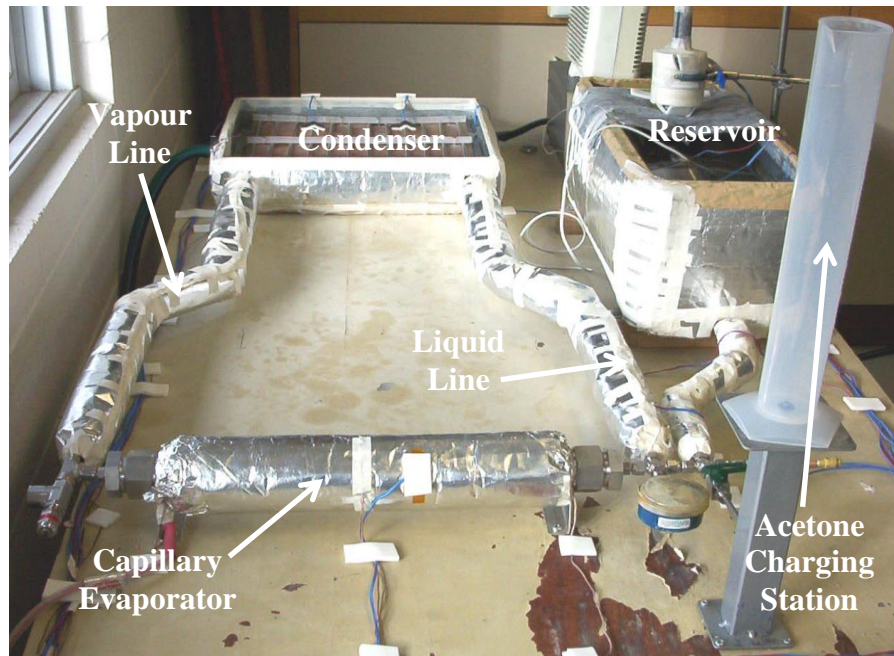


Figure B.8 CPL Test Bed

High grade Acetone, a saturated aliphatic ketone, with a minimum assay level of 99.95% was used as working fluid due to its chemical compatibility with aluminium and stainless steel at low as well as with high temperatures. Acetone is also very cheap to obtain in a high purity state and the working pressures are not very high. Proper consideration was given to the purity level and chemical compatibility of the acetone with the material and seals used in the system. Acetone is fully compatible with aluminium, stainless steel and UHMW polyethylene material used in the system. Also, the heat transfer characteristics are optimum from heat pipe working fluid point of view and it is easily available at low cost.

B.6 Experimental Procedure

Presence of moisture in the working fluid can corrode the aluminium evaporator and act as potential for non-condensable gas (NCG) generation with time. NCGs, if present, will potentially accumulate inside the evaporator core and hinder the liquid supply to the wick which will consequently result in dry out of the evaporator wick. To avoid this, the system was thoroughly cleaned using compressed air and acetone before installing the wick inside it. Being polar in nature, acetone is soluble in water and helped to get rid of the leftover water from hydrostatic testing. The procedure was repeated 2-3 times to clean the system of any grease or impurities from the process of manufacturing. Next, the system was kept under vacuum of approximately 0.001 mm of Hg for 24 hours to check for any leaks that might degrade its operation. After the system passed the vacuum test, it was charged with liquid inventory equal to 50-60 % of its total internal volume (Chen and Lin, 2001) which was calculated to be 550 ml. Before the start-up of the CPL, the reservoir was heated to the operating temperature of the loop. As vapours are formed inside the reservoir, this will pressurise the system and fill the entire loop with the liquid. Any vapour bubble, if present, inside the evaporator core will condense due to subcooling of fluid at elevated pressure. The system was maintained under so called pressure priming for around 6-7 hours to ensure that only liquid and no vapour bubbles were present inside the core. After this, the evaporator heater was turned on and the required heat load was set by use of the transformer.

B.7 Results and Discussion

Figure B.9 shows the start-up behaviour of the CPL at 50 W of power input to the evaporator. The reservoir temperature was set at 40 °C. As the temperature inside the evaporator rises above the two-phase reservoir, phase change occurs inside it. The resulting vapour pushes the liquid and clears the grooves of the evaporator. This helps in the formation of the meniscus on the evaporating face of the wick which is responsible for developing the capillary pressure to circulate the working fluid around the loop. The excess liquid cleared from the evaporator grooves and vapour line by vapour is displaced to the reservoir. The loop presented very smooth start-up and achieved a stable state without any signs of wick de-prime. However, it was observed that the system produced reliable start-up only if the pressure priming of the capillary structure was done for 6-7 hours. Otherwise, if start up was attempted without prior preheating of the reservoir, the device showed elevated temperature trends at the evaporator and ultimately resulted in wick dry out that was evident from the back flow of vapour from evaporation zone to the wick core and out of the evaporator to the liquid line. The rise in temperature of the liquid line at the evaporator inlet indicated the occurrence of back flow.

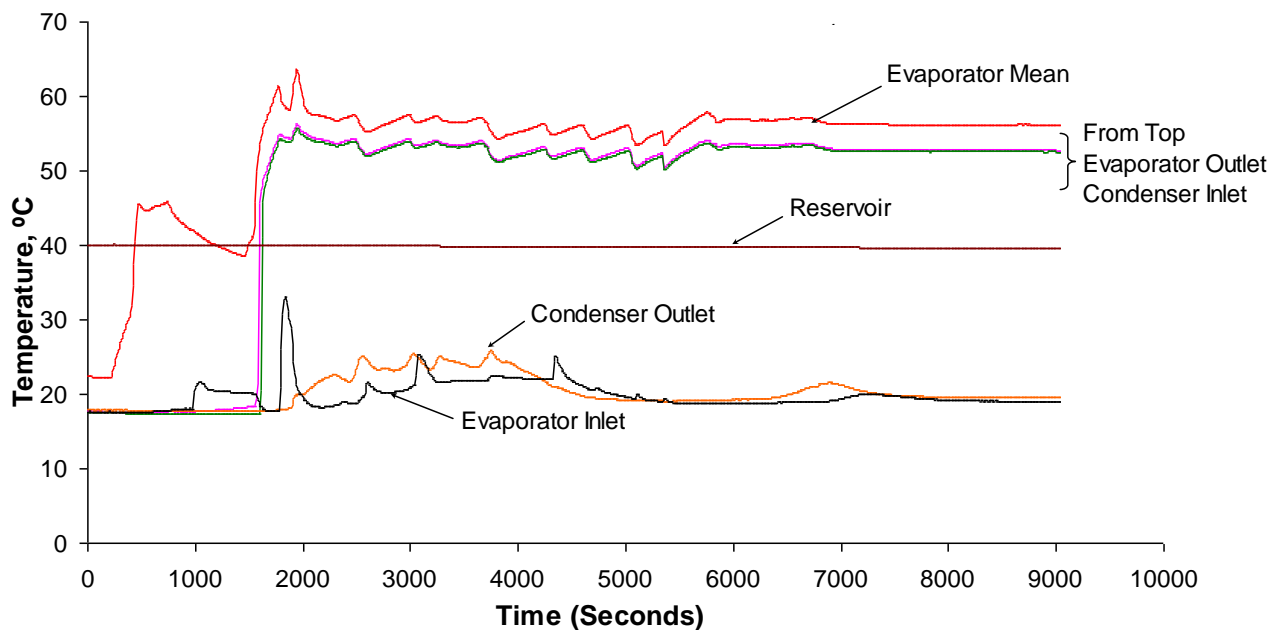


Figure B.9 Start up of CPL at 50 W heat load

The system showed some temperature fluctuations after start-up before the evaporator attained a stable temperature of around 52°C. The temperature or pressure oscillations were generally observed at very low heat load. These fluctuations can be due to the possibility that for low applied heat load to the evaporator, the power level was too close to the minimum calculated power for the proper CPL operation, which may have resulted in some fluctuation due to intermittent vapour flow. The minimum power is required to set up the pressure and thus temperature difference across the wick structure for continuous circulation of the fluid in the closed loop circuit. To some extent this minimum power is dictated by the fraction of the total applied heat load that is conducted back to the evaporator core via the wick structure.

Figure B.10 shows the start-up results for the CPL for the input heat load of 100 W. In this case the reservoir temperature was set at 50 °C and a steady state evaporator temperature of 55°C was achieved.

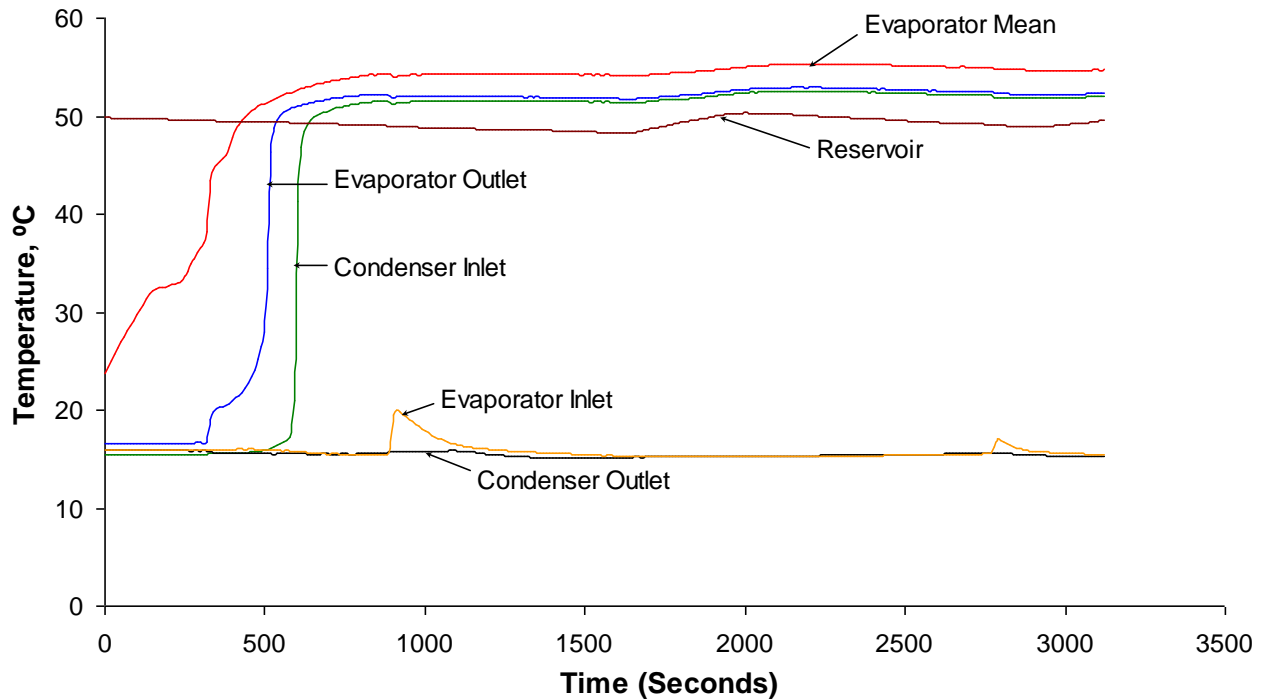


Figure B.10 Start-up of CPL at 100 W heat load

In the current design of the CPL, the length of the evaporator section is as high as 0.5 meter. This can possibly result in superheating of the vapour as it moves along the heated wall of the evaporator in the vapour removal passages. It should be noted that difference in the evaporator and reservoir temperature helps to evaluate the degree of superheating of the

vapours coming out of the evaporator. From the two start-up trends it is seen that in the former case the degree of superheat of vapours is high compared with the latter case. It is expected that for start-up of the CPL under low heat load the liquid flow rate to the evaporator core will be lower than for the high heat load case. As a result, consequences of back heat conduction and vapour bubble formation inside the evaporator core for the low heat load are greater. Production of any vapour bubbles inside the evaporator core can decrease the quantity of liquid filtered through the capillary structure which ultimately increases the evaporator wall temperature and produces a high degree of superheat. Presence of any NCG inside the core can produce similar results. For that reason, the CPL is more sensitivity to the non condensable gases (NCG) than LHP.

Tests were conducted on the CPL at low heat loads ranging from 30 to 100 watts and high heat loads from 100 to 210 W. These tests were conducted on the CPL with the condenser maintained at room temperature by air cooling using forced convection. Figure B.11 shows the test results of the CPL under low heat loads as the power input to the evaporator was increased from 30 to 100 W. In this test the reservoir temperature was fixed at 40 °C. The CPL presented very good response to changing heat loads and reached steady state within a short time period. It is observed from these results that the CPL was able to maintain the temperature at the evaporator within 52 to 57 °C for change in heat load from 30 to 100 W. In these low power tests again the degree of superheat was as high as 12 °C due to any of the causes stated above.

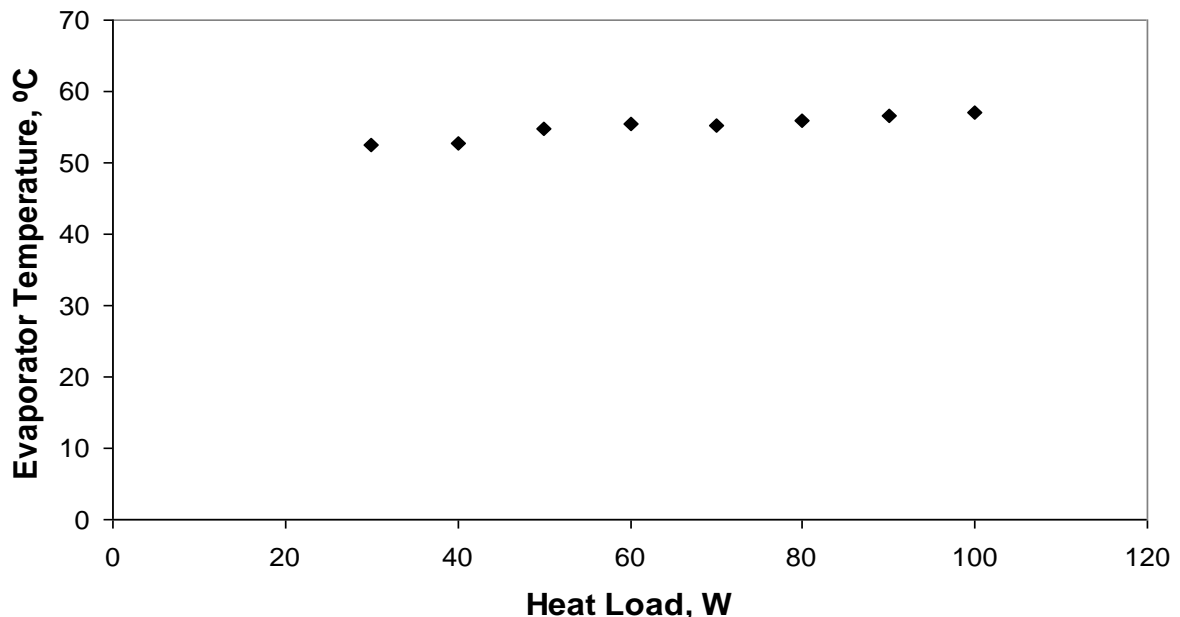


Figure B.11 Evaporator temperature versus applied heat load for low heat inputs

Figure B.12 shows the results of a test, conducted on the CPL for input heat load from 100 to 210 W, as a relationship between evaporator temperature and applied heat load. The reservoir temperature was set at 50 °C. It is evident from the outcomes that the CPL exhibited very efficient control over the operating temperature of the evaporator for the entire range of input power. The evaporator temperature was maintained within 55 to 58 °C for applied heat load in the range of 100 to 210 W.

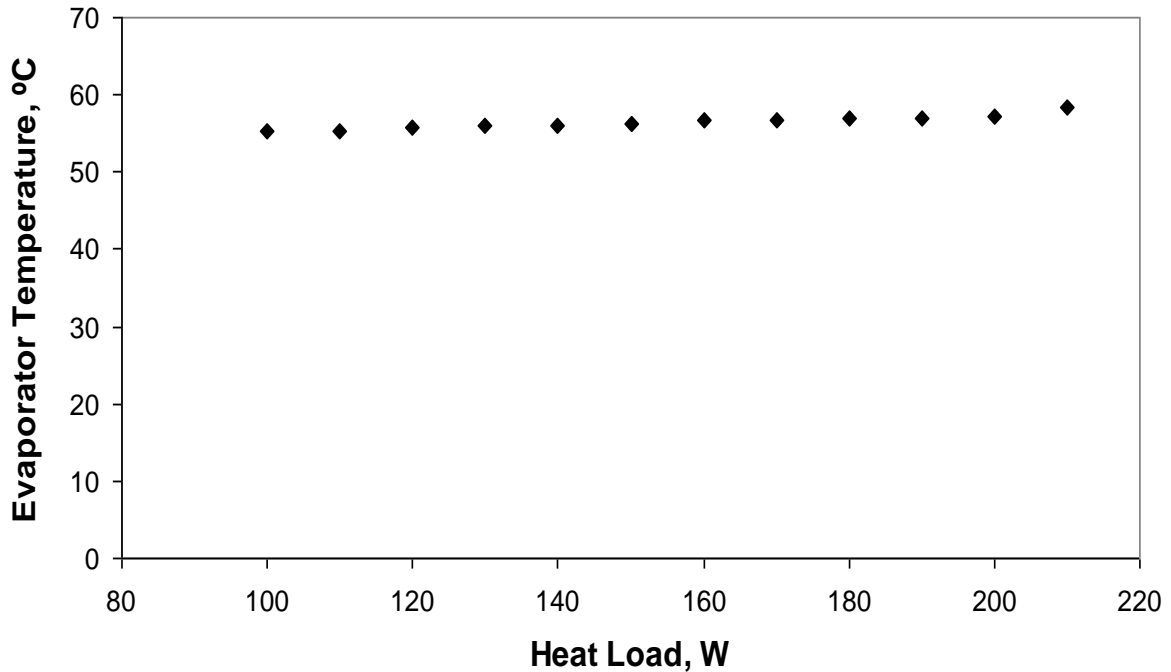


Figure B.12 Evaporator temperature versus applied heat load for high heat inputs

It is noted from the above results that the system presents poor thermal resistance when the reservoir temperature is low (i.e. near to ambient). If the reservoir temperature is finely adjusted, the thermal performance of the CPL increases as well as the degree of superheating of the vapour decrease. This particular behaviour of the CPL can be better explained by taking into account the relative liquid inventory present in reservoir and evaporator for a particular heat load and set point at the reservoir. At steady state, it is expected that for lower reservoir temperature the local saturation pressure inside the reservoir is low which results in the accumulation of the major liquid inventory inside the reservoir. Due to the low fluid charge inside the evaporator core, improper wetting of the porous structure can result which produces high evaporator temperature. In the same manner, as the reservoir temperature is adjusted at a high level, the saturation temperature and thus pressure inside the reservoir increases and

pushes the liquid into the evaporator core. Due to the large inventory of fluid inside the evaporator core, the wick is properly saturated with liquid and thus heat leaks from the evaporation zone to the evaporator/wick core decrease. The overall effect of this phenomenon is to produce a decrease in the degree of the superheating of vapour coming out of the evaporator as well as the evaporator operating temperature.

In Figure B.13, the evaporator thermal resistance, R_e of the CPL is shown with respect to the applied heat load. Values of R_e around 0.02 to 0.07 °C/W were achieved for applied heat loads in the range of 30 to 210 W.

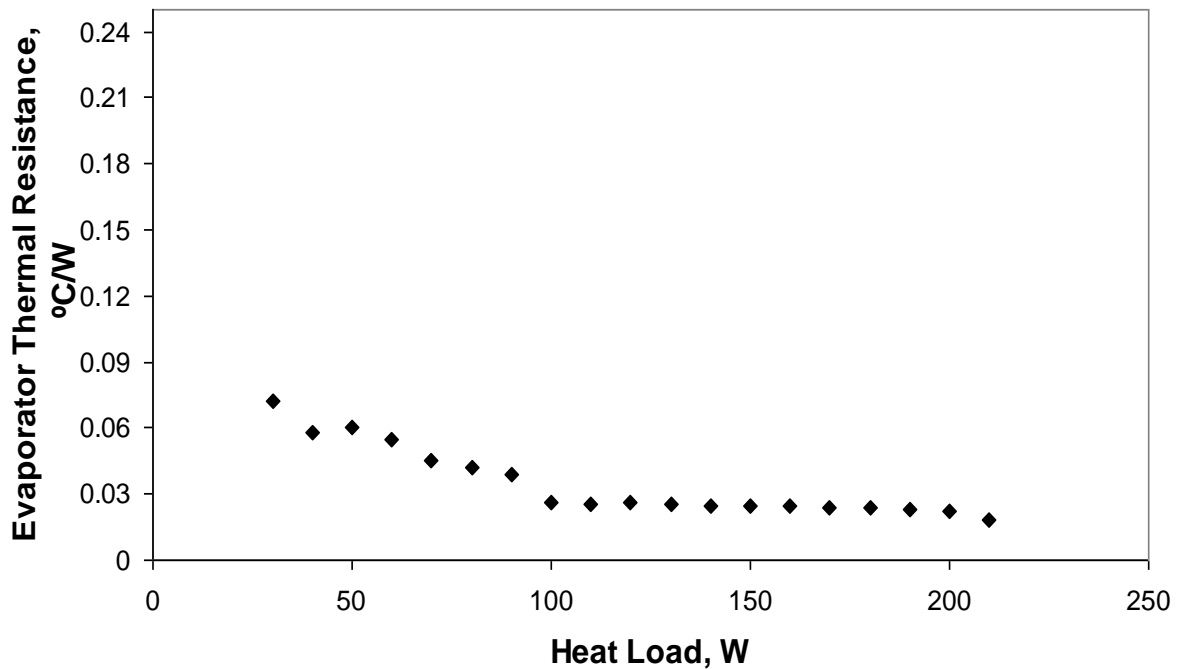


Figure B.13 Variation of the evaporator thermal resistance with the applied heat load

Figure B.14 shows the relationship between the total thermal resistance, R_t , calculated on the basis of “evaporator-heater interface temperature and ambient temperature”, and the applied heat load. For the R_t a minimum value of 0.19 °C/W was achieved at the maximum heat load of 210 W with the corresponding evaporator temperature of 58.33 °C.

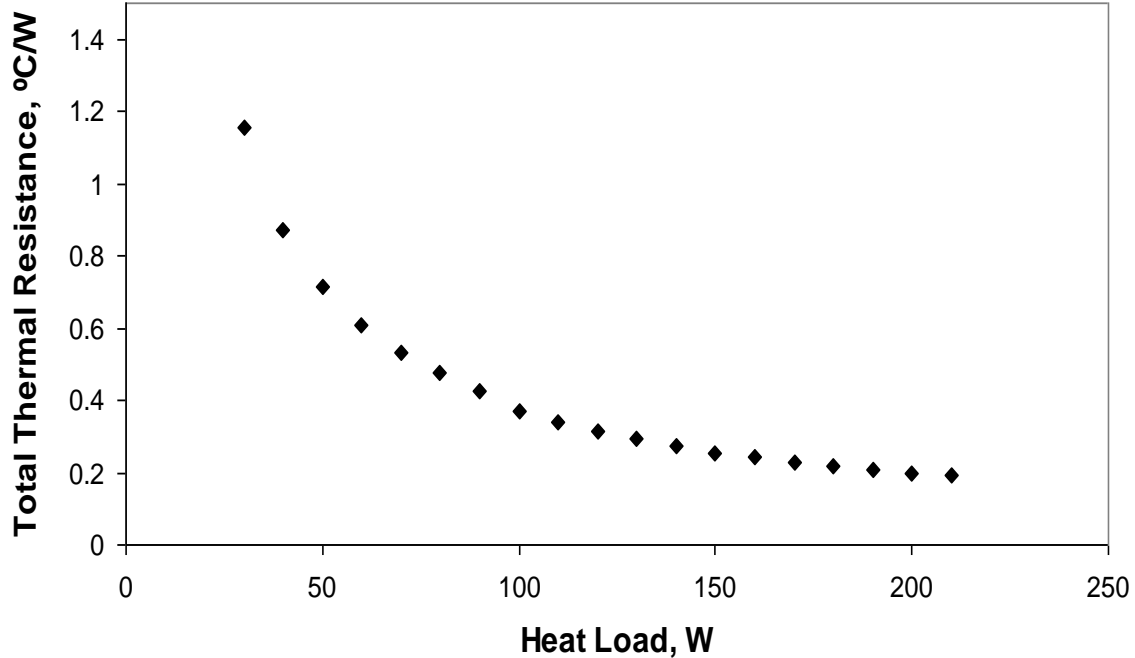


Figure B.14 Variation of the total thermal resistance with the applied heat load

The study on the CPL reveals the heat transfer potential of loop systems. With the above design of the CPL, heat load up to 210 W was transferred from the evaporator to condenser at a distance of up to 1 m with differential temperature of as small as 0.29 – 0.46 °C. The current investigation helps in the classification of capillary pumped loops as efficient thermal management systems that can be use for the precise control of the source temperature within limits which are decided by the system design and heat transfer requirements. This study also helps to differentiate CPL from the LHP technology.

B.8 Summary

The following conclusions are made form the above study:

- A medium scale capillary pumped loop with an aluminium evaporator, Ø 31.70 and 500 mm in length, was designed and successfully transferred a maximum heat load of 210 W over a distance of 1 meter, using acetone as the working fluid.
- The loop was able to control the temperature of the evaporator within 55 ± 3 °C for 30 to 210 W input heat load

-
- A total thermal resistance - R_t minimum value of 0.19 °C/W was achieved at the maximum heat load of 210 W with the corresponding evaporator temperature of 58.33 °C.
 - The CPL proved to be a very efficient thermal control device and provided effective control over the operating temperature with changing input power

Appendix C

Experimental Determination of Properties of a Porous Structure

In this appendix, test procedures to measure permeability, pore radius, porosity and effective thermal conductivity of a porous structure are discussed in detail. Plastic wicks made from Ultra High Molecular Weight (UHMW) polyethylene and metal wicks made from different grades of copper powder were used in the study. Wicks can be processed to desired porosity and pore size using powder processing (or sintering) technique. Porous structures are very suitable material for heat pipe applications to promote working fluid circulation around the loop. Permeability of the porous structure has been determined at both low and high flow rates. Methods to measure the largest pore size and the mean effective pore size of the porous structures are discussed. To measure the porosity, two different methods known as the density method and soaking method were used. Effective thermal conductivity of the porous structure saturated with the working fluid was also evaluated experimentally. In the last section, the conclusions drawn from the study are given.

C.1 Introduction

Porous structures are excellent for use in widespread applications for wicking, diffusing, venting and muffling. Wicks can be made from plastic or metals by powder processing techniques that involve sintering of powder material at a temperature close to its melting point. Two-phase heat transfer systems invariably employ the capillary pressure generated by a wick to passively transfer waste heat from heat source to heat sink. Wicks are key parts of a loop system including a loop heat pipe and a capillary pumped loop. Physical properties of the wick like porosity, permeability and the pore size are very important for heat transfer applications. High capillary pressure is expected to increase the heat transfer capability and to pump the working fluid against gravity. The capillary force generated by a porous structure depends on the pore size which can be varied over a wide range by using

powders of different sizes during the sintering process. High values of porosity and permeability are expected to decrease the flow resistance and back heat conduction through the wick. However the permeability of the wick decreases with decreasing pore size. So the optimisation of the wick with respect to pore size and permeability by using powders of different size, shape, density and compactibility is necessary for the design of high efficiency loop heat transfer systems.

Apart from the necessary capillary pressure, the selection of the wick must provide hydraulic and thermal resistance against the flow of vapour and heat from the evaporation zone to the compensation chamber. Uniform porosity in all the three axes and the tortuous path of the fine pores provides an efficient network of porous matrix for fluid flow through the wick and thus helps to provide these functionalities to the wick. A wick should possess low effective thermal conductivity to qualify it as a thermal lock between the evaporator and compensation chamber. Also, it must be chemically compatibility with the working fluid to avoid any consequences of NCG production.

The evaporator wick is the most critical component of the loop heat pipe system. It provides the pumping pressure to circulate the working fluid around the loop and thus avoid the need for a pump for the loop's operation. In order to carry out a complete pressure and thermal analysis of the loop, physical properties of the wick should be known. However, due to the microscopic nature of these properties their precise measurement requires very costly and dedicated instrumentation.

Different methods for the assessment of the wick properties for a heat-pipe solar receiver have been discussed by Adkins and Moss (1990). In his work on porous media Scheidegger (1974) has summarized information on hydrodynamics and properties of the porous structures. Faghri (1995) in his work on heat pipes discussed methods for measuring the flow properties of a wick. An overview and detailed analysis of the classical theory of capillarity by Zhmud et al (2000) and capillary rise in porous media by Lago and Araujo (2001) are very useful for understanding the fluid dynamics inside porous structures.

C. 2 Description of Experimental Samples

To undertake this study, sintered wick samples made from polymeric/plastic and made from copper powder were used in the experimentation. Polyethylene wicks which were in the shape of annular cylindrical tubes were procured from an outside supplier. The copper wick samples in the form of solid cylinders were fabricated in the laboratory by a sintering process. Three different samples of copper wick were manufactured by using copper powder of different grain sizes as follow:

- # 100-200 mesh size copper powder
- # -200 mesh size copper powder
- # -350 mesh size copper powder

Note that these numbers specifies the range of the granule sizes that are contained in the given powder sample. For example, # 100-200 mesh size powder means that granules with size in the range of # 100-200 mesh number are contained in the given powder sample. The # -200 mesh size means that powders with granule sizes less than 200 mesh number are contained in this sample. Mesh size is the unit to measure the granule size of the powder. The # 100 mesh number means 100 granules of the designated powder can be contained in the given area of one inch square (6.45 cm²).

Sintered metal wicks such as those made from copper and nickel can be obtained in relatively small pore sizes and high porosity compared with plastic wicks. Copper due to its high thermal conductivity helps to achieve very high values of heat transfer coefficient in the evaporation zone. It has a very strong chemical compatibility and wettability with water, which is the most widely used heat transfer fluid inside two-phase systems.

Porous plastic wicks used in the study were made from the high molecular grade of the polyethylene known as Ultra High Molecular Weight (UHMW) Polyethylene. The UHMW Polyethylene is a long chain linear polymer of ethylene with an extremely high molecular weight in the range of 3.1 million atomic mass units (amu) or above. The UHMW Polyethylene is a Food and Drug Administration (FDA) compliant material that is used in a

wide range of filtration and separation applications. The high molecular weight gives a unique combination of properties including high impact strength, low coefficient of friction and abrasion resistance, which outwears carbon steel, thus making it more suitable for the applications where lower molecular weight grades fail. UHMW Polyethylene is naturally hydrophobic (water repellent) but it can be made hydrophilic (water absorbent) and favourable to work with different chemicals by special treatment procedures. These might include application of different surfactants (surface modifying end groups) that are covalently bonded to the base polymer during synthesis. In another process known as plasma treatment (Nickerson 1998), the substrate is exposed to ionized gas to impart different properties to it. This method has an advantage that no additives are adhered to the surface so it leaves virtually no residual chemicals that can later dislodge from the surface.

C.3 Experimental Scope

The experimental methods devised in this study are very simple to set up and gave very accurate and consistent results for the flow properties of the porous media. Results of such experiments can assist in the investigation of heat transfer characteristics and flow through porous media. This helps in better understanding of the physical behaviour inside loop evaporators. The methods described are simple and do not require the construction of any complicated experimental equipment. Also, due to the simple nature of these experiments the interactive parameters and instrumentation errors are minimised, and the results are consistent when repeated.

C.4 Objectives of the Study

In the present study, laboratory methods to determine the effective thermal conductivity of a wick saturated with liquid, and physical properties of the wick including permeability, pore size and porosity are presented.

C.5 Physical Properties

The physical properties that are of importance to the proper functioning of capillary wicks in heat pipes are now considered with respect to the basic concept and the measurement methods.

C.5.1 Permeability

C.5.1.1 Concept

Permeability is a property of porous materials which describes their ability to transport liquid under an applied pressure gradient. The mathematical description of liquid flow in porous media is based on the Darcy's law, which states that the volumetric flow rate, V_l^* of liquid through a specimen of porous material is proportional to the hydrostatic pressure difference ΔP_w across the wick specimen, inversely proportional to the thickness/length t_w of the specimen, and proportional to the cross sectional area A_w .

The Darcy permeability, K is indicative of the permeability of a certain medium to a particular fluid. It depends on the properties of both the medium and the fluid. In order to separate the influence of the porous medium from that of the liquid a term known as specific permeability, $k_{ws} = K\mu_l$ is stated, where μ_l is the viscosity of the fluid.

$$k_{ws} = \frac{V_l^* \mu_l t_w}{A_w \Delta P_w} \quad (C.1)$$

C.5.1.2 Measurement

To measure the permeability of a wick structure, two different systems, which differ in the method to maintain constant head across the wick sample, were developed. The wick samples were in the shape of solid and annular cylindrical tubes. In annular cylindrical samples, the central hole was plugged with impermeable material as shown in Figure C.1. The wick sample was force-fitted securely inside the flexible pipe to ensure that liquid only flowed through the wick and did not bypass it. The fluid used for the permeability measurement was water.

In the first method, as shown schematically in Figure C.1, a constant water head is maintained across the wick specimen using a constant pressure reservoir. This reservoir is connected to the water supply and an overflow duct to maintain constant water level in it. The reservoir can be raised or lowered to vary pressure across the wick sample. At steady conditions, the mass flow rate of fluid was measured with the help of a stop watch and a graduated cylinder placed on a sensitive balance. The pressure difference across the sample was found by measuring the

height of the free water surface in the constant pressure reservoir above the top of the sample. This information is used with Darcy law to calculate the specific permeability at different pressures.

The method explained above is straightforward but with this arrangement pressure that can be generated across the sample is limited by the height through which the constant pressure reservoir can be raised. As the wick samples used in the experiment had mean pore radius of the order of micrometers, high pressure tests were considered necessary to validate the results fully.

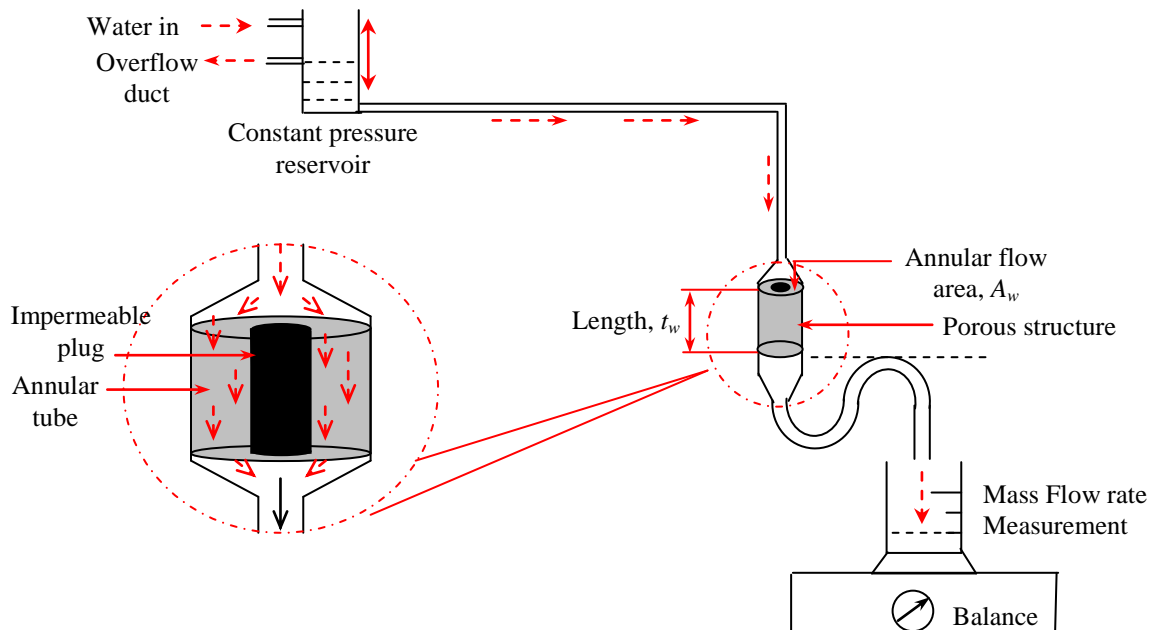


Figure C.1 Apparatus to measure permeability using a constant pressure reservoir

In order to measure the permeability at high pressure, the system shown in Figure C.2 was developed. In this system a pressure regulating arrangement was established to produce high pressures across the wick sample. Pressure indicated by the pressure gauge was set to different values by adjusting the pressure regulating valve. The excess water was drained to the sink with the help of this valve and the desired pressure was maintained across the wick.

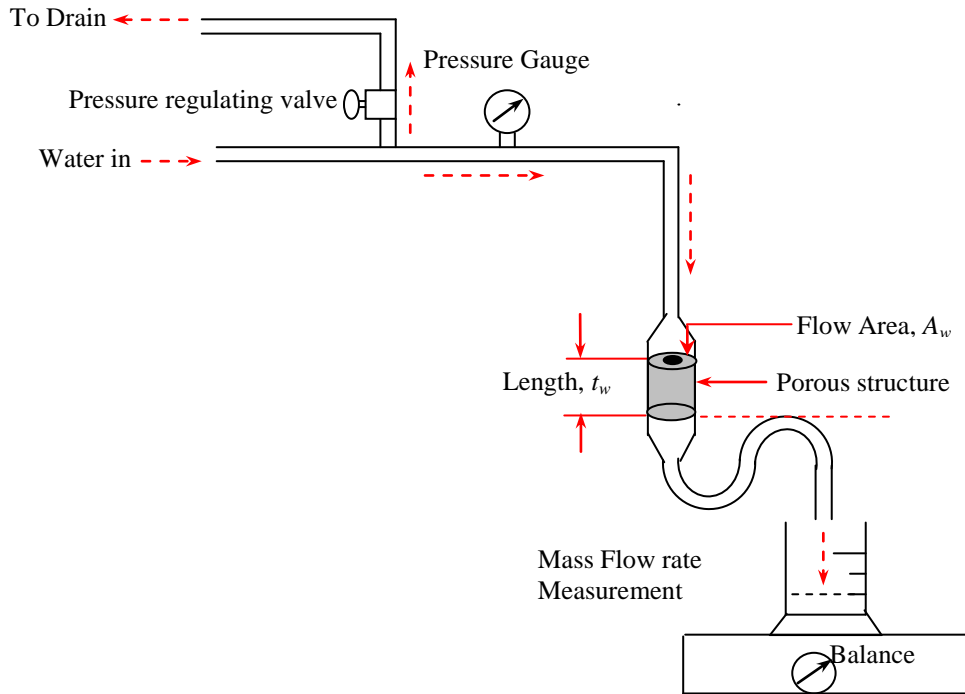


Figure C.2 Apparatus to measure permeability using pressure tuning arrangement

As the pressure across the wick sample is increased the volume flow rate increases. As shown in Figure C.3, the mass flow rate through a porous plastic wick sample showed a nearly linear trend with applied pressure.

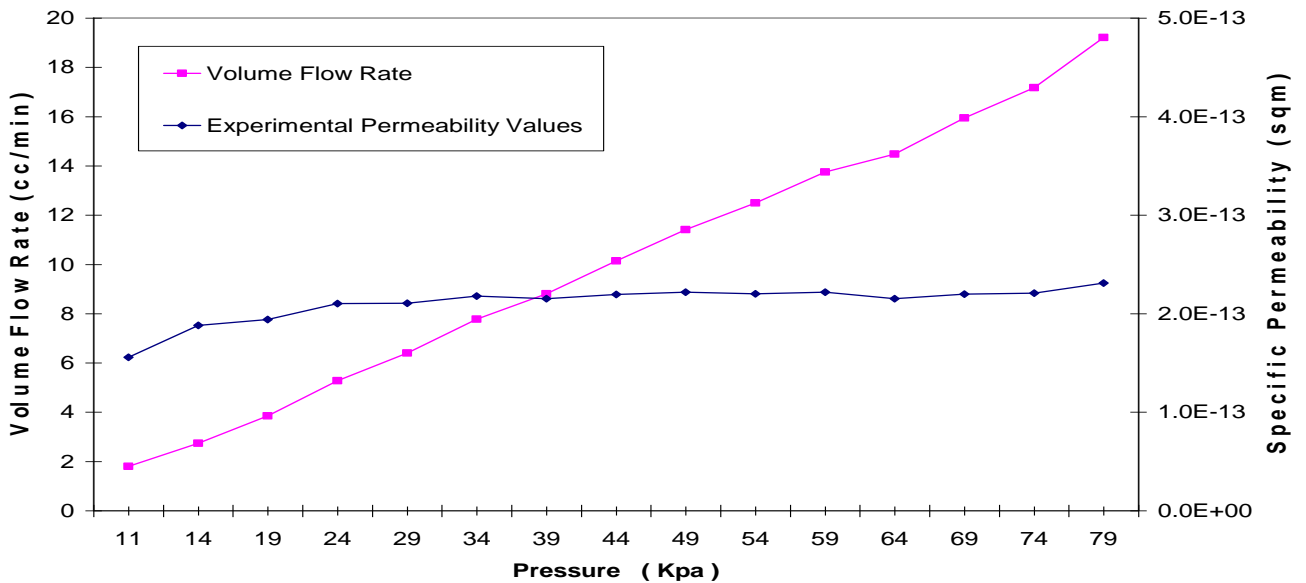


Figure C.3 Variation of specific permeability and mass flow rate with applied pressure across the porous structure

The permeability of the wick sample remained constant at low pressures. For high pressures a slight increase in permeability was observed. This can be attributed to the fact that at high

pressure, viscous forces in the micro pores are overcome and flow is channelled through the micro pores which otherwise retard the flow at low pressure. In some tests permeability decreases with time which can be due to the deposition of impurities and particles from water over the top upstream face of the porous media. Particle deposition resulted from the microscopic nature of the pores, in spite of the fact that filtered water was used in some tests while in others filters were fitted if mains water was used from the tap. The specific permeability calculated from the experimental tests showed close agreement with the permeability value for the UHMW polyethylene wick of $2 \times 10^{-13} \text{ m}^2$ which was provided by the manufacturer. Table C.1 shows the results of the permeability measurements on the different grades of sintered copper wick. The testing was done under constant pressure of 40 KPa that was maintained across the wick sample using the pressure regulating arrangement discussed above.

Table C.1 Permeability measurement for different types of copper wick

Copper Wick Sample (Mesh Number)	Specific Permeability (m^2) $\times 10^{-11}$
100-200	1.08 – 1.79
-200	0.36 - 0.72
-350	0.15 - 0.44

C.5.2 Pore Radius

C.5.2.1 Concept

Extremely small voids in a solid are called molecular interstices and very large ones are called caverns (Scheidegger, 1974). Pores are void spaces intermediate in size between caverns and molecular interstices which are distributed more or less frequently throughout the porous material. In a permeable material the pore spaces are interconnected. Due to the inherent process of manufacturing by powder processing technology, pores of different size exist inside the porous medium. The range of the pore radii within a given sample is largely dependent upon the powder size, powder density and the sintering temperature during processing. The effective pore radius is used to determine the pumping capability of a wick. A measuring technique was used for determining the mean or effective pore radius of the given specimen. In addition to the effective pore radius, the largest pore radius in the given

specimen is very important to validate the operation of the loop heat pipe under given heat load. Unlike for conventional heat pipes, the capillary structure in the loop system must provide hydraulic/vapour locking from the evaporator to the compensation chamber. If the total pressure losses inside the loop exceed the capillary pressure on the working fluid generated by the largest pore, dry-out of this pore will result. Eventually this will provide the least resistance vapour flow passage from the evaporator to the compensation chamber thereby hampering the loop operation. It can therefore be argued that information of the largest pore size is very necessary in the design and thus successful operation of loop heat pipes. Following the current line of discussion, methods were devised to measure the value of the largest pore size in the given sample of the porous structure.

C.5.2.2 Measurement

C.5.2.2.1 Measurement of Largest Pore Radius

The largest pore radius of the wick sample was measured using a U-tube bubble point testing system as illustrated in Figure C.4. A PVC tube is bent in the form of a U shape with one leg longer than the other. The centre hole of the wick sample is plugged, in case of the annular cylindrical samples, and the wick is fitted on the shorter leg of the U-tube. A pool of liquid is maintained over the wick and an air pocket is formed below it by pouring water from the other leg. The air pressure under the wick is increased in small increments by putting more liquid into the extended stem of the U-tube.

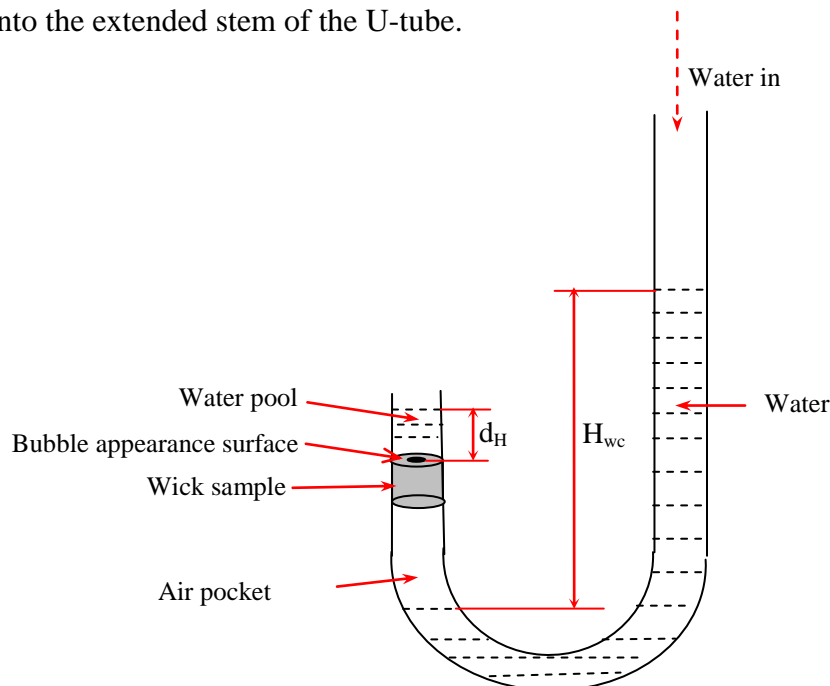


Figure C.4 U-Tube bubble point testing system

The hydrostatic pressure due to the height of the water column in the longer leg of U-tube results in increase of pressure in the air pocket. When this air pressure due to height of the water column equals the surface tension forces of water then bubbles will appear on the surface of the wick as shown in the Figure C.5. The liquid-air interface exists at the top of the wick, from which the bubbles emerge. When the first bubble appears, the procedure is to stop adding water to the tube and note the hydrostatic height. More water is then added to the point that the bubble starts departing the porous surface. This helps to validate that the bubble do not pre-exist there and was formed due to the applied pressure. If H_{wc} is the height of the water column in the extended stem of U-tube and d_p is the pool depth over the first bubble, then the largest pore radius, r_{max} of the wick sample is given by equating surface tension force with the hydrostatic force due to the height H_{wc} of the water column as follows:

Assuming a hydrophilic wick where the contact angle is very small

$$2\pi r_{max} \sigma_l = \pi r_{max}^2 (H_{wc} - d_p) \rho_l g \quad (C.2)$$

$$r_{max} = \frac{2\sigma_l}{(H_{wc} - d_p) \rho_l g} \quad (C.3)$$

Where, σ_l and ρ_l are the liquid surface tension and liquid density respectively. In order to obtain valid results water was used as the working fluid which provided good wetting quality with the hydrophilic UHMW polyethylene wicks and copper wicks.

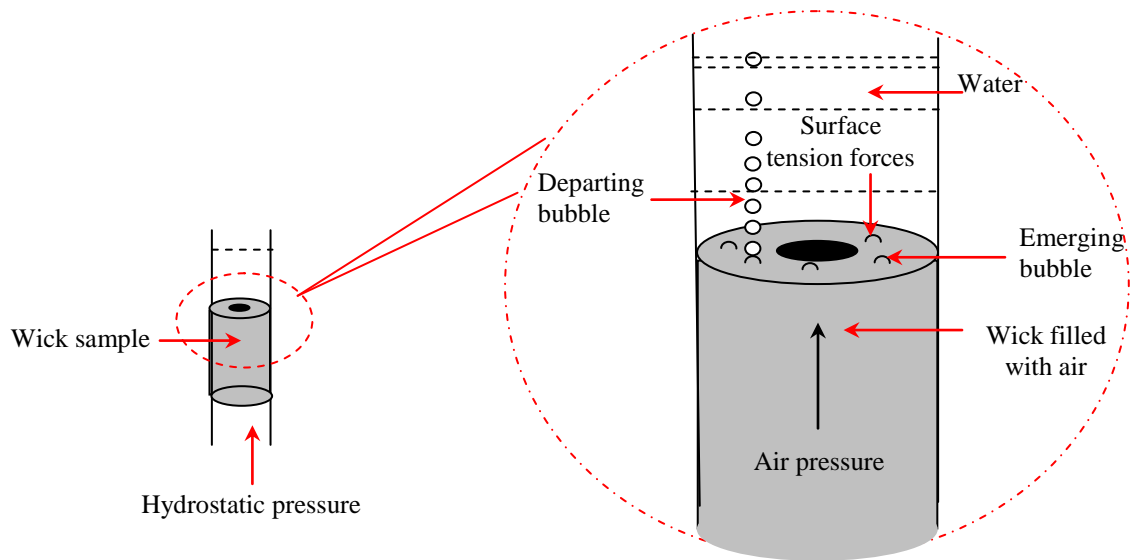


Figure C.5 Mechanism of bubble formation

Results obtained from the U-tube bubble point testing system for nine samples of hydrophilic UHMW wick with pore radii believed by the manufacturer to be in the range of 4 to 10 μm and with water as the working fluid, are shown in Table C.2. In the Table $\Delta H_w = (H_{wc} - d_p)$ is the head difference across the wick meniscus when a bubble first emerges and r_{max} is the associated deduced maximum effective pore radius of the wick sample.

It was noted that the samples from the same tube/batch showed different pore sizes owing to the process of manufacturing by powder technology which resulted in range of pore radii.

Table C.2 Largest Pore radius for UHMW Polyethylene wicks measured with U-tube bubble point testing system.

ΔH_w (m – H ₂ O)	r_{max} (μm)
1.75	8.53
1.72	8.69
1.65	9.06
1.389	10.83
1.36	11.04
1.02	14.65
0.981	15.44
0.95	16.05
0.834	18.27

It should be noted that the above method gives the largest pore size in the test sample, which in most cases is more than the mean value of 7.8 μm as provided by the manufacturer. In order to determine average largest pore size, different samples from the given specimen were used to perform bubble point testing.

The above approach had a limitation imposed by the maximum hydrostatic height that can be achieved by the liquid column in the longer leg. In case of a fine pore wick, height up to several meters may be required to initiate the bubble on the top surface of the wick which was impractical. To solve this problem, another approach to exert air pressure under the wick was

developed. In this technique, the liquid column was replaced with the piston and cylinder arrangement shown in Figure C.6. The air pressure under the wick sample was increase in small increments by putting force on the piston. A digital pressure gauge was used to measure the air pressure at the bottom of the wick. Equation (C.2) can be modified for the given method as follow:

$$2\pi r_{\max} \sigma_l = \pi r_{\max}^2 (P_a - d_p \rho_l g) \quad (\text{C.4})$$

$$r_{\max} = \frac{2\sigma_l}{(P_a - d_p \rho_l g)} \quad (\text{C.5})$$

where, P_a is the air pressure under the wick as measured from the pressure gauge.

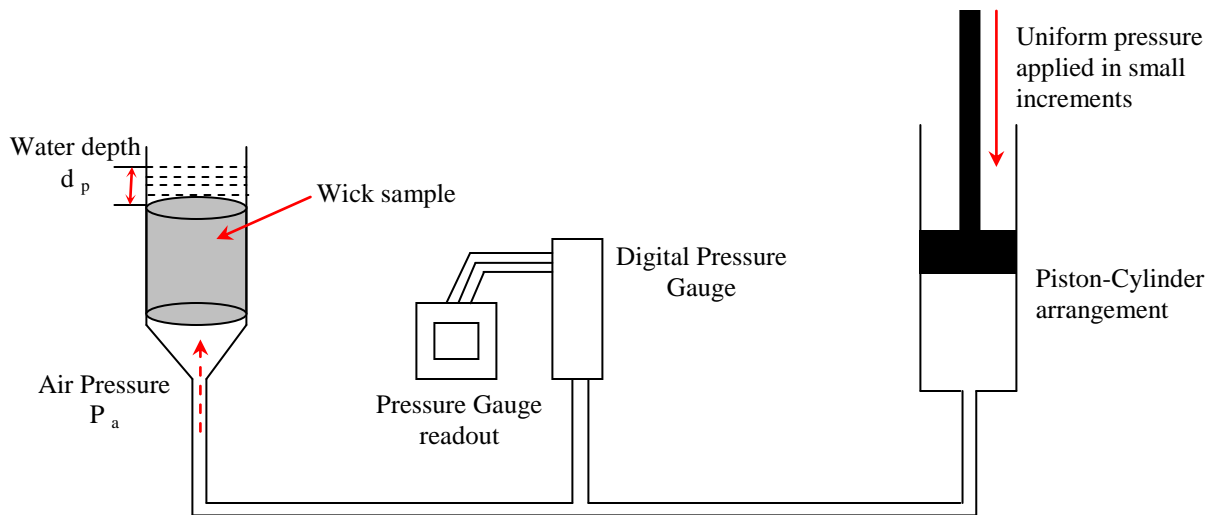


Figure C.6 Modified form of bubble point testing system to measure the largest pore size in the fine pored wicks

The results of the experiments on the copper wick samples by using the above approach are given in Table C.3

Table C.3 Largest pore radius measurement for different grades of copper wick with the help of U-tube bubble point testing system.

Sample (no)	Water Height above wick- d_p (cm)	Air pressure under the wick- P_a (Pa)	r_{max} - Pore radius (μm)
100-200 (1)	0.8	5000	29.62
100-200 (2)	1	4000	37.36
100-200 (3)	1	5000	29.73
100-200 (4)	1	4000	37.36
-200 (1)	0.8	10000	14.69
-200 (2)	0.5	12000	12.20
-200 (3)	0.5	10000	14.65
-200 (4)	0.5	10000	14.65
-350 (1)	1	14000	10.48
-350 (2)	1	11000	13.37
-350 (3)	0.5	16000	9.14
-350 (4)	0.5	17000	8.60

C.5.2.2.2 Measurement of Effective Pore Radius

In another method steady state height gained by the fluid in the wick was used to determine the mean pore radius of the wick sample directly. The wick sample was in the shape of a hollow tube of UHMW polyethylene with OD 25 mm, ID 13 mm and length 440 mm. In order to note the height gained by fluid in the wick it was marked with temporary colour that dissolves when it comes into contact with the working fluid which was ethanol in this case. This method is based on the principle that working fluid with high surface tension like water will achieve relatively higher steady state height compared to the low surface tension fluids like ethanol. As wick samples of limited length were available for the experimentation therefore ethanol was used as the test fluid. Due to the high affinity of the alcohol towards hydrophobic plastics, wick structure made from the natural grade of UHMW which is water repellent was used in the experiment.

The sample was covered with a transparent sheath to avoid evaporation of the fluid from the porous surface and then placed perpendicular to a dish containing ethanol as shown in Figure C.7. The fluid attains steady height when the gravitational head balances the maximum capillary head.

$$i.e. \frac{2\sigma_{et}}{r_{me}} = \rho_{et} g H_{ec} \quad (C.6)$$

where σ_{et} , ρ_{et} , are the surface tension and density of the ethanol respectively, H_{ec} is the steady height attained by ethanol column and r_{me} is the effective pore radius of the wick sample.

For the wick sample with manufacturer specified mean pore radius of 20 μm , the method gave a reading of 20.79 μm which, assuming the manufacturer was correct gives confidence in the integrity of the experimental method.

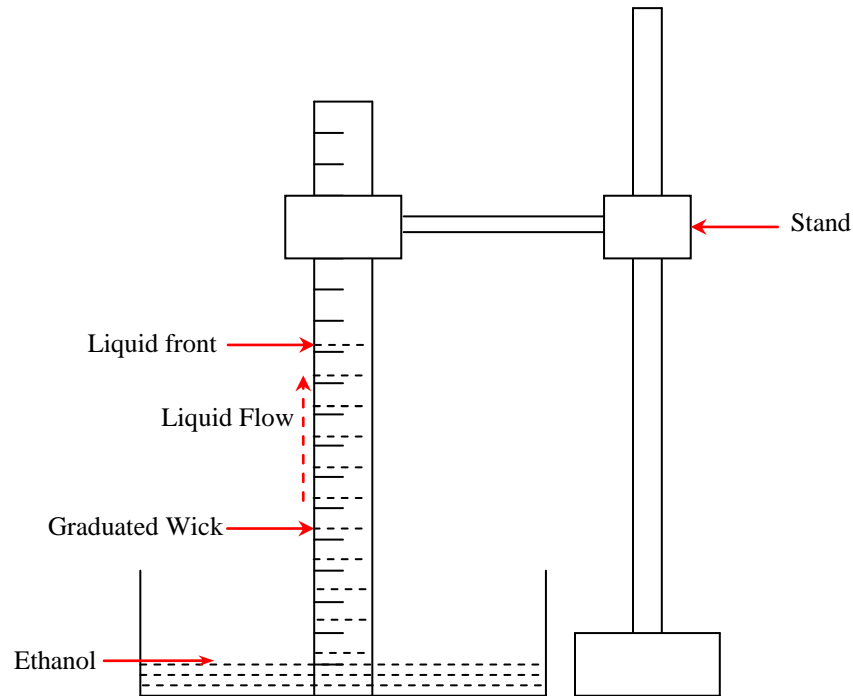


Figure C.7 Method to determine mean pore size of the wick sample

C.5.3 Porosity

12.5.3.1 Concept

Porosity is defined as the ratio of the void volume to the total (bulk) volume of the wick sample. It is the fraction of the cross section available for fluid flow. Normally, it is expressed either as a fraction or a percentage of the total volume.

Porosity (ϵ) of a porous material is given by:

$$\epsilon_w = \frac{V_{ps}}{V_{sp}} \quad (C.7)$$

where V_{ps} and V_{sp} is the volume of porous space (i.e. pores) and specimen respectively

Porosity of a wick sample can be adjusted and customized to meet requirements by using powder of different sizes and changing sintering temperature during the manufacturing process. Sintered wick structures have uniform porosity in all three axes which is vital for constant liquid flow. In its naturally hydrophobic state, porous UHMW polyethylene is an excellent medium to work with laboratory solvents like alcohols, ketones, aromatics and strong organic acids and bases. For aqueous solutions the material can be converted to a hydrophilic form by various methods such as surfactant coating and plasma treatments as discussed before. Copper is strongly hydrophilic and shows very good wetting characteristics with water.

C.5.3.2 Measurement

Basically two methods were employed to measure the porosity of the hydrophilic as well as hydrophobic UHMW-Polyethylene wick samples and different grades of copper wick. Proper care was taken to dry the sample before measurements in order to get rid of any absorbed moisture from the atmosphere. Precise measurements for mass were done using a mass balance of sensitivity 0.01 grams. In the first method the bulk density (ρ_w) of the wick or porous medium is determined by measuring the outside dimensions (i.e. outer radius, inner radius and length) and weighing the sample on the balance. As the density (ρ_{wm}) of the material of wick (i.e. UHMW-polyethylene or copper material) making up the wick sample is known in the non-porous state, porosity (ϵ_w) of the specimen can be calculated as follows.

$$\rho_w = \rho_{wm}(1 - \varepsilon_w) \quad (\text{C.8})$$

$$\therefore \varepsilon_w = 1 - \frac{\rho_w}{\rho_{wm}} \quad (\text{C.9})$$

This method, known as the density method, gave very accurate and consistent results when compared with the porosity values given by the manufacturer, as shown in the Figure C.8.

In the second method known as the soaking method, the sample of porous medium being tested was placed in a dish containing enough liquid to soak the sample completely. While placing the sample in the pool of liquid it is important to ensure that no air bubbles keep sticking to the wick which might inhibit the process of absorption of liquid into the pores. Keep the wick dipped until a free standing layer of liquid is observed on the top of the sample. By measuring the mass of the dry porous medium and the soaked porous medium, the volume of the liquid that was soaked up can be determined. This volume V_{ps} is same as the volume of the pore spaces. If V_{sp} be the measured volume of the specimen then porosity (ε_w) can be determine by taking their ratio. The soaking method was performed on hydrophilic UHMW-PE wick samples using water and ethanol as the test fluids and on hydrophobic UHMW-PE wicks using ethanol as the test fluid. Results of experiments are shown graphically in Figure C.8.

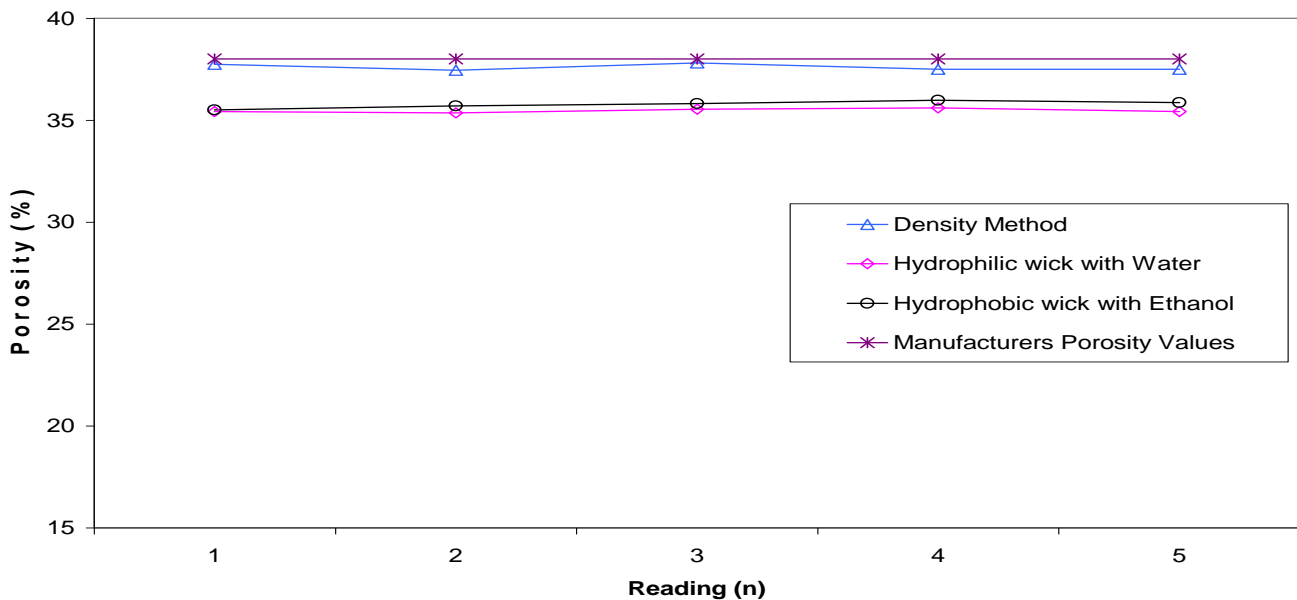


Figure C.8 Comparison of porosity of the UHMW Polyethylene wick as determine by different methods

In the soaking method, porosity values determined by using a hydrophilic wick with water and a hydrophobic wick with ethanol as the working fluid predicted values somewhat less than the actual values given by the manufacturer. The difference arises presumably due to manufacturing defects like close spaces, dead ends or improper wetting of the wick substrate by working fluid.

Outcomes of testing with copper wicks by using water as the working fluid are presented in Table C.4.

Table C.4 Porosity measurement for different grades of copper wick

Sample	Porosity by Density Method (%)	Porosity by Soaking method (%)	Porosity value by Manufacturer Value (%)
<i>100-200</i>	40.03 – 41.12	34.89- 37.36	42.35
<i>-200</i>	45.06 – 46.03	40.94- 44.12	46.67
<i>-350</i>	48.82 – 50.15	45.95-49.94	50.29

It is clear from the results that the density method which is simple and straightforward gave better results than the soaking method.

C.5.4 Effective Thermal Conductivity

C.5.4.1 Concept

Thermal conductivity, k of the material relates to its ability to conduct heat. It is defined as a quantity of heat, Q^{\bullet} , transmitted through a thickness, t , in a direction normal to a surface of area, A , due to a temperature gradient, ΔT , under steady state conditions. The definition can be mathematically expressed as follow:

$$k = \frac{Q^{\bullet}t}{(\Delta T)A} \quad (\text{C.10})$$

Since the porous structures are widely used as wicking structures in two-phase heat transfer devices, the effective thermal conductivity of the porous wick saturated with liquid is of great interest for the design and performance evaluation of these devices. Effective conductivity of the wick is a very important parameter to be considered during the choice of the wick material and design of the capillary evaporator. Different correlations have been developed by researchers worldwide for this purpose. Because of the large difference in thermal conductivity of the wick material and the saturating liquid and sharp dependence of effective thermal conductivity on the porosity of the wick, the predictions made by these correlations are not always satisfactory. Consequently, an experimental approach to estimate the effective thermal conductivity of the saturated wick is needed.

C.5.4.2 Measurement

An experiment was conducted to determine the effective thermal conductivity of a copper wick saturated with water. A copper container was prepared in the shape of rectangle and then fitted with a tube for vacuuming and charging purpose as shown in Figure C.9. The container was thoroughly cleaned by using acetic acid to get rid of any impurities. After this, it was filled with the copper powder of #100-200 mesh number and sintered. During the sintering process proper care should be taken to provide proper attachment between the heat transfer surfaces of the container and the wick.

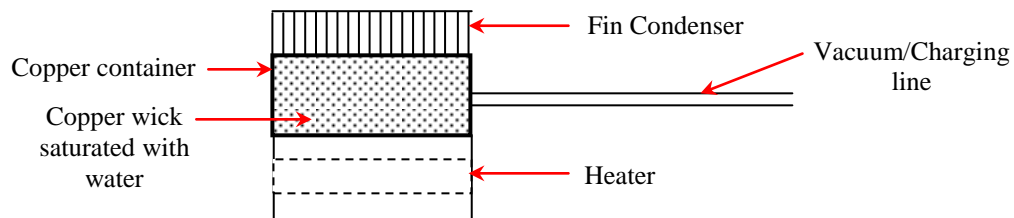


Figure C.9 Test sample showing the location of the heater and the finned heat exchanger

To ensure a high degree of saturation of the wick with the working fluid, first the air was evacuated from the wick using a vacuum pump and then it was charged with the degassed and distilled water. After charging, the copper line was permanently sealed. A condenser in the

form of a fin heat exchanger was fixed to one side of the sample using thermal epoxy. It should be noted that soldering or welding should be avoided to prevent any changes in wick properties including its oxidation. Forced air flow was ducted through the condenser by using a centrifugal fan. A heat load simulator made from a copper block, embedded with two cartridge heaters was attached to the opposite side of the condenser. The heat source and the sample were completely shielded using fiber wool glass insulation to prevent any heat losses to the environment. A digital power meter was used to input precise heat loads to the source. Temperatures at different locations were monitored and measured using T-type thermocouples with an error of ± 0.5 °C. Figure C.10 shows the experimental setup along with the location of the temperature measurement points.

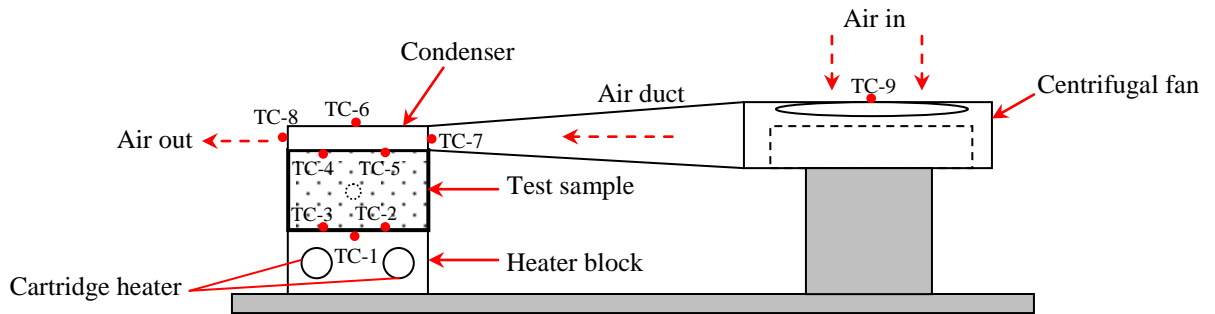


Figure C.10 Experimental setup for measuring the effective thermal conductivity of the copper wick saturated with water

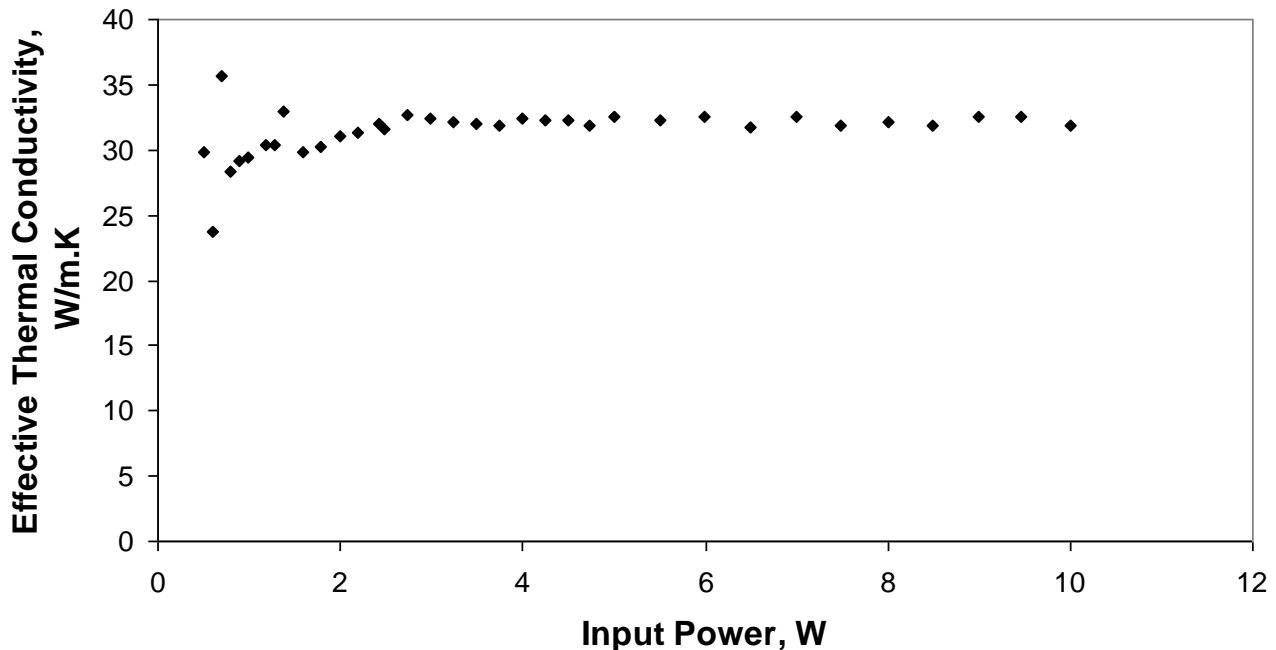


Figure C.11 Effective thermal conductivity versus applied heat load for the copper wick saturated with water

During testing the heat load was applied in the range of 0.1 – 10 W by varying the input power in steps of 0.5 W while maintaining constant conditions at the condenser. Figure C.11 presents the result of the experiment as a plot of effective thermal conductivity of the wick against applied heat load. It is clear that the effective thermal conductivity of a water saturated copper wick showed a constant value of $32 (\pm 2)$ W/m.K in the range of applied heat load and demonstrated the reliability of the experimental method.

Prediction for the effective thermal conductivity of the wick, k_e was made on the basis of the correlation proposed by Alexander (1972) as:

$$k_e = k_l \left(\frac{k_l}{k_w} \right)^{-(1-\varepsilon)\alpha} \quad (\text{C.10})$$

Where, α is the constant equal to 0.59.

k_l and k_w is the thermal conductivity of the saturating liquid and the wick material and ε is the porosity of the wick structure.

It was seen that the values predicted from the correlation showed a satisfactory agreement with the experimental measurements only if the porosity values used in the relation are higher than the experimentally predicted porosity value by 10-15%. For example, the predicted values for the k_e shows close agreement with the experimental values and lies between 27.71 – 36.20 W/m.K for the porosity in the range of 55 – 60%. However for the wick sample, the experimentally determined porosity value is 40-45%. This discrepancy in the predicted and experimental results can arise due to the errors introduced by number of unaccountable factors that include improper contact point between the wick and container wall, natural convection of the fluid inside the wick, vapour bubble formation inside the sample, incomplete saturation of the wick with the liquid etc. To classify the effect of these factors detailed study on the determination of the k_e that look precisely at these factors should be carried out.

C.6 Summary

Test procedures to determine the physical properties including permeability, pore radius and porosity, and material property i.e. effective thermal conductivity of the porous structures are considered in detail in this chapter. The study was done using hydrophilic and hydrophobic

grades of ultra high molecular weight polyethylene (UHMW) wicks and copper wicks made from powder of different granular sizes. Permeability of the wick was tested at low as well as high pressure using different test arrangements. It was seen that the permeability readings at high pressure were larger due to the increase in flow rate through the micro pores as the viscous forces are overcome at such pressures. Pore radius of the wick sample was measured using two different methods. The bubble point testing method gave the largest pore radius in the test sample, and the method that gave mean pore radius made use of the steady height achieved by the fluid under capillary head. The second method gave results that were in close agreement with the manufacturer's specified values. Porosity of hydrophilic as well as hydrophobic UHMW polyethylene wicks and copper wicks was determined by a density method and a soaking method using appropriate working fluids. The density method showed better results than the soaking method due to the problems of incomplete wetting of the wick by the fluid or presence of close spaces and dead ends in the porous media. Also, a simple method to determine effective thermal conductivity of the copper wick saturated with the water was conducted. The experiment gave a constant value of the effective thermal conductivity over the test range of applied power. However, further work needs to be done for the precise determination of the effective thermal conductivity of the liquid saturated porous structure.

Results of the various experiments explained in this study showed close agreement with the manufacturer's values of the physical properties of the wicks. These methods are applicable to hydrophobic as well as hydrophilic wicks when used with working fluids that exhibit good wetting characteristics with the test sample. Also, these methods are simple to set up.